TECHNISCHE
UNIVERSITÄT
DRESDEN

Pulsed-perturbative QED:

A study of trident pair production in pulsed laser fields

Dissertation

zur Erlangung des akademischen Grades
Doktor rerum naturalium

vorgelegt von

Uwe Hernandez Acosta

INSTITUT FÜR THEORETISCHE PHYSIK
FAKULTÄT PHYSIK
BEREICH MATHEMATIK UND NATURWISSENSCHAFTEN
DER TECHNISCHEN UNIVERSITÄT DRESDEN

2020

Eingereicht am: 16. Juli 2020

Verteidigt am: 9. März 2021

1. Gutachter:	Prof. Dr. Thomas E. Cowan
2. Gutachter:	Prof. Dr. Ralf Schützhold
3. Gutachter:	Prof. Dr. Burkhard Kämpfer

Abstract

Modern laser facilities provide highly intense light with a very short temporal structure, which brings the phenomena originally found near the strong radiating stars in the universe into the laboratory. Accordingly, there are, among others, wide theoretical investigations w.r.t. scattering processes of particles impinging this extreme light sources. This has been done by applying the strong-field quantum electrodynamics, which is a theory of electromagnetic interactions within coherent highly intense light treated as a semi-classical background field. For instance, the treatment of the Compton process (inelastic electron-photon scattering) and the Breit-Wheeler process (pair production of a collision of two photons) with strong-field quantum electrodynamics revealed a vast amount of novel non-linear structures and phenomena, which were to some extent experimentally verified. Of particular interest and the central object of investigation within this thesis is also the trident process: a second order process in (strong-field) quantum electrodynamics producing an electron-positron pair within the collision of a photon beam (e.g. produced by a laser) with a counter-propagating electron. However, in the context of highly intense fields, the trident process is more than the product of its parts, the mentioned Compton and Breit-Wheeler process, since the intermediate photon yields both virtual and real contributions producing exceedingly complicated structures. Over the last years, there are several theoretical contributions to the non-linear treatment of the trident process w.r.t. a wide range of laser properties, but the trident process has not yet been fully understood due to its demanding mathematical nature.

Within the present thesis, we focus on the dependence of the trident process to the short temporal structures of the involved light source at high energies. Loosely speaking, this means the short pulsed structure of modern light sources provide a wide energy spectrum of the respective photons, which is imprinted on the considered scattering processes. Accordingly, we elaborate a new approximation to strong-field quantum electrodynamics capable to describe the spectral dependence of processes within laser-electron collisions at high energies. Then we apply this new approximation to the trident process and reveal

the novel structures generated by the spectrum of the light source. Therefore, we provide an analysis of the spectral impact to the trident process involving the total cross section as well as several inclusive and exclusive distributions of its final particles. Consequently, we examine in principle the experimental capabilities of present or planed extreme light sources by combining them with a suitable electron beam, whether they are sensitive to the encountered spectral effects of the trident process and discuss further applications of the newly introduced approximation.

Kurzdarstellung

Moderne Lasereinrichtungen stellen hochintensives Licht mit sehr kurzer zeitlicher Struktur zur Verfügung. Damit bringen diese Einrichtungen die Phänomene in die Laboratorien, welche normalerweise nur in der Nähe von stark strahlenden Sternen im Weltall zu finden sind. Bezüglich der Streuprozesse von Teilchen innerhalb dieser extremen Lichtquellen gibt es eine Vielzahl an theoretischen Untersuchungen. Vorwiegend geschehen diese unter der Verwendung der Starkfeld-Quantenelektrodynamik, einer Theorie zur quantentheoretischen Beschreibung von elektromagnetischen Wechselwirkungen innerhalb eines kohärenten hochintensiven Feldes, welches als semi-klassisches Hintergrundfeld beschrieben wird. Zum Beispiel zeigte die theoretische Behandlung des Compton-Prozesses (die inelastische Elektron-Photon-Streuung) oder des Breit-Wheeler-Prozesses (der Paarproduktion in der Kollision von zwei Photonen) innerhalb der Starkfeld-Quantenelektrodynamik eine große Menge an neuen nicht-linearen Effekten und Phänomen, welche stellenweise in zukunftsweisenden Experimenten nachgewiesen werden konnten.
Von großem Interesse und auch zentrales Untersuchungsobjekt der vorliegenden Arbeit ist ebenso der Trident-Prozess: ein Prozess zweiter Ordnung in der (Starkfeld-) Quantenelektrodynamik, bei dem ein Elektron-Positron-Paar innerhalb der Kollision eines Photonstrahls (z.B. erzeugt von einem Laser) und eines gegenläufigen Elektronenstrahls entsteht. Allerdings ist der Trident-Prozess im Zusammenhang mit hochintensiven Feldern nicht ausschließlich das Produkt seiner Teile, den erwähnten Compton- und Breit-Wheeler-Prozessen, vielmehr erzeugt das Vorhandensein des intermediären Photons durch seine virtuellen und reellen Beträge überaus komplizierte Strukturen. In den letzten Jahren gab es daher eine große Menge an theoretischen Beiträgen zur nicht-linearen Behandlung des Trident-Prozesses bezüglich eines weiten Bereichs an Eigenschaften der verwendeten Lichtquelle. Jedoch ist der nicht-lineare Trident-Prozess wegen seiner anspruchsvollen mathematischen Natur bisher nicht als völlig verstanden anzusehen. In der vorliegenden Arbeit liegt der Fokus auf der Abhängigkeit des Trident-Prozesses von den kurzen zeitlichen Strukturen der verwendeten Lichtquellen bei hohen Energien. Grob gesprochen

bedeutet dies, dass die kurz gepulsten Strukturen der modernen Lichtquellen zu breiten Spektren der Photonstrahlen führen, welche sich dann auch in den betrachteten Prozessen widerspiegeln. Demfolgend wird in der vorliegenden Arbeit eine neue Approximation an die Starkfeld-Quantenelektrodynamik erarbeitet, welche in der Lage ist, die spektralen Abhängigkeiten in den Prozessen zu beschreiben, die in Laser-Elektron-Kollisionen bei hohen Energien vorzufinden sind. Diese neue Approximation wird dann auf den Trident-Prozess angewendet und es werden die neuen Strukturen herausgearbeitet, welche durch das breite Spektrum der betrachteten Lichtquelle entstehen. Ferner werden bestehende oder geplante extreme Lichtquellen dahingehend untersucht, in welcher Weise diese, kombiniert mit einem passendem Elektronenstrahl, sensitiv für die vorgestellten spektralen Effekte im Trident-Prozess sind. Abschließend werden weitere mögliche Anwendungsbereiche der neuen Approximation diskutiert.

Contents

1 Introduction

The primary motivation of theoretical physics is the modeling of phenomena in nature by the use of a system of equations, i.e. a theoretical model, where the main ambition is predicting as many as possible observables using as few as possible parameters. It becomes experimentally apparent that every physical phenomenon in nature is ascribable to four fundamental interactions: the gravitation, the electromagnetic interaction as well as the weak- and the strong nuclear interaction. In this context, one of the most precise theory describing nature on a fundamental level (in the absence of gravity) is the standard model of particle physics (originally proposed in [307]). This theory is a conceptional combined description of the strong interaction, by the theory of quantum chromodynamics and electro-weak interaction employing the Glashow-Weinberg-Salam theory (GWS; originally in [100, 254, 307]).

One of the pillars of the standard model of particle physics (as one of the results of the spontaneous symmetry breaking in the Higgs sector of the GWS theory) is the description of the electromagnetic interaction in the context of the theory of quantum electrodynamics (QED; originally in [76, 87, 88, 264, 265, 295]), which combines the classical electrodynamics (by means of Maxwell's equations) with quantum mechanics. Several calculations made in QED using the series expansion of certain quantities in its coupling α (also referred to as perturbation theory) are ranked as the most precise predictions w.r.t. high-precision experimental measurements (see, e.g., [83] for further details). For instance, the prediction of the anomalous magnetic moment of the electron using QED perturbation theory (currently up to $\mathcal{O}(\alpha^5)$; see [14, 15]) shows an outstanding agreement with the experimental results with an exact match of ten significant digits [112]. This great success of perturbation theory gives QED the reputation of the most precise theoretical model in physics.

First as a conceptional study and later highly motivated through the invention of the laser (light amplification by stimulated emission of radiation [181] based on [258] and originally conceived in [80]), there was, and still is, a high demand on considering coherent electromagnetic fields with high intensities within the framework of QED. As it turns out, the involvement of highly intense fields leads to qualitatively different and novel non-linear phenomena, which require a non-perturbative treatment.

Vacuum pair production

One of the first investigated example of such non-linear phenomena is the spontaneous production of particle and anti-particle pairs from the vacuum in the presence of a high-intensity static electric field, also referred to as the Sauter-Schwinger effect [129, 257, 263]. Considering the QED vacuum, i.e. the quantised state with minimum energy, there are always virtual electron-positron pairs (as well as heavier particle anti-particle pairs, but much less likely) produced by quantum fluctuations, which annihilate after a short period of time in agreement with the Heisenberg uncertainty relation. The mean distance of these pairs is in the order of the Compton wavelength $\lambda_{\mathrm{C}} = \frac{h}{mc}$, where h denotes the Planck constant, m is the mass of the electron and c is the speed of light in vacuum. Thereby the Compton wavelength λ_{C} acts as the fundamental length scale of QED. In the presence of an electromagnetic field, e.g. a static electric field E, the dipoles formed by the electron-positron pairs are aligned along the field lines yielding a polarisation of the vacuum. However, if the electric field exceeds a critical value E_{S}, where the produced particles gain energy of mc^2 along the distance of the Compton wavelength, the electron-positron pairs become real and one has actual pair production out of the vacuum. Here, the critical electric field is given as $E_{\mathrm{S}} = \frac{m^2c^3}{e\hbar} \approx 1.32 \times 10^{16}\,\mathrm{V/cm}$, where $\hbar = \frac{h}{2\pi}$ denotes the reduced Planck constant, which is commonly referred to as the critical Schwinger field or shortly the Schwinger limit [263]. Equivalently one has the critical field intensity $I_{\mathrm{S}} = \frac{c\varepsilon_0}{2}E_{\mathrm{S}}^2 \approx 2.32 \times 10^{29}\,\mathrm{W/cm^2}$ with the vacuum permittivity ε_0, which is also associated with the Schwinger limit. However, for field intensities below the Schwinger limit, the pair production via the Sauter-Schwinger mechanism is usually highly suppressed. For instance, considering a homogenous constant electric field E, the pair production probability P scales in the leading order like $P \sim E^2 \exp\left(-\pi\frac{E_{\mathrm{S}}}{E}\right)$. Nevertheless, in order to enhance the pair production rate, extensive investigations had been done, for instance, w.r.t. possible configurations of the electric and magnetic field (see, e.g.,[10, 18, 37, 43, 74, 106, 126, 159, 196, 246, 252]), by combining high-intensity electromagnetic fields with the strong Coulomb field of heavy nuclei or ions (see, e.g., [57, 58, 60, 89, 203–205, 240, 241]) as well as by considering the superposition of two or more different light sources (see, e.g., [7, 9, 42, 73, 86, 121, 142, 143, 226–230, 233, 262, 296–298]). A more detailed outline of the different aspects of the Sauter-Schwinger mechanism as well as their experimental implications can be found in the review articles [61, 98, 114].

Non-linear scattering processes

Another possible point of view for the investigation of non-linear QED phenomena, and rather complimentary to the Sauter-Schwinger mechanism, is given by the scattering processes of probe particles with a coherent and highly intense electromagnetic field. Here the electromagnetic field is divided into a coherent part, which will be treated in a (semi-)classical way as a background field, and a quantised photon field, which interacts with the quantised fermion fields within this background field. This approach is also referred to as the background field approximation (or the Furry picture representation) of QED and provides a powerful model to investigate non-linear QED effects w.r.t. scattering processes.
First, we mention the scattering of an electron with a high-intensity electromagnetic field yielding the emission of a single photon, also referred to as the non-linear Compton scattering, which was initially investigated in the pioneering work of [39, 103, 150, 213, 216–219, 247] (as revised in [117, 124, 164]) by applying the background field approximation, where a (infinitely extended) plane-wave field and a constant-crossed field was used to model the background field, respectively. Since then the non-linear Compton scattering is extensively investigated in the literature w.r.t. a large variety of features of the background field as well as in several different parameter regimes. We mention the involvement of high-intensities and pulsed structures of the light source, e.g. produced by using chirped pulse amplification [283] in modern laser facilities, by applying the pulsed plane-wave approach [29, 30, 124, 173, 176, 212, 267, 269, 275, 292, 294]. In this context, non-linear Compton scattering is established as one of the main test cases for the investigation of analytical and numerical methods, respectively, as well as several approximations, for instance, the slowly-varying envelope approximation [212, 269, 271, 290], stationary phase analysis [176, 212, 271, 272] and the expansion into harmonics in pulsed plane-waves [276], to name a few. Furthermore, we mention the treatment in locally constant fields and its improvements [28, 62, 63, 116, 134] in order to include non-linear Compton scattering in large-scale simulations with emphases in plasma-physical applications [312].

The second extensively investigated scattering process in the background field approximation is the scattering of a single probe photon with a highly intense electromagnetic field producing an electron-positron pair also referred to as the non-linear Breit-Wheeler pair production, which is the cross-channel process to non-linear Compton scattering. As for the latter, the pioneering work w.r.t. the non-linear Breit-Wheeler pair production was done assuming infinite plane-waves as well as constant crossed fields for the background field, respectively [213, 216–219, 243, 247]. Since then and similar to the non-linear Compton process, the non-linear Breit-Wheeler process is extensively investigated w.r.t. several different features of the background field (see, e.g., [122, 127, 140, 161, 162, 191, 221, 287, 290]).

However, in contrast to the non-linear Compton scattering, the non-linear Breit-Wheeler pair production is a threshold-process, i.e. the attained energy in the center-of-momentum frame needs to exceed a threshold energy in order to produce the pair. This leads to unique phase space structures, which are rather different compared to those found for non-linear Compton scattering. For instance, the pair production probability P of the non-linear Breit-Wheeler process scales in the regime of ultra-high intensities and small center-of-momentum energies (also referred to as the tunneling regime) with the electric field like $P \sim \exp\left(-\frac{4m}{3\omega'}\frac{E_S}{E}\right)$ (cf. [243, 247]), where $\hbar\omega'$ denotes the energy of the probe photon, which is similar to the scaling of the above mentioned Sauter-Schwinger effect. Furthermore, we mention the sub-threshold enhancements of the non-linear Breit-Wheeler process due to the application of the pulsed plane-wave approach [127, 221, 290] as well as the consideration of polarisation effects [140, 289, 291].

Together with the non-linear Compton process, the non-linear Breit-Wheeler pair production is one of the driving forces of cascade formations in non-linear QED [81, 104, 244]. This is of particular interest since the Bohr conjecture [281] suggests that a field as high as the Schwinger field E_S mention above is not reachable, because the intensity of a strong laser system is, in general, bounded above due to the formation of such cascades [22, 85, 214, 280].

Furthermore, we mention the pioneering experiment E-144 at the SLAC National Accelerator Laboratory [20, 40, 47], where for the first time multi-photon contributions to the Compton and Breit-Wheeler process were measured during a collision of a highly energetic electron beam and a medium intense optical laser.

Besides the two fundamental processes, non-linear Compton and non-linear Breit-Wheeler, there is a vast amount of other processes elaborated in literature. Here, we mention the processes related to vacuum polarisation, e.g. vacuum birefringence [36, 66, 128, 148, 149, 259, 279] and ”matterless double slit“ invesigations [153, 154]. Since the particle treatment in QED has a universal character, there are also investigations w.r.t. exotic particles [99, 163, 180] as well as considerations beyond the standard model of particle physics, for instance non-commutativity of space-time [136, 166] and the hidden gauge sector [6] as well as axion-like particles [65, 155]. Furthermore, there are investigations about the photon splitting and merging process [4, 8, 59, 234] as well as the consideration of non-linear QED applications w.r.t. other particle processes in the standard model of particle physics, e.g. muon decay [64, 84, 277] and neutrino scattering [190, 193, 288]. Furthermore, we mention the application of the dynamical assistance approach mentioned above to non-linear Compton [23, 224, 268] and non-linear Breit-Wheeler process [220, 261] as well as to other scattering processes as for instance Mott scattering [232, 285, 301] and bremsstrahlung [45, 169, 261]. Of particular interest are the non-linear processes with more than one vertex within a strong electromagnetic field, for instance, laser-assisted electron-electron scattering (also referred to as Møller scattering; see, e.g., [223, 231, 251, 301]), laser-assisted electron-positron scattering (also referred to as Bhabha scattering; see [53, 54, 238]), lepton conversion (e.g. process like $e^-e^+ \to \mu^-\mu^+$ in external fields; see [206, 207]), the double and higher-order Compton processes (see, e.g., [67, 68, 151, 152, 170, 174, 177, 199, 224, 270, 273]) as well as the trident process (see below). These kinds of processes lead to rich phase space structures due to the on-/off-shell contributions of their intermediate particles. For a more detailed outline of the literature about scattering processes and their experimental investigations, we refer the reader to the review articles [61, 79, 113, 183, 202, 256, 301].

Trident pair production

Of particular interest in literature, as within this thesis, is the trident process, i.e. in general the scattering of an electromagnetic field with an incoming electron producing an electron-positron pair as well as an additional (recoil) electron:

$$e^- + \gamma \to e^+ + e^- + e^-, \tag{1.1}$$

which is also referred to as the triplet pair production (especially in older literature). Since the origin of QED, there are a vast amount of publications about the perturbative (monochromatic) treatment w.r.t. the trident process (1.1), e.g. the investigations within several kinematic limits [32, 33, 306] (see [147, 200] for a review). The first full (monochromatic) derivation of the trident process (1.1) was given in [118, 120, 144, 197, 198], where the rich structures of the respective cross sections were revealed. Of particular interest are the investigations w.r.t. the distribution of the recoil electron [284], since the consideration of polarised incoming photons and electrons (see, e.g., [302, 303], as revised in [93, 95]) lead to further use in polarisation measurements [31, 72]. Considering the latter, there are recent applications using the (perturbative) trident process in order to control the polarisation of a highly energetic photon beam as produced in the gamma-ray sources of the Jefferson Laboratory experiments PrimEX [12] and GlueX [3] as well as the polarisation measurements in the LEPS/LEPS2 experiment at the SPring-8 (Laser Electron Photon Experiment at Super Photon Ring - 8 GeV; see, e.g., [208, 209]). We also mention the consideration of the perturbative trident process (1.1) in polarisation measurements of cosmic gamma-rays [26, 110], e.g. in the HARPO experiment (Hermetic Argon Polarimeter;

see, e.g., [109]).
Considering a strong electromagnetic field the trident process appears in the form of

$$e^-_{\mathrm{L}} \to e^+_{\mathrm{L}} + e^-_{\mathrm{L}} + e^-_{\mathrm{L}}, \tag{1.2}$$

where the label L indicates a laser field dressed fermion (in difference to the single photon interaction given in (1.1)). The process (1.2) is also referred to as strong-field or non-linear trident pair production, respectively, and was firstly investigated in the pioneering work of [19, 249] by considering a constant background field. Due to the vast improvements of the experimental capabilities, the theoretical treatment of the non-linear trident process has recently attracted a high degree of interest in literature. For instance, the consideration of the trident process in an infinite plane-wave background field [132, 133], as well as in a constant crossed field [157, 158]. Furthermore, there are investigations within the (arbitrary) pulsed plane-wave approach [135, 175] as well as an equivalent full derivation in the light-front quantisation approach [69, 70], both targeting an application for high-intensity laser experiments. A different direction is taken in [131], where the impact of the bandwidth effects on the trident process at low to medium intensities is elaborated.
Considering the above mentioned cascades, the strong-field trident process is the very first step in an electron-seeded avalanche in strong electromagnetic fields. Furthermore, the evaluation of the non-linear trident processes is the corresponding cross channel to the above mentioned non-linear Møller scattering, Bhabha scattering as well as lepton conversion. Therefore, of particular interest are the conceptional investigations of the involvement of non-linear (virtual) Compton and Breit-Wheeler contributions in the off-/on-shell decomposition of the strong-field trident matrix element w.r.t. the intermediate photon, as well as the extension of similar concepts to higher order processes [67].
Considering the experimental point of view, we mention the trident process as a high-precision test case for strong-field QED as it will be investigated in the promising upcoming experiments LUXE (Laser Und XFEL Experiment; see [2, 34, 46]) at the europeanXFEL and the E320 at FACET-II ([186, 310]), which are modern next-generation experiments in progression to the above mentioned E-144. These experiments are emphases to the high-intensity effects in strong-field QED with particular respect to the trident process.
Another conceivable application of the trident process could be situated in the dark matter search. Given the high repetition rate of the europeanXFEL a potentially interesting option is to combine the x-ray beam with a synchronised electron beam of about 50 MeV in order to facilitate a high-statistics search for the dark photon. A dark photon (also referred to as U boson or hidden photon) is a candidate for dark matter beyond the

standard model of particle physics, which is considered both theoretically [21, 52, 250] as well as experimentally [5, 24, 50, 242]. A corresponding analysis in the context of the perturbative (monochromatic) trident was given in [94]. In fact, the trident process includes a sub-process of the type $\gamma^* \to e^+e^-$, i.e. the above mentioned intermediate (virtual) photon which decays into an electron-positron pair. Via kinetic mixing, that virtual photon may "temporarily" couple to a dark photon A', e.g. $\gamma^* \to A' \to \gamma^*$, thus signalising its presence as a peak of the invariant mass distribution of the electron-positron pair. The peak would be at the mass of the dark photon and its width is related to the kinetic mixing strength.
Another, and rather complementary, entry-point to measurements involving non-linear trident could be seen in upcoming coherent light sources as proposed in the XLEAP project at the LCLS-II (X-ray Laser-Enhanced Attosecond Pulse generation at the Linac Coherent Light Source; see, e.g.,[115]) or the SYLOS light source at ELI-ALPS (Single Cycle Laser at Extreme Light Infrastructure – Attosecond Light Pulse Source; see, e.g.,[195]). Those will provide sub-femtosecond pulsed soft x-ray beams by applying beam modulation (e.g. Enhanced Self Amplified Spontaneous Emission; ESASE [171]) as well as higher-harmonic generation [111], respectively. Assuming a combination of such x-ray beams with a sub-GeV electron beam, one can assume the intensity effects on the particles produced by the trident process to be suppressed due to the high energy of the respective light source. However, the leading property influencing the particle distributions of such a conceivable experimental setup would be the broad spectrum of the light source originated from the very short temporal structure. Furthermore, the consideration of the bandwidth of high-energy photon sources could also lead to an updated tool in order to refine the polarisation measurements (as mentioned above in the context of the GlueX, PrimEX, and LEPS/LEPS2 experiments) by involving the spectral information of the light source to the analysis of the measured azimuthal recoil electron distribution.

This motivates the main investigation of the present thesis: the elaboration of the impact of broad spectra from the light source to the phase space distributions of the trident process near to the threshold. This can also be seen from two perspectives: (i) the consideration of low to medium intensities within a strong-field QED framework by means of the background field approximation, targeting highly energetic coherent photon sources, or (ii) as an extension of the monochromatic perturbative QED treatment in order to include spectral effects of the incoming photon beam.

Outline of this thesis

In chapter 2 we outline the background field approximation to QED. We begin in section 2.1 with the description the general properties of the background field and specialise it to the pulsed plane-wave field. Then in section 2.2, we introduce the position space rules of strong-field QED as widely used in literature by derivation from the QED Lagrangian in the Furry representation. In section 2.3 we transform this position space rules into momentum space by introducing the strong-field dressed vertex, which was done in a similar way in [187, 189, 192]. There we isolate the finite part of the strong-field dressed vertex, where we keep the pulse envelope function arbitrary. We show the connection of the regularisation result to the gauge invariance w.r.t. the quantised photon field by considering its Ward identity in section 2.4. Finally, in section 2.5 we derive the matrix element of the trident process in the background field approximation considering an arbitrary pulsed plane-wave field by applying the momentum space rules mentioned above. Furthermore, we show a refined decomposition of the trident matrix element, not only in on- and off-shell contributions w.r.t. the intermediate photon, but also due to a partial coupling of the background field exclusively to one of the vertices. As it turns out, this is a direct implication of the regularisation of the strong-field dressed vertex and furthermore, the resulting sub-contributions to the matrix element are key for the pathway back to the perturbative monochromatic case as well.

Motivated by these observations, we introduce in chapter 3 a new model called pulsed-perturbative QED, which is capable to approximate QED processes at low intensities, but with the inclusion of the spectral information of the involved light source. In section 3.1 we show that this approximation turns out to be a missing piece in the limiting cases of strong-field QED w.r.t. the connection to perturbative monochromatic QED. Therefore, we elaborate in section 3.2 the first order approximation in the intensity parameter (cf. section 2.1) and show that the resulting vertex still obeys the Ward identity, thus is capable to produce gauge invariant scattering amplitudes. In section 3.3 we discuss the properties of the light spectrum in the pulsed plane-wave approach, its influence on the pulsed-perturbative vertex as well as its connection to the perturbative monochromatic case.

In chapter 4 we apply the pulsed-perturbative QED approximation to the trident process (within this thesis also referred to as pulsed-perturbative trident). Therefore we derive in section 4.1 the matrix element as well as the six-fold differential cross section of pulsed-perturbative trident for an arbitrary pulse envelope function. Furthermore, we elaborate the limiting case of infinitely wide pulsed with only weak constraints to the envelope function (it needs to be at least an even function). In section 4.2 we numerically calculate

the total cross section of pulsed-perturbative trident and compare the resulting curves with the monochromatic case. Following that, we discuss in section 4.3 the inclusive positron distribution, i.e. the three-fold differential cross section w.r.t. the positron momentum in transverse coordinates. We illustrate the modification of the positron phase space due to the finite bandwidth of the used incoming laser field and again compare the resulting contributions with the respective monochromatic case. In section 4.4, we consider the exclusive electron distributions, i.e. the six-fold differential cross sections treated as functions of a final electron three-momentum and for a given fixed positron three-momentum. Here, the modifications of the final phase space of the electron due to the broad laser spectrum are illustrated for both, the transverse momentum and rapidity distribution as well as the azimuthal distribution. Furthermore, we derive in this section an analytical estimation for the extent of the final phase space of the electron based directly on the spectral width of the laser field. Finally, in section 4.5, we examine certain (operating or planned) light sources, whether they are sensitive to the effects found for the pulsed-perturbative trident and briefly discuss further applications.
In chapter 5, we summarise the present thesis and give a brief outlook for conceivable further investigations.

In appendix A and B, we outline the notations and conventions used in this thesis w.r.t. the relativistic particle kinematics as well as the Feynman rules of perturbative monochromatic QED. In appendix C, we elaborate on the perturbative monochromatic trident, which is used as the monochromatic limiting case within this thesis. Therefore, we derive the matrix element as well as the cross section. In section C.2 we illustrate the used numerical treatment and verify our implementation against literature data. Furthermore, in section C.3, we calculate the double-differential cross section of monochromatic trident w.r.t. a final electron momentum and show the kinematical distinction of the two final electrons for high energies of the incoming photon with the initial electron at rest. Finally, in appendix C.4, we give a brief illustration of capabilities to measure (hypothetical) dark matter particles by using the trident process.

Publication containing results obtained during the elaboration of this thesis:

> Uwe Hernandez Acosta and Burkhard Kämpfer, ‘Laser pulse-length effects in trident pair production’, Plasma Phys. Control. Fusion **61**, 084011 (2019).

Publication (currently in peer review) produced during the doctoral studies and not directly related to this thesis:

> Uwe Hernandez Acosta, Andreas Otto, Burkhard Kämpfer, Alexander I. Titov, ‘Non-perturbative signatures of non-linear Compton scattering’, arXiv:2001.03986 [hep-ph].

2 | Strong-field quantum electrodynamics

The fundamental way to describe the elementary interaction of charged particles and an electromagnetic field and/or photons taking into account all relativistic and quantum mechanical properties is the usage of quantum electrodynamics, commonly referred to as QED (for an introduction, see the well-known textbooks about quantum field theory, e.g. [25, 107, 108, 139, 145, 179, 236, 253, 282, 308, 309]). A common method to compute probabilities of processes in QED is the Feynman diagram technique, where Feynman rules are used to represent the mathematical expressions of a perturbative expansion in the QED coupling α. Since the value of this coupling strength is given at small energy or momentum scales by $\alpha \approx 137.035\,999\,084(21)^{-1}$ [194, 286], the expansion in powers of α can be truncated at a certain order, which results in controlled analytical approximations of fundamental interaction processes. However, modern laser facilities provide laser pulses with mean photon numbers in the order of $10^{18}\,\text{photons}/\lambda^3$ (normalised on a cube with the edge length equal to the wavelength λ; [61, 117]) and a high degree of coherence, which results in the need of evaluation of very large numbers of Feynman diagrams in such a perturbative approach [77, 78, 91], which is organised solely in powers of α. Consequently, the usage of single photon couplings to describe the fundamental interaction involving laser fields is computationally very expensive and therefore impracticable [215].

An extensively used approach to overcome these difficulties is the description of the asympthotics of the laser fields as coherent states, which results in a distinction of the electromagnetic field in (i) a semi-classical background field, as a model for the laser, and (ii) a quantised photon field, for the single photon interactions within this background field [90]. This decomposition of the electromagnetic field within QED leads to the Furry picture outlined in section 2.2.

2.1 Description of the laser field

Within the present thesis, as is done widely over the recent literature, we model a laser as a classical electromagnetic field $A^\mu(x)$. Generally, such a field is characterised by two field invariants[1] [25]

$$\mathcal{F} := \frac{e^2}{4m^4} F^{\mu\nu} F_{\mu\nu}, \qquad \mathcal{G} := \frac{e^2}{4m^4} F^{\mu\nu} G_{\mu\nu}, \tag{2.1}$$

where $F_{\mu\nu} := \partial_\mu A_\nu - \partial_\nu A_\mu$ denotes the electromagnetic field-tensor and $G_{\mu\nu} =: {}^*F_{\mu\nu} =: \frac{1}{2}\varepsilon_{\mu\nu\tau\lambda}F^{\tau\lambda}$ its pseudo-tensorial conjugate, with the Levi-Civita symbol $\varepsilon_{\mu\nu\tau\lambda}$, which obeys $\varepsilon_{0123} = -1$ and is fully skew symmetric in its indices. The prefactors of the contraction of the tensors are chosen in order to make the invariants dimensionless, where e and m denote the absolute value of the elementary charge and the electron mass, respectively. One can show that these invariants are the only linearly independent invariants to characterise Lorentz-invariant gauge fields [82], which means every Lorentz scalar depending only on the Abelian gauge field A^μ needs to be a (smooth) function of the field invariants (2.1). Considering a laser field we assume A^μ is a null-field, which means that the field invariants (2.1) vanish:

$$\mathcal{F} = \mathcal{G} = 0. \tag{2.2}$$

This (strong) assumption is valid for focused laser scattering experiments if the transit time of the scattering partner through the focal point is longer than the interaction time scale of the scattering process [178, 255]. In this thesis, the null-field condition (2.2) is fulfilled by assuming A^μ is a Lorenzian plane-wave field, i.e. it only depends on a phase variable $\varphi := k^\mu x_\mu$, with a reference four-momentum k^μ and obeys the Lorenz gauge condition

$$\partial_\mu A^\mu = 0, \tag{2.3}$$

which implies $k_\mu A^\mu = 0$. Since the Lorenz gauge does not completely exhaust the gauge freedom in the sense that it does not fix the complete gauge freedom of A^μ, we additionally assume that the laser field obeys the Weyl condition $A^0 = 0$. This fully avoids (combined with the Lorenz condition) the presence of longitudinal components in the laser field, i.e. for the spatial components one has $k_i A^i = 0$ with $i = 1, 2, 3$. Since the processes investigated extensively in the literature as well as in this thesis are scattering processes, there are two additional gauge and Lorentz-invariant quantities to characterise the system of the laser

---

[1] Within this thesis, we work in natural units, where $c = \hbar = 1$.

field and scattering partner [125, 218, 247]: the classical non-linearity parameter[1] a_0 and the quantum non-linearity parameter χ. These invariants are given in a general Lorentz and gauge invariant form by

$$a_0 := \frac{|e|}{m(kq)}\sqrt{\langle q_\mu T^{\mu\nu} q_\nu\rangle}, \tag{2.5}$$

$$\chi := \frac{e}{m^3}\sqrt{\langle |q_\mu F^{\mu\nu}|\rangle}, \tag{2.6}$$

where q^μ denotes the 4-momentum of the scattering partner (mostly an electron or a photon). The angle brackets $\langle\ldots\rangle$ denote the proper time average of the respective quantity, although it is also common practice to use the maximum value of the respective quantities instead [157, 247], as we will do within this thesis. Again, $F^{\mu\nu} = \partial^\mu A^\nu - \partial^\nu A^\mu$ is the electromagnetic field-tensor, and $T^{\mu\nu}$ denotes the energy-momentum tensor of the electromagnetic field A^μ, which is given by [141]

$$T^{\mu\nu} := -g_{\tau\lambda} F^{\tau\mu} F^{\lambda\nu} + \frac{1}{4} g^{\mu\nu} F^{\tau\lambda} F_{\tau\lambda}, \tag{2.7}$$

where $g_{\mu\nu} := \mathrm{diag}\,(1, -1, -1, -1)$ denotes the Minkowski metric. The component T^{00} is also denoted as the energy density of the laser field, which is an important quantity since the incident photon flux [140, 269, 273]

$$I_\gamma := \frac{1}{\omega^2}\int_{-\infty}^{\infty} \mathrm{d}\varphi\, T^{00}(\varphi), \tag{2.8}$$

with the frequency (energy) $\omega := |\underline{k}|$ of the laser field, is used to normalise certain emission probabilities to obtain the cross section of the respective process (see below in equation (2.40)).

The classical non-linearity parameter a_0 is especially important within the description of laser-matter interaction, since a_0 acts as an effective intensity parameter of the laser field seen from the perspective of the scattering partner [125]. Especially for electrons as respective scattering partner, a_0 is the work which needs to be done on one electron (initially at rest) by the laser field within one wavelength $\lambda = \frac{2\pi c}{\omega} \equiv \frac{2\pi}{\omega}$ in order to accelerate the electron to the relativistic regime. Compared to that, the quantum non-linearity parameter

---

[1] The relation of a_0 versus the laser pear intensity I_L and frequency ω reads

$$a_0 \simeq 7.5 \frac{\mathrm{eV}}{\omega}\sqrt{\frac{I_L}{10^{20}\,\mathrm{W\,cm^{-2}}}}, \tag{2.4}$$

see for instance [61].

χ denotes the work done to the electron over its Compton wavelength $\lambda_C = \frac{h}{mc} \equiv \frac{2\pi}{m}$ [247]. According to the null-field property (2.2), the invariants a_0 and χ are the characterising invariant quantities for laser-matter interaction and are given in the explicit form

$$a_0 = \frac{|e|}{m}\sqrt{-\left\langle \frac{\partial A^\mu}{\partial\varphi}\frac{\partial A_\mu}{\partial\varphi}\right\rangle}, \qquad \chi = \frac{e\omega}{m^2}\sqrt{\left\langle \left| \frac{\partial A^\mu}{\partial\varphi}\frac{\partial A_\mu}{\partial\varphi}\right| \right\rangle}. \tag{2.9}$$

Considering the assumptions made above, there is a large amount of various explicit expressions for the field A^μ given in the literature, all of which are Lorenzian null-fields and used to model different aspects of laser-matter interaction.

Parametrisation of Lorenzian pulsed plane-wave fields

As mentioned in the introduction 1, an important class of laser fields are pulsed fields, i.e. the field vanishes outside of a given interval referred to as the support of the field. As a model of this behavior, a widely used approach is the so called pulsed plane-wave field

$$A^\mu_{\text{ppw}}(\varphi|\Delta\varphi,\xi) = ag(\varphi,\Delta\varphi)\left[\varepsilon_1^\mu\cos(\xi)\cos(\varphi+\varphi_{\text{CEP}}) + \varepsilon_2^\mu\sin(\xi)\sin(\varphi+\varphi_{\text{CEP}})\right] \tag{2.10}$$

where a denotes the maximum value of the laser field, $g(\varphi,\Delta\varphi)$ is the pulse envelope with pulse width $\Delta\varphi > 0$ and φ_{CEP} the carrier envelope phase. The elementary polarisations are given as $\varepsilon_i^\mu := (0, \underline{\varepsilon}_i)$ with $i = 1,2$, where $\underline{\varepsilon}_i$ denote the spatial components, which are normalised such that $\varepsilon_i^\mu \varepsilon_{j\mu} = -\delta_{ij}$ and obey $k_\mu\varepsilon_i^\mu = 0$ for $i = 1,2$ in order to make sure that A^μ_{ppw} fulfils the Lorenz condition (2.3) as well as the Weyl condition $A^0_{\text{ppw}} = 0$. For numerical calculations, we explicitly use $\underline{\varepsilon}_1 = (1,0,0)$ and $\underline{\varepsilon}_2 = (0,1,0)$, where we assume, without loss of generality, that the spatial part $\underline{k}$ of the reference momentum k^μ of the laser field is aligned along the 3-axis in momentum space. The polarisation parameter ξ characterises the different kinds of polarisations (cf. [141, 273]). For $\xi = 0$ ($\xi = \frac{\pi}{2}$), the field (2.10) is called linearly polarised with respect to the $\underline{\varepsilon}_1$- ($\underline{\varepsilon}_2$-) direction, whereas for $\xi = \frac{\pi}{4}$ ($\xi = -\frac{\pi}{4}$) the field (2.10) is referred as left hand-side (right hand-side) circularly polarised. For every other value of ξ, the field (2.10) is generally called elliptically polarised. For very short pulses, the carrier envelope phase becomes important. Since short pulses are not considered here, we put henceforth $\varphi_{\text{CEP}} = 0$.

The pulse envelope $g(\varphi,\Delta\varphi)$ is a smooth function, which in addition ensures the pulsed behavior of the field (2.10) by the assumption

$$\lim_{|\varphi|\to\infty} g(\varphi,\Delta\varphi) = 0 \tag{2.11}$$

for all $\varDelta\varphi$. Additionally, we assume the pulse envelope to be normalised in the sense of $g(0,\varDelta\varphi) = 1$ for all $\varDelta\varphi$ and $g(\varphi,\varDelta\varphi \to \infty) = 1$ for all φ, respectively. The special limit $g \equiv 1$ is also referred to as the infinite plane-wave case and was a widely used approach in the past [25, 218, 247] to investigate laser-matter interactions considering only the influence of the intensity of the laser field, without any interferences caused by the pulse form. For regularity purposes, we assume that the characteristic moments of the envelope function

$$\nu_n[g] := \frac{1}{\varDelta\varphi}\int_{-\infty}^{\infty} g^n(\varphi,\varDelta\varphi)\,\mathrm{d}\varphi \tag{2.12}$$

to be independent w.r.t. the pulse width $\varDelta\varphi$ for all $n \in \mathbb{N}$ with $n > 0$. This assumption seems to be rather strong, however, most of the pulse-shape functions used in literature about scattering processes in strong-field QED have $\varDelta\varphi$-independent characteristic moments (cf. [273] appendix A).

Considering the parametrisation (2.10), the invariants (2.9) read

$$\begin{aligned} a_0 &= \frac{e}{m}a, && (2.13)\\ \chi &= \frac{e\omega}{m^2}a = \frac{\omega}{m}a_0. && (2.14) \end{aligned}$$

We mention, that these quantities are chosen in such a way that they are independent of the pulse envelope as well as any polarisation properties of the laser field, which enables the comparison of different cases.

Assuming not too small pulse widths, e.g. $\varDelta\varphi > 5$, the incident photon flux (2.8) of a pulsed plane-wave background field can be written as [140, 269]

$$I_\gamma = \frac{a_0^2 m^2}{2e^2}\nu_2[g]\varDelta\varphi, \tag{2.15}$$

where the second moment ν_2 is defined in equation (2.12). Having in mind brief mathematical expressions within this thesis for the pulsed plane-wave background field defined in equation (2.10), we introduce the following abbreviations:

$$A^\mu_{\mathrm{ppw}}(\varphi|a_0,\varDelta\varphi,\xi) = a_0\left[\varepsilon_1^\mu f_1(\varphi|\varDelta\varphi,\xi) + \varepsilon_2^\mu f_2(\varphi|\varDelta\varphi,\xi)\right], \tag{2.16}$$

where we used the connection of the laser intensity parameter a_0 and the maximum amplitude a of the background field given in equation (2.13) and define the amplitude functions

$$f_1(\varphi|\Delta\varphi,\xi) := \frac{m}{e} g(\varphi|\Delta\varphi)\cos(\xi)\cos(\varphi), \quad f_2(\varphi|\Delta\varphi,\xi) := \frac{m}{e} g(\varphi|\Delta\varphi)\sin(\xi)\sin(\varphi), \tag{2.17}$$

respectively. For the later use, we further define $f_3(\varphi) := f_1^2(\varphi) + f_2^2(\varphi)$ as well as the functions $\beta_1^\mu(\varphi) := \int_0^\varphi \left(\varepsilon_1^\mu f_1(\varphi') + \varepsilon_2^\mu f_2(\varphi')\right) \mathrm{d}\varphi'$ and $\beta_2(\varphi) := -\int_0^\varphi f_3(\varphi')\,\mathrm{d}\varphi'$, respectively. Considering the pulse dependence of the background field A^μ via the appearance of the function $g(\varphi)$ in the amplitude functions (2.17), the explicit expression of the pulse envelope is not fixed here, because we want to derive the respective quantities not depending on a special pulse form. However, for explicit numerical calculations, we use the $\cos^2$-pulse form given by

$$g(\varphi|\Delta\varphi) = \cos^2\left(\frac{\pi\varphi}{2\Delta\varphi}\right)\left(\Theta(\varphi+\Delta\varphi) - \Theta(\varphi-\Delta\varphi)\right), \tag{2.18}$$

where $\Theta(x)$ denotes the Heaviside step function with $\Theta(x) = 1$ if $x > 0$ and $\Theta(x) = 0$ anywhere else, which sets the envelope function (2.18) to zero outside of the interval $[-\Delta\varphi, \Delta\varphi]$, i.e. this envelope function has a compact support. Furthermore, since the cosine square function becomes one, if its argument vanishes, the envelope function (2.18) obeys the required constraints to become unity for $\varphi = 0$ and in the limit $\Delta\varphi \to \infty$, respectively. Additionally, the characteristic moments ν_n defined in equation (2.12) w.r.t. the $\cos^2$-pulse are given by

$$\nu_n[\cos^2] = \frac{2}{\sqrt{\pi}} \frac{\Gamma\left(n+\frac{1}{2}\right)}{\Gamma(n+1)}, \tag{2.19}$$

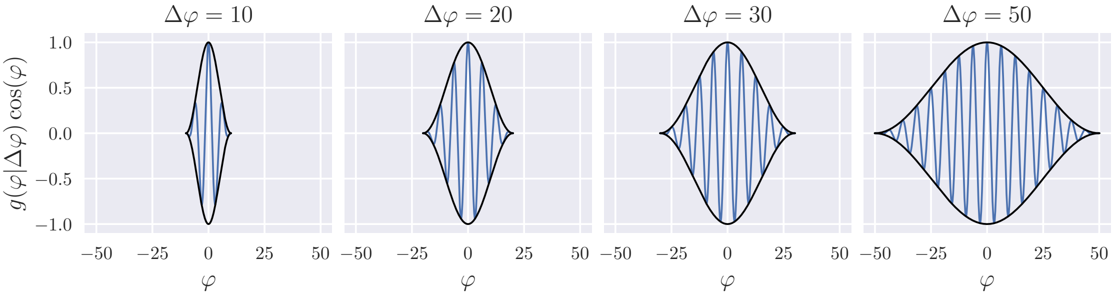

Figure 2.1: The $\cos^2$-pulse envelope function times the oscillatory function $\cos(\varphi)$ (blue curve) for different pulse widths (from left to right: $\Delta\varphi = 10, 20, 30, 50$) and the envelope function itself (black curve; positive and negative branch). With increasing $\Delta\varphi$, the pulse becomes wider and the number of cycles of the oscillatory function increases as well.

with the gamma function $\mathit{\Gamma}(z) := \int_0^\infty x^{z-1} e^{-x}\,\mathrm{d}x$ (cf. [225]), which obeys the assumption, that ν_n is independent of the pulse width $\mathit{\Delta}\varphi$.

In order to illustrate the impact of the pulse envelope function $g(\varphi|\mathit{\Delta}\varphi)$ on a plane wave, e.g. given by the oscillatory term $\cos\varphi$, in figure 2.1 the product $g(\varphi|\mathit{\Delta}\varphi)\cos(\varphi)$ is depicted in the case of the $\cos^2$-pulse defined in equation (2.18) as a function of the phase variable φ for several values of the pulse width $\mathit{\Delta}\varphi$. One recognises the typical bell-shaped behavior of the envelope function is imprinted on the extrema of the oscillatory term. Furthermore, with increasing pulse width $\mathit{\Delta}\varphi$ the distribution becomes wider and the number of cycles from the oscillatory term increases as well.

In order to provide a notion about the impact of the pulse envelope function on the background field A^μ, in figure 2.2 the $(1,2)$-components of A^μ_{ppw} defined in equation (2.10) are depicted in the case of a $\cos^2$-pulse as a function of the scaled time mt with the electron mass m, for different polarisations and at the point of origin in space. The left panel shows that in the case of linear polarisation in $\underline{\varepsilon}_1$-direction, i.e. $\xi = 0$ with $\underline{\varepsilon}_1 = (1{,}0{,}0)$, the component A^2_{ppw} vanishes, of course, and the component A^1_{ppw} performs a pulsed oscillation similar to that depicted in figure 2.1. The panel in the middle of figure 2.2 shows the analogous situation, but for the case of linear polarisation in $\underline{\varepsilon}_2$-direction, i.e. $\xi = \frac{\pi}{2}$ with $\underline{\varepsilon}_2 = (0{,}1{,}0)$, where the component A^1_{ppw} vanishes and the component A^2_{ppw} performs a pulsed oscillation similar to that depicted in figure 2.1. However, in the right panel of figure 2.2, the case of a circularly polarised background field is depicted, i.e. $\xi = \frac{1}{4}$ with $\underline{\varepsilon}_1 = (1{,}0{,}0)$ and $\underline{\varepsilon}_2 = (0{,}1{,}0)$, respectively. In this case, the vector $(A^1_{\mathrm{ppw}}, A^2_{\mathrm{ppw}})$ rotates around the time axis and the amplitude $(A^1_{\mathrm{ppw}})^2 + (A^2_{\mathrm{ppw}})^2$ describes the bell-shaped behavior imprinted from the pulse envelope function.

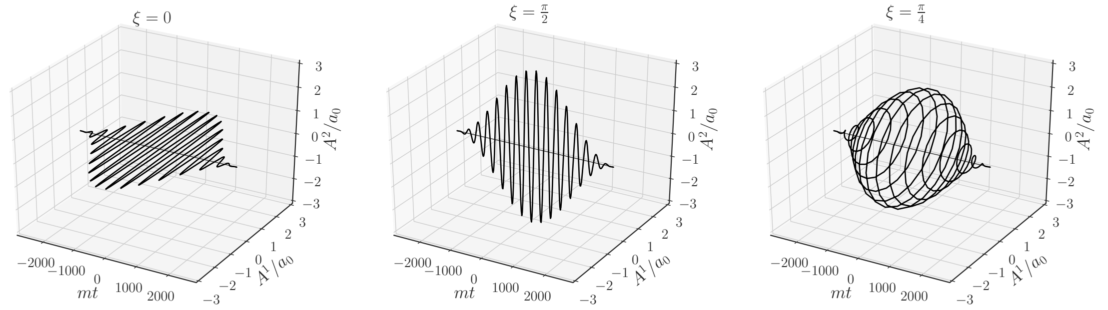

Figure 2.2: The $(1,2)$-component of the background field A^μ (black curve) scaled with the laser intensity parameter a_0 with $\omega = 2\times 10^{-2}\,m = 10.212\,\mathrm{keV}$ for several polarisation parameter (from left to right: $\xi = 0, \frac{\pi}{2}, \frac{\pi}{4}$) are depicted as functions of the scaled time mt at the point of origin, where m denotes the electron rest mass.

2.2 Background field approximation

Within this section, we summarise the assumptions and notations for the background field approximation of QED; for a more detailed introduction, the interested reader is referred to the reviews [90, 192, 215, 256, 274, 293] and references given there.

In QED the photon field is described as a quantised field $\hat{B}^{\mu}(x)$. A key ingredient to calculate processes are the free asymptotic states. As pointed out in [117] it is not feasible to define a proper asymptotic state for a laser field due to the unknown number of photons involved. Therefore, the central approach of the strong-field QED, or more precisely the background field approximation, is the introduction of coherent states to describe the asymptotic states of a laser field (cf. [90, 101, 102, 266]). Here, a coherent state represents the most classical part of the electromagnetic field, i.e. the state with minimum uncertainty. This approach results in a shift of the electromagnetic field by a non-vanishing vacuum expectation value $\hat{B}^{\mu} \to \hat{B}^{\mu} + A^{\mu}$, where $A^{\mu}(x)$ is a classical non-quantised background field. This field A^{μ} does not interact directly with the other particles, but distorts the free fermion fields by minimal coupling to their conditional equation. Concerning the large number of coherent photons in a laser field, it is assumed that a scattering process does not change the laser field itself; in other words: there is no back-reaction or depletion taken into account, which is analog to the test particle assumption of classical electrodynamics. Therefore, using coherent asymptotic states as the background field A^{μ} is a feasible model for a laser field.

The Furry picture

The coherent-state approach was first used to describe bound fermions in a Coulomb field [92], where the expressions containing the background field A^{μ} were seen as a part of the free Hamiltonian of the theory. This model is also referred as the Furry representation (also known as bound-interaction picture or Furry picture) of QED and can be formulated by the use of the classical Dirac-Furry Lagrangian

$$\mathcal{L}_{\mathrm{F}} = \mathcal{L}_{f} + \mathcal{L}_{\gamma} + \mathcal{L}_{\mathrm{i}}. \tag{2.20}$$

The particular terms are given by

$$\mathcal{L}_{f} = \overline{\Psi}_{p\sigma}(x)\left(i\not{\partial} - e\not{A} - m\right)\Psi_{p\sigma}(x), \tag{2.21}$$

$$\mathcal{L}_{\gamma} = -\frac{1}{4}B_{\mu\nu}B^{\mu\nu} - \frac{1}{2\eta}\left(\partial_{\mu}B^{\mu}(x)\right)^{2}, \tag{2.22}$$

$$\mathcal{L}_{\mathrm{i}} = -e\overline{\Psi}_{p\sigma}(x)\not{B}\Psi_{p\sigma}(x), \tag{2.23}$$

where $\mathit{\Psi}_{p\sigma}(x)$ denotes the Dirac field describing the 'free' fermions involving the classical background field A^μ (also referred as Volkov states; see below) with four-momentum p, electric charge e and spin σ. Here we use Feynman's slash notation $\gamma_\mu v^\mu = \not{v}$ for an arbitrary four-vector v^μ, where γ_μ denote Dirac's gamma matrices. In detail, the term $\mathcal{L}_f$ describes the 'free' motion of the Dirac field $\mathit{\Psi}_{p\sigma}(x)$ with respect to the classical background field A^μ. Note the Euler-Lagrange operator $\left(i\not{\partial} - e\not{A} - m\right)$ is the usual Dirac differential operator extended by a minimal coupling to the classical field A^μ, which is a manifestation of the test particle approximation. The term $\mathcal{L}_\gamma$ represents the free motion of the photon field B^μ, where $B^{\mu\nu} = \partial^\mu B^\nu - \partial^\nu B^\mu$ denotes the electromagnetic field tensor and η the gauge fixing parameter. Since there is no interaction between the photon field B^μ and the background field A^μ, this term is exactly the same as in QED in its usual representation without the background field and consequently the free photon field B^μ obeys the homogenous Maxwell equations. The last term $\mathcal{L}_\mathrm{i}$ represents the interaction between the Dirac field $\mathit{\Psi}_{p\sigma}$ deformed by the background field and the photon field B^μ. Analogously to other established quantum field theories, the classical Lagrangian (2.20) is the defining quantity of strong-field QED and needs to be quantised using the canonical quantisation (see e.g. [117]) or Feynman's path integral approach (see, e.g., [299]) in order to be applicable to scattering processes. However, in order to use this theory for practical calculations within the present thesis, we use the fast track procedure of applying the Feynman diagram technique (see, e.g., [236]) and hence need to establish the Feynman rules resulting from the Lagrangian (2.20).
As mentioned above, the Lagrangian (2.20) closely resembles the QED Lagrangian, but differs only in the Euler-Lagrange operator $\left(i\not{\partial} - e\not{A} - m\right)$ and, by implication, in the Dirac fields $\mathit{\Psi}_{p\sigma}(x)$. Therefore the resulting position-space Feynman rules (directly derived from the Lagrangian) in strong-field QED will only differ from the QED position-space Feynman rules in the external as well as internal fermion lines.

Volkov states

In order to get an analytical expression for the 'free' fields from the Lagrangian (2.20), we need to derive the conditional equations by the use of the Euler-Lagrange equations

$$\frac{\partial \mathcal{L}_\mathrm{F}}{\partial \psi(x)} - \partial_\nu \frac{\partial \mathcal{L}_\mathrm{F}}{\partial\left(\partial_\nu \psi(x)\right)} = 0, \tag{2.24}$$

where ψ represents $\mathit{\Psi}_{p\sigma}, \overline{\mathit{\Psi}}_{p\sigma}$, and B^μ, respectively, and the remaining fields are assumed to be zero, which represents the free field case. For the field $\mathit{\Psi}_{p\sigma}$, this results in the well known Dirac equation with minimal coupling to the classical background field $A^\mu(x)$:

$$\left(i\not{\partial} - e\not{A}(x) - m\right)\mathit{\Psi}_{p\sigma}(x) = 0. \tag{2.25}$$

On the one hand, for general fields A_μ, no general analytical solution of equation (2.25) is known, neither in terms of elementary mathematical functions, nor special functions. On the other hand, closed solutions of equation (2.25) for special classes of fields A^μ have been well known for a long time [305] (revised, for instance, in [17, 25, 192, 248, 274]). However, with the additional assumption that A^μ is a Lorenzian null-field (as in this thesis and extensively in literature; see section 2.1), the equation (2.25) is called Volkov-Dirac equation and its solution is given by the Volkov wave function [248]

$$\mathit{\Psi}_{p\sigma}(x) = E_p(x)u_{p\sigma}, \tag{2.26}$$

where $u_{p\sigma}$ denotes the free Dirac bi-spinor describing an on-shell fermion in momentum space with four-momentum p and spin σ, which obeys $\left(\not{p} - m\right)u_{p\sigma} = 0$ and is normalised by the orthogonality relation $\overline{u}_{p\sigma}u_{p\sigma'} = 2m\delta_{\sigma\sigma'}$. The Ritus matrix $E_p(x)$ reads

$$E_p(x) = \left(\mathbb{1} + e\frac{\not{k}\not{A}(\varphi)}{2\,(kp)}\right)e^{iS_p(x)}, \tag{2.27}$$

where the exponent is given by the Hamilton-Jacobi action of a classical particle with four-momentum p in a Lorenzian null-field A^μ:

$$S_p(x) = -px - \frac{1}{2\,(kp)}\int_0^\varphi \mathrm{d}\varphi' \,\left[2e\left(pA(\varphi')\right) - e^2A^2(\varphi')\right] \equiv -px - \tilde{S}_p(\varphi). \tag{2.28}$$

The term $\tilde{S}_p(\varphi)$ is also referred to as the non-linear Volkov phase.
By the use of the Volkov solution (2.26), we can easily derive the Dirac-adjoint Volkov solution

$$\overline{\mathit{\Psi}}_{p\sigma}(x) = \mathit{\Psi}^*_{p\sigma}(x)\gamma^0 = \overline{u}_{p\sigma}\overline{E}_p(x), \tag{2.29}$$

where the Dirac-adjoint Ritus matrix reads

$$\overline{E}_p(x) = \gamma^0E_p^\dagger(x)\gamma^0 = \left(\mathbb{1} - e\frac{\not{k}\not{A}}{2\,(kp)}\right)e^{-iS_p(x)}, \tag{2.30}$$

which is coincidentally the inverse of the Ritus matrix (2.27) at the same position and momentum:

$$\overline{E}_p(x)E_p(x) = E_p(x)\overline{E}_p(x) = \mathbb{1}. \tag{2.31}$$

Compared to the Volkov solution (2.26), which describes a 'free' fermion propagating through the background field, the corresponding anti-fermion is described by the charge conjugated field $\Psi^{(+)}_{p\sigma}(x) = C\left[\Psi_{p\sigma}(x)\right]$. The occurring charge operator $C = i\gamma^2\gamma^0$ (in Dirac representation of the gamma matrices) causes the replacements $e \to -e$ and $u_{p\sigma} \to v_{p\sigma}$, where $v_{p\sigma}$ denotes the free Dirac bi-spinor describing an on-shell anti-fermion in momentum space with four-momentum p and spin σ, which obeys $\left(\not{p} + m\right) v_{p\sigma} = 0$ and is normalised by the orthogonality relation $\overline{v}_{p\sigma}v_{p\sigma'} = -2m\delta_{\sigma\sigma'}$. This results in the Volkov solution for anti-fermions

$$\Psi^{(+)}_{p\sigma}(x) = E_{-p}(x)v_{p\sigma} = \left(\mathbb{1} - e\frac{\not{k}\not{A}}{2\,(kp)}\right) v_{p\sigma}e^{ipx+i\tilde{S}_{-p}(\varphi)}. \tag{2.32}$$

In analogy to equation (2.29), the Dirac-adjoint of the anti-fermion Volkov solution reads

$$\overline{\Psi}^{(+)}_{p\sigma}(x) = \left(\Psi^{(+)}_{p\sigma}(x)\right)^{\dagger}\gamma^0 = \overline{v}_{p\sigma}\overline{E}_{-p}. \tag{2.33}$$

This completes the set of solutions of Volkov-Dirac's equation (2.25). For further details and properties of the Volkov solution, see for instance [17, 25, 274].

Propagators of photons and fermions

A crucial part of the Feynman diagram technique are the internal fermion and photon lines, respectively. These represent the propagators of photons and fermions, where the latter ones are special solutions (Green's function) of the respective conditional equations to the fields describing these particles. Considering the Furry-Lagrangian (2.20) one may derive the (free) Feynman-propagator of the photon field B^μ in position space, which leads to

$$D_{\mu\nu}(x-y) = \int \frac{\mathrm{d}^4k'}{(2\pi)^4}\frac{e^{-ik'(x-y)}}{k'^2 + i\epsilon}\left(-g_{\mu\nu} + \frac{k'_\mu k'_\nu}{k'^2 - i\epsilon}\,(1-\eta)\right), \tag{2.34}$$

where η is the gauge-fixing constant [236]. For calculations within this thesis, we use the Feynman gauge $\eta = 1$, where the photon propagator takes the handy form

$$D_{\mu\nu}(x-y) = \int \frac{\mathrm{d}^4k'}{(2\pi)^4}\frac{-g_{\mu\nu}e^{-ik'(x-y)}}{k'^2 + i\epsilon}. \tag{2.35}$$

As mentioned in section 2.2, there is no direct interaction between the photon field B^μ and the background field A^μ, which implies the (free) photon propagator (2.35) is the same as in QED without a background field.
The (free) Dirac-propagator of fermions in a background field can also be derived from the Furry-Lagrangian (2.20) and is given in the Ritus representation [247] by

$$S_A(x-y) = \int \frac{\mathrm{d}^4 p}{(2\pi)^4} E_p(x) \frac{\not{p} + m}{p^2 - m^2 + i\epsilon} \overline{E}_p(y), \tag{2.36}$$

where p and m denote the momentum and mass of the propagating fermion and E_p and $\overline{E}_p$ denote the Ritus matrix (2.27) as well as its Dirac-adjoint (2.30), respectively. In contrast to the photon propagator (2.35), the fermion propagator depends directly on the background field A^μ due to the appearance of the Ritus matrices.

Position space rules of strong-field QED

Summarising this section, the position space rules are listed in table 2.1, where the incoming and outgoing fermions are represented by double lines connected to exactly one vertex, which stands for the respective Volkov state of the fermion. The external photons are represented by wave lines also connected to exactly one vertex, which stands for the respective photon state. The internal fermions and photons are represented by double or waved lines connecting two vertices, respectively, which stand for the respective propagator, where the vertex itself is represented by a single full dot as known from QED. These position space rules are widely used to calculate the scattering matrix elements of the respective processes in strong-field QED by applying the following scheme [192]:

1. Draw all Furry-Feynman diagrams for a given initial and final state.
2. Exchange the distinct parts of the diagrams with the respective mathematical expression according to the rules given in table 2.1, where the order of the terms at each fermion line needs to be contrary to the fermion arrow.
3. Perform an integration $\int \mathrm{d}^4 x$ on each vertex position x.
4. Apply symmetrisation and insert symmetry factors as usual in perturbative QED.

The usage of this scheme for a given process leads to the scattering matrix element S_{fi}, which contains all information about the transition from the initial to the final state of the process [25, 236, 282] and is a function of all external momenta (either incoming or

Table 2.1: Position space rules of strong-field QED (see, e.g., [71, 90, 192, 247]). In the first column the diagrammatical representation of the respective rule is depicted, in the second column the symbol used within this thesis is shown, the third column indicates the common name of the expression and in the fourth column the definition in the text is referred.

	$\Psi_{\sigma p}(x)$	dressed incoming fermion	(eq. (2.26))
	$\overline{\Psi}^{(+)}_{\sigma p}(x)$	dressed incoming anti-fermion	(eq. (2.33))
	$\overline{\Psi}_{\sigma p}(x)$	dressed outgoing fermion	(eq. (2.29))
	$\Psi^{(+)}_{\sigma p}(x)$	dressed outgoing anti-fermion	(eq. (2.32))
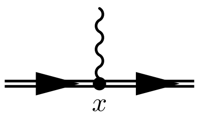	$-ie\gamma^{\mu}$	fermion-fermion-photon vertex	
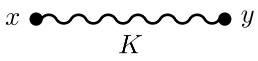	$D_{\mu\nu}(x-y)$	photon propagator	(eq. (2.35))
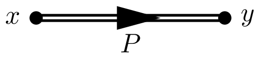	$S^{A}(x-y)$	dressed fermion propagator	(eq. (2.36))
	$\varepsilon'^{\mu}_{\lambda}(k')e^{-i(k'x)}$	incoming photon	
	$\varepsilon'^{*\mu}_{\lambda}(k')e^{i(k'x)}$	outgoing photon	

outgoing):

$$S_{\text{fi}} = \sum_{\text{diagrams}} \int \prod_{\substack{\text{vertex}\\ \text{position } x}} \mathrm{d}^4x \begin{pmatrix} \text{product of all rules according to the} \\ \text{certain Feynman diagram} \end{pmatrix}. \tag{2.37}$$

Assuming we have a process where one particle, e.g. an electron or a photon, collides with a laser field producing n outgoing particles and further we derive the scattering matrix element S_{fi} of such a process by applying the calculation scheme given above, then the differential probability of that process is defined as [25, 247]

$$\mathrm{d}w := |S_{\mathrm{fi}}|^2 \,\mathrm{d}\mathit{\Phi}_n, \tag{2.38}$$

with the invariant integral measure $\mathrm{d}\mathit{\Phi}_n$ of the final n-particle phase space, which is given by

$$\mathrm{d}\mathit{\Phi}_n := \prod_{i=1}^{n} \frac{\mathrm{d}^3 p_i}{(2\pi)^3 \, E_i^0}, \tag{2.39}$$

where $E_i = \sqrt{\underline{p}_i + m_i^2}$ denotes the energy of the i-th particle in the final state with spatial momentum components $\underline{p}_i = (p_i^1, p_i^2, p_i^3)$. Using the definition (2.38), the differential cross section is defined by [269]

$$\mathrm{d}\sigma := \frac{\mathrm{d}w}{I_\gamma V_{\mathrm{lf}}}, \tag{2.40}$$

where I_γ denotes the incident photon flux defined in equation (2.8) and V_{lf} is a large but finite volume, which occurs due to regularity purposes. This volume will eventually cancel out, due to the appearance of a delta-distribution in the matrix element caused by the global conservation of certain light-front components of the external momenta (cf. section 2.5). We mention, that the usage of the incident photon flux I_γ as the normalisation towards getting the differential cross section results directly from the assumption to have exactly one particle alongside the laser field in the initial state. For multiple particles colliding within a laser field, one needs to use another normalisation. The differential cross section (2.40), as well as (partial) integrations of it over the final phase space, is the measurable quantity for a given process and will be the central object of investigation within the present thesis.

2.3 Momentum space rules of strong-field QED

A common practice utilising the Feynman diagram technique in QED is to transform the Feynman rules from position into momentum space. To perform this transformation for the position space rules given in table 2.1, we need to collect all possible expressions which may depend on the position of each vertex. As it turns out, the only term that appears on each vertex is given as the dressed vertex [187–189, 192]

$$\mathit{\Delta}^\mu(p,p',k'|k) := \int \mathrm{d}^4x\, \overline{E}_{p'}(x)\,(-ie\gamma^\mu)\, E_p(x)e^{ik'x}, \tag{2.41}$$

where p, p', and k' denote the momenta of the incoming, outgoing fermion and the outgoing photon, respectively, and E_p is the Ritus matrix given in equation (2.27). We mention that none of the momenta p, p', or k' appearing in equation (2.41) is generally assumed to be on-shell since the terms came either from an external state (on-shell momentum) or from a propagator (off-shell momentum). Utilising the equations (2.27) and (2.30), the dressed vertex results in

$$\mathit{\Delta}^\mu(p,p',k'|k) = -ie\int \mathrm{d}^4x \left(\mathbb{1} - e\frac{\not{k}\not{A}}{2kp'}\right)\gamma^\mu\left(\mathbb{1} + e\frac{\not{k}\not{A}}{2\,(kp)}\right) e^{i\left(\tilde{S}_{p'}-\tilde{S}_p\right)}e^{i(p'+k'-p)x}, \tag{2.42}$$

where $\tilde{S}_p(\varphi)$ denotes the non-linear Volkov phase defined in the r.h.s. of equation (2.28). One may note that all factors of the integrand, except the last exponential term, depend on the phase $\varphi = (kx)$ of the background field A^μ. This motivates the usage of the Fourier transform of this part of the integrand:

$$\left(\mathbb{1} - e\frac{\not{k}\not{A}}{2kp'}\right)\gamma^\mu\left(\mathbb{1} + e\frac{\not{k}\not{A}}{2\,(kp)}\right) e^{i\left(\tilde{S}_{p'}-\tilde{S}_p\right)} =: \int \frac{\mathrm{d}l}{2\pi}\mathit{\Gamma}^\mu(l,p,p',k'|k)e^{-il\varphi}, \tag{2.43}$$

where $\mathit{\Gamma}^\mu$ denotes the dressed vertex function; its argument l is referred to as the photon number parameter, which is the Fourier conjugate of the phase φ. Inserting this definition in the dressed vertex results in

$$\begin{aligned}\mathit{\Delta}^\mu(p,p',k'|k) &= -ie\int \mathrm{d}^4x \int \frac{\mathrm{d}l}{2\pi}\mathit{\Gamma}^\mu(l,p,p'|k)\exp(i\left(p'+k'-p-lk\right)x) && (2.44)\\ &= -ie\int \frac{\mathrm{d}l}{2\pi}\,\mathit{\Gamma}^\mu(l,p,p'|k)\;(2\pi)^4\,\delta^{(4)}\!\left(p'+k'-p-lk\right), && (2.45)\end{aligned}$$

where we used the integral representation of the delta-distribution $\int \mathrm{d}^4x e^{iqx} = (2\pi)^4\,\delta^{(4)}(q)$. Here, one should emphasize that due to the appearing delta-distribution in fact the photon number parameter l parameterizes the amount of momentum k from the background field, which is involved in the dressed vertex. Certainly, it is straightforward to solve the remaining integral over l applying the delta-distribution, but in some cases, it is better to use the delta-distribution for other integrations, e.g. four-dimensional integrals over one or more of the occurring momenta.

Since we collect every positional dependency of the position space rules in table 2.1 and include them in the dressed vertex, the remaining expressions for external legs as well as for the propagators become fairly simple. If a leg of the dressed vertex is connected to an external (on-shell) particle, the remaining expression in the Feynman diagram is one of the free Dirac bi-spinors u,v, $\overline{u}$, $\overline{v}$ (for fermions) or one of the free polarisations $\varepsilon', \varepsilon'^*$ (for photons), respectively. Furthermore, if two position space vertices are connected by a propagator and each of these vertices is transformed to a dressed vertex according to equation (2.41), the remaining expression of the propagator is $\frac{\not{p}+m}{p^2-m^2+i\epsilon}$ (for fermions) or $\frac{-g_{\mu\nu}}{k^2-i\epsilon}$ (for photons) as well as additionally an integration $\int \frac{\mathrm{d}^4p}{(2\pi)^4}$ (similarly for k) over the (off-shell) momentum of the respective propagator. Therefore, the transformation to dressed vertices causes the reduction of all other position space rules in table 2.1 (except the vertex) to the Feynman rules of perturbative monochromatic QED (see table B.1). This also implies that the whole dependence of the position space rules in table 2.1 on the background field A^μ is attributed to the dressed vertex due to the transformation from position to momentum space.

Dressed vertex function

From definition (2.43) we get the dressed vertex function as

$$\begin{aligned} \mathit{\Gamma}^\mu(l,p,p'|k) &= \int \mathrm{d}\varphi \left(\mathbb{1} - e\frac{\not{k}\not{A}}{2kp'}\right)\gamma^\mu\left(\mathbb{1} + e\frac{\not{k}\not{A}}{2\,(kp)}\right) e^{i\left(\tilde{S}_{p'}-\tilde{S}_p\right)} e^{il\varphi} && (2.46)\\ &= \mathit{\Gamma}_0^\mu B_0(l) + \mathit{\Gamma}_1^{\mu\nu} B_{1\nu}(l) + \mathit{\Gamma}_2^\mu B_2(l), && (2.47)\end{aligned}$$

where we absorb all dependencies on the photon number parameter l as well as the remaining integration over the phase φ, i.e. all dependencies on the background field A^μ, in the so called phase integrals B_0, B_1^μ and B_2. The appearing elementary vertices are given by

$$\Gamma_0^\mu(p,p'|k) := \gamma^\mu, \tag{2.48}$$

$$\Gamma_1^{\mu\nu}(p,p'|k) := e\left(\frac{\gamma^\mu \not{k} \gamma^\nu}{2(kp)} + \frac{\gamma^\nu \not{k} \gamma^\mu}{2(kp')}\right), \tag{2.49}$$

$$\Gamma_2^\mu(p,p'|k) := -e^2 \frac{\not{k}}{2(kp)(kp')} k^\mu, \tag{2.50}$$

which have no dependence on the background field A^μ. The phase integrals are defined by

$$B_0(l,p,p'|k) = \int \mathrm{d}\varphi \, \exp(il\varphi + iG(\varphi)), \tag{2.51}$$

$$B_1^\mu(l,p,p'|k) = \int \mathrm{d}\varphi \, A^\mu(\varphi) \exp(il\varphi + iG(\varphi)), \tag{2.52}$$

$$B_2(l,p,p'|k) = \int \mathrm{d}\varphi \, A^2(\varphi) \exp(il\varphi + iG(\varphi)), \tag{2.53}$$

where we use the abbreviation

$$G(\varphi,p,p'|k) := \alpha_1^\mu \int_0^\varphi \mathrm{d}\varphi' \, A_\mu(\varphi') + \alpha_2 \int_0^\varphi \mathrm{d}\varphi' \, A^2(\varphi') \tag{2.54}$$

with the kinematic factors

$$\alpha_1^\mu(p,p'|k) := e\left(\frac{p'^\mu}{kp'} - \frac{p^\mu}{kp}\right), \qquad \alpha_2(p,p'|k) := e^2\left(\frac{1}{kp} - \frac{1}{kp'}\right). \tag{2.55}$$

These factors contain the complete dependence of the phase integrals on the kinematics of the process, i.e. the appearing momenta.

Considering the phase integrals (2.51) – (2.53), one can gather the reason, why the regime for intensity parameters $a_0 > 1$ is difficult to elaborate. Assuming $A^\mu \sim a_0$, as explicitly shown for the pulsed plane-wave approach (2.16), the exponent appearing in the integrand of the phase integrals has the form $c_1 a_0^2 + c_2 a_0 + c_3$, where c_i with $i = 1,2,3$ are complex-valued functions of the momenta, the phase variable φ, and the photon number parameter l, but independent of a_0. Consequently, if one assumes $a_0 < 1$, the exponential function can be expanded in the intensity parameter a_0, which results to some extent in analytical solutions for the phase integrals for a vast variety of field configurations (especially if the Fourier transform of the background field A^μ is known, see chapter 3). However, for $a_0 \geq 1$, the exponential function in the integrand of the phase integrals needs to be treated exactly, which results in a highly oscillatory behavior of the integral. In this case, analytical solutions are known for constant field approaches, i.e. $A^\mu(\varphi) = a_0 \varepsilon^\mu \varphi$, where the phase integrals are reduced to expressions involving Airy functions (see for instance [158, 247]). However, only in certain parameter regimes (e.g. $a_0 \gg 1, \chi \ll 1$), the constant field approaches are capable to describe scattering processes accurately (see for instance [28, 62, 63, 134]). Conclusively, in the case of $a_0 \geq 1$ and for more general background fields, the evaluation of the phase integrals can be fairly challenging and require advanced numerical methods, e.g. highly oscillatory integrals, methods of steepest descent, or stationary phase analysis, to name a few.

Regularisation of B_0

The integral defining B_0 in equation (2.51) tends to be divergent. We insert a regulator term $e^{-\varepsilon|\varphi|}$ with $\varepsilon > 0$ in the integral (2.51) and we get

$$
\begin{aligned}
B_0(l) &= \lim_{\varepsilon\to 0^+} \int_{-\infty}^{\infty} \mathrm{d}\varphi\, e^{-\varepsilon|\varphi|} e^{il\varphi} e^{iG(\varphi)} && (2.56)\\
&= \lim_{\varepsilon\to 0^+} \left[\int_{-\infty}^{0} \mathrm{d}\varphi\, e^{(il+\varepsilon)\varphi} e^{iG(\varphi)} + \int_{0}^{\infty} \mathrm{d}\varphi\, e^{(il-\varepsilon)\varphi} e^{iG(\varphi)} \right.\\
&\qquad \left. + \left.\frac{e^{(il-\varepsilon)\varphi} e^{iG(\varphi)}}{il-\varepsilon}\right|_0^{\infty} - \frac{i}{il-\varepsilon}\int_0^{\infty} \mathrm{d}\varphi\, e^{(il-\varepsilon)\varphi} G'(\varphi) e^{iG(\varphi)} \right], && (2.57)
\end{aligned}
$$

where we use partial integration and the shortcut $G' := \frac{\mathrm{d}}{\mathrm{d}\varphi} G$. Considering the non-integral terms of B_0, one gets

$$
\lim_{\varepsilon\to 0^+} \left[\left.\frac{e^{(il+\varepsilon)\varphi} e^{iG(\varphi)}}{il+\varepsilon}\right|_{-\infty}^{0} + \left.\frac{e^{(il-\varepsilon)\varphi} e^{iG(\varphi)}}{il-\varepsilon}\right|_{0}^{\infty} \right] = 2 \lim_{\varepsilon\to 0^+} \left[\frac{\varepsilon}{\varepsilon^2 + l^2} \right] = 2\pi\delta(l), \tag{2.58}
$$

where we use $G(0) = 0$ deduced from equation (2.54). In the very last step, we execute the limit in a distributional manner, i.e. it exists in a product with a test function. To evaluate the terms in (2.57), we consider the integral $\int_{-\infty}^{0} \mathrm{d}\varphi\, e^{(il+\varepsilon)\varphi} G'(\varphi) e^{iG(\varphi)}$ which is finite for every $\varepsilon \geq 0$ due to the proportionality $G'(\varphi) \sim A^{\mu}(\varphi)$, where A^{μ} is assumed to vanish at the lower limit of the integral. The same holds for the other integral, so the limit in these integrals can be performed trivially and we get

$$
\begin{aligned}
&\lim_{\varepsilon\to 0^+} \left[\frac{i}{il+\varepsilon} \int_{-\infty}^{0} \mathrm{d}\varphi\, e^{il\varphi} G' e^{iG} + \frac{i}{il-\varepsilon} \int_{0}^{\infty} \mathrm{d}\varphi\, e^{il\varphi} G' e^{iG} \right] && (2.59)\\
&= \lim_{\varepsilon\to 0^+} \frac{1}{2} \Bigg[\left(\frac{i}{il+\varepsilon} + \frac{i}{il-\varepsilon} \right) \int_{-\infty}^{\infty} \mathrm{d}\varphi\, e^{il\varphi} G' e^{iG}\\
&\qquad + \left(\frac{i}{il+\varepsilon} - \frac{i}{il-\varepsilon} \right) \left(\int_{-\infty}^{0} \mathrm{d}\varphi\, e^{il\varphi} G' e^{iG} - \int_{0}^{\infty} \mathrm{d}\varphi\, e^{il\varphi} G' e^{iG} \right) \Bigg], && (2.60)
\end{aligned}
$$

where we apply the identity $uw+vz=\frac{u+v}{2}(w+z)+\frac{u-v}{2}(w-z)$ with $u,v,w,z\in\mathbb{C}$. Starting with the first term of equation (2.60), we get

$$\lim_{\varepsilon\to 0^+}\frac{1}{2}\left(\frac{i}{il+\varepsilon}+\frac{i}{il-\varepsilon}\right)\int_{-\infty}^{\infty}\mathrm{d}\varphi\, e^{il\varphi}G'e^{iG}=\mathcal{P}\left[\frac{1}{l}\int_{-\infty}^{\infty}\mathrm{d}\varphi\, e^{il\varphi}G'e^{iG}\right], \tag{2.61}$$

by using

$$\lim_{\varepsilon\to 0^+}\int_a^b\frac{x^2}{x^2+\varepsilon^2}H(x)\,\mathrm{d}x=\mathcal{P}\int_a^b H(x)\,\mathrm{d}x, \tag{2.62}$$

with an arbitrary function $H:(a,b)\to\mathbb{C}$. The symbol $\mathcal{P}$ denotes the Cauchy principal value. The second term of equation (2.60) contains again a delta-distribution:

$$\begin{aligned}
&\lim_{\varepsilon\to 0^+}\frac{1}{2}\left(\frac{i}{il+\varepsilon}-\frac{i}{il-\varepsilon}\right)\left(\int_{-\infty}^{0}\mathrm{d}\varphi\, e^{il\varphi}G'e^{iG}-\int_{0}^{\infty}\mathrm{d}\varphi\, e^{il\varphi}G'e^{iG}\right) && (2.63)\\
&=i\pi\delta(l)\left(\int_{-\infty}^{0}\mathrm{d}\varphi\, e^{il\varphi}G'e^{iG}-\int_{0}^{\infty}\mathrm{d}\varphi\, e^{il\varphi}G'e^{iG}\right) && (2.64)\\
&=i\pi\delta(l)\left(\int_{-\infty}^{0}\mathrm{d}\varphi\, G'e^{iG}-\int_{0}^{\infty}\mathrm{d}\varphi\, G'e^{iG}\right), && (2.65)
\end{aligned}$$

where we used $\delta(x)H(x)=\delta(x)H(0)$ in the last step. To evaluate the integrals, we use $G'e^{iG}=-i\left(e^{iG}\right)'$ and get

$$\int_{-\infty}^{0}\mathrm{d}\varphi\, G'e^{iG}-\int_{0}^{\infty}\mathrm{d}\varphi\, G'e^{iG}=\frac{1}{i}\left(e^{iG}\Big|_{-\infty}^{0}-e^{iG}\Big|_{0}^{\infty}\right)=\frac{1}{i}\left(2-e^{iG_+}-e^{iG_-}\right) \tag{2.66}$$

with the abbreviation $G_\pm:=\lim_{\varphi\to\infty}G(\pm\varphi)$. Finally, we insert (2.58) and (2.60) in equation (2.57) and take a use of the evaluation above, to obtain

$$B_0(l)=\left(e^{iG_+}+e^{iG_-}\right)\pi\delta(l)-\mathcal{P}\left[\frac{1}{l}\int_{-\infty}^{\infty}\mathrm{d}\varphi\, e^{il\varphi}G'e^{iG}\right]. \tag{2.67}$$

Considering $G'(\varphi)=\alpha_1^\mu A_\mu(\varphi)+\alpha_2A^2(\varphi)$ and the definition of B_1^μ in equation (2.52) as well as B_2 in (2.53), respectively, we can write B_0 in terms of the other phase integrals as

$$\begin{aligned}
B_0(l)&=\pi\delta(l)\left(e^{iG_+}+e^{iG_-}\right)-\mathcal{P}\left[\frac{\alpha_1^\mu}{l}B_{1\mu}(l)+\frac{\alpha_2}{l}B_2(l)\right] && (2.68)\\
&=\pi\delta(l)\mathcal{G}+\tilde{B}_0(l), && (2.69)
\end{aligned}$$

where we introduce the abbreviation $\mathcal{G} := e^{iG_+} + e^{iG_-}$ as well as the finite phase integral $\tilde{B}_0(l) := -\mathcal{P}\frac{1}{l}\left[\alpha_1^\mu B_{1\mu}(l) + \alpha_2 B_2(l)\right]$. Inserting the regularised version of the phase integral (2.68) in the definition of the vertex function (2.47) yields

$$\begin{aligned} \varGamma^\mu(l,p,p'|k) &= \pi\mathcal{G}\delta(l)\varGamma_0^\mu + \varGamma_0^\mu\tilde{B}_0(l) + \varGamma_1^{\mu\nu}B_{1\nu}(l) + \varGamma_2^\mu B_2(l) && (2.70)\\ &= \pi\mathcal{G}\delta(l)\varGamma_0^\mu + \tilde{\varGamma}^\mu(l,p,p'|k), && (2.71) \end{aligned}$$

where the finite part of the vertex function is denoted by

$$\tilde{\varGamma}^\mu := \varGamma_0^\mu\tilde{B}_0 + \varGamma_1^{\mu\nu}B_{1\nu} + \varGamma_2^\mu B_2. \tag{2.72}$$

The first summand of the regularised vertex function (2.71), proportional to $\delta(l)$, can be interpreted as the part of the dressed vertex function with no momentum transition from the background field, which has in fact no contribution to one-vertex processes like nonlinear Compton scattering or nonlinear Breit-Wheeler pair production due to the vanishing physical phase space, i.e. there is neither single-photon absorption nor single-photon emission in perturbative QED. However, for processes with more than one vertex, e.g. the trident process investigated in this thesis, the vanishing momentum transition from the background field to one vertex may eventually be compensated due to the momentum transfer at another vertex. Since the only dependence of this non-transfer term on the background field is condensed in the factor $\mathcal{G}$, the leading order of the whole non-vanishing term in A^μ is actually constant through $\mathcal{G} = 2 + \mathcal{O}(A^\mu)$. Furthermore, the appearance of the non-transfer term has a strong connection to the analyticity of the amplitudes calculated within the framework of strong-field QED. However, this is beyond the scope of this thesis (see [137] for a recent discussion about this connection).

The second summand $\tilde{\varGamma}^\mu$ of the regularised vertex function (2.71) will be interpreted as a part of the dressed vertex function with a genuine momentum transfer from the background field to the vertex, which is indicated by the occurring principal value in the finite part $\tilde{B}_0(l)$ of the regularised phase integral (2.68), considering the other phase integrals are regular for $l \to 0$. Moreover, since the elementary vertices given in the equations (2.48) to (2.50) as well as the kinematic factors α_i given in equations (2.55) are independent of the background field, the leading order of the finite part $\tilde{\varGamma}^\mu$ of the vertex function $\varGamma^\mu$ is linear in A^μ, i.e. there is no A^μ-independent term in an expansion of $\tilde{\varGamma}^\mu$ w.r.t the background field A^μ.

Momentum space rules

The introduction of the dressed vertex in equation (2.41) leads to the reductions of all other position space rules given in table 2.1 to their momentum space counterpart known from perturbative QED (see appendix B for details). Every external double line becomes a solid line representing the external field-free fermions, which are given in momentum space by the fundamental Dirac bispinors $u(p), \overline{u}(p), v(p)$ and $\overline{v}(p)$ with the momentum p of the respective particle. The dressed fermion propagator reduces to its momentum space counterpart from perturbative QED given by $S(P) = \frac{\not{P}+m}{P^2-m^2+i\epsilon}$ with the transferred momentum P and the mass m of the respective particle. Admittedly, the internal and external photon lines do not depend on the background field, however, the transformation to momentum space causes a reduction of the respective rules as well. The external incoming (outgoing) photon is represented by its polarisation four-vector $\varepsilon_\lambda^\mu(k)$ $(\varepsilon_\lambda^{*\mu}(k))$, where λ denotes the polarisation and k is the momentum of the photon. The photon propagator is reduced to its perturbative QED counterpart in momentum space, which is given in the Feynman-gauge as $D_{\mu\nu}(K) = \frac{ig_{\mu\nu}}{K^2+i\epsilon}$, where K denotes the transferred momentum and $g_{\mu\nu}$ is the Minkowski metric tensor. We mention that the transformation of the propagators to momentum space leads to integrations $\int \frac{\mathrm{d}^4Q}{(2\pi)^4}$ of the matrix element with the respective transferred momentum Q at each appearing propagator. Accordingly, the whole dependence of the resulting momentum space rules on the background field is condensed in the dressed vertex, which makes this approach conceptually simple.

We summarise the momentum space rules in table 2.2, where the bold lines represent the respective rest of a certain diagram. As we mentioned above, these rules represent the momentum space description of a given process in strong-field QED and similarly to the position space rules, the momentum space rules can be used to derive the scattering matrix element. However, here we need to adjust the calculation scheme in order to apply the momentum space rules. On the one hand, in contrast to the position space rules, there is no integration $\int \mathrm{d}^4x$ over the position of any vertex left in the momentum space description. Instead, an integration $\int \frac{\mathrm{d}l}{2\pi}$ over the photon-number parameter at each dressed vertex appears. On the other hand, we extract the momentum integration for each propagator from the respective momentum space rule and make them part of the calculation scheme. This leads to the new calculation scheme for the scattering matrix element using the momentum space formulation:

1. Draw all Furry-Feynman diagrams for a given initial and final state (in momentum space).
2. Exchange the distinct parts of the diagrams with the mathematical expression

according to the momentum space rules given in table 2.2, where the order of terms for each fermion line needs to be contrary to the fermion arrow.

3. Perform the integrations $\int \frac{\mathrm{d}l}{2\pi}$ over the photon-number parameter for each dressed vertex as well as $\int \frac{\mathrm{d}^4 Q}{(2\pi)^4}$ for each propagator, i.e. internal line, with respective transferred momentum Q.
4. Apply symmetrisation and insert symmetry factors as usual in perturbative QED.

Applying this scheme leads to the same scattering matrix element S_{fi} as given in equation

Table 2.2: Momentum space rules of strong-field QED. In the first column the diagrammatical representation of the respective rule is depicted, in the second column the symbol used within this thesis is shown, the third column indicates the common name of the expression and in the fourth column the definition in the text is referred.

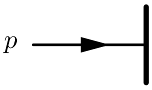	$u_{\sigma p}$	incoming fermion	
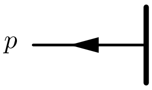	$\overline{v}_{\sigma p}$	incoming anti-fermion	
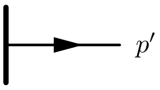	$\overline{u}_{\sigma p}$	outgoing fermion	
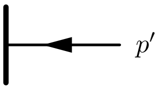	$v_{\sigma p}$	outgoing anti-fermion	
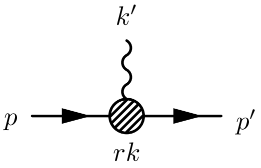	$-ie\Gamma^{\mu}$	dressed vertex function	(eq. (2.47) seqq.)
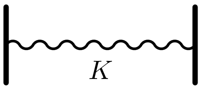	$D_{\mu\nu}(k')$	photon propagator	
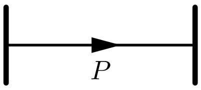	$S(p')$	fermion propagator	
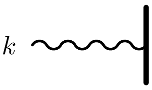	$\varepsilon_{\lambda}^{\prime\mu}(k')$	incoming photon	
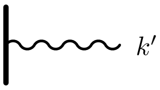	$\varepsilon_{\lambda}^{\prime *\mu}(k')$	outgoing photon	

(2.37) for the position space, but using the momentum space rules given in table 2.2, which means the momentum space formulation introduced in this section is an equivalent description of processes in strong-field QED. Especially the definition of the differential probability and cross section given in equations (2.38) and (2.40) stay the same within the momentum space formulation. In conclusion, we mention that for the derivation of the momentum space rules, as well as any scattering matrix element eventually derived with them, only the constraint was used, that the background field is a Lorenzian null-field as described in section 2.1. This means, using these rules, one can derive matrix elements of several processes for a general Lorenzian background null-field and then specialise to a certain background field shape afterward.

2.4 Ward identity and gauge invariance

It is widely known that QED is gauge invariant term by term in the perturbative expansion, and one implication of this fact is the absence of longitudinal contributions of the coupled photons, i.e. parts of the photon polarisation which are parallel to its four-momentum. However, the application of the background approximation (see section 2.2) does not a priori preserve this behavior. In the language of the momentum space rules listed in table 2.2, that means the longitudinal contributions of photons coupling to the dressed vertex function (2.47) do not automatically disappear. Explicitly, there are two cases where photons may couple to the dressed vertex: by external polarisations $\varepsilon'^{\mu}, \varepsilon'^{*\mu}$ or by photon propagators $D_{\mu\nu}(k')$. In the case of an external outgoing photon (the reasoning is similar for incoming photons), the gauge transformation of the polarisation reads $\varepsilon'^{*}_{\mu} \to \varepsilon'^{*}_{\mu} + q(k')k'_{\mu}$, where $q(k')$ is an arbitrary smooth function also referred to as gauge function. The coupling of the transformed polarisation to the dressed vertex then reads $\varGamma^{\mu}\varepsilon'^{*}_{\mu} \to \varGamma^{\mu}\varepsilon'^{*}_{\mu} + q(k')\varGamma^{\mu}k'_{\mu}$. Since the resulting amplitude may not depend on the gauge function $q(k')$, the requirement of gauge invariance is equivalent to the Ward identity

$$\varGamma^{\mu}k'_{\mu} = 0. \tag{2.73}$$

In addition, if a photon propagator connects two dressed vertices, the appearing term would have the form $\varGamma^{\mu}(l)D_{\mu\nu}(k')\varGamma^{\nu}(r)$, where l,r denote the respective photon number parameters (the dependence on the momenta is suppressed for now) and $D_{\mu\nu}(k')$ is given in its general form by the Fourier transform of equation (2.34). The resulting expression reads

$$\varGamma^{\mu}(l)D_{\mu\nu}(k')\varGamma^{\nu}(r) = -i\frac{\varGamma^{\mu}(l)\varGamma_{\mu}(r)}{k'^2 + i\epsilon} + i(1-\eta)\frac{(k'_{\mu}\varGamma^{\mu}(l))(k'_{\nu}\varGamma^{\nu}(r))}{(k'^2)^2 + \epsilon^2}, \tag{2.74}$$

where η denotes again the gauge fixing parameter. Since the resulting amplitude must not depend on η, the requirement of gauge invariance is equivalent to the same Ward identity $k'_{\mu}\varGamma^{\mu} = 0$.

After this brief description of gauge invariance in strong-field QED, we will use the Ward identity (2.73) to enforce gauge invariance of the dressed vertex function. With the dressed vertex function from equation (2.47) the Ward identity results in

$$0 = \overline{u}_{p'}k'_{\mu}\varGamma^{\mu}u_p \tag{2.75}$$

$$= \left(\overline{u}_{p'}k'_{\mu}\gamma^{\mu}u_p\right)B_0 + \left(\overline{u}_{p'}k'_{\mu}\varGamma_1^{\mu\nu}u_p\right)B_{1\nu} + \left(\overline{u}_{p'}k'_{\mu}\varGamma_2^{\mu}u_p\right)B_2, \tag{2.76}$$

where $B_0, B_{1\nu}, B_2$ denote the phase integrals (2.51) – (2.53) and $\varGamma_0^\mu, \varGamma_1^{\mu\nu}, \varGamma_2^\mu$ are the elementary vertices (2.48) – (2.50) (for both we suppress the momentum dependence for now). We will eventually use the regularised version of B_0 from equation (2.68). The usage of the free Dirac bi-spinors in the side-condition (2.75) is reasonable since, during calculations of amplitudes using the momentum space rules, these will always appear, either trivially from the external fermions or from the fermion propagator due to the spin sum decomposition $\not{p} + m = \sum_\sigma u_{\sigma p} \overline{u}_{\sigma p}$ (analog for the other bi-spinors) of the nominator. Since we have energy-momentum conservation $p + lk = p' + k'$ at each vertex, which is implied by the delta-distribution in the full dressed vertex (2.45), the Ward identity (2.76) of the dressed vertex function reads $0 = (lB_0(l) + \alpha_1^\mu B_{1\mu}(l) + \alpha_2 B_2(l))\,(\overline{u}_{p'} \not{k} u_p)$, where we used Dirac's equations in momentum space $(\not{p} - m)u_p = 0$ and $\overline{u}_{p'}(\not{p}' - m) = 0$, respectively. This implies a severe constraint for the phase integrals:

$$0 = lB_0(l) + \alpha_1^\mu B_{1\mu}(l) + \alpha_2 B_2(l), \tag{2.77}$$

which is equivalent to the Ward identity (2.73) and shows that the phase integrals are not independent. One may notice, inserting the regularised version of B_0 from equation (2.68) and assuming the phase integrals $B_{1\nu}, B_2$ are finite (which is the case if the background field obeys $A^\mu(\varphi) \to 0$ if $|\varphi| \to \infty$), the condition (2.77) is automatically fulfilled. In summary, this means that the usage of the regularised version of B_0 from equation (2.68) for calculations with the dressed vertex (2.47) implies gauge invariance of the resulting amplitude. However, it should be stressed that this is not an equivalence, since the prefactor of the delta-distribution in equation (2.47) is not determined by the Ward identity (2.77).

2.5 Strong-field trident process

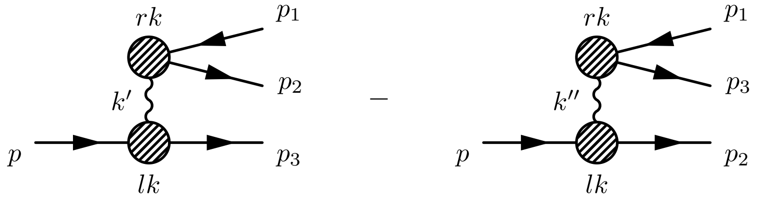

Figure 2.3: The diagrammatical representation of the strong-field trident in momentum space, where p denoted the momentum of the initial electron, p_1 the momentum of the outgoing positron, and p_2, p_3 the momenta w.r.t. the two outgoing electrons, respectively. The momentum transfer from the background field (with momentum k) to each vertex is denoted by l and r, respectively. The respective momentum of the intermediate photon is k' for the first and k'' for the second diagram.

The trident process within strong-field QED (also referred to as strong-field trident) is on the tree-level represented by the momentum space diagrams given in figure 2.3. Due to the indistinguishability of the two final electrons, there are two diagrams differing w.r.t. the exchange $p_2 \leftrightarrow p_3$, where the relative sign represents the Fermi statistic of those electrons. Accordingly, we use the denotation $S_{\mathrm{fi}}^{\mathrm{d}}$ for the scattering matrix element corresponding to the first diagram (referred to as direct part) and $S_{\mathrm{fi}}^{\mathrm{ex}}$ for the second diagram depicted in figure 2.3 (referred to as exchange part). Having in mind brief mathematical expressions in the following sections, we demonstrate the following only using the direct part $S_{\mathrm{fi}}^{\mathrm{d}}$, since the reasoning can be done completely analogously for the exchange part $S_{\mathrm{fi}}^{\mathrm{ex}}$ and leads easily to the full scattering matrix element $S_{\mathrm{fi}} = S_{\mathrm{fi}}^{\mathrm{d}} - S_{\mathrm{fi}}^{\mathrm{ex}}$.

Using the momentum space rules given in table 2.2 the respective (direct) scattering matrix element results in

$$
\begin{aligned}
S_{\mathrm{fi}}^{\mathrm{d}} = &\int \frac{\mathrm{d}^4 k'}{(2\pi)^4} \int \frac{\mathrm{d}l}{2\pi} \int \frac{\mathrm{d}r}{2\pi}\, D_{\mu\nu}(k') \\
&\times \overline{u}(p_3)\,(-ie\Gamma^{\mu}(l,C))\,u(p)\ (2\pi)^4\,\delta^{(4)}\big(p + lk - p_3 - k'\big) \\
&\times \overline{u}(p_2)\,(-ie\Gamma^{\nu}(r,BW))\,v(p_1)\ (2\pi)^4\,\delta^{(4)}\big(k' + rk - p_1 - p_2\big) && (2.78) \\
= &\,(2\pi)^2\, e^2 \int \mathrm{d}l \int \mathrm{d}r\, \frac{g_{\mu\nu}}{k'^2 + i\epsilon} \delta^{(4)}(p + (l+r)k - p_t) \\
&\times \left[\overline{u}(p_3)\Gamma^{\mu}(l,C)u(p)\right]\left[\overline{u}(p_2)\Gamma^{\nu}(r,BW)v(p_1)\right], && (2.79)
\end{aligned}
$$

where $p_t = p_1 + p_2 + p_3$ denotes the total momentum transfer of the process and we introduce the short-hand notation C and BW to mean the evaluation of the vertex functions at the momenta p, p_3, k and $-p_1, p_2, k$, respectively. In the last step, we used one of the delta-distributions to solve the integral over k', which leads to $k' = p + lk - p_3 = p_1 + p_2 - rk$ for the momentum of the intermediate photon. Kinematically, this 4-momentum conservation corresponds to the two one-vertex sub-processes:

$$p + lk = k' + p_3 \qquad \text{(virtual) strong-field Compton ,} \tag{2.80}$$

$$k' + rk = p_1 + p_2 \qquad \text{(virtual) strong-field Breit-Wheeler.} \tag{2.81}$$

However, this generally does not mean, that the strong-field trident process is just the combination of the two subprocesses Compton scattering and Breit-Wheeler pair production, since the intermediate photon may be either on-shell $k'^2 = 0$ or off-shell $k'^2 \neq 0$, which plays an important role later on.
Considering the remaining delta-distribution in equation (2.79), which represents the global energy-momentum conservation, it is useful to introduce the light-cone coordinates $q^{\pm}, q^{\perp}$ for the appearing 4-momenta (see appendix A), similar to the one-vertex processes. This leads to

$$\delta^{(4)}(p + (l+r)k - p_1 - p_2 - p_3) = \delta^{\mathrm{lf}}(p_t - p)\delta(p_t^+ - p^+ - (l+r)\,k^+), \tag{2.82}$$

where we use the abbreviation $\delta^{\mathrm{lf}}(q) := \frac{1}{2}\delta(q^-)\,\delta^{(2)}(q^{\perp})$, with an arbitrary momentum q. Inserting this into equation (2.79) and solving the integral over l results in

$$S_{\mathrm{fi}}^{\mathrm{d}} = \frac{(2\pi)^2}{k^+} e^2 \delta^{\mathrm{lf}}(p - p_t) \int \mathrm{d}r \, \frac{g_{\mu\nu}}{k'^2 + i\epsilon} \left[\overline{u}(p_3)\varGamma^{\mu}(l_r, C)u(p)\right] \left[\overline{u}(p_2)\varGamma^{\nu}(r, BW)v(p_1)\right], \tag{2.83}$$

where we introduce $l_r = \frac{p_t^+ - p^+}{k^+} - r \equiv \frac{p_t^2 - m^2}{2(kp)} - r$. For a given point in the final phase space, the dependence of the photon number parameter at one vertex on the one at the other vertex is a direct consequence of the global energy-momentum conservation. This means, loosely speaking, for a given amount of momentum transferred from the background field to one vertex (here r), the transfer of momentum to the other vertex (here l_r) is exactly arranged in such a way, that the given point of the phase space will be reached. Since there is no explicit condition for the momentum transfer from the background field to a certain vertex for a given point in the final phase space, an integral over all possible r appears in $S_{\mathrm{fi}}^{\mathrm{d}}$.

Decomposition of the matrix element

Considering the decomposition (2.71) of the dressed vertex function in a part without and a part with a genuine momentum transfer from the background field, we can decompose the direct part $S_{\mathrm{fi}}^{\mathrm{d}}$ of the scattering matrix element S_{fi} from equation (2.83) (and analogously the exchange part) w.r.t. every combination of these circumstances:

$$S_{\text{fi}}^{\text{d}} = S_0 + S_{11} + S_{12} + S_2, \tag{2.84}$$

where we suppress the denotation for the direct part for now. The first term of this decomposition is given by

$$S_0 = \frac{4\pi^4}{k^+} e^2 \delta^{\text{lf}}(p - p_t) \mathcal{G}(C) \mathcal{G}(BW) \int \mathrm{d}r \, \frac{\delta(r)\delta(l_r) g_{\mu\nu}}{k'^2 + i\epsilon} \left[\overline{u}(p_3)\gamma^\mu u(p)\right] \left[\overline{u}(p_2)\gamma^\nu v(p_1)\right] \tag{2.85}$$

$$= \frac{4\pi^4}{k^+} e^2 \delta^{\text{lf}}(p - p_t) \delta(l_0) \mathcal{G}(C) \mathcal{G}(BW) \frac{g_{\mu\nu}}{k'^2 + i\epsilon} \left[\overline{u}(p_3)\gamma^\mu u(p)\right] \left[\overline{u}(p_2)\gamma^\nu v(p_1)\right], \tag{2.86}$$

where $l_0 = \frac{p_t^+ - p^+}{k^+}$ with $p_t = p_1 + p_2 + p_3$ and again C and BW stand for evaluation at the momenta p, p_3, k and $-p_1, p_2, k$, respectively. Since one has $\frac{1}{k^+}\delta^{\text{lf}}(p_t - p)\delta(l_0) = \frac{1}{k^+}\delta^{\text{lf}}(p_t - p)\delta\left(\frac{p_t^+ - p^+}{k^+}\right) = \delta^{(4)}(p_t - p)$, the appearance of $\delta(l_0)$ in equation (2.86) leads to the constraint $p = p_1 + p_2 + p_3$, which can not be fulfilled for on-shell momenta because there is no physical final phase space for the contribution from the part S_0 to the matrix element S_{fi}^{d}. This is also clear, since the product of the delta-distributions in equation (2.85) implies $r = 0 = l_r$, which means there is no momentum transfer from the background field to one of the vertices. Speaking in the sense of perturbative QED, this results in a kinematically forbidden contribution, since if one assumes the initial electron to be at rest, there is no emission of a (virtual) photon possible due to the absence of acceleration of the initial electron.

The second term of the decomposition (2.84) corresponds to the case, where the upper vertex has no momentum transfer with the background field, i.e. $r = 0$, which results in

$$S_{11} = \frac{4\pi^3}{k^+} e^2 \delta^{\text{lf}}(p - p_t) \mathcal{G}(BW) \frac{g_{\mu\nu}}{(p_1 + p_2)^2 + i\epsilon} \left[\overline{u}(p_3)\tilde{\Gamma}^\mu(l_0,C) u(p)\right] \left[\overline{u}(p_2)\gamma^\nu v(p_1)\right], \tag{2.87}$$

where we used $k'^2 = (p_1 + p_2)^2$ from equation (2.81) for $r = 0$. Concerning the absence of a delta-distribution for l_0 (in difference to S_0), and the reasoning above, one has $l_0 = \frac{p_t^+ - p^+}{k^+} \neq 0$ within the entire physical phase space, which implies that in the case of $r = 0$ at the upper vertex, there is a non-vanishing momentum transfer from the background field at the lower vertex.

The third term of the decomposition (2.84) results from the case, where the lower vertex has no momentum transfer from the background field and is given by

$$S_{12} = \frac{4\pi^3}{k^+} e^2 \delta^{\mathrm{lf}}(p - p_t) \mathcal{G}(C) \frac{g_{\mu\nu}}{(p - p_3)^2 + i\epsilon} \left[\overline{u}(p_3)\gamma^\mu u(p)\right] \left[\overline{u}(p_2)\tilde{\Gamma}^\nu(l_0, BW)v(p_1)\right], \tag{2.88}$$

where we used $k'^2 = (p - p_3)^2$ due to equation (2.80) with $l_r = 0$, which also implies $r_0 = \frac{p_t^+ - p^+}{k^+} \equiv l_0$. Considering that, the same reasoning as for S_{11} also holds here, which means S_{12} corresponds to the case, where only the upper vertex has a non-vanishing momentum transfer from the background field.

The last term of the decomposition (2.84) results from the case, where both vertices have a non-vanishing momentum transfer from the background field, i.e. $r \neq 0 \neq l_r$, and is given by

$$\begin{aligned} S_2 = &\frac{(2\pi)^2 e^2}{2k^+(kp_p)} \delta^{\mathrm{lf}}(p - p_t) \int \mathrm{d}r \, \frac{g_{\mu\nu}}{r_{\mathrm{on}} - r + i\epsilon} \\ &\times \left[\overline{u}(p_3)\tilde{\Gamma}^\mu(r, C)u(p)\right] \left[\overline{u}(p_2)\tilde{\Gamma}^\nu(l_r, BW)v(p_1)\right], \end{aligned} \tag{2.89}$$

where $p_p = p_1 + p_2$ is the total pair momentum and $r_{\mathrm{on}} = \frac{p_p^2}{2(kp_p)} \neq 0$ denotes the momentum transfer from the background field, which implies $k'^2 = 0$, due to the equations (2.80) and (2.81), respectively, i.e. the case where the intermediate photon becomes on-shell. As pointed out in [133, 135], this leads to an apparent singularity within the integral in equation (2.89), which can be resolved due to the application of the Sokhotski-Plemelj theorem [237] (also referred to as Kramers relation [278]) on the real line:

$$\lim_{\epsilon \to 0^+} \int \frac{f(x)}{x \pm i\epsilon} \, \mathrm{d}x = \mp i\pi f(0) + \mathcal{P} \int \frac{f(x)}{x} \, \mathrm{d}x, \tag{2.90}$$

where $f(x)$ denotes an arbitrary smooth complex-valued function and $\mathcal{P}$ is the Cauchy principal value. The application of the relation (2.90) to equation (2.89) results in an additional decomposition $S_2 = S_2^{\mathrm{on}} + S_2^{\mathrm{off}}$, where S_2^{on} denotes the part of S_2, where the intermediate photon is on-shell ($r = r_{\mathrm{on}}$), and is given by

$$S_2^{\mathrm{on}} = \frac{-i4\pi^3 e^2}{2k^+(kp_p)} \delta^{\mathrm{lf}}(p - p_t) g_{\mu\nu} \left[\overline{u}(p_3)\tilde{\Gamma}^\mu(r_{\mathrm{on}}, C)u(p)\right] \left[\overline{u}(p_2)\tilde{\Gamma}^\nu(l_{\mathrm{on}}, BW)v(p_1)\right], \tag{2.91}$$

where we use the short-hand notation $l_{\mathrm{on}} := l_{r_{\mathrm{on}}}$. Considering the energy-momentum conservations at each vertex given in equations (2.80) and (2.81), respectively, this part

of S_2 corresponds to the case, where the strong-field trident entirely decomposes into the two subprocesses, i.e. strong-field Compton and strong-field Breit-Wheeler process, where each subprocess has its separate physical phase space. Therefore, the part S_2^{on} is widely referred to as the two-step process.
The second term S_2^{off} from the decomposition of S_2 denotes the part, where the intermediate photon is off-shell ($r \neq r_{\mathrm{on}}$) for every point in the final phase space, and is given by

$$\begin{aligned} S_2^{\mathrm{off}} = {} & \frac{(2\pi)^2 e^2}{2k^+(kp_p)} \delta^{\mathrm{lf}}(p - p_t)\, \mathcal{P} \int \mathrm{d}r \, \frac{g_{\mu\nu}}{r_{\mathrm{on}} - r} \\ & \times \left[\overline{u}(p_3) \tilde{\Gamma}^{\mu}(r, C) u(p)\right] \left[\overline{u}(p_2) \tilde{\Gamma}^{\nu}(l_r, BW) v(p_1)\right], \end{aligned} \tag{2.92}$$

where $\mathcal{P}$ is the Cauchy principal value w.r.t. the variable r. Combined with the other contributions of $S_{\mathrm{fi}}^{\mathrm{d}}$, where the intermediate photon is off-shell, i.e. S_{11} and S_{12}, the sum $S_{11} + S_{12} + S_2^{\mathrm{off}}$ is also referred to as the one-step process. Summarising this section, the full scattering matrix element of strong-field trident results in

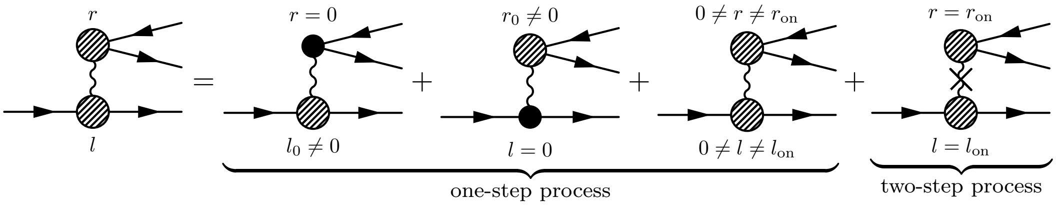

Figure 2.4: Decomposition of the direct part of the strong-field trident process (analogously for the exchange part) according to the decomposition in one- and two-step process as well as the partial absence of a momentum transfer from the background field to one of the respective vertex. On the l.h.s. the shaded vertices are given by the vertex function in momentum space by equation (2.47) for arbitrary r and l, respectively. On the r.h.s., the shaded vertices are evaluated at the stated values of r and l, respectively, except in the third summand, where r and l obey the stated constraint. The full vertices represent the vanishing momentum transfer from the background field and are given by $\bullet = -i\pi\mathcal{G}\gamma^{\mu}$. The cross on the intermediate photon line depicted in the two-step process indicates the appearing intermediate on-shell photon.

$$S_{\mathrm{fi}} = S_{11} + S_{12} + S_2^{\mathrm{off}} + S_2^{\mathrm{on}} - (p_2 \leftrightarrow p_3), \tag{2.93}$$

where S_{11}, S_{12} are given by (2.87) and (2.88) and $S_2^{\mathrm{on}}, S_2^{\mathrm{off}}$ are given in (2.91) and (2.92), respectively. We mention that for the derivation of the matrix element (2.93) of strong-field trident process, the only property of the background field we used, was that A^{μ} is a Lorenzian null-field as described in section 2.1. The diagrammatical representation of the full decomposition (2.93) of the direct scattering matrix element (2.83) is depicted in figure

2.4, where on the left-hand side, the momentum transfer from the background field to each vertex, i.e. r and l, may have arbitrary values, but on the right-hand side, at each vertex, there is a constraint which needs to be fulfilled. As mentioned above, this leads to the denotation one-step process for the sum of the first three summands, due to the off-shell intermediate photon, as well as two-step process for the last summand, according to the on-shell intermediate photon.

We mention, there are similar decompositions of the trident matrix element as well as its probability density in arbitrary plane-wave background fields (cf. [69, 135, 175]) as well as constant crossed fields (cf. [157, 158]). For instance, based on a light-front hamiltonian approach, the decomposition of the trident probability density given in [69] is originated among others in the split of the matrix element in a light-front time ordered and a light-front instantaneous term. This leads to excellent, in some cases analytical, results in arbitrary plane-wave background fields for a wide range of intensity parameters a_0 as well as the quantum non-linearity parameter χ (see definition (2.6)). However, since the aim of the present thesis is the investigation of the strong-field trident for $a_0 < 1$, it is more convenient to retain the decomposition given in equation (2.93) because here we can directly point out, which parts of the matrix element contain the leading order for small a_0. Considering $A^\mu \sim a_0$ as well as the respective number of appearances of the finite part $\tilde{\Gamma}^\mu$ (which is linear in A^μ; see equation 2.72) in the terms of decomposition (2.93), one has $S_{11}, S_{12} \sim \mathcal{O}(a_0)$ and $S_2^{\mathrm{on}}, S_2^{\mathrm{off}} \sim \mathcal{O}(a_0^2)$, for $a_0 < 1$. Therefore, we conclude that the first two diagrams on the r.h.s. of figure 2.4 (also referred to as the partial diagrams; corresponding to S_{11}, S_{12}) contain the leading order of the strong-field trident matrix element in an expansion for small a_0. Furthermore, this leading order is linear in a_0, which is key for the connection to the perturbative monochromatic case. In other words, the first term in the regularised version of the vertex function (2.71) (which produces the partial diagrams) is not only mandatory to preserve gauge invariance due to the Ward identity (see section 2.4), but also necessary to ensure the contact to the perturbative monochromatic QED, especially in the trident process considered in this thesis (see chapter 4 for further details).

3 | Pulsed-perturbative quantum electrodynamics

3.1 Approaches and approximations to strong-field QED

In chapter 2, we outlined the theory of strong-field QED assuming the background field to be a Lorenzian null-field. However, for practical purposes, strong-field QED is only applicable if one chooses an appropriate field approach in order to mathematically model the laser field for a given experimental situation. Considering the description of scattering processes involving a single particle (or several, but few particles) with a laser field, we mention there are several well established field models.

First, there is the widely used constant-cross field (CCF) approximation [25], where one assumes the background field to be in the form of $A^\mu_{\mathrm{CCF}} = a^\mu \varphi$, where a^μ denotes a general constant polarisation vector and $\varphi = k^\mu x_\mu$ is the phase variable of the background field. This approach implies the electric field $\underline{E} = -\partial_t \underline{A}$ and the magnetic field $\underline{B} = \mathrm{rot}\, \underline{A}$, where $\underline{A}$ denote the spatial components of the Lorenzian null-field A^μ, to be constant, with the same magnitude and perpendicular to each other and the reference momentum k^μ of the background field, respectively. Despite the apparently strong constraint made in this approach w.r.t. the background field, applying the constant-cross field approximation, very noticeable results are achieved, e.g. for Compton scattering and Breit-Wheeler pair production [217, 218, 247], double-Compton scattering [151, 152] and trident pair production [157, 158], where especially the regime of high laser intensity parameters $a_0 \gg 1$ is considered.

Another well established and widely used approach for the background field is the pulsed plane-wave model introduced within this thesis in section 2.1 and especially exposed in definition (2.10). In general, this approach is suitable to calculate scattering processes in strong-field QED for arbitrary laser intensity parameters a_0 as well as address the pulsed behavior of modern laser systems due to the introduction of a pulse-envelope function. Therefore, in addition to the a_0 and the quantum non-linearity parameter χ, defined in the equations (2.9), there is another parameter in order to describe the background field: the pulse width $\Delta\varphi$, which depends on the choice of the envelope function. However, despite the fact, that the pulsed plane-wave model is one of the more general approaches, the occurring mathematical expressions can be rather complicated, which makes the numerical treatment fairly challenging. This is especially true for strong-field QED processes with higher numbers of vertices, e.g. non-linear double-Compton scattering [68, 174, 270] and the strong-field trident process [69, 70, 135, 175].

This leads to the necessity of analytical approximations for the pulsed plane-wave approach in order to produce more manageable descriptions of the involved processes and getting deeper insights to the occurring phenomena w.r.t. the respective properties of the background field. For infinitely wide pulses, i.e. $\Delta\varphi \to \infty$, one has the well known infinite plane-wave (IPW) approach of the laser field, which is, besides CCF, widely used to investigate strong-field QED processes w.r.t. their dependence to the laser intensity parameter a_0. In the IPW approach, there is no spectral information of the laser field involved (besides the central frequency) and the photon number parameter becomes integer-valued, which is actually more convenient to be interpreted as a photon number. The expansions of transition amplitudes w.r.t. the harmonics of the laser field leads in the IPW approach to analytical expressions for the cross sections of the one-vertex processes, e.g. non-linear Compton scattering [38, 103, 117, 213, 217–219, 247] and non-linear Breit-Wheeler pair production [140, 213, 216–218, 243, 247] in terms of special functions. However, the infinite extent of the background field leads to regularity issues of the transition amplitude for processes with more than one vertex, like the trident process [133]. We mention that on the level of probabilities, the CCF approximation turns out to be the limiting case of the IPW approach for $a_0 \gg 1$ with suitable side conditions (see [247] for a more detailed discussion of this connection).

Nevertheless, since modern laser collision experiments apply pulsed laser sources with shorter and shorter pulse widths, the spectral information of the laser field become more important for the investigation of involved scattering processes. Furthermore, the development of new x-ray sources provides highly energetic electromagnetic fields, which implies small to medium intensity parameters $a_0 \lesssim 1$ (see section 4.5 for further details in the context of the trident process). Therefore, within the present thesis, we investigate a new approximation to the pulsed plane-wave approach, referred as pulsed-perturbative QED and introduced in section 3.2, in order to address the finite spectral width of modern pulsed radiation sources combined with the low to medium values of the intensity parameter a_0 implied by the x-ray regime reached by their central frequency.

Before we summarise this section, we honorably mention other types of approximations and approaches for strong-field QED, which are beyond the scope of this thesis. First of all, there are the "localised" approaches, namely the locally-constant field approximation (LCFA; cf. [62, 81, 116, 134, 191, 244]) and locally-monochromatic approximation (LMA; cf. [123]), which are motivated by their application to large-scale simulations [27, 44, 81, 97, 104, 105, 146, 156, 214, 244, 245] w.r.t. local informations about the background field. Furthermore, there is the approximation for slowly varying envelopes within the pulsed plane-wave approach, which is capable to simplify the mathematical expressions for not too short pulses (cf. [212, 269, 271, 290]).

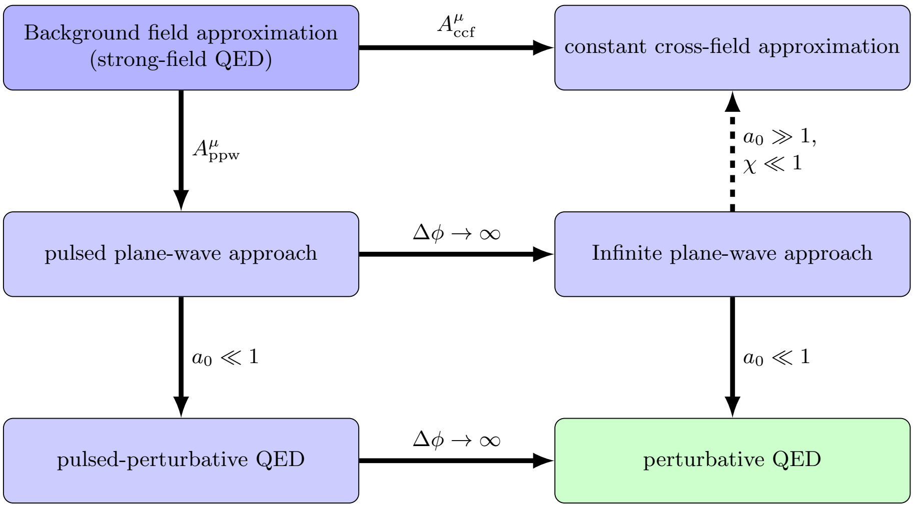

Figure 3.1: Schematic illustration of some approximations in strong-field QED w.r.t. their approaches and parametric limits, respectively.

In order to summarise this section, in figure 3.1 the approaches outlined above and their connections w.r.t. the parameter limits are depicted schematically. In the upper left corner, we start with strong-field QED as the most general concept, which is generally the manifestation of the background field approximation outlined in section 2.2. From this panel, there are the two approaches outlined in this section and given by an ansatz for the background field: the CCF approach (upper right panel) and the pulsed plane-wave approach (center left panel). From the pulsed plane-wave panel, the outgoing arrows indicate the two directions in the parameter space in order to get an approximation: on the one hand, we have the IPW approximation (center right panel) for infinitely wide pulses, i.e. $\varDelta\varphi \to \infty$, but arbitrary intensity parameters a_0. On the other hand, there is the pulsed-perturbative QED approach for small laser intensity parameter $a_0 \lesssim 1$ but arbitrary pulse widths. Finally, the connections of these two approximations to the perturbative monochromatic QED are displayed w.r.t. the two different limits in the respective remaining parameter space. For the IPW approach, the monochromatic QED description results in the low-a_0 limit, i.e. the leading order for $a_0 \to 0$. In the case of pulsed-perturbative QED, the monochromatic QED results from the limit for infinitely wide pulses, i.e. the reduction to the central frequency of the laser field for $\mathit{\Delta} \to \infty$. Therefore, the model of pulsed-perturbative QED can be seen as a missing piece in the pathway from the pulsed plane-wave approach back to the perturbative monochromatic QED w.r.t. the impact of the pulsed structures of the background field. Furthermore, one may read the arrows displayed in figure 3.1 the other way round, where the panel at the tail of the arrow represents an extension of the panel at the head of the arrow w.r.t. to a certain feature. Looking at it this way, pulsed-perturbative QED can also be seen as a possible extension of the monochromatic QED in order to integrate exclusively the finite spectra of the involved electromagnetic field.

3.2 Momentum space rules in pulsed-perturbative QED

Within this section, we specialise the laser field A^μ to the pulsed plane-wave case, which was defined by equation (2.10) and take advantage of the abbreviations introduced in equation (2.16). The reader is referred to section 2.1 for further discussions on the pulsed plane-wave background field.

As mentioned at the beginning of this chapter, we want to derive an approximate set of momentum space rules for the case $a_0 < 1$, therefore we start with the expansion of the vertex function (2.46) in powers of the laser intensity parameter a_0, where our approach is to preserve the terms up to order linear in a_0. First, it is mentioned that the elementary vertices from equations (2.48) to (2.50), as well as the kinematic factors (2.55), are independent of the intensity parameter a_0. However, the whole dependency on the background field A^μ, i.e. the intensity parameter a_0, is encoded in the phase integrals. Since the regularised expression (2.68) for B_0 contains among others the phase integral B_1, it is reasonable to start with the expansion of the latter.

Expansion of B_1^μ

Using equation (2.52), as well as the sum representation of the complex exponential function the phase integral B_1^μ is expanded as

$$B_1^\mu(l) = a_0 \int_{-\infty}^{\infty} \mathrm{d}\varphi\, \left(\varepsilon_1^\mu f_1(\varphi) + \varepsilon_2^\mu f_2(\varphi)\right) e^{il\varphi} \sum_{n=1}^{\infty} \frac{\left(ia_0\alpha_1^\nu\beta_{1\nu}(\varphi) + ia_0^2\alpha_2\beta_2(\varphi)\right)^n}{n!} \tag{3.1}$$

$$= a_0 \int_{-\infty}^{\infty} \mathrm{d}\varphi\, \left(\varepsilon_1^\mu f_1(\varphi) + \varepsilon_2^\mu f_2(\varphi)\right) e^{il\varphi} + \mathcal{O}(a_0^2) \tag{3.2}$$

$$= a_0 \left(\varepsilon_1^\mu F_1(l) + \varepsilon_2^\mu F_2(l)\right) + \mathcal{O}(a_0^2) \tag{3.3}$$

where amplitude functions and the internal integrals β_1^μ, β_2 are defined in equations (2.17) and the following, respectively. We mention the integral and the infinite sum are interchangeable due to the absolute convergence of the complex exponential function. In the leading terms of the expansion of B_1^μ in a_0, we abbreviate the Fourier transforms of the amplitude functions $f_i(\varphi)$ as

$$F_i(l|\Delta\varphi,\xi) := \mathcal{FT}[f_i](l) = \int_{-\infty}^{\infty} \mathrm{d}\varphi\, f_i(\varphi|\Delta\varphi,\xi)\, \mathrm{e}^{il\varphi}, \text{ with } i = 1,2. \tag{3.4}$$

These important functions eventually contain the whole pulse shape dependence of the first order in a_0.

In order to give a notion about the performance of the linearisation for small intensity parameters a_0, in figure 3.2 the real part of the $\mu = 1$ component of the phase integral $B_1^\mu(l)$ given in equation (2.52) is depicted (including all orders of a_0) for linear polarisation in $\underline{\varepsilon}_1$-direction, i.e. $\xi = 0$ as a function of the photon number parameter l and for several combinations of the pulse width $\Delta\varphi$ and the laser intensity parameter a_0. Treating only the 1-component of $B_1^\mu(l)$ is reasonable since we chose without loss of generality $\underline{\varepsilon}_1 = (1{,}0{,}0)$ for the spatial components of the elementary polarisation vector ε_1^μ. For comparison we also depicted the real part of the 1-component of the linear approximation of $B_1^\mu(l)$ given by equation (3.3), neglecting the $\mathcal{O}(a_0^2)$, for the same polarisation and scaled both quantities with the factor $\frac{e}{ma_0\Delta\varphi}$ in order to make them dimensionless as well as bring their respective distribution in the same order of magnitude. Furthermore, we fixed the kinematic factors

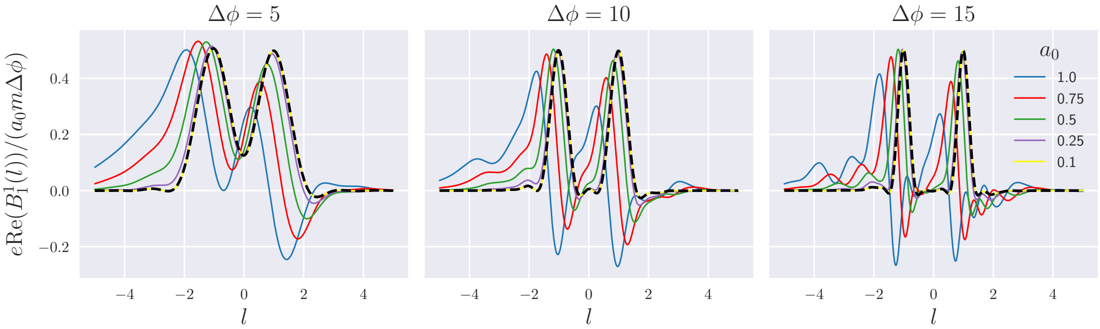

Figure 3.2: The real part of the $\mu = 1$ component of the phase integral $B_1^\mu(l)$ given in equation (2.52) is depicted for linear polarisation in $\underline{\varepsilon}_1$-direction, i.e. $\xi = 0$ with $\underline{\varepsilon}_1 = (1{,}0{,}0)$, as a function of the photon number parameter l for several combinations of the pulse widths $\Delta\varphi$ (left: 5, center: 10, right: 15) and the intensity parameter a_0 (blue: 1.0, red: 0.75, green: 0.5, purple: 0.25, yellow: 0.1). The kinematic parameters were chosen as $\alpha_1^\mu \varepsilon_{1\mu} = \alpha_2 = 0.2$ and the function is scaled by the factor $\frac{|e|}{ma_0\Delta\varphi}$. Additionally, the real part linear approximation of $B_1^1(l)$ w.r.t. the intensity parameter a_0 given in equation (3.3) is depicted (dashed black line) with the same scaling (which makes it independent of a_0) and for the same pulse widths.

with $\alpha_1^\mu \varepsilon_{1\mu} = \alpha_2 = 0.2$, which are typical values for the kinematic situations investigated in the context of trident pair production within this thesis. First of all, we mention that for all depicted values of $\Delta\varphi$ and a_0, there are two main maxima grouped around $l = 0$, where the decreasing of a_0 brings the positions of these maxima closer and closer to $l = \pm 1$, and overall the global distributions become more symmetric w.r.t. the axis $l = 0$. Furthermore, for $a_0 \sim 1$, there are several side extrema, which become more distinct if $\Delta\varphi$ increases. The origin of these minor structures can be identified in the phase function $G(\varphi|a_0, \Delta\varphi)$ defined in equation (2.54) as part of the oscillatory factor in the integrand of the general phase integral $B_1^\mu(l)$, where $G(\varphi|a_0, \Delta\varphi)$ becomes more important if a_0 approaches unity. However, if a_0 decreases, the side structures become smaller, and finally for the depicted case of $a_0 = 0.1$, the distribution of the general phase integral (solid yellow line) nearly perfect matches the linear approximation (dashed black line) for all shown values of $\Delta\varphi$.

Expansion of B_2

Since the integrand of the phase integral B_2 defined in equation (2.53) has the pre-exponential factor $A_{\text{ppw}}^2 \sim a_0^2$ and its exponential function contains no negative powers of a_0, the expansion of B_2 in a_0 has neither an independent, nor a linear term: $B_2(l) = \mathcal{O}(a_0^2)$. Consequently, we may suppress the terms in the vertex function, which contain the phase integral B_2.

Expansion of B_0

By the use of the regularised expression (2.68) for the phase integral B_0, there are two components, which we need to expand in a_0. First we start with the prefactor of the delta-distribution in the first summand of equation (2.68), which results in

$$\mathcal{G} = \sum_{n=0}^{\infty} \frac{(iG_+)^n}{n!} + \sum_{j=0}^{\infty} \frac{(iG_-)^j}{j!} \tag{3.5}$$

$$= 2 + ia_0 \lim_{\eta\to\infty} \left(\alpha_1^\mu \beta_{1\mu}(\eta) + \alpha_1^\mu \beta_{1\mu}(-\eta)\right) + \mathcal{O}(a_0^2), \tag{3.6}$$

where we inserted the function $G(\varphi)$ given in equation (2.54) into the limits $G_\pm = \lim_{\varphi\to\infty} G(\pm\varphi)$. The second term is given by $\tilde{B}_0(l) := -\mathcal{P}\frac{1}{l}\left[\alpha_1^\mu B_{1\mu}(l) + \alpha_2 B_2(l)\right]$, where only the first summand contributes to the first order in a_0 since the leading order of B_2 in a_0 is quadratic. Therefore if we use the expansion of B_1 in powers of a_0 given in equation (3.3), the leading order of $\tilde{B}_0$ in a_0 results in

$$\tilde{B}_0 = -a_0 \mathcal{P}\left[\frac{\alpha_1^\mu}{l}\left(\varepsilon_{1\mu} F_1(l) + \varepsilon_{2\mu} F_2(l)\right)\right] + \mathcal{O}(a_0^2), \tag{3.7}$$

where the symbol $\mathcal{P}$ denotes the Cauchy principal value operator w.r.t. the variable l and the functions F_i are given in equation (3.4).
Combining the two expansions (3.6) and (3.7), the phase integral B_0 reads

$$\begin{aligned} B_0(l) = \pi &\left(2 + ia_0\alpha_1^\mu \lim_{\eta\to\infty} \left(\beta_{1\mu}(\eta) + \beta_{1\mu}(-\eta)\right)\right)\delta(l) \\ &- a_0\mathcal{P}\left[\frac{\alpha_1^\mu}{l}\left(\varepsilon_{1\mu}F_1(l) + \varepsilon_{2\mu}F_2(l)\right)\right] + \mathcal{O}(a_0^2), \end{aligned} \tag{3.8}$$

which reveals again the importance of the Fourier transforms (3.4) as a distinctive part of the second summand, i.e. the part with a genuine momentum transfer from the background field to the vertex.

Vertex function of pulsed-perturbative QED

In order to investigate the pulse width dependence separated from the multi-photon contributions, we define the pulsed-perturbative QED vertex as the part of the strong-field QED vertex up to the order which is linear in laser intensity parameter a_0. Combining the expansions (3.3) and (3.8) with (2.47), the expansion of the strong-field QED vertex function reads

$$\Gamma^\mu(l) = \Gamma^\mu_{\mathrm{pp}} + \mathcal{O}(a_0^2), \tag{3.9}$$

with the pulsed-perturbative QED vertex

$$\begin{aligned} \Gamma^\mu_{\mathrm{pp}} &= \pi\delta(l)\left(2 + a_0\alpha_1^\nu \lim_{\varphi\to\infty}\left(\beta_{1\nu}(\varphi) + \beta_{1\nu}(-\varphi)\right)\right)\Gamma_0^\mu \\ &\quad + a_0\left(\Gamma_1^{\mu\nu} - \Gamma_0^\mu\mathcal{P}\frac{\alpha_1^\nu}{l}\right)\left(\varepsilon_{1\nu}F_1(l) + \varepsilon_{2\nu}F_2(l)\right) && (3.10) \\ &=: \delta(l)\tilde{\Gamma}_0^\mu(p,p') + a_0\tilde{\Gamma}^\mu_{\mathrm{pp}}(l,p,p'). && (3.11) \end{aligned}$$

In analogy to the regularised version of the dressed vertex function given in equation (2.71), the expansion up to the first order in a_0 contains also two qualitatively different parts. On the one hand, a term proportional to $\delta(l)$ (denoted as $\tilde{\Gamma}_0^\mu$), parametrising the absence of transitions of momentum from the background field to the vertex. On the other hand, a term proportional to the intensity parameter a_0 (denoted as $\tilde{\Gamma}^\mu_{\mathrm{pp}}$), where the photon number parameter l does not vanish across the whole physical phase space, which is indicated by the Cauchy principal value (see the explanations to equation (2.71) for further details).

Momentum space rules of pulsed-perturbative QED

Similar to the momentum space rules given in table 2.2, especially similar to the dressed vertex, the pulsed-perturbative QED vertex function might be used as a building block of Feynman diagrams describing a variety of processes. Accordingly, we define the diagrammatical representation of the pulsed-perturbative vertex as

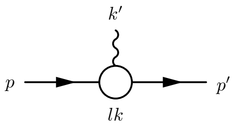

$$= -ie\Gamma^{\mu}_{\mathrm{pp}}(l,p,p'|k)\ (2\pi)^4\,\delta^{(4)}\left(p+lk-p'-k'\right), \tag{3.12}$$

where the vertex function is given by equation (3.10).

Considering that the other momentum space rules, except the dressed vertex, have no dependence on the background field, they stay the same as given in table 2.2. According to the purpose of the model outlined in this section, to derive scattering matrix elements up to and including the linear order in the intensity parameter a_0, we reduce the full dressed vertex given in equation (2.47) to its linear approximation in a_0 constituted by the pulsed-perturbative vertex given in equation (3.12). In fact, the usage of the pulsed-perturbative vertex might produce scattering matrix elements, which contain higher order terms in a_0 as the purposed linear order, which is especially the case for multiple-vertex processes like the trident process investigated within the present thesis. However, since our primary goal is to derive differential cross sections as defined in equation (2.40) using only the linear order in S_{fi}, we can eventually avoid the issue of higher order terms by defining the differential cross section within this approximation as

$$\mathrm{d}\sigma_{\mathrm{ppQED}} := \lim_{a_0\to 0}\mathrm{d}\sigma \equiv \lim_{a_0\to 0}\mathrm{d}\sigma\Big|_{\Gamma^{\mu}\to\Gamma^{\mu}_{\mathrm{pp}}}. \tag{3.13}$$

The r.h.s of equation (3.13) denotes the differential cross section as defined in equation (2.40), but with the usage of the pulsed-perturbative vertex (3.12) instead of the full dressed vertex. Since the incident photon flux given by equation (2.15) is proportional to a_0^2 and the cross section is proportional to $\frac{|S_{\mathrm{fi}}|^2}{I_\gamma}$, the limit $a_0 \to 0$ cancels out all terms provided by the scattering matrix element S_{fi} with higher than the linear order in a_0. However, one may notice the pulsed-perturbative vertex function (3.10) contains terms independent of a_0, which could produce singularities in the cross section by performing the limit $a_0 \to 0$ due to the appearance of terms scaling with negative powers in a_0. But as it turns out, there will never be a physical phase space for such contributions to the matrix element. The a_0-independent terms in the vertex function are proportional to $\delta(l)$, where l is the photon number parameter at the respective vertex. This implies, that those terms are the contributions to the matrix element, which have no momentum transfer from the background field to any vertex. However, if we recall the assumption made to define the cross section given in equation (2.40), that we have a process with exactly one particle incoming alongside the laser field, terms in the scattering matrix element on tree-level without any transition of momentum from the background field will not contribute to the cross section due to the vanishing physical phase space, i.e. there is no emission nor absorption of a single photon allowed in perturbative QED. Accordingly, this means that the limit in equation (3.13) leads to a differential cross section, which contains only contributions from the scattering matrix element linear in a_0. Furthermore, the restriction to the linear order within the calculation of the scattering matrix element implies, that each momentum space diagram must contain exactly one vertex with a genuine momentum transfer from the background field, i.e. per diagram there is exactly one occurrence of the function $\tilde{\mathit{\Gamma}}^{\mu}_{\mathrm{pp}}$ defined in equation (3.11).

Ward identity and gauge invariance

As we mentioned above the elementary spinors, the external photon states as well as the electron and the photon propagator in the momentum space rules in table 2.2 neither depend on a_0 nor the laser amplitude functions $f_i(\varphi)$. Accordingly, they build, together with the pulsed-perturbative vertex function given in equation (3.12), a valid system of Feynman rules for the linear order in the a_0 expansion as well. However, as we mentioned in section 2.4, the usage of an approximation within a gauge invariant theory may eventually break the gauge invariance. Considering that, we need to prove that our approach of pulsed-perturbative QED and the usage of the momentum space rules w.r.t. the first order in a_0, still result in gauge invariant expressions for given processes. In order to do that, we need to show that the pulsed-perturbative vertex function (3.10) also obeys a Ward identity $k'_\mu \mathit{\Gamma}^{\mu}_{\mathrm{pp}} = 0$. Following the reasoning in section 2.4, we consider $k'_\mu \mathit{\Gamma}^{\mu}_{\mathrm{pp}}$ sandwiched between the two respective Dirac bi-spinors, which results in

$$\begin{aligned} \overline{u}(p')k'_\mu \mathit{\Gamma}^{\mu}_{\mathrm{pp}} u(p) &= \pi\delta(l)\left(2 + a_0 \alpha_1^\nu \lim_{\varphi\to\infty}\left(\beta_{1\nu}(\varphi) + \beta_{1\nu}(-\varphi)\right)\right)\overline{u}(p')\not{k}'u(p) \\ &\quad + a_0\left(\overline{u}(p')k'_\mu \mathit{\Gamma}^{\mu\nu}_1 u(p) - \overline{u}(p')\not{k}'u(p)\mathcal{P}\frac{\alpha_1^\nu}{l}\right)\left(\varepsilon_{1\nu}F_1(l) + \varepsilon_{2\nu}F_2(l)\right). \end{aligned} \tag{3.14}$$

Considering the relation $k' = p - p' + lk$ obtained from the delta-distribution in the pulsed-perturbative vertex (3.12) and using the identities $\overline{u}(p')\not{k}'u(p) = l\overline{u}(p')\not{k}u(p)$ and

$\overline{u}(p')k'_\mu \varGamma_1^{\mu\nu}u(p) = \alpha_1^\nu \overline{u}(p')\not{k}u(p)$, one has

$$\begin{aligned}\overline{u}(p')k'_\mu \varGamma^\mu_{\mathrm{pp}} u(p) = {} & \pi\delta(l) l \left(2 + a_0\alpha_1^\nu \lim_{\varphi\to\infty}\left(\beta_{1\nu}(\varphi)+\beta_{1\nu}(-\varphi)\right)\right)\overline{u}(p')\not{k}u(p) \\ & + a_0 \left(\alpha_1^\nu \overline{u}(p')\not{k}u(p) - l\overline{u}(p')\not{k}u(p)\mathcal{P}\frac{\alpha_1^\nu}{l}\right)\left(\varepsilon_{1\nu}F_1(l)+\varepsilon_{2\nu}F_2(l)\right) \qquad (3.15) \\ = {} & 0, \qquad (3.16)\end{aligned}$$

where we used $x\delta(x) = 0$. Therefore, the pulsed-perturbative vertex (3.12) still obeys the Ward identity, which implies the capability of producing gauge invariant amplitudes as explained in section 2.4.

3.3 Spectrum of the background field

Since the model of strong-field QED (as well as pulsed-perturbative QED) is based on Lorenzian null-fields, the dependence of the background field to the laser phase φ plays a crucial role for the interpretation of the respective quantities derived within the theory. As we mentioned above (cf. section 2.5), the usage of light-cone coordinates (see appendix A.2) is suitable to simplify the appearing mathematical expressions. However, the deeper reason for this circumstance is given in the laser phase φ itself, which is a (scaled) light-cone coordinate:

$$\varphi = k^\mu x_\mu = \omega x^-, \qquad (3.17)$$

where $\omega \equiv k^+$ denotes the reference angular frequency of the laser field and x^- is the position on the negative branch of the light-cone (w.r.t. the spatial direction $\underline{k}/\omega$ of reference momentum $k^\mu = (\omega, \underline{k})$ of the background field), commonly referred to as the light-cone time. Accordingly, since the photon number parameter l defined in equation (2.43) is the Fourier-conjugate of the laser phase φ w.r.t. the strong-field vertex function, it is reasonable to interpret the parameter l as the dimensionless counterpart to the energy transferred from the background field (more precisely the fraction of energy) corresponding to the light-cone time x^-. With this in mind, we can interpret the Fourier transforms (3.4) w.r.t. the amplitude functions (2.17) as the (light-cone) spectra of the background field, i.e. the distribution of the parameter l. More explicitly, if we consider the light-cone coordinate representative of the laser phase from equation (3.17), the Fourier transforms (3.4) result in $F_i(l\omega) = \omega \int \mathrm{d}x^- \, f_i(\omega x^-) \exp\left(il\omega x^-\right)$, which implies, that $l\omega$ is the Fourier-conjugate of the light-cone time x^- and therefore corresponds to the energy fraction of the background field, distributed through the Fourier transforms F_i (see [247] for further discussions).

As we mentioned in section 2.1 one widely considered edge case of the pulsed plane-wave background field (2.10) is the infinite plane-wave field, which one obtains through the limit $\Delta\varphi \to \infty$. For this special case, the parameter l is interpreted as the number of photons with each referenced by the momentum k^μ involved in the respective process (even if there is no photon in the quantum theoretical sense in a classical background field), which implies that the parameter l has only integer values. However, considering the general pulsed plane-wave approach (2.10), there is no constraint of such a kind, since, in the case of a pulsed plane-wave, the parameter l may attain every continuous value on the real line. This is a direct implication of the finite pulse width encoded in the Fourier transform in the definition of the strong-field vertex function (2.43) as well as more explicitly in the Fourier transforms (3.4) appearing in the pulsed-perturbative vertex function (3.10). Since the latter contains the pulse-width effects w.r.t. the first order in the intensity parameter a_0, in the edge case of an infinite plane-wave, the limit $\Delta\varphi \to \infty$ reproduces the discrete behavior of the values of l in the sense of

$$\lim_{\Delta\varphi\to\infty} F_i(l,\Delta\varphi) \sim \delta(l+1) \pm \delta(l-1), \tag{3.18}$$

which constrains the fraction of momentum transferred from the background field to the pulsed-perturbative vertex to $|l| = 1$. Accordingly, this means the model introduced in section 3.2 is capable of describing QED processes involving apparent multi-photon effects in the sense of including continuous fractions of the momentum of the background field but reduces to the one-photon interaction, i.e. perturbative monochromatic QED, in the case of infinitely wide pulse widths. Therefore we refer to the approximation of strong-field QED involving at most the linear order of a_0 on the level of matrix elements (introduced in section 3.2) as pulsed-perturbative QED.

As we mentioned above, each diagram within pulsed-perturbative QED will eventually contain exactly one vertex with a genuine momentum transfer from the background field, which is the part, where the spectra F_i appear as factors in the vertex function. This means, on the level of cross sections, the impact of the pulse width dependence, encoded completely in the functions F_i, will eventually factorise out and occur in terms of the form $\frac{F_i F_j^*}{\Delta\varphi}$ with $i, j = 1, 2$, where the asterisk is the complex conjugation and $\Delta\varphi$ denotes the pulse width, which comes from the incident photon flux within the definition of the differential cross section (cf. equation (2.40)).

Special case of a cos²-envelope

Here we specialise the envelope function $g(\varphi, \varDelta\varphi)$ of the pulsed plane-wave background field to the case of a $\cos^2$-pulse defined in equation (2.18). In this case, the Fourier transforms (3.4) can be derived analytically, where the first Fourier transform F_1 is given by

$$F_1(l, \varDelta\varphi) = \frac{m}{e}\cos(\xi)\int_{-\infty}^{\infty} \mathrm{d}\varphi\,\cos^2\left(\frac{\pi\varphi}{2\varDelta\varphi}\right)\cos(\varphi)\,\mathrm{e}^{il\varphi}\left(\varTheta(\varphi+\varDelta\varphi)-\varTheta(\varphi-\varDelta\varphi)\right) \tag{3.19}$$

$$= \frac{m\pi^2}{2e}\cos(\xi)\varDelta\varphi\left[\frac{\mathrm{sinc}(\varDelta\varphi(l+1))}{\pi^2-\varDelta\varphi^2(l+1)^2}+\frac{\mathrm{sinc}(\varDelta\varphi(l-1))}{\pi^2-\varDelta\varphi^2(l-1)^2}\right]. \tag{3.20}$$

Here the function $\mathrm{sinc}(x) = \frac{\sin(x)}{x}$ for $x \neq 0$ and $\mathrm{sinc}(0) = 1$ denotes the non-normalised sine cardinal function (also shortly referred to as sinc function), where its appearance is reasonable since the sinc function is the Fourier transform of the rectangular function encoded here in the factor $(\varTheta(\varphi+\varDelta\varphi)-\varTheta(\varphi-\varDelta\varphi))$, with the Heaviside step-function $\varTheta$. We mention that F_1 derived in equation (3.20) is real-valued, which is always the case, if the function $f_1(\varphi, \varDelta\varphi)$ is even (e.g. as for the $\cos^2$-pulse), but is, in general, a complex-valued function. The second Fourier transform F_2 follows analogously:

$$F_2(l, \varDelta\varphi) = \frac{m\pi^2}{2ie}\sin(\xi)\varDelta\varphi\left[\frac{\mathrm{sinc}(\varDelta\varphi(l+1))}{\pi^2-\varDelta\varphi^2(l+1)^2}-\frac{\mathrm{sinc}(\varDelta\varphi(l-1))}{\pi^2-\varDelta\varphi^2(l-1)^2}\right], \tag{3.21}$$

where in contrast to F_1, the result given in equation (3.21) is an imaginary-valued function, which is always the case if the function $f_2(\varphi, \varDelta\varphi)$ is odd (e.g. as for the $\cos^2$ pulse). Using the analytic expressions given in (3.20) and (3.21), respectively, the infinite plane-wave limit $\varDelta\varphi \to \infty$ results in

$$\lim_{\varDelta\varphi\to\infty} F_1(l, \varDelta\varphi) = 2\pi\frac{m}{e}\cos(\xi)\left(\delta(l+1)+\delta(l-1)\right) \tag{3.22}$$

$$\lim_{\varDelta\varphi\to\infty} F_2(l, \varDelta\varphi) = 2\pi\frac{m}{ie}\sin(\xi)\left(\delta(l+1)-\delta(l-1)\right), \tag{3.23}$$

where we used the limit $a\,\mathrm{sinc}(ax) \to \pi\delta(x)$ for $a \to \infty$ in the distributional sense, which makes the assumption (3.18) explicit.

As we mentioned above, the impact of the Fourier transforms F_i on cross sections on tree-level will always occur as a factor of the form $\frac{F_iF_j}{\varDelta\varphi}$. Considering this as well as the equations (3.20) and (3.21), in figure 3.3 the expressions $\frac{|F_1|^2}{\varDelta\varphi}$ and $\frac{|F_2|^2}{\varDelta\varphi}$ are depicted for the special case of the $\cos^2$-pulse envelope given in equation (2.18) as functions of the photon number parameter l for several values of the pulse width $\varDelta\varphi$. First of all, we observe that

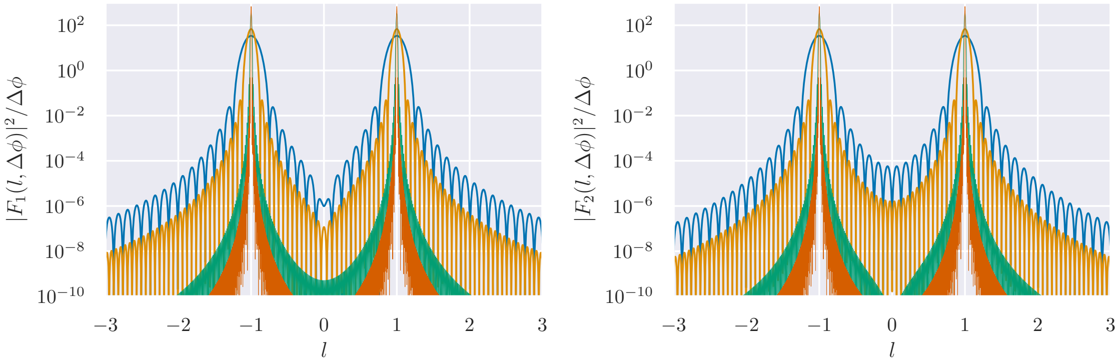

Figure 3.3: The expressions $\frac{|F_1|^2}{\Delta\varphi}$ (left panel) and $\frac{|F_2|^2}{\Delta\varphi}$ (right panel) are depicted for the $\cos^2$-pulse envelope as functions of the photon number parameter l for several values of the pulse width $\Delta\varphi$ (blue: 25, orange: 50, green: 250, red: 500).

both functions are symmetric w.r.t. the parameter l, which results from the fact, that the function F_1 (F_2) is originally even (odd) for the case of a $\cos^2$-pulse shape. Furthermore, we mention that in each panel as well as for each value of $\Delta\varphi$, there are two distinct main maxima centred around the values $l = 1$ and $l = -1$, respectively. This shows explicitly that the impact of the pulse envelope on cross sections within pulsed-perturbative QED will occur similar to a one-photon interaction, but with a certain bandwidth indicated by the non-vanishing of the expressions depicted in figure 3.3 over a wide range of values l, especially those with $|l| \neq 1$. Accordingly, the first side maximum at each side of the respective main maximum is placed between $l_{\max} \pm \frac{2\pi}{\Delta\varphi}$, and $l_{\max} \pm \frac{3\pi}{\Delta\varphi}$, where $l_{\max} = \pm 1$ and their heights are about 6×10^{-4} of the respective main maximum. This means the contribution of these side effects is not negligible. Moreover, in both panels in figure 3.3 the width (height) of each distinct main maximum decreases (increases) for increasing pulse widths $\Delta\varphi$, which will eventually result in the delta-distributions similar to those in the equations (3.22) and (3.23), respectively (see equations (4.43) and (4.47)).

4 | Pulsed-perturbative trident process

4.1 Matrix element and cross section

In order to investigate the pulse shape dependence of the strong-field trident process (see section 2.5) separately from intensity effects, we consider the lowest order of an expansion in the intensity parameter a_0, which will be referred to as pulsed-perturbative trident process. However, since the framework of pulsed-perturbative QED envisaged in section 3.2 provides a valid description of the pulse dependence of strong-field QED processes w.r.t. to the linear order in the intensity parameter a_0 in general, we use pulsed-perturbative QED to derive the pulsed-perturbative trident process instead of expanding each quantity derived in section 2.5 in a_0 separately. This convenient approach enables the investigation of the pulse shape dependency in terms of the general structures illustrated in section 3.3, i.e. the effect of the spectrum of the background field on the matrix element and cross sections of the pulsed-perturbative trident process.

In terms of pulsed-perturbative QED, the pulsed-perturbative trident process is described on tree-level by the momentum space diagrams depicted in figure 4.1, where p denotes the

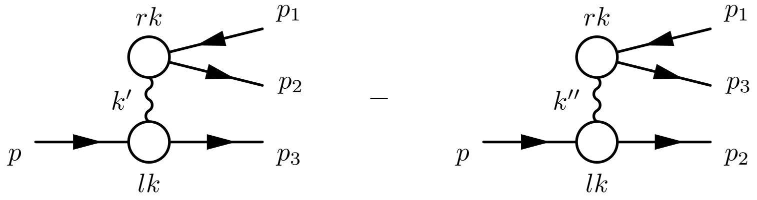

Figure 4.1: The diagrammatical representation of the pulsed-perturbative trident in momentum space, where p denoted the momentum of the initial electron, p_1 the momentum of the outgoing positron and p_2, p_3 the momenta w.r.t. the two outgoing electrons, respectively. The momentum transfer from the background field (with momentum k) to each vertex is denoted by l and r, respectively. The respective momentum of the intermediate photon is k' for the first (direct) and k'' for the second (exchange) diagram.

momentum of the incoming electron, k the reference momentum of the laser field, p_1 is the momenta of the outgoing positron, and p_2, p_3 are the momenta of the two outgoing electrons. The occurring pulsed-perturbative vertices are defined in equation (3.12), where r, l denote the respective photon number parameter at each vertex. Similar to the full strong-field trident case, there are two diagrams representing the pulsed-perturbative trident on tree-level, due to the indistinguishability of the two final electrons: the direct contribution (l.h.s. of figure 4.1) and the exchange contribution (r.h.s. of figure 4.1), where the relative sign is determined by the Pauli exclusion principle. Using the momentum-space rules illustrated in section 3.2, the matrix element of the direct part of pulsed-perturbative trident is given by

$$\begin{aligned}
S_{\mathrm{fi}}^{\mathrm{d}} &= \int \frac{\mathrm{d}l}{2\pi} \int \frac{\mathrm{d}r}{2\pi} \int \frac{\mathrm{d}^4 k'}{(2\pi)^4} D_{\mu\nu}(k') \\
&\quad \times \overline{u}(p_3) \left(-ie\Gamma^{\mu}_{\mathrm{pp}}(l, p, p_3)\right) u(p)\, (2\pi)^4\, \delta^{(4)}(p + lk - p_3 - k') \\
&\quad \times \overline{u}(p_2) \left(-ie\Gamma^{\nu}_{\mathrm{pp}}(r, -p_1, p_2)\right) v(p_1)\, (2\pi)^4\, \delta^{(4)}(k' + rk - p_2 - p_1) && (4.1) \\
&= -ie^2\, (2\pi)^2 \int \mathrm{d}l \int \mathrm{d}r\, \frac{g_{\mu\nu}}{k'^2 + i\epsilon} \delta^{(4)}(p + (l + r)k - p_t) \\
&\quad \times \left[\overline{u}(p_3)\Gamma^{\mu}_{\mathrm{pp}}(l, p, p_3) u(p)\right] \times \left[\overline{u}(p_2)\Gamma^{\nu}_{\mathrm{pp}}(r, -p_1, p_2) v(p_1)\right], && (4.2)
\end{aligned}$$

where we use the abbreviation $p_t := p_1 + p_2 + p_3$. The pulsed-perturbative vertex function $\Gamma^{\mu}_{\mathrm{pp}}$ is defined in equation (3.10) and $D_{\mu\nu}$ denotes the photon propagator from perturbative QED, which is given along with all occurring fundamental Dirac bi-spinors in table B.1 in the appendix. In the last step, we used one delta-distribution to solve the integral over the four-momentum of the intermediate photon, which leads to $k' = p + lk - p_3 = p_1 + p_2 - rk$. This is analogous to the strong-field trident process yielding to the same kinematically attribution w.r.t. the virtual sub-processes:

$$\begin{aligned}
p + lk &= k' + p_3 && \text{(virtual) pulsed-perturbative Compton ,} && (4.3) \\
k' + rk &= p_1 + p_2 && \text{(virtual) pulsed-perturbative Breit-Wheeler,} && (4.4)
\end{aligned}$$

but with the denotation as pulsed-perturbative (sub-) processes, due to the usage of the pulsed-perturbative vertex rather than the strong-field vertex. This leads to the global energy-momentum conservation $p + (l + r)k = p_t = p_1 + p_2 + p_3$ indicated by the delta-distribution in equation (4.2).

As shown for the strong-field trident, here it is also suitable to use the light-cone coordinates for the momenta as illustrated in section A.2 in the appendix with the assumption that the spatial part of the reference momentum k of the laser field is aligned along the 3-axis in momentum space, which implies k^+ is the only non-vanishing component of k. Then the matrix element results in

$$\begin{aligned} S_{\mathrm{fi}}^{\mathrm{d}} = &\frac{-ie^2\,(2\pi)^2}{k^+}\delta^{\mathrm{lf}}(p-p_t)\int \mathrm{d}l\,\frac{g_{\mu\nu}}{k'^2+i\epsilon} \\ &\times \left[\overline{u}(p_3)\mathit{\Gamma}^{\mu}_{\mathrm{pp}}(l,p,p_3)u(p)\right]\left[\overline{u}(p_2)\mathit{\Gamma}^{\nu}_{\mathrm{pp}}(r_l,-p_1,p_2)v(p_1)\right], \end{aligned} \tag{4.5}$$

where we used the identity $\delta^{(4)}(q) = \delta^{\mathrm{lf}}(q)\delta(q^+)$ with the abbreviation $\delta^{\mathrm{lf}}(q) := \frac{1}{2}\delta^{(2)}(q^\perp)\delta(q^-)$ for an arbitrary four-momentum q. The resulting delta-distribution for the plus-components of global energy-momentum conservation yields $p^+ + (l+r)k^+ = p_t^+$ and leads to a relation between the occurring photon number parameters $r_l := l_0 - l$, where

$$l_0 = \frac{p_t^+ - p^+}{k^+} = \frac{p_1^+ + p_2^+ + p_3^+ - p^+}{k^+}, \tag{4.6}$$

with $l_0 = r_0 \neq 0$ (see section 2.5 for a more complete reasoning). Up to this point, the kinematical behavior of strong-field and pulsed-perturbative trident is the same, of course. However, due to the restriction on the linear order in the laser intensity parameter a_0, the pulsed-perturbative vertex function will generate kinematical constraints different from the corresponding strong-field case. Especially considering the photon number parameter: it depends in pulsed-perturbative trident only on the final momenta due to equation (4.6) (see below), but needs to be integrated over for certain contributions in the general strong-field case (e.g. see equation (2.92)).

Considering the separation of the pulsed-perturbative vertex given in equation (3.11), the matrix element (4.5) decomposes into four distinct parts:

$$\begin{aligned} S_{\mathrm{fi}}^{\mathrm{d}} = &\frac{-ie^2\,(2\pi)^2}{k^+}\delta^{\mathrm{lf}}(p-p_t)\int \mathrm{d}l\,\frac{g_{\mu\nu}}{k'^2+i\epsilon} \\ &\times \overline{u}(p_3)\left[\delta(l)\tilde{\mathit{\Gamma}}^{\mu}_{0}(p,p_3) + a_0\tilde{\mathit{\Gamma}}^{\mu}_{\mathrm{pp}}(l,p,p_3)\right]u(p) \\ &\times \overline{u}(p_2)\left[\delta(l_0-l)\tilde{\mathit{\Gamma}}^{\nu}_{0}(-p_1,p_2) + a_0\tilde{\mathit{\Gamma}}^{\nu}_{\mathrm{pp}}(l_0-l,-p_1,p_2)\right]v(p_1) && (4.7) \\ = &\,S_0^{\mathrm{pp}} + S_{11}^{\mathrm{pp}} + S_{12}^{\mathrm{pp}} + S_2^{\mathrm{pp}}. && (4.8) \end{aligned}$$

This decomposition of the matrix element is similar to the case of strong-field trident given in equation (2.84), but in the case of pulsed-perturbative trident, the expansion in the intensity parameter a_0 is truncated due to the linear order of a_0 in the respective pulsed-perturbative vertex. Starting with the first summand in equation (4.8), the term

S_0^{pp} is given as

$$S_0^{\mathrm{pp}} = \frac{-ie^2\,(2\pi)^2}{k^+}\delta^{\mathrm{lf}}(p-p_t)\delta(l_0)\frac{g_{\mu\nu}}{k'^2+i\epsilon}$$
$$\times\left[\overline{u}(p_3)\tilde{\Gamma}_0^{\mu}(p,p_3)u(p)\right]\left[\overline{u}(p_2)\tilde{\Gamma}_0^{\nu}(-p_1,p_2)v(p_1)\right], \tag{4.9}$$

where l_0 is given in equation (4.6). Analogous to the strong-field case stated in equation (2.86), one has again $\frac{1}{k^+}\delta^{\mathrm{lf}}(p-p_t)\delta(l_0)=\delta^{(4)}(p-p_t)$, which implies the part S_0^{pp} of the matrix element has no final physical phase space, through $p=p_t=p_1+p_2+p_3$ violates the energy momentum conservation. This is also clear, since the term S_0^{pp} corresponds to the case, where no momentum from the background field is transferred to either of the vertices, which is kinematically forbidden as we already mentioned. The second summand of equation (4.8) is given as

$$S_{11}^{\mathrm{pp}} = \frac{-ie^2a_0\,(2\pi)^3}{k^+}\delta^{\mathrm{lf}}(p-p_t)\frac{g_{\mu\nu}}{(p_1+p_2)^2+i\epsilon}$$
$$\times\left[\overline{u}(p_3)\tilde{\Gamma}_{\mathrm{pp}}^{\mu}(l_0,p,p_3)u(p)\right]\left[\overline{u}(p_2)\tilde{\Gamma}_0^{\nu}(-p_1,p_2)v(p_1)\right] \tag{4.10}$$
$$= \frac{-ie^2a_0\,(2\pi)^3}{k^+}\delta^{\mathrm{lf}}(p-p_t)M_{11}^{\mathrm{pp}}+\mathcal{O}(a_0^2), \tag{4.11}$$

where we used the energy-momentum conservation at the upper vertex given in (4.4) with $r=0$ (implied from $l=l_0$) to replace the intermediate momentum k'. We introduce the abbreviation

$$M_{11}^{\mathrm{pp}} := \frac{g_{\mu\nu}}{(p_1+p_2)^2+i\epsilon}\left[\overline{u}(p_3)\tilde{\Gamma}_{\mathrm{pp}}^{\mu}(l_0,p,p_3)u(p)\right]\left[\overline{u}(p_2)\gamma^{\nu}v(p_1)\right], \tag{4.12}$$

which is a function of all momenta with l_0 is given in equation (4.6) and has no dependence to the intensity parameter a_0. Here S_{11}^{pp} represents the case, where the momentum transfer from the background field to the upper vertex vanishes but is finite to the lower vertex due to $l_0\neq 0$. The third summand in the decomposition in equation (4.8) is given as

$$S_{12}^{\mathrm{pp}} = \frac{-ie^2a_0\,(2\pi)^3}{k^+}\delta^{\mathrm{lf}}(p-p_t)\frac{g_{\mu\nu}}{(p-p_3)^2+i\epsilon}$$
$$\times\left[\overline{u}(p_3)\tilde{\Gamma}_0^{\mu}(p,p_3)u(p)\right]\left[\overline{u}(p_2)\tilde{\Gamma}_{\mathrm{pp}}^{\nu}(l_0,-p_1,p_2)v(p_1)\right] \tag{4.13}$$
$$= \frac{-ie^2a_0\,(2\pi)^3}{k^+}\delta^{\mathrm{lf}}(p-p_t)M_{12}^{\mathrm{pp}}+\mathcal{O}(a_0^2), \tag{4.14}$$

where we used the energy-momentum conservation at the lower vertex given in (4.3) with $l=0$ (implied from $r=l_0$) to replace the intermediate momentum k'. We introduce the abbreviation

$$M_{12}^{\mathrm{pp}} := \frac{g_{\mu\nu}}{(p-p_3)^2 + i\epsilon} \left[\overline{u}(p_3)\gamma^\mu u(p)\right] \left[\overline{u}(p_2)\tilde{\Gamma}^\nu_{\mathrm{pp}}(l_0, -p_1, p_2)v(p_1)\right], \tag{4.15}$$

which is also a function of all momenta and has neither any dependence to the intensity parameter a_0. Here S_{12}^{pp} represents the case, where the momentum transfer from the background field to the upper vertex is finite due to $l_0 \neq 0$, but the transfer vanishes at the lower vertex. We mention, that the photon number parameter l_0 present in equation (4.15) turns out to be the same as occurred in equation (4.12).

The last term in the decomposition (4.8) is given by

$$\begin{aligned} S_2^{\mathrm{pp}} &= \frac{-ie^2 a_0^2\,(2\pi)^2}{k^+}\delta^{\mathrm{lf}}(p-p_t)\int \mathrm{d}l\,\frac{g_{\mu\nu}}{k'^2 + i\epsilon} \\ &\quad\times \left[\overline{u}(p_3)\tilde{\Gamma}^\mu_{\mathrm{pp}}(l, p, p_3)u(p)\right]\left[\overline{u}(p_2)\tilde{\Gamma}^\nu_{\mathrm{pp}}(l_0 - l, -p_1, p_2)v(p_1)\right] && (4.16) \\ &= \mathcal{O}(a_0^2). && (4.17) \end{aligned}$$

Within the framework of pulsed-perturbative QED (see section 3.2), it is assumed that the only terms of a matrix element, which contribute to the cross section, are linear w.r.t. the intensity parameter a_0. This is induced automatically on the level of cross sections due to the definition (3.13) and indicates the main difference to the strong-field case regarded in section 2.5. Considering this, we can neglect each occurring term with $\mathcal{O}(a_0^2)$ in equation (4.10) and (4.13), respectively, and the term S_2^{pp} entirely, as well. More precisely compared to the strong-field case, as it turns out, the derived a_0-linear parts of equation (4.10) and (4.13) are exactly the a_0-linear terms of the parts S_{11}, S_{12} from the strong-field trident matrix element (see equation (2.87) and (2.88)), where the vertices have one vanishing and one non-vanishing momentum transfer from the background field, which is, of course, the same property as derived above for S_{11}^{pp} and S_{12}^{pp}, respectively. This means one has

$$S_{11} = \frac{-ie^2 a_0\,(2\pi)^3}{k^+}\delta^{\mathrm{lf}}(p-p_t)M_{11}^{\mathrm{pp}} + \mathcal{O}(a_0^2), \tag{4.18}$$

$$S_{12} = \frac{-ie^2 a_0\,(2\pi)^3}{k^+}\delta^{\mathrm{lf}}(p-p_t)M_{12}^{\mathrm{pp}} + \mathcal{O}(a_0^2), \tag{4.19}$$

where it is explicitly shown, that in the decomposition (2.93) of the matrix element of strong-field trident, the linear order in a_0 (and with that the limiting case of perturbative trident) is only contained in the parts with partial momentum transfer from the background field.

In order to avoid denotation issues, we define $S_{\mathrm{ppT}}^{\mathrm{d}}$ as the linear part of the matrix element

$S^{\mathrm{d}}_{\mathrm{fi}}$ given in equation (4.2) w.r.t. the intensity parameter a_0, i.e. $S^{\mathrm{d}}_{\mathrm{fi}} =: S^{\mathrm{d}}_{\mathrm{ppT}} + \mathcal{O}(a_0^2)$, where $S^{\mathrm{d}}_{\mathrm{ppT}}$ is given as

$$S^{\mathrm{d}}_{\mathrm{ppT}} = \frac{-ie^2 a_0 \,(2\pi)^3}{k^+} \delta^{\mathrm{lf}}(p - p_t)\,(M^{\mathrm{pp}}_{11} + M^{\mathrm{pp}}_{12})\,, \tag{4.20}$$

where $M^{\mathrm{pp}}_{11}, M^{\mathrm{pp}}_{12}$ are defined in equation (4.12) and in equation (4.15), respectively. Subsequently going forward to the full matrix element of pulsed-perturbative trident (including the exchange part), we introduce

$$M^{\mathrm{pp}}_{\mathrm{C}} = M^{\mathrm{pp}}_{11} - M^{\mathrm{pp}}_{11}(p_2 \leftrightarrow p_3), \tag{4.21}$$

$$M^{\mathrm{pp}}_{\mathrm{BW}} = M^{\mathrm{pp}}_{12} - M^{\mathrm{pp}}_{12}(p_2 \leftrightarrow p_3), \tag{4.22}$$

where $M^{\mathrm{pp}}_{\mathrm{C}}$ denotes the virtual Compton part, i.e. the part with a genuine momentum transfer from the background field at the lower vertex and a vanishing transfer at the upper vertex, and $M^{\mathrm{pp}}_{\mathrm{BW}}$ denotes the virtual Breit-Wheeler part, i.e. the part with a genuine momentum transfer from the background field at the upper vertex and a vanishing transfer at the lower vertex. Accordingly the full matrix element of pulsed-perturbative trident reads

$$S_{\mathrm{ppT}} = \frac{1}{2}\left(S^{\mathrm{d}}_{\mathrm{ppT}} - S^{\mathrm{d}}_{\mathrm{ppT}}(p_2 \leftrightarrow p_3)\right) = \frac{-ie^2 a_0\,(2\pi)^3}{2k^+}\delta^{\mathrm{lf}}(p - p_t)\left(M^{\mathrm{pp}}_{\mathrm{C}} + M^{\mathrm{pp}}_{\mathrm{BW}}\right), \tag{4.23}$$

which is by definition linear in the intensity parameter a_0. Therefore, there is no effect through higher orders in the intensity parameter a_0, but a distinct pulse shape dependence encrypted in the function $\tilde{\mathit{\Gamma}}^{\mu}_{\mathrm{pp}}$ (cf. to equation (3.11)) occurring in the expressions $M^{\mathrm{pp}}_{\mathrm{C}}, M^{\mathrm{pp}}_{\mathrm{BW}}$ through equation (4.12) and (4.15).
Using the matrix element from equation (4.23) as well as the definition (3.13), the (six-fold) differential cross section of pulsed-perturbative trident reads

$$\mathrm{d}\sigma_{\mathrm{ppT}} = \frac{a_0^2 e^4\,(2\pi)^6}{I_\gamma (2k^+)^2}\frac{1}{V_{\mathrm{lf}}}\delta^{\mathrm{lf}}(p - p_t)\frac{p^0}{4p^+\,(2\pi)^3}V_{\mathrm{lf}} N \sum_{\mathrm{spins,pol.}} \left|M^{\mathrm{pp}}_{\mathrm{C}} + M^{\mathrm{pp}}_{\mathrm{BW}}\right|^2 \mathrm{d}\mathit{\Phi}_3, \tag{4.24}$$

where I_γ denotes the incident photon flux defined in equation (2.8) and $N = \frac{1}{4}$ is the normalization factor caused by averaging over the spin and polarization of the incoming electron and photon, respectively. Considering the case of a polarized incoming photon, the normalization factor is given as $N = \frac{1}{2}$. Here, $\mathrm{d}\mathit{\Phi}_3$ denotes the three-particle invariant phase space integral measure, which is given in light-cone coordinates as

$$\mathrm{d}\Phi_3 := \Theta(p_1^-)\Theta(p_2^-)\Theta(p_3^-)\frac{\mathrm{d}^2p_1^\perp\,\mathrm{d}p_1^-}{(2\pi)^3\,2p_1^-}\frac{\mathrm{d}^2p_2^\perp\,\mathrm{d}p_2^-}{(2\pi)^3\,2p_2^-}\frac{\mathrm{d}^2p_3^\perp\,\mathrm{d}p_3^-}{(2\pi)^3\,2p_3^-}, \tag{4.25}$$

with Θ denotes the Heaviside step-function (cf. section A.2). Considering the square of the delta-distribution coming from the square of the absolute value of the matrix element given in equation (4.23), we used the (Lorentz-invariant) identity $(2\pi)^3\left(\delta^{\mathrm{lf}}(p-p_t)\right)^2 = V_{\mathrm{lf}}\frac{p^0}{p^+}\delta^{\mathrm{lf}}(p-p_t)$ from [247] (cf. [177]). Since this identity is Lorentz-invariant, the quotient of the initial electron momentum components can be evaluated in its rest system (cf. section A.3): $\frac{p^0}{p^+}=2$. Finally, the differential cross section results in

$$\mathrm{d}\sigma_{\mathrm{ppT}} = \frac{a_0^2e^4\pi^3}{I_\gamma(k^+)^2}\delta^{\mathrm{lf}}(p-p_t)N\sum_{\mathrm{spins,pol.}}\left|M_{\mathrm{C}}^{\mathrm{pp}}+M_{\mathrm{BW}}^{\mathrm{pp}}\right|^2\,\mathrm{d}\Phi_3, \tag{4.26}$$

where we eventually use the delta-distribution to integrate over one final particle leading to six remaining independent momentum components in the final phase space, i.e. two kinematically independent outgoing particles.

Pulse shape dependence: factorisation the differential cross section

As we illustrated in chapter 3, the main conceptional advantage of pulsed-perturbative QED (i.e. the assumption of small laser intensities and therefore the consideration of the leading order in a_0 exclusively) is the emphasis of the pulse shape dependence of processes due to the Fourier transforms $F_i(l)$ defined in (3.4) of the amplitude functions $f_i(\varphi)$ given in (2.17). Consequently, the dependence of the differential cross section (4.26) on the pulse shape function $g(\varphi)$ (in terms of the Fourier transforms F_i) plays a crucial role for the understanding of the trident process at small intensity parameters a_0, especially compared to the perturbative case.

Firstly, we mention that the momentum dependence of the photon number parameter l occurring in the pulsed-perturbative vertex function (3.10) neither changes through the exchange $p_2 \leftrightarrow p_3$ nor for the virtual Compton or virtual Breit-Wheeler parts of the matrix element, i.e. in every part of the matrix element (4.26), the photon number parameter obeys $l = l_0$, where l_0 is given in equation (4.6). This implies a factorisation of the pulse shape dependence in terms of the Fourier transforms (3.4) occurring in the pulsed-perturbative vertex for each term in the matrix element. Considering the part $\tilde{\Gamma}^\mu_{\mathrm{pp}}$ of the pulsed-perturbative vertex function (3.10) and inserting it in the parts (4.21) and

(4.22) of the matrix element by the use of the terms (4.12) and (4.15), one has

$$M_{\mathrm{C}}^{\mathrm{pp}} = M_{\mathrm{C}}^{(1)} F_1(l_0) + M_{\mathrm{C}}^{(2)} F_2(l_0), \tag{4.27}$$

$$M_{\mathrm{BW}}^{\mathrm{pp}} = M_{\mathrm{BW}}^{(1)} F_1(l_0) + M_{\mathrm{BW}}^{(2)} F_2(l_0), \tag{4.28}$$

where F_i are the Fourier transforms defined in equation (3.4) (cf. section 3.3). The remaining factors are given as

$$\begin{aligned} M_{\mathrm{C}}^{(i)} = {} & \frac{g_{\mu\nu}\varepsilon_{i\tau}}{(p_1+p_2)^2+i\epsilon}\left[\overline{u}(p_3)\left(\mathit{\Gamma}_1^{\mu\tau}(p,p_3) - \mathit{\Gamma}_0^{\mu}\frac{\alpha_1^{\tau}(p,p_3)}{l_0}\right)u(p)\right]\left[\overline{u}(p_2)\gamma^{\nu}v(p_1)\right] \\ & - (p_2 \leftrightarrow p_3), \end{aligned} \tag{4.29}$$

$$\begin{aligned} M_{\mathrm{BW}}^{(i)} = {} & \frac{g_{\mu\nu}\varepsilon_{i\tau}}{(p-p_3)^2+i\epsilon}\left[\overline{u}(p_3)\gamma^{\mu}u(p)\right]\left[\overline{u}(p_2)\left(\mathit{\Gamma}_1^{\nu\tau}(-p_1,p_2) - \mathit{\Gamma}_0^{\nu}\frac{\alpha_1^{\tau}(-p_1,p_2)}{l_0}\right)v(p_1)\right] \\ & - (p_2 \leftrightarrow p_3), \end{aligned} \tag{4.30}$$

where $\varepsilon_{i\tau}$ with $i = 1{,}2$ denote the elementary polarisation vectors introduced according to the general definition of the pulsed plane-wave background field in equation (2.10). We mention, that the factors $M_{\mathrm{C}}^{(i)}, M_{\mathrm{BW}}^{(i)}$ given in (4.29) and (4.30) do not depend on the pulse shape itself (this dependence is accumulated in the Fourier transforms F_i), but have a dependence on the momentum transfer from the background field due to the photon number parameter l_0. Inserting the factorisations (4.27) and (4.28) into the differential cross section (4.26) leads to

$$\begin{aligned} \mathrm{d}\sigma_{\mathrm{ppT}} = {} & \frac{a_0^2 e^4 \pi^3}{I_\gamma (k^+)^2}\delta^{\mathrm{lf}}(p-p_t)N \\ & \times \sum_{\mathrm{spins,pol.}} \left|(M_{\mathrm{C}}^{(1)} + M_{\mathrm{BW}}^{(1)})F_1(l_0) + (M_{\mathrm{C}}^{(2)} + M_{\mathrm{BW}}^{(2)})F_2(l_0)\right|^2 \mathrm{d}\mathit{\Phi}_3, \end{aligned} \tag{4.31}$$

where indeed on the level of the differential cross section, for general pulse envelope functions $g(\varphi)$ there is no complete factorisation w.r.t. the Fourier transforms F_i. However, as we illustrated in section 3.3, if we assume the pulse envelope function $g(\varphi)$ is an even function, which means for the amplitude functions of the background field (cf. equation (2.17)) one has $f_1(\varphi)$ ($f_2(\varphi)$) is an even (odd) function, the Fourier transform $F_1(l)$ ($F_2(l)$) is a real- (imaginary-)valued function. We mention, this assumption is not far to seek, since most of the pulse envelope functions used in literature to describe scattering processes are indeed even functions, e.g. the $\cos^2$-pulse used in this thesis, which was defined in (2.18). Considering this case and using the abbreviation $M^i := M_{\mathrm{C}}^{(i)} + M_{\mathrm{BW}}^{(i)}$ with $i = 1{,}2$, the square of the absolute value in equation (4.31) leads to

$$\left|M^{(1)}F_1 + M^{(2)}F_2\right|^2 = \left|M^{(1)}F_1\right|^2 + \left|M^{(2)}F_2\right|^2 + 2\mathrm{Re}\left(M^{(1)}F_1M^{(2)*}F_2^*\right) \tag{4.32}$$

$$= \left|M^{(1)}\right|^2 F_1^2 + \left|M^{(2)}\right|^2 |F_2|^2 + 2\left(iF_1F_2^*\right)\mathrm{Im}\left(M^{(1)}M^{(2)*}\right), \tag{4.33}$$

where the asterisk denotes the complex conjugation, Re (Im) the real (imaginary) part of a complex number and $iF_1F_2^* \in \mathbb{R}$ as a result of F_1 (F_2) being a real-(imaginary-)valued function. In the last step, we used the homogeneity of the real-part function, i.e. for $u \in \mathbb{C}$ and $\lambda \in \mathbb{R}$ it is $\mathrm{Re}(\lambda u) = \lambda\mathrm{Re}(u)$, as well as the identity $\mathrm{Re}(iu) = -\mathrm{Im}(u)$ for $u \in \mathbb{C}$. Consequently, the assumption, that the pulse envelope $g(\varphi)$ is an even function yields a factorisation of the matrix element w.r.t. the Fourier transforms F_i, i.e. each summand in equation (4.33) is a product of two factors, one with and one without dependence to the pulse shape function, hence they can be derived separately.

Furthermore, if we assume the background field to be linearly polarized, say in the $\underline{\varepsilon}_1$-direction (i.e. $\xi = 0$), one has $f_2(\varphi) = 0$, which implies $F_2(\varphi) = 0$ (cf. equations (2.17) and (3.4)). Then the differential cross section reads

$$\mathrm{d}\sigma_{\mathrm{ppT}}\Big|_{\xi=0} = \frac{a_0^2e^4\pi^3}{I_\gamma(k^+)^2}\delta^{\mathrm{lf}}(p-p_t)\left|F_1(l_0)\right|^2 N\sum_{\mathrm{spins}}\left|M_{\mathrm{C}}^{(1)} + M_{\mathrm{BW}}^{(1)}\right|^2 \mathrm{d}\varPhi_3, \tag{4.34}$$

yielding again a factorisation of the differential cross section w.r.t. the pulse shape dependence, despite the pulse shape function $g(\varphi)$ is even or not. In summary, the factorisation of the differential cross section of pulsed-perturbative trident shown above leads to a more feasible numerical treatment of the trident process at small intensity parameters a_0, because mostly the pulse shape dependence can be treated fully analytically, as we illustrated in section 3.3. Furthermore, it is conceivable, that the factorisation opens up the possibility to obtain the pulse shape dependence or, more explicitly, the energy distribution of the laser field from another source, e.g. from experimental data or simulations, rather than the definition of a pulse envelope function. However, such data-driven approaches are beyond the scope of this thesis and require further investigations.

Infinitely wide pulses: the perturbative monochromatic limit

Generally, we refer to as the perturbative (monochromatic) limit of a certain scattering process derived in the framework of strong-field QED in pulsed plane-wave fields, as the simultaneous limit of weak-fields, i.e. $a_0 \ll 1$, and infinitely wide pulses, i.e. $\varDelta\varphi \to \infty$ (cf. section 3.1). Since the cross section given in equation (4.26) is by definition the leading term in the weak-field limit $a_0 \to 0$ (see equation (3.13)) the perturbative limit of strong-field trident results as the limiting case of pulsed-perturbative trident for infinitely wide pulses, i.e. we propose

$$\mathrm{d}\sigma_{\mathrm{pT}} = \lim_{\Delta\varphi\to\infty} \lim_{a_0\to 0} \mathrm{d}\sigma_{\mathrm{sfT}} = \lim_{\Delta\varphi\to\infty} \mathrm{d}\sigma_{\mathrm{ppT}}, \tag{4.35}$$

where $\mathrm{d}\sigma_{\mathrm{pT}}$ denotes the differential cross section of perturbative trident given in equation (C.9), $\mathrm{d}\sigma_{\mathrm{sfT}}$ is the differential cross section of strong-field trident (see section 2.5) and $\mathrm{d}\sigma_{\mathrm{ppT}}$ the differential cross section of pulsed-perturbative trident given in equation (4.26). In order to actually perform the last limit given in equation (4.35), we exploit the factorization of the differential cross section of pulsed-perturbative trident as illustrated in equation (4.33) and/or (4.34) w.r.t. the pulse-shape dependent functions $F_i(l)$, which are defined in equation (3.4). Here, we assume a general pulse envelope function $g(\varphi, \Delta\varphi)$ with pulse width $\Delta\varphi$, which is defined as part of the pulse plane-wave approach for the background field defined in equation (2.10). Assuming the pulse envelope function to be even, i.e. symmetric w.r.t. the y-axis, there are three types of factors encoding the whole pulse shape dependence of the differential cross section (cf. equation (4.33)):

$$\frac{|F_1(l,\Delta\varphi)|^2}{\Delta\varphi}, \qquad \frac{|F_2(l,\Delta\varphi)|^2}{\Delta\varphi}, \qquad \frac{iF_1(l,\Delta\varphi)F_2^*(l,\Delta\varphi)}{\Delta\varphi}, \tag{4.36}$$

where the pulse width $\Delta\varphi$ in the respective denominator comes from the normalization factor I_γ defined in equation (2.8), which is in the case of wide pulses given by $I_\gamma(\Delta\varphi \gg 1) = \frac{m^2 a_0^2}{2e^2}\nu_2[g]\Delta\varphi$ with the second momentum $\nu_2[g] := \int g^2(\varphi)\,\mathrm{d}\varphi$ of the pulse envelope function $g(\varphi, \Delta\varphi)$.

Independently, the first two terms in (4.36) also occur in the factorisation of the differential cross section, if one assumes linear polarisation (cf. equation (4.34)).

Using the definition (3.4), one may rewrite the Fourier transforms F_i as

$$F_1(l,\Delta\varphi) = \frac{m}{2e}\cos\xi\left(F_g(l+1,\Delta\varphi) + F_g(l-1,\Delta\varphi)\right), \tag{4.37}$$

$$F_2(l,\Delta\varphi) = \frac{m}{2ie}\sin\xi\left(F_g(l+1,\Delta\varphi) - F_g(l-1,\Delta\varphi)\right), \tag{4.38}$$

where ξ denotes the polarisation parameter, m the electron mass, and e the absolute value of the elementary electric charge. The function

$$F_g(l) := \int_{-\infty}^{\infty} g(\varphi,\Delta\varphi)e^{il\varphi}\,d\varphi \tag{4.39}$$

denotes the Fourier transform of the pulse envelope function, where we remark the distinction to the functions $F_i(l)$ with $i = 1{,}2$, which are the Fourier transforms of the respective amplitude functions $f_i(\varphi, \varDelta\varphi)$, which in turn are the pulse envelope function multiplied by an oscillatory term (see equation (2.17)). We mention, that the representations (4.37) and (4.38) in terms of the Fourier transform (4.39) leads easily to the limits

$$\lim_{\varDelta\varphi\to\infty} F_1(l,\varDelta\varphi) = 2\pi\frac{m}{e}\cos\xi(\delta(l+1)+\delta(l-1)), \tag{4.40}$$

$$\lim_{\varDelta\varphi\to\infty} F_2(l,\varDelta\varphi) = 2\pi\frac{m}{e}\sin\xi(\delta(l+1)-\delta(l-1)), \tag{4.41}$$

where we used the elementary limit $F_g(l,\varDelta\varphi) \to 2\pi\delta(l)$ for $\varDelta\varphi \to \infty$, which was derived in lemma D.1 in the appendix. This shows again explicitly the assumption (3.18), but here for an arbitrary pulse envelope function g. However, due to the occurrence of a squared delta-distribution, the application of the limits (4.40) and (4.41) are not expedient for the terms listed in (4.36). Instead, the limit $\varDelta\varphi \to \infty$ must be performed explicitly for the squared Fourier transforms.

Consequently, using equation (4.37), the limiting case $\varDelta\varphi \to \infty$ of the first factor in (4.36) leads to

$$\begin{aligned}\lim_{\varDelta\varphi\to\infty}\frac{|F_1(l,\varDelta\varphi)|^2}{\varDelta\varphi} &= \frac{m^2}{4e^2}\cos^2\xi \lim_{\varDelta\varphi\to\infty}\\ &\left[\frac{|F_g(l+1)|^2}{\varDelta\varphi}+\frac{|F_g(l-1)|^2}{\varDelta\varphi}+\frac{2}{\varDelta\varphi}\mathrm{Re}\left(F_g(l+1)F_g^*(l-1)\right)\right] \qquad (4.42)\\ &= \frac{\pi m^2}{2e^2}\nu_2[g]\cos^2\xi\left(\delta(l+1)+\delta(l-1)\right), \qquad (4.43)\end{aligned}$$

where $\nu_2[g] = \frac{1}{\varDelta\varphi}\int g^2(\varphi,\varDelta\varphi)\, d\varphi$ denotes the second characteristic moment of the pulse envelope function, which is by definition independent of the pulse width $\varDelta\varphi$ (cf. section 2.1). In the last step of equation (4.43), we used the elementary limits

$$\lim_{\varDelta\varphi\to\infty}\frac{|F_g(l,\varDelta\varphi)|^2}{\varDelta\varphi} = 2\pi\nu_2[g]\delta(l), \qquad \text{for all } l, \tag{4.44}$$

$$\lim_{\varDelta\varphi\to\infty}\frac{F_g(l_1,\varDelta\varphi)F_g^*(l_2,\varDelta\varphi)}{\varDelta\varphi} = 0 \qquad \text{for all } l_1 \neq l_2, \tag{4.45}$$

which are derived in lemma D.2 in the appendix. Similarly, using equation (4.38), the limit of the second possible factor listed in (4.36) results in

$$\lim_{\Delta\varphi\to\infty} \frac{|F_2(l,\Delta\varphi)|^2}{\Delta\varphi} = \frac{m^2}{4e^2}\sin^2\xi \lim_{\Delta\varphi\to\infty} \left[\frac{|F_g(l+1)|^2}{\Delta\varphi} + \frac{|F_g(l-1)|^2}{\Delta\varphi} - \frac{2}{\Delta\varphi}\mathrm{Re}\left(F_g(l+1)F_g^*(l-1)\right)\right] \tag{4.46}$$

$$= \frac{\pi m^2}{2e^2}\nu_2[g]\sin^2\xi\left(\delta(l+1)+\delta(l-1)\right), \tag{4.47}$$

where in the last step we applied again the elementary limits (4.44) and (4.45), respectively. In order or perform the limit of the third term given in (4.36), we use again the equations (4.37) and (4.38), which leads to

$$\lim_{\Delta\varphi\to\infty} \frac{iF_1(l)F_2^*(l)}{\Delta\varphi} = -\frac{\pi m^2}{2e^2}\nu_2[g]\cos\xi\sin\xi\left(\delta(l+1)-\delta(l-1)\right). \tag{4.48}$$

Summarizing, we showed that, on the level of the differential cross section of pulsed-perturbative trident given in equation (4.26), the limit $\Delta\varphi\to\infty$ results in a constraint of the photon-number parameter l due to the occurrence of the delta-distributions $\delta(l\pm 1)$ in all pulse shape dependent terms listed in (4.36). In the case of pulsed-perturbative trident, the photon-number parameter is related to the momenta of the external particles due to equation (4.6), where consequently the constraint of l_0 in the limit $\Delta\varphi\to\infty$ results in an additional constraint in the final phase space yielding a reduction of the dimension of the final phase space from six to five, which leads to the first hint w.r.t. the five-dimensional phase space of perturbative trident (see appendix C).

Considering the complicated mathematical structure of the differential cross sections, we rather show the explicit convergence of pulsed-perturbative trident against perturbative trident on the level of the scattering matrix element (4.23). In order to have brief mathematical expressions, we limit the reasoning to the case of linear laser polarisation, although other polarisation states can be treated similarly. Assuming linear polarisation say in $\underline{\varepsilon}_1$-direction (i.e. $\xi = 0$), one has $f_2(\varphi)\equiv 0$, which implies $F_2(l)\equiv 0$ due to the definition of the amplitude function of the pulsed plane-wave background field given in equation (2.17) as well as the definition (3.4). In this case, the matrix element of pulsed-perturbative trident given in (4.23) reads

$$S_{\mathrm{ppT}}\Big|_{\xi=0} = \frac{-ie^2a_0(2\pi)^3}{2k^+}\delta^{\mathrm{lf}}(p-p_t)\left(M_{\mathrm{C}}^{(1)}+M_{\mathrm{BW}}^{(1)}\right)F_1(l_0)\Big|_{\xi=0}, \tag{4.49}$$

where $p_t = p_1 + p_2 + p_3$ denotes the total momentum of the final particles and $\delta^{\mathrm{lf}}(q) = \frac{1}{2}\delta(q^-)\delta^{(2)}(q^\perp)$ for an arbitrary four-momentum q in light-cone coordinates (see appendix A.2). The factors $M_{\mathrm{C}}^{(1)}$ and $M_{\mathrm{BW}}^{(1)}$ are given in (4.29) and (4.30), respectively, and the Fourier transform $F_1(l_0)$ is defined in equation (3.4), where l_0 is related to the final phase space according to equation (4.6). Considering the limit (4.40), the limiting case $\varDelta\varphi \to \infty$ for the matrix element (4.49) results in

$$\lim_{\varDelta\varphi\to\infty} S_{\mathrm{ppT}}\Big|_{\xi=0} = \frac{-ie^2 a_0 (2\pi)^4}{2k^+}\delta^{\mathrm{lf}}(p-p_t)\left(M_{\mathrm{C}}^{(1)} + M_{\mathrm{BW}}^{(1)}\right)\frac{m}{e}\left(\delta(l_0+1)+\delta(l_0-1)\right). \tag{4.50}$$

Consequently, the constraint of the photon number parameter l_0 due to the occurring delta-distribution, i.e. $l = \pm 1$, is indeed the same as obtained by the reasoning above on the level of the differential cross section. The resulting product of delta-distributions in equation (4.50) can be written in cartesian coordinates as

$$\begin{aligned} \frac{1}{k^+}\delta^{\mathrm{lf}}(p-p_t)\delta(l_0\pm 1) &= \frac{1}{2k^+}\delta(p^- - p_t^-)\delta^{(2)}(p^\perp - p_t^\perp)\delta\left(\frac{p_t^+ - p^+ \pm k^+}{k^+}\right) && (4.51)\\ &= \frac{1}{2}\delta(p^- - p_t^-)\delta^{(2)}(p^\perp - p_t^\perp)\delta\left(p_t^+ - p^+ \pm k^+\right) && (4.52)\\ &= \delta^{(4)}(p \mp k - p_t). && (4.53) \end{aligned}$$

The plus sign in the resulting delta-distribution encodes the global energy momentum conservation $p + k = p_t = p_1 + p_2 + p_3$, where the minus sign has no distribution to the matrix element since $p = k + p_t$ is kinematically forbidden. Therefore, the matrix element (4.50) reads

$$\lim_{\varDelta\varphi\to\infty} S_{\mathrm{ppT}}\Big|_{\xi=0} = \frac{-ie^2 a_0 (2\pi)^4}{2k^+}\frac{m}{e}\delta^{(4)}(p+k-p_t)\left(M_{\mathrm{C}}^{(1)} + M_{\mathrm{BW}}^{(1)}\right) \tag{4.54}$$

where the terms $M_{\mathrm{C}}^{(1)}$ and $M_{\mathrm{BW}}^{(1)}$ must be evaluated at $l_0 = 1$. Accordingly, using equation (4.29) and inserting the elementary vertices (2.48) and (2.49) as well as the kinematic factor (2.55), the virtual Compton contribution is given in the case of $l_0 = 1$ by

$$M_{\mathrm{C}}^{(1)}\Big|_{l_0=1} = g_{\mu\nu}\frac{\overline{u}(p_2)\gamma^\mu v(p_1)}{(p_1+p_2)^2+i\epsilon}\overline{u}(p_3)\left[\mathit{\Gamma}_1^{\nu\tau}(p,p_3) - \mathit{\Gamma}_0^{\nu}\alpha_1^{\tau}(p,p_3)\right]u(p)\varepsilon_{1\tau} - (p_2 \leftrightarrow p_3) \tag{4.55}$$

$$= eg_{\mu\nu}\frac{\overline{u}(p_2)\gamma^\mu v(p_1)}{(p_1+p_2)^2+i\epsilon}\overline{u}(p_3)\left[\frac{\gamma^\nu \not{k}\gamma^\tau + 2\gamma^\nu p^\tau}{2(kp)} + \frac{\gamma^\tau \not{k}\gamma^\nu - 2\gamma^\nu p_3^\tau}{2(kp_3)}\right]u(p)\varepsilon_{1\tau} - (p_2 \leftrightarrow p_3). \tag{4.56}$$

Here, we rewrite the nominators in the square brackets by using the identities

$$(\not{k}\gamma^\tau + 2p^\tau)\,u(p) = \left(\not{k} + \not{p} + m\right)\gamma^\tau u(p), \tag{4.57}$$

$$\overline{u}(p_3)\,(\gamma^\tau\not{k} - 2p_3^\tau) = \overline{u}(p_3)\gamma^\tau(\not{k} - \not{p}_3 - m), \tag{4.58}$$

where we applied the Dirac equation in momentum space $(\not{p} - m)u(p) = 0$ for the respective bi-spinor. Furthermore, if we rewrite the respective denominators using $2(kp) = (k+p)^2 - m^2$, and $2(kp_3) = -\big((k-p_3)^2 - m\big)$, respectively, the virtual Compton contribution given in equation (4.56) reads

$$\begin{aligned} M_{\mathrm{C}}^{(1)}\Big|_{l_0=1} &= eg_{\mu\nu}\frac{\overline{u}(p_2)\gamma^\mu v(p_1)}{(p_1+p_2)^2+i\epsilon} \\ &\quad\times \overline{u}(p_3)\left[\gamma^\nu\frac{\not{k}+\not{p}+m}{(k+p)^2-m^2}\gamma^\tau + \gamma^\tau\frac{\not{p}_3-\not{k}+m}{(k-p_3)^2-m^2}\gamma^\nu\right]u(p)\varepsilon_{1\tau} \\ &\quad - (p_2 \leftrightarrow p_3) \end{aligned} \tag{4.59}$$

$$= eg_{\mu\nu}\frac{\overline{u}(p_2)\gamma^\mu v(p_1)}{(p_1+p_2)^2+i\epsilon}\overline{u}(p_3)\mathcal{C}^{\nu\tau}(p,p_3|k)u(p)\varepsilon_{1\tau} - (p_2 \leftrightarrow p_3), \tag{4.60}$$

where $\mathcal{C}^{\mu\nu}$ denotes the Compton tensor defined in equation (C.2) in the context of perturbative trident (see appendix C). Analogously, using $l_0 = 1$, the virtual Breit-Wheeler contribution (4.30) results in

$$M_{\mathrm{BW}}^{(1)}\Big|_{l_0=1} = eg_{\mu\nu}\frac{\overline{u}(p_3)\gamma^\mu u(p)}{(p-p_3)^2+i\epsilon}\overline{u}(p_2)\mathcal{C}^{\nu\tau}(-p_1,p_2|k)v(p_1)\varepsilon_{1\tau} - (p_2 \leftrightarrow p_3). \tag{4.61}$$

Finaly, inserting the expressions (4.60) and (4.61) into the matrix element (4.54), one has

$$\begin{aligned}
\lim_{\varDelta\varphi\to\infty} S_{\mathrm{ppT}}\Big|_{\xi=0} &= \frac{-ie^2 a_0 m (2\pi)^4}{2k^+}\delta^{(4)}(p+k-p_t) g_{\mu\nu}\varepsilon_{1\tau} \\
&\quad\times\left[\frac{\overline{u}(p_2)\gamma^\mu v(p_1)}{(p_1+p_2)^2+i\epsilon}\overline{u}(p_3)\mathcal{C}^{\nu\tau}(p,p_3|k)u(p)\right. \\
&\quad\left.+\frac{\overline{u}(p_3)\gamma^\mu u(p)}{(p-p_3)^2+i\epsilon}\overline{u}(p_2)\mathcal{C}^{\nu\tau}(-p_1,p_2|k)v(p_1)\right] - (p_2\leftrightarrow p_3) \qquad (4.62) \\
&= \frac{a_0 m}{e} M_{\mathrm{pT}}(2\pi)^4\delta^{(4)}(p+k-p_t), \qquad (4.63)
\end{aligned}$$

where M_{pT} denotes the matrix element of perturbative trident at tree level, which is given in equation (C.5).

4.2 Total cross section

To begin with the numerical investigation of the trident process for low intensity parameter a_0, we calculate the total cross section of pulsed-perturbative trident for the special case of a linearly polarized background field in $\underline{\varepsilon}_1$-direction, i.e. $\xi = 0$ and $\underline{\varepsilon}_1 = (1{,}0{,}0)$, with a $\cos^2$-pulse envelope function as defined in equation (2.18). Generally, the total cross section results from the integration over the whole final phase space:

$$\sigma_{\mathrm{ppT}}\Big|_{\xi=0} := \int \mathrm{d}\sigma_{\mathrm{ppT}}\Big|_{\xi=0}, \tag{4.64}$$

where $\mathrm{d}\sigma_{\mathrm{ppT}}$ denotes the six-fold differential cross section of pulsed-perturbative trident given in equation (4.34) (from here on we only consider $\xi = 0$ and suppress any annotation). Accordingly, the total cross section given in equation (4.64) yields a function of the initial momenta as well as the laser pulse width $\varDelta\varphi$. Here, we assume the special case of a heads-on-collision, where the spatial part $\underline{k}$ of the reference momentum k^μ of the laser field is aligned along the 3-axis in momentum space, and we parameterize the initial momenta by the center-of-momentum energy $\sqrt{s} := \sqrt{(p+k)^2}$ (cf. appendix A.3). Since the total cross section as a function of $\sqrt{s}$ is a Lorentz-invariant quantity, we choose without loss of generality the frame of reference with the initial electron at rest (within this thesis referred to as the laboratory system).

Generally, the total cross section is a measure for the probability of a certain process, here the trident process, to actually happen for a given initial state, here the collision of a laser with an electron, despite from the actual point in the phase space, where the final particles are scattered into. More accurately, the total cross section results from the sum over all possible final states. Considering the perturbative (monochromatic) case (cf. appendix C), the trident pair production is a threshold process, which means that for center-of-momentum energies $\sqrt{s}$ lower than a certain level $\sqrt{s_{\mathrm{th}}}$ (also referred to as the threshold), the process is kinematically forbidden and therefore the total cross section vanishes exactly: $\sigma_{\mathrm{pT}}(\sqrt{s} < \sqrt{s_{\mathrm{th}}}) \equiv 0$, where σ_{pT} denotes the total cross section of perturbative trident given in equation (C.11) and the threshold center-of-momentum energy of the trident process is given by $\sqrt{s_{\mathrm{th}}} = 3\,m$, with m is the rest mass of an electron. This means, loosely speaking, there is a minimum amount of energy needed for the final particles to be produced, i.e. to reach the sum of their rest masses. However, as we mentioned in section 3.3, the presence of a finite pulse width, and especially for short pulses, the amount of momentum transfer between the background field and the process, measured with the photon number parameter l, implies the capability of the process to absorb more energy from the background field in order to gain a finite signal even below the monochromatic threshold. Here we point out, that the used center-of-momentum energy $\sqrt{s}$ is defined w.r.t. the reference momentum k^μ of the laser field, despite its bandwidth. Therefore, the phrase "below the monochromatic limit" refers to the reference energy obtained from the central frequency of the laser. In other words, the finite spectrum of the background field implies an expansion of the kinematic limits, e.g. the monochromatic threshold, apparently producing new kinematic limits shifted w.r.t. the one obtained from the reference center-of-momentum energy $\sqrt{s}$.

In figure 4.2, the result of the numerical integration according to equation (4.64) is depicted as a function of the center-of-momentum energy $\sqrt{s}$ for several values of the pulse width $\Delta\varphi$ (solid colored lines), where we used the VEGAS Monte-Carlo integration algorithm [167, 168, 222] in order to actually perform the numerical integration.

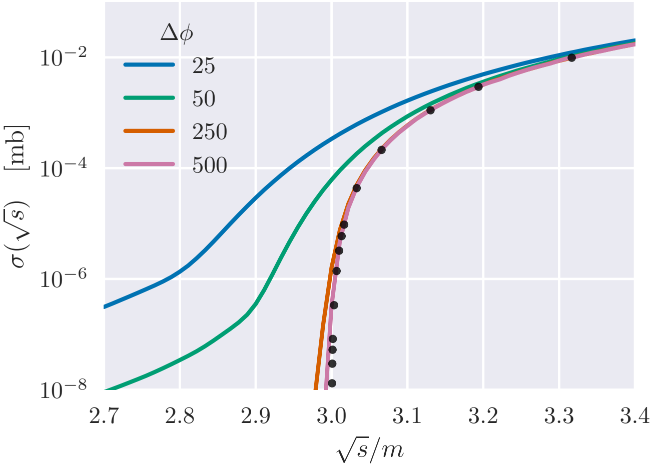

Figure 4.2: The total cross section σ_{ppT} of pulsed-perturbative trident as a function of the scaled center-of-momentum energy $\sqrt{s}/m$ for several values of the pulse width $\Delta\varphi$ (solid lines; blue: 25, green: 50, red: 250, pink: 500). Additionally the total cross section σ_{pT} of perturbative (monochromatic) trident is depicted by black dots.

Additionally, the total cross section of the perturbative trident in the monochromatic limit is depicted (black dots), which is given in equation (C.11). Firstly, we mention that for finite values of $\Delta\varphi < \infty$, the (pseudo-) threshold of the total cross section is shifted to lower values of $\sqrt{s}$ compared to the monochromatic threshold $\sqrt{s_{\mathrm{th}}} = 3\,m$, producing a finite total cross section in this region. Furthermore, the sub-threshold signal increases for decreasing values of $\Delta\varphi$ and reaches a region where, even below the monochromatic threshold, the pulsed-perturbative trident total cross section has comparable values w.r.t. the monochromatic case. For instance, considering the depicted value $\Delta\varphi = 25$ for the pulsed-perturbative trident, the total cross section at the point $\sqrt{s} = 2.95\,m$ (slightly below the threshold) has a comparable value w.r.t. the total cross section of the perturbative case at the point $\sqrt{s} = 3.05\,m$ (slightly above the monochromatic threshold): in both cases $\approx 10^{-4}\,\mathrm{mb}$.

Furthermore, we mention that the total cross section of pulsed-perturbative trident rapidly decreases for decreasing values of $\sqrt{s}$, but for $\sqrt{s} > 0$ the total cross section never vanishes exactly. This is reasonable, since, as we illustrated in section 3.3, the finite spectrum of the background field caused by the finite pulse duration indeed decreases rapidly for values l of the photon number parameter with $l \gg 1$, but never vanishes identically beyond a certain threshold. This behavior is imprinted on the total cross section for finite pulse widths due to the presence of the Fourier transform F_1 in equation (4.34), causing the absence of a distinct threshold. Nevertheless, the total cross section of pulsed-perturbative trident has an apparent threshold behavior, in the sense of decreasing below a level of measurability for decreasing values of $\sqrt{s}$.

Considering values of $\sqrt{s}$ slightly above the monochromatic threshold, the total cross section of pulsed-perturbative trident increases for decreasing values of the pulse width $\Delta\varphi$ as well. However, the larger the values of $\sqrt{s}$ compared to the monochromatic threshold, the smaller is the impact of the finite pulse width compared to the perturbative case. Finally, one observes a convergence of the pulsed-perturbative trident to the monochromatic case for $\sqrt{s} \gg \sqrt{s_{\mathrm{th}}}$.

4.3 Inclusive positron distributions

The total cross section discussed in section 4.2 provides an assessment in which region of the initial parameters (i.e. the center-of-momentum energy $\sqrt{s}$ and the pulse width $\mathit{\Delta}\varphi$) the impact of the finite pulse width on the trident process at low laser-intensity parameters a_0 is, in principle, observable compared to the monochromatic case. However, to understand the kinematical behavior of the final particles in order to provide detector specifications for possible laser-electron collision experiments, it is necessary to investigate the differential distributions of the final particles of pulsed-perturbative trident as well. Considering a possible experimental setup to measure the trident process, it is not always possible to detect all final particles of a single collision event. This is especially the case, if one has a competing process, like the Compton process in the case of trident, with the same initial state, which produces a non-negligible underground to the electron measurements. However, despite the Compton process, the trident process provides the possibility to partially distinguish the kind of its final particles due to their charge. Since there is a positron in the final state, it can be used as a trigger particle to select the trident process in a laser-electron collision experiment w.r.t. other underground processes. In order to apply this trigger approach, it is necessary to investigate the inclusive positron distribution of the (pulsed-perturbative) trident process, which is accumulated over all possible final states of the electrons.

Accordingly, we calculate the three-fold differential cross section of pulsed-perturbative trident w.r.t. to the final positron for the special case of a linearly polarized background field in $\underline{\varepsilon}_1$-direction, i.e. $\xi = 0$ and $\underline{\varepsilon}_1 = (1,0,0)$, with a $\cos^2$-pulse envelope function as defined in equation (2.18):

$$\left.\frac{\mathrm{d}\sigma_{\mathrm{ppT}}}{\mathrm{d}^3 p_1}\right|_{p_1 = p_1'} := \int \delta^{(3)}(\underline{p}_1 - \underline{p}_1')\,\mathrm{d}\sigma_{\mathrm{ppT}}, \tag{4.65}$$

where $\underline{p}_1'$ denotes the three-momentum of the final positron, i.e. the point in the final phase space the positron is scattered in, and $\mathrm{d}\sigma_{\mathrm{ppT}}$ the (full) differential cross section of pulsed-perturbative trident given in equation (4.34). In order to parameterize the final phase space of the remaining positron, we use the transverse coordinates w.r.t. the beam axis along the reference three-momentum $\underline{k}$ of the background field: rapidity y_1, transverse momentum p_{T1} and azimuth angle ϕ_1, which are defined in appendix A.2. Inserting equation (4.34) into (4.65), the three-fold differential cross section (4.65) of the positron in transverse coordinates is given by

$$\frac{\mathrm{d}\sigma_{\mathrm{ppT}}}{\mathrm{d}y_1\,\mathrm{d}p_{T1}\,\mathrm{d}\phi_1} = |\underline{p}_1| \int \mathscr{A}(p_1,p_2) \frac{\Theta(p_1^-)\Theta(p_2^-)\Theta(p_3^-)}{8(2\pi)^9 p_2^- p_3^-}\, \mathrm{d}^2 p_2^\perp\, \mathrm{d}p_2^- \Big|_{\substack{p_3^- = p^- - p_1^- - p_2^- \\ p_3^\perp = p^\perp - p_1^\perp - p_2^\perp}} \tag{4.66}$$

where $\underline{p}_1, \underline{p}_2, \underline{p}_3$ denote the three-momenta of the final positron as well as the two final electrons, respectively. We use the invariant three-particle phase space integral measure $d\Phi_3$ in light-cone coordinates defined in equation (4.25) and transformed the positron-related part according to equation (A.34). Further, we apply the delta-distribution in equation (4.34) to solve the integral w.r.t. the final electron with momentum p_3 and we use the abbreviation

$$\mathscr{A}(p_1,p_2) = N \frac{a_0^2 e^4 \pi^4}{I_\gamma (k^+)^2} |F_1(l_0)|^2 \sum_{\text{spins}} \left| M_{\mathrm{C}}^{(1)} + M_{\mathrm{BW}}^{(1)} \right|^2 , \tag{4.67}$$

where the occurring quantities are introduced in section 4.1. As already mentioned, the resulting differential cross section (4.66) does not depend on the laser intensity parameter a_0 due to the relation $I_\gamma \sim a_0^2$ as given in equation (2.15).

In figure 4.3, the inclusive positron distribution is depicted as a contour plot over the (y_1,p_{T1})-plane for several values of the pulse width $\varDelta\varphi$. The center-of-momentum energy $\sqrt{s} = 3.353\,m$, is somewhat above the monochromatic threshold $\sqrt{s_{\mathrm{th}}}$. First of all, we observe that the distribution has a distinct maximum around the point $y_1 = 1.5, p_{T1} = 0.3\,m$ with a value of $0.7 \times 10^{-2}\,\mathrm{mb}/m$, for all depicted values of $\varDelta\varphi$. For large values of the pulse

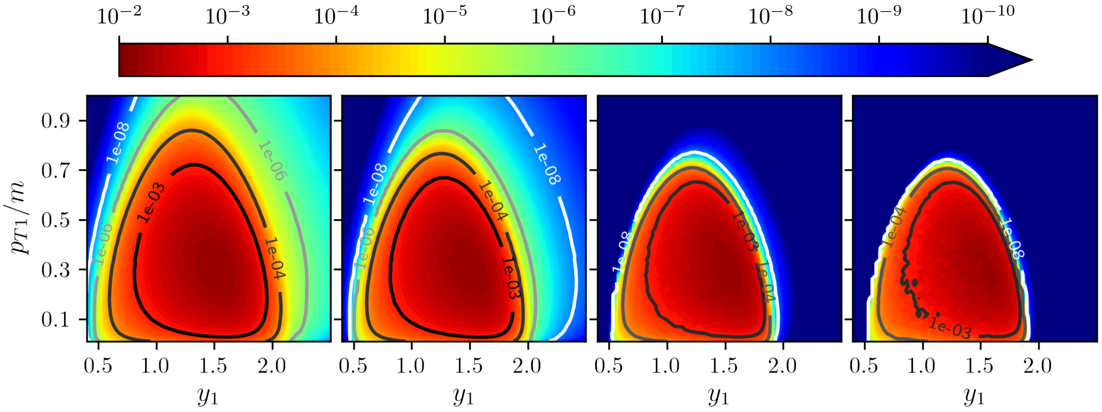

Figure 4.3: Contour plot of the three-fold differential cross section $\frac{\mathrm{d}\sigma_{\mathrm{ppT}}}{\mathrm{d}y_1\,\mathrm{d}p_{T1}\,\mathrm{d}\phi_1}$ in mb/m of pulsed-perturbative trident for a linearly polarized background field with the $\cos^2$-envelope, depicted in the (y_1,p_{T1})-plane for $\phi_1 = 0$, for $\sqrt{s} = 3.353\,m$ with the initial electron at rest and for several values of the pulse width $\varDelta\varphi$ ($\varDelta\varphi = 25, 50, 250, 500$ f.l.t.r.).

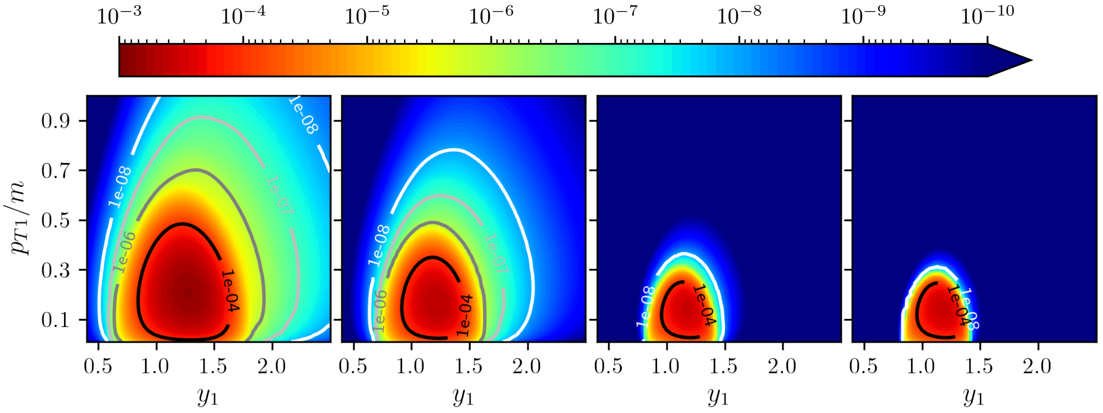

Figure 4.4: Same as in figure 4.3 but for a center-of-mass energy of $\sqrt{s} = 3.05\,m$, i.e. only slightly above the monochromatic threshold.

width, e.g. $\Delta\varphi = 500$, there is a sharply bounded region, wherein the distribution is located; at the boundary, the distribution drops rapidly from $10^{-4}\,\mathrm{mb}/m$ to $10^{-16}\,\mathrm{mb}/m$. This indicates the shrinking of the physical phase space of the positron of pulsed-perturbative trident towards the monochromatic case for large pulse widths. However, for decreasing values of $\Delta\varphi$, these sharp boundaries blur out and the phase space of the positron expands, e.g. for $\Delta\varphi = 500$ the positron distribution at the point $y_1 = 1.5, p_{T1} = 0.8\,m$ is negligibly small ($< 10^{-16}\,\mathrm{mb}/m$), but for $\Delta\varphi = 25$, at the same phase space point, there is an observable signal of about $10^{-4}\,\mathrm{mb}/m$) comparable to the maximum of the distribution.

This behavior is observed to be even stronger, in approaching the monochromatic threshold $\sqrt{s_{\mathrm{th}}} = 3\,m$. In figure 4.4, the inclusive positron distribution is exhibited for the same setting as in figure 4.3, but for $\sqrt{s} = 3.05\,m$, which is only slightly above the monochromatic threshold. Here, the distinct maximum of the positron distribution is situated around $y_1 = 1.25, p_{T1} = 0.125\,m$ and its value is slightly lower compared to the case $\sqrt{s} = 3.353\,m$, which is in accordance with the $\sqrt{s}$ dependence of the total cross section in figure 4.2. Consequently, for large values of the pulse width, e.g. $\Delta\varphi = 500$, one observes again a similar sharp-bounded phase space of the positron, which is smaller in size compared to the case of figure 4.3. However, near but above the monochromatic threshold, the blurring-out effect of the positron distribution for decreasing pulse widths $\Delta\varphi$ is extensively stronger. For instance, comparing the cases of $\Delta\varphi = 500$ and $\Delta\varphi = 25$ for $\sqrt{s} = 3.05\,m$, the area of the region with values of the distribution above $10^{-4}\,\mathrm{mb}/m$ increases by a factor of about 4.5, where in the case of $\sqrt{s} = 3.353\,m$ the area of the same region increases only by a factor of about 1.5.

Generally, this blurring-out effect of the phase space of the final positron is to be expected,

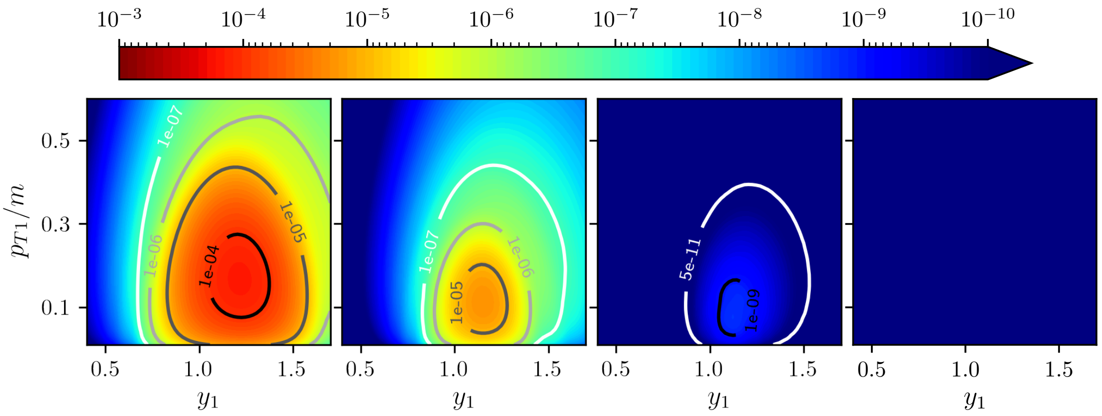

Figure 4.5: The same as in figure 4.3 but for $\sqrt{s} = 2.95\,m$, i.e. slightly below the monochromatic threshold.

since – for decreasing values of the pulse width $\Delta\varphi$ – the energy spectrum of the background field becomes wider, as indicated in section 3.3. Therefore, the positron can, loosely speaking, gain more energy from the laser field to reach a wider region in the final phase space. Looking at it the other way round, for increasing values of the pulse width $\Delta\varphi$, the photon number parameter reaches $l \to 1$ (cf. section 4.1, e.g. equation (4.43)) implying the phase space of the positron in pulsed-perturbative trident becomes constrained to the sharp-bounded region characteristically for the perturbative monochromatic case (cf. section A.4 in the appendix), which is the exact limiting case for $\Delta\varphi \to \infty$, or $l = 1$, respectively.

However, as mentioned in section 4.2, even for (reference) center-of-momentum energies lower than the monochromatic threshold, there is a non-negligible signal of pulsed-perturbative trident for sufficiently small values of the pulse width $\Delta\varphi$. Therefore, in figure 4.5 the inclusive positron distribution of pulsed-perturbative trident is displayed with the same setting as in figures 4.3 and 4.4, respectively, but for a (reference) center-of-momentum energy of $\sqrt{s} = 2.95\,m$, which is slightly below the monochromatic threshold. In contrast to the cases above the threshold, for increasing values of $\Delta\varphi$, there is no sharp-bounded region, i.e. the positron distribution vanishes completely due to the absence of a physical phase space in the monochromatic limit $\Delta\varphi \to \infty$. However, for finite and decreasing values of $\Delta\varphi$, one observes a rising distribution, which reaches values of about $10^{-4}\,\text{mb}/m$ for $\Delta\varphi = 25$. This is comparable to the values observed for the cases above the threshold depicted in figures 4.3 and 4.4, respectively, and can be related to the total cross section in figure 4.2. Consequently, this means that even if the center-of-mass energy obtained by the central frequency of the laser is below the monochromatic threshold of the trident process, the finite bandwidth of the laser causes a positron signal with comparable strength, which is not negligible.

Comparison to perturbative (monochromatic) trident

In order to compare the results for the inclusive positron distribution of pulsed-perturbative trident in figures 4.3, 4.4 and 4.5, with the monochromatic limit, we consider slices through the distributions along the y_1-axis for a fixed value of $p_{T1} = 0.15\,m$. The results of such slicing are shown in figure 4.6, where we compare the different values of $\Delta\varphi$ (solid colored lines) with the explicit calculation of the perturbative (monochromatic) trident for the cases $\sqrt{s} = 3.353\,m$ (above the threshold; left panel), $\sqrt{s} = 3.05\,m$ (only slightly above the threshold; middle panel) and $\sqrt{s} = 2.95\,m$ (slightly below the threshold; right panel). In the two cases with $\sqrt{s} > \sqrt{s_{\text{th}}} = 3\,m$, we obtain the perturbative trident distribution (black dashed lines) by transforming equation (C.9) to transverse coordinates (cf. appendix A.2) and integrating over the remaining final electron momentum-components. First of all, one observes that, for increasing pulse widths $\Delta\varphi$, the pulsed-perturbative distributions with $\sqrt{s} > \sqrt{s_{\text{th}}}$ converge against the monochromatic case up to a near-perfect match for $\Delta\varphi = 500$. In the sub-threshold case of $\sqrt{s} = 2.95\,m$, the distributions of pulsed-perturbative trident vanish for increasing values of $\Delta\varphi$, since the limiting monochromatic case is kinematically forbidden for $\sqrt{s} < \sqrt{s_{\text{th}}}$ as mentioned above. Looking at it the other

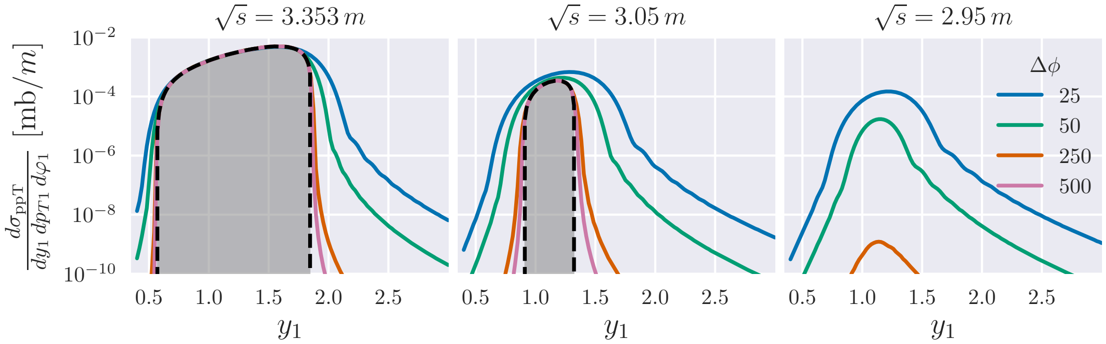

Figure 4.6: The three-fold differential cross section $\frac{d\sigma_{\text{ppT}}}{dy_1\,dp_{T1}\,d\phi_1}$ in $\frac{\text{mb}}{m}$ of pulsed-perturbative trident for a linearly polarized background field with the $\cos^2$-envelope as a function of the transverse coordinates of the positron, depicted as a function of y_1 for fixed values $p_{T1} = 0.15\,m$, $\phi_1 = 0$ and for several values of $\sqrt{s}$ (left panel: 3.353, center panel: 3.05, right panel: 2.95) as well as for several values of the pulse width $\Delta\varphi$ (solid lines; blue: 25, green: 50, red: 250, pink: 500). For comparison, the three-fold differential cross section of the perturbative (monochromatic) trident w.r.t. the positron is depicted in the same setting (black dashed lines), obtained from the transformation of equation (C.9) to transverse coordinates and numerical integration over the remaining final electron. The kinematically accessible domain for the monochromatic case is indicated by a grey shaded area.

way round, for decreasing $\varDelta\varphi$ one observes that the distributions of pulsed-perturbative trident, in general, are lifted up, where within the kinematically accessible region of perturbative (monochromatic) trident (i.e. the phase space of the final positron; indicated by the grey shaded area), the increase is larger for values of $\sqrt{s}$ near the threshold. However, as mentioned above, the upswing of the pulsed-perturbative trident distributions is not restricted to this monochromatically accessible region, but even stronger outside of the grey shaded area, where for short pulses, the resulting signal is comparable to the monochromatically produced distribution. This is most drastically for (reference) center-of-momenta below the monochromatic threshold, where one has no physical phase space available for the final positron in the monochromatic case, but for short pulses (e.g. the depicted case of $\varDelta\varphi = 25$) there is a non-zero distribution of the positron, which has comparable values w.r.t. the case $\sqrt{s} = 3.05\,m$, slightly above the threshold.

Summarizing, we observe an important impact of the bandwidth of a pulsed laser field on the inclusive positron distribution. The finite pulse width causes an expansion of the accessible phase space of the positron compared to the monochromatic limit. This effect becomes stronger for center-of-momentum energies closer to the monochromatic threshold. Furthermore, the finite bandwidth yields a comparable positron distribution even if the center-of-momentum energy obtained from the reference momentum of the laser field (i.e. from the central laser frequency) is below the monochromatic threshold. Additionally, we show that the treatment of the trident process in the context of pulsed-perturbative QED (as an approximation for small intensity parameters a_0; cf. chapter 3) leads to an explicit and smooth convergence to the monochromatic case for large pulse widths. This continues the treatment w.r.t total cross section (cf. section 4.2) and emphasizes the insights on the level of differential cross sections w.r.t. a tight connection to possible experimental investigations.

4.4 Exclusive electron distributions

As mentioned in section 4.3, in a conceivable experimental setup one could use the final positron as a trigger particle in order to select the trident process w.r.t. possible underground processes. Applying this trigger-particle approach, the momentum of the final positron has a fixed (e.g. measured) value and one needs to investigate the respective distribution of the final electrons. In the case of small intensity parameters a_0, as considered in this thesis, this leads to the investigation of the exclusive electron distribution of pulsed-perturbative trident, which is given in the form of the six-fold differential cross section

$$\left.\frac{\mathrm{d}^6\sigma_{\mathrm{ppt}}}{\mathrm{d}^3p_1\,\mathrm{d}^3p_2}\right|_{\underline{p}_{1,2}=\underline{p}'_{1,2}} := \int \delta^{(3)}\left(\underline{p}_1 - \underline{p}'_1\right)\delta^{(3)}\left(\underline{p}_2 - \underline{p}'_2\right)\mathrm{d}\sigma_{\mathrm{ppT}}, \tag{4.68}$$

where $\underline{p}'_1$ ($\underline{p}'_2$) denotes the three-momentum of the final positron (electron) and $\mathrm{d}\sigma_{\mathrm{ppT}}$ is given in equation (4.26). Since we treat the momentum components of the final positron as given fixed parameters, the six-fold differential cross section (4.68) is a function of the final electron momentum. Furthermore, since the positron momentum $\underline{p}_1$ is given here, the electron momentum $\underline{p}_2$ is used as an independent variable, where the remaining electron momentum $\underline{p}_3$ is determined by energy-momentum conservation. Therefore, we speak of an exclusive electron distribution (cf. [48]). Analogous to the discussion of the inclusive positron distributions in section 4.3, we choose transverse coordinates to parameterize the final electron momenta (cf. appendix A.2) and we use again a linearly polarized plane-wave background field ($\xi = 0$ and $\underline{\varepsilon}_1 = (1, 0, 0)$) with a $\cos^2$-envelope function, as introduced in equation (2.10) and (2.18), respectively. Accordingly, we can reuse the factorised version of $d\sigma_{\mathrm{ppT}}$ in the case of linear polarisation given in equation (4.34), where the six-fold differential cross section (4.68) results in

$$\frac{\mathrm{d}^6\sigma_{\mathrm{ppt}}}{\mathrm{d}y_1\,\mathrm{d}p_{T1}\,\mathrm{d}\phi_1\,\mathrm{d}y_2\,\mathrm{d}p_{T2}\,\mathrm{d}\phi_2} = \left.\frac{|\underline{p}_1||\underline{p}_2|}{8\,(2\pi)^9\,p_3^-}\mathscr{A}(p_1,p_2)\Theta(p_1^-)\Theta(p_2^-)\Theta(p_3^-)\right|_{\substack{p_3^-=p^--p_1^--p_2^-\\ p_3^\perp=p^\perp-p_1^\perp-p_2^\perp}}, \tag{4.69}$$

where we use the invariant three-particle phase space integral measure $\mathrm{d}\Phi_3$ in light-cone coordinates defined in equation (4.25) and transform the (p_1, p_2)-related part according to equation (A.34). Further, we apply the delta-distribution in equation (4.34) to solve the integral w.r.t. the final electron with momentum $\underline{p}_3$ and we use again the abbreviation given in equation (4.67). At the r.h.s. of equation (4.69), we understand the occurring light-cone coordinates as functions of the transverse coordinates from the l.h.s. (according to the transformations given in table A.1).

Exclusive electron distribution for fixed azimuth

First, we consider the exclusive electron distribution for a fixed azimuthal angle ϕ_2 of the remaining final electron in the (y_2, p_{T2})-plane, where y_2 denotes the rapidity and p_{T2} the transverse momentum of the electron, respectively.

In figure 4.7 the six-fold differential cross section (4.69) is depicted as a function of y_2 and p_{T2} for a fixed azimuthal angle $\phi_2 = \pi/2$ and several values of $\varDelta\varphi$ (column-wise; 1: 25, 2: 50, 3: 250, 4: 500) as well as several values of the reference center-of-momentum energy $\sqrt{s}/m$ (row-wise; top: 3.353, middle: 3.05, bottom: 2.95). The positron's momentum components are fixed at $y_1 = 1.0, p_{T1} = 0.15\,m, \phi_1 = 0$, which is a point within the monochromatic phase space in both cases with $\sqrt{s} > \sqrt{s_{\text{th}}}$ according to the inclusive

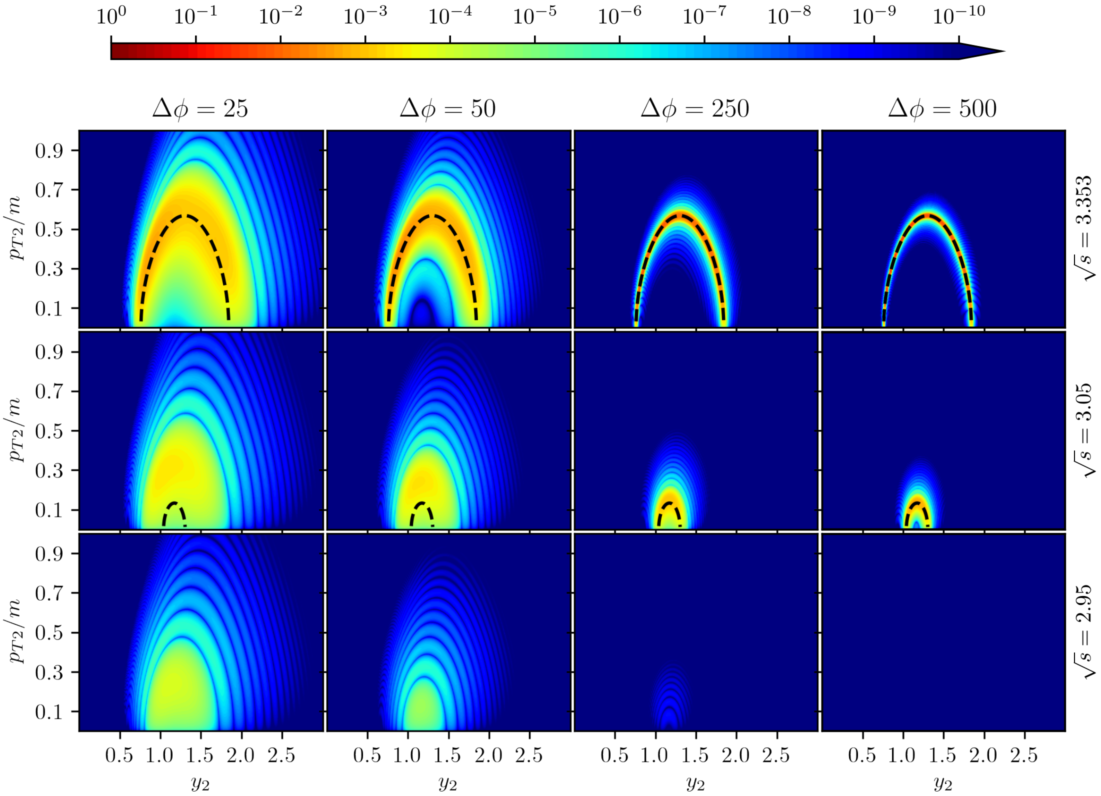

Figure 4.7: Contour plots of $\frac{\mathrm{d}^6\sigma_{\text{ppt}}}{\mathrm{d}y_1\,\mathrm{d}p_{T1}\,\mathrm{d}\phi_1\,\mathrm{d}y_2\,\mathrm{d}p_{T2}\,\mathrm{d}\phi_2}$ given in equation (4.69) in units of mb/m^2 for a linearly polarized background field with the $\cos^2$-envelope, depicted in the (y_2, p_{T2})-plane with $\phi_2 = \frac{\pi}{2}$ for several values of the pulse width $\varDelta\varphi$ ($\varDelta\varphi = 25, 50, 250, 500$ f.l.t.r.), several values of the center-of-momentum energy $\sqrt{s}$ (from top to bottom: $\sqrt{s}/m = 3.353, 3.05, 2.95$) and for a fixed positron momentum with $y_1 = 1.0, p_{T1} = 0.15\,m, \phi_1 = 0.0$. Additionally, the “physical phase space” of perturbative (monochromatic) trident given in equation (A.94) is depicted as a single back dashed curve.

positron distribution in figure 4.3 and 4.4.

Here, we observe, that for values of the center-of-momentum energy with $\sqrt{s} > \sqrt{s_{\text{th}}}$ and for increasing values of $\Delta\varphi$, the differential cross section is reduced from a widespread two-dimensional distribution in the (y_2, p_{T2})-plane towards a single one-dimensional curve. This is to be expected, since in the monochromatic case, i.e. the limiting case for $\Delta\varphi \to \infty$, the perturbative (monochromatic) trident has a five-dimensional physical phase space (cf. appendix A.4), i.e. for fixed positron momentum (three dimensions) and fixed electron azimuth (the fourth dimension) the remaining phase space is one-dimensional. Therefore, the six-dimensional phase space of pulsed-perturbative trident (or strong-field trident in general; cf. section 2.5) needs to be reduced by one dimension. Additionally, the "phase space" of perturbative (monochromatic) trident, resulting from the four-momentum conservation given by equation (A.94), is inserted in figure 4.7 (black dashed curve) in each panel, where it exists. We emphasize that this single line is near perfectly matched by the pulsed-perturbative trident distribution for large pulse widths $\Delta\varphi$ in both cases where $\sqrt{s} > \sqrt{s_{\text{th}}}$ (top and middle row).

Looking at it the other way round, for decreasing values of $\Delta\varphi$, the exclusive electron distribution of pulsed-perturbative trident in both cases with $\sqrt{s} > \sqrt{s_{\text{th}}}$ expands from this one-dimensional line to a genuinely two-dimensional distribution in the (y_2, p_{T2})-plane. Therefore, the presence of a finite laser pulse (implying a finite bandwidth of the laser) causes a blow-up of the five-dimensional phase space in the monochromatic case into a six-dimensional phase space, which is indicated by the blurring of the black dashed curve depicted in figure 4.7 in the case of pulsed-perturbative trident. This expansion of the phase space is in agreement with the reasoning about the total cross section (see section 4.2) as well as the inclusive positron distribution (see section 4.3): the shorter the pulse width the broader is the spectrum of the laser, which means that, loosely speaking, the final particles (here the electron) can gain more energy from the background field.

Similar to the inclusive positron distribution (see figures 4.3 and 4.4), the phase space expansion is the stronger the closer to the monochromatic threshold the reference center-of-momentum energy $\sqrt{s}$ is chosen. Furthermore, one may compare the case $\sqrt{s} = 3.353\,m$, not too close to the threshold (figure 4.7; top row), and the case $\sqrt{s} = 3.05\,m$, slightly above the threshold (figure 4.7; middle row). Considering the case slightly above the monochromatic threshold, one observes that the one-dimensional monochromatic limit occupies a smaller area compared to the case $\sqrt{s} = 3.353\,m$. However, the dimensional expansion in the (y_2, p_{T2})-plane for decreasing values of $\Delta\varphi$ is more extensive and results in an exclusive electron distribution of comparable area and strength.

Finally, in the bottom row of figure 4.7, the exclusive electron distribution is depicted for

$\sqrt{s} = 2.95\,m$ and fixed positron momentum and electron azimuth. This case is slightly below the monochromatic threshold, and there is no monochromatic limit, due to the absence of a physical phase space of perturbative (monochromatic) trident for $\sqrt{s} < \sqrt{s_{\text{th}}} = 3\,m$. Therefore, the exclusive electron distribution of pulsed-perturbative trident vanishes for large values of the pulse width $\varDelta\varphi$. However, one observes that for a finite-width laser pulse, implying higher frequencies in the laser spectrum, a finite electron distribution emerges for decreasing pulse widths, despite the reference center-of-momentum energy is below the monochromatic threshold. This "sub-threshold" behavior enhances the electron signal up to an area and strength, which is comparable to the case of $\sqrt{s} = 3.05\,m$ (middle row of figure 4.7) and therefore not negligible.

Summarizing, we mention that the presence of a finite laser pulse causes two types of modifications of the physical phase space of perturbative (monochromatic) trident: (*i*) the blurring-out w.r.t. the sharp-boundary kinematical region as observed in the inclusive positron distributions (section 4.3) as well as (*ii*) the expansion into an additional dimension in the physical phase space as observed in the exclusive electron distributions. However, these two effects of the finite pulse width are not independent but interrelated by the integration of the differential cross section over one or more momentum components.

As mentioned in section 4.3, these modifications might be used to distinguish data obtained by an experiment into a signal produced by the perturbative (monochromatic) trident, due to the central frequency of the laser (which is encoded in $\sqrt{s}$), and a signal which is produced due to the higher frequencies due to the finite bandwidth of the laser pulse.

Azimuthal electron distribution

Within this section, we investigate the dependence of the exclusive electron distribution of pulsed-perturbative trident on the azimuthal angle. Accordingly, along with the fixed positron momentum $\underline{p}_1$, we keep the rapidity y_2 of the electron fixed, but allow its transverse momentum p_{T2} and azimuthal angle ϕ_2 to vary in a certain range. On the one hand, this leads to a better understanding of the electron phase space in the pulsed-perturbative trident w.r.t. the impact of the finite laser pulse. On the other hand, the azimuthal distribution provides deeper insights into the connection of pulsed-perturbative trident to its monochromatic limit. For instance, in the calculation of the perturbative (monochromatic) trident cross sections, it is common practice to fix the value of the azimuthal angle of one final particle in order to fulfil the global energy-momentum conservation, which is outlined in appendix A.4, see equations (A.57) and (A.87).

We begin with the discussion of the case not to close to the monochromatic threshold. In figure 4.8, the six-fold differential cross section (4.69) is exhibited for the same setting as in the top row of figure 4.7 (i.e. $y_1 = 1.0, p_{T1} = 0.15, \phi_1 = 0, \sqrt{s} = 3.353\,m$ and

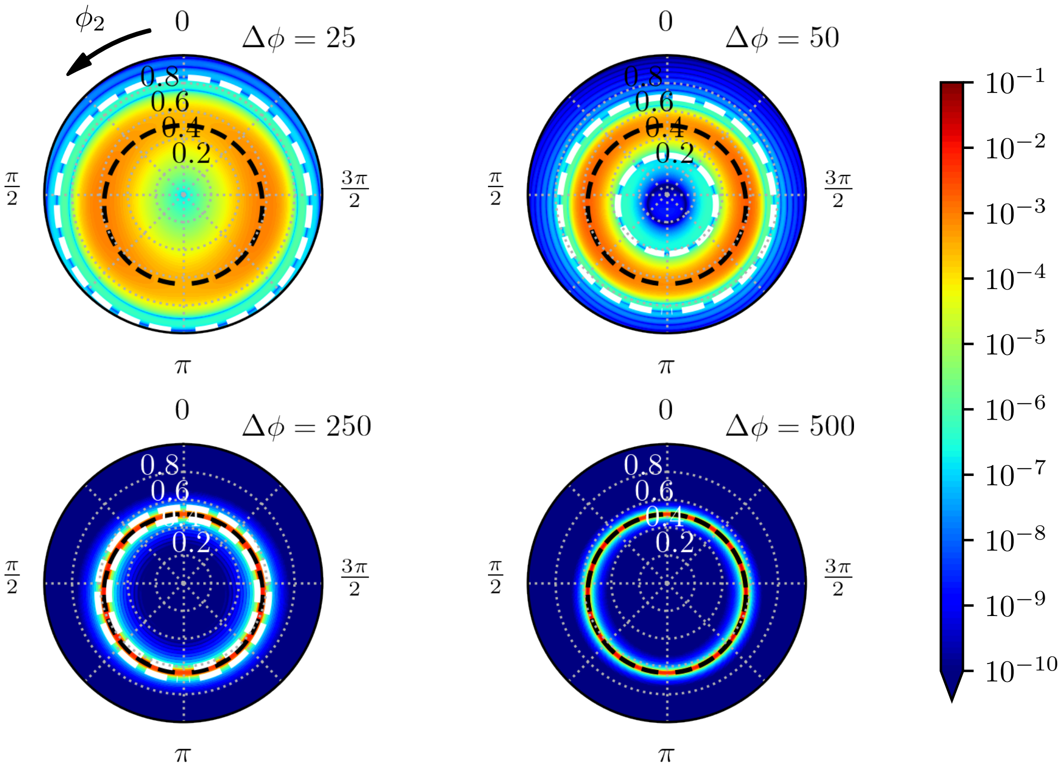

Figure 4.8: Contour plot of $\frac{\mathrm{d}^6\sigma_{\mathrm{ppt}}}{\mathrm{d}y_1\,\mathrm{d}p_{T1}\,\mathrm{d}\phi_1\,\mathrm{d}y_2\,\mathrm{d}p_{T2}\,\mathrm{d}\phi_2}$ given in equation (4.69) in units of mb/m^2 for a linearly polarized background field with the $\cos^2$-envelope, depicted as a function of the azimuthal angle ϕ_2 (polar axis) and the transverse momentum p_{T2} (radial axis) for $y_2 = 1.25$, $\sqrt{s} = 3.353\,m$, several values of the pulse width $\Delta\varphi$ (top left: 25, top right: 50, bottom left: 250, bottom right: 500) and for a fixed positron momentum with $y_1 = 1.0, p_{T1} = 0.15\,m, \phi_1 = 0.0$. Additionally, the “physical phase space” of perturbative (monochromatic) trident given in equation (A.87) is depicted as a single back dashed circle.

$\Delta\varphi = 25, 50, 250, 500$), but for a fixed value of the electron rapidity of $y_2 = 1.25$. The transverse momentum p_{T2} is assigned to the radial direction and the azimuthal angle to the polar direction of the diagram, where the azimuthal zero point corresponds to the 1-axis in momentum space. In this representation, the beam axis, i.e. the direction of the reference three-momentum $\underline{k}$ of the laser field, is positioned in the origin of the polar diagram and points at the viewer perpendicular to the diagram plane. First, we observe for all depicted cases a ring-like structure of the distributions, where its origin is slightly shifted w.r.t. the beam axis, independent of the value of the pulse width. The direction of this shift (here denoted as ϕ_2^{shift}) only depends on the azimuthal angle φ_1 of the positron due to the relation $\phi_2^{\mathrm{shift}} = (\phi_1 + \pi) \mod 2\pi$, i.e. for the displayed setting $\phi_2^{\mathrm{shift}} = \pi$. This can be understood by the following kinematically reasoning. Since we assume a head-on collision, there is no momentum component perpendicular to the beam axis in the initial state, which implies that all azimuths of the final particles need to summed up to zero due to the global three-momentum conservation. Here, if one assumes a collinear propagation of the intermediate particles (virtual intermediate photon and “recoil electron”) at the lower vertex of the diagram representation displayed in figure 4.1, then there is still no azimuthal direction preferred in this intermediate state. Therefore, if the intermediate photon decays into an electron-positron pair, the parts of their respective three-momenta perpendicular to the beam axis need to cancel out each other, i.e. their azimuths need to include an angle of π. We mention that this simple reasoning is only kinematical and only considers the azimuthal angles of the final particles. Furthermore, since there is no collinear propagation of the intermediate state of the trident process due to a dead-cone effect (cf. Compton scattering), the reasoning does not predict the actual azimuthal angle of the electron, but a principle shift of the whole electron distribution dependents on the azimuth of the final positron.

Considering again figure 4.8, for large values of the pulse width $\Delta\varphi$, one observes a reduction of the two-dimensional ring-like structure to a single one-dimensional circle, similar to the dimensional reduction in the (y_2,p_{T2})-plane in figure 4.7 (top row). Therefore, combining figure 4.8 with the top row of figure 4.7, we observe that in the monochromatic limit and for a fixed positron momentum, the treated final electron is forced onto the surface of an ellipsoid-like structure in the cylindric (y_2, p_{T2}, ϕ_2)-space. Consequently, we insert the ϕ_2-values obtained from the energy-momentum conservation in the monochromatic case according to equation (A.87), which will be referred to as the monochromatic circle. Here, we mention again the near-perfect match of the electron phase space of pulsed-perturbative trident with the monochromatic limit for the case of large $\Delta\varphi$, as formerly observed in the top row of figure 4.7 in the (y_2, p_{T2})-plane.

Looking at it the other way round, for decreasing values of the pulse width $\Delta\varphi$, the azimuthal electron distribution is modified from a one-dimensional circle in the case of perturbative trident to a two-dimensional ring-like structure in the case of pulsed-perturbative trident. This modification was formerly observed in the (y_2, p_{T2})-plane displayed in figure 4.7 and reaches a finite signal even in the center of the ring-like distribution providing a wider kinematical range, where the trident process becomes experimental accessible, as mentioned in section 4.3.

In figure 4.9, the exclusive electron distribution is depicted with the same setting as in figure 4.8, but for a reference center-of-momentum energy of $\sqrt{s} = 3.05\,m$, which is slightly above the monochromatic threshold of $\sqrt{s_{\mathrm{th}}} = 3\,m$. Similar to the behavior observed for the

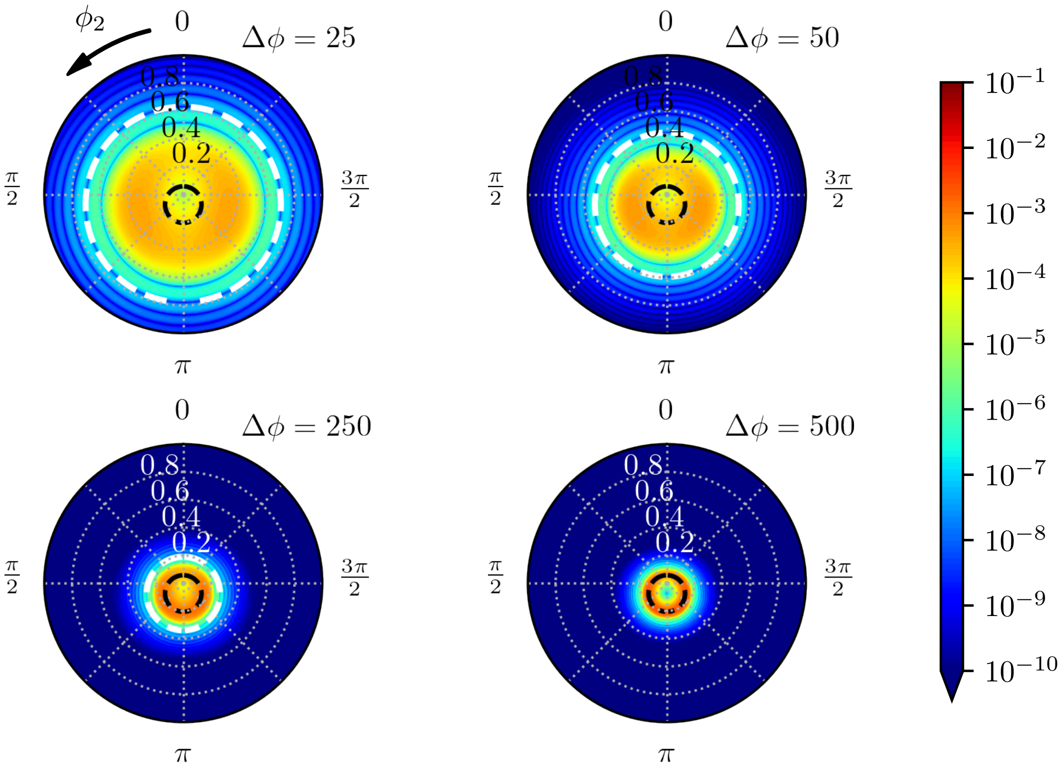

Figure 4.9: Exclusive electron azimuthal distribution with same setting as in figure 4.8 but for a center-of-mass energy of $\sqrt{s} = 3.05\,m$.

distribution in the (y_2, p_{T2})-plane (cf. figure 4.7, middle row), the dimensional expansion for decreasing values of $\Delta\varphi$ is even stronger near to the monochromatic threshold. Despite the smaller area occupied by the monochromatic circle, the enhancement due to the finite pulse width yields for the depicted value of $\Delta\varphi = 25$ a similar area and signal strength as in the case of $\sqrt{s} = 3.353\,m$. Of course, the signal strength, i.e. the maximum values of the depicted distribution, is slightly lower near the threshold, which was initially indicated by the total cross section of pulsed-perturbative trident displayed in figure 4.2. Therefore, in the data analysis related to a conceivable experimental setup, one may introduce a cutoff in the transverse momentum channel of the electrons, e.g. $p_{T2}^{\text{cutoff}} = 0.3\,m$ for the case with $\sqrt{s} = 3.05\,m$, in order to remove the electron signal originating from the monochromatic trident (caused by the central frequency of the laser). The remaining signal is produced due to the finite bandwidth of the laser.

This also holds, if there is no monochromatic trident signal caused by the central frequency of the laser in the first place, i.e. even if the reference center-of-momentum energy is below the monochromatic threshold. The finite observable signal of the trident process emerges due to the finite bandwidth of the laser.

Consequently, in figure 4.10 the exclusive electron distribution of pulsed-perturbative trident is exhibited in the same setting as in figures 4.8 and 4.9, respectively, but for a reference center-of-momentum energy of $\sqrt{s} = 2.95\,m$, which is slightly below the monochromatic threshold. First, we observe that the exclusive electron distribution vanishes for large values of $\varDelta\varphi$ due to the absence of physical phase space in the monochromatic limit. However, for small pulse widths, e.g. the displayed case of $\varDelta\varphi = 25$ (first panel in figure 4.10), the resulting distribution enhances up to a non-negligible level, which is in phase space area and signal strength comparable to the case of $\sqrt{s} = 3.05\,m$ (see figure 4.9). Additionally, the ring-like structures observed in cases with $\sqrt{s} > \sqrt{s_{\text{th}}}$ is dissolved for $\sqrt{s} = 2.95\,m$ and one has a more disk-like structure of the exclusive electron distribution in the (p_{T2}, ϕ_2)-plane.

Finally, we want to quantify the impact of the finite pulse width of the laser field (see section 3.3 and especially figure 3.3) on the modification of the electron phase space for

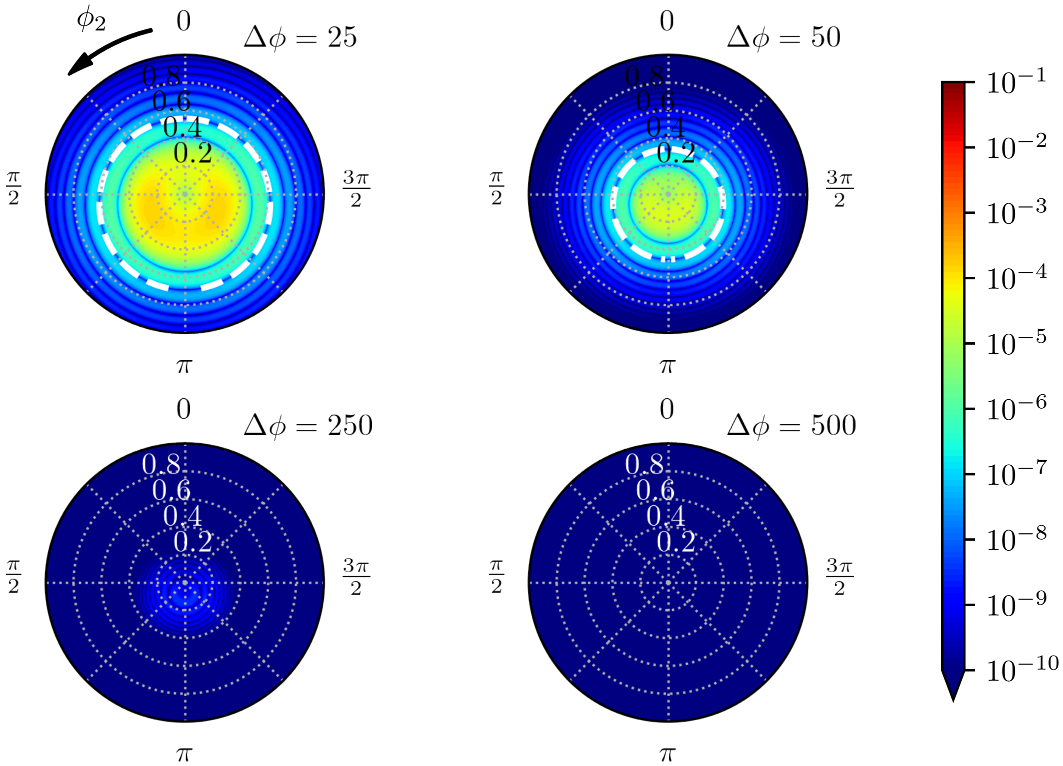

Figure 4.10: Exclusive electron azimuthal distribution with same setting as in figure 4.8 but for a center-of-mass energy of $\sqrt{s} = 2.95\,m$. There is no physical phase space of perturbative (monochromatic) trident in this case.

a fixed positron momentum. Accordingly, we mention additional monochromatic circles given by

$$\phi_2^{(1,2)}(l) \equiv \phi_2^{(1,2)}(\sqrt{s_l}), \tag{4.70}$$

where $\phi_2^{(1,2)}(\sqrt{s})$ is given in equation (A.87), $s_l = (p + lk)^2$ denotes the shifted center-of-momentum energy with p (k) is the momentum of the initial electron (photon) and l is the photon number parameter, i.e. the argument of the Fourier transform $F_1(l)$ given in equation (3.4) encoding the laser spectrum (see section 3.3). In contrast to the calculation of the pulsed-perturbative trident matrix element (where l is given as a function of the external momenta), we gather the values of l directly from the (squared) spectral distribution of the laser field depicted in figure 3.3, e.g. by considering the first side maxima of the spectrum on both sides at the main maximum, which results in $l = 1 \pm \frac{3\pi}{\Delta\varphi}$. The resulting monochromatic circles $\phi_2^{(1,2)}\left(1 \pm \frac{3\pi}{\Delta\varphi}\right)$ obtained from equation (4.70), supposing they exist, are inserted in the figures 4.8, 4.9, and 4.10, respectively. We mention, that in every displayed case, this shifted monochromatic circles provide a good approximation of the inner and outer boundaries of the extent of the exclusive electron distribution due to the finite pulse width. Accordingly, one has an explicit connection between the width of the laser spectrum and the enlarged electron phase space of pulsed-perturbative trident, despite the complicated structure of the trident matrix element. This leads to an easy to use method in order to predict the expansion of the phase space of pulsed-perturbative trident, at least w.r.t. the momentum components transverse to the beam axis, directly from the laser spectrum. For instance, considering $\sqrt{s} = 2.95\,m$, the outer boundary given by equation (4.70) provides a good estimation of the kinematical boundaries of trident electrons expected for short laser pulses, even if the reference center-of-momentum energy, related to the central frequency of the laser, is below the monochromatic threshold.

Comparison to monochromatic limit

We found that one of the major differences in the exclusive electron distribution comparing the pulsed-perturbative QED calculation with the monochromatic case is the dimension of the respective phase space: (i) six-dimensional for pulsed-perturbative trident and (ii) five-dimensional for perturbative (monochromatic) trident. Considering the exclusive electron distribution, we observed that the extent of the dimensional expansion highly depends on the bandwidth of the laser field, caused by the finite pulse duration. As mentioned above, this dimensional expansion is connected to the blurring and broadening of the monochromatic phase space boundaries in partially or fully integrated cross sections of pulsed-perturbative , e.g. as set out for the inclusive positron distribution in section 4.3

and the total cross section in section 4.2, respectively. In order to illustrate this connection, here we compute the electron distribution given by equation (4.69) with a fixed positron momentum, but integrated over one momentum component of the electron, say ϕ_2. The resulting five-fold differential cross section reads

$$\frac{\mathrm{d}^5\sigma_{\mathrm{ppt}}}{\mathrm{d}y_1\,\mathrm{d}p_{T1}\,\mathrm{d}\phi_1\,\mathrm{d}y_2\,\mathrm{d}p_{T2}} = \int \frac{\mathrm{d}^6\sigma_{\mathrm{ppt}}}{\mathrm{d}y_1\,\mathrm{d}p_{T1}\,\mathrm{d}\phi_1\,\mathrm{d}y_2\,\mathrm{d}p_{T2}\,\mathrm{d}\phi_2}\,\mathrm{d}\phi_2. \tag{4.71}$$

In order to numerically perform the integration (4.71), we apply the method of shifted monochromatic circles as introduced by the use of equation (4.70).

In figure 4.11 a circle-shaped slice through the exclusive electron distribution displayed in figure 4.8 for a constant $p_{T2} = 0.6\,m$ is depicted. One observes for increasing pulse widths $\Delta\varphi$ the above mentioned reduction of the dimension of the electron phase space due to the transition to the monochromatic case, which is indicated by the resulting two sharp peaks. Additionally, where they exist we insert in figure 4.11 the distinct values of ϕ_2 for the monochromatic case (black dashed lines) given in equation (A.87), as well as the expected boundaries of the spectral expansion (grey dashed lines) according to equation (4.70). We mention that, on the one hand, the centers of the forming peaks in the high $\Delta\varphi$ case match near to perfectly with the monochromatic values of ϕ_2. On the other hand, considering the dimensional expansion for decreasing $\Delta\varphi$, one observes that the expected boundaries, if they exist, enclose the peaks fairly well. Therefore, in general, one can apply the boundary expectation of the peaks according to equation (4.70), in order to adapt the domain of the ϕ_2-integration. Considering this adaption method, the integration in (4.71)

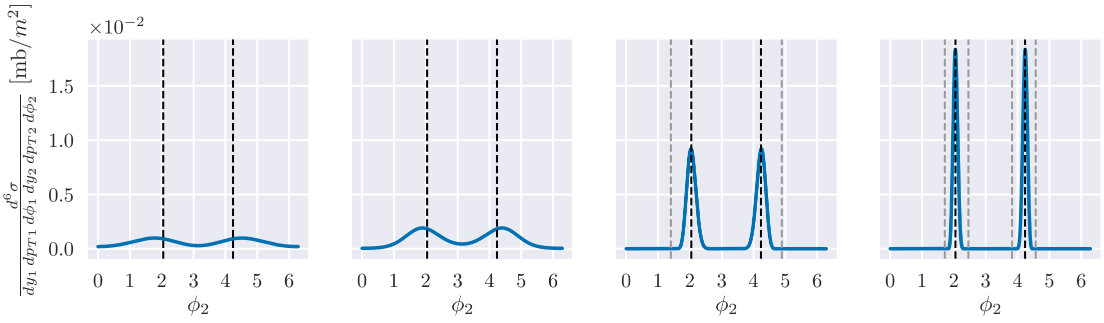

Figure 4.11: Exclusive electron azimuthal distribution with same setting as in figure 4.8 but as a function of ϕ_2 for $p_{T2} = 0.6\,m$ (i.e. a circle-shaped slice through the distributions exhibited in figure 4.8). Additionally, the fixed values $\phi_2^{(1,2)} \approx \pi \pm 1.09$, given in the monochromatic case by equation (A.87), are depicted by black dashed lines along with the expected boundaries (grey dashed lines) caused by the finite pulse width according to equation (4.70) and considering the first side maximum of the laser spectrum, i.e. $l = 1 \pm \frac{3\pi}{\Delta\varphi}$ (cf. figure 3.3).

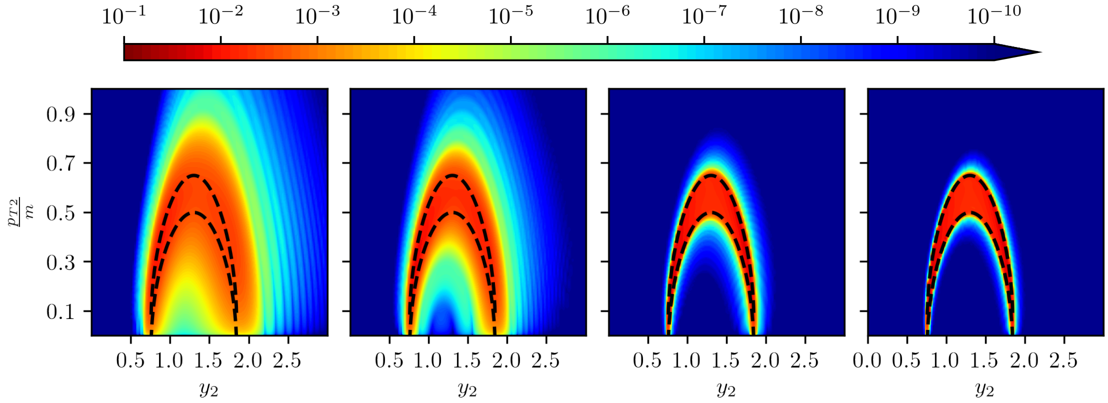

Figure 4.12: A contour plot of $\frac{\mathrm{d}^5\sigma_{\mathrm{ppt}}}{\mathrm{d}y_1\,\mathrm{d}p_{T1}\,\mathrm{d}\phi_1\,\mathrm{d}y_2\,\mathrm{d}p_{T2}}$ in units of mb/m^2, given in equation (4.71) for a linearly polarized background field with the $\cos^2$-envelope, depicted in the (y_2, p_{T2})-plane for $\sqrt{s} = 3.353\,m$, several values of the pulse width $\Delta\varphi$ ($\Delta\varphi = 25, 50, 250, 500$ f.l.t.r.) and for a fixed positron momentum with $y_1 = 1.0, p_{T1} = 0.15\,m, \phi_1 = 0.0$. Additionally, the boundaries of the physical phase space of perturbative (monochromatic) trident given in equation (A.94) are depicted by back dashed curves.

becomes numerically very stable, even if the peaks are steep (as observed in figure 4.11 for large values of $\Delta\varphi$).

In figure 4.12 the resulting five-fold differential cross section (4.71) is depicted as a function of the rapidity y_2 and the transverse momentum p_{T2} of the remaining final electron for a linearly polarized background field ($\xi = 0$) with a $\cos^2$-pulse envelope and for several values of the pulse width $\Delta\varphi$. Here, we choose $\sqrt{s} = 3.353\,m$ (i.e. above the threshold) and fix the positron momentum at $y_1 = 1.0, p_{T1} = 0.15\,m, \phi_1 = 0.0$. First, we mention that the respective monochromatic exclusive electron distribution covers a two-dimensional area in the (y_2, p_{T2})-plane with sharp arc-shaped boundaries, in difference to the one-dimensional curves shown above for a fixed value of ϕ_2 (see figure 4.7). For large $\Delta\varphi$ the pulsed-perturbative QED calculation approaches this sharp-bounded area indicating that the ϕ_2-integration in (4.71) extracts the correct monochromatic values of ϕ_2 given in equation (A.87). Loosely speaking, this property is a sort of a numerical representation of the delta-distribution, which is used to analytically fix the values of ϕ_2 in the monochromatic case (cf. appendix A.4). On the other hand, for decreasing values of $\Delta\varphi$, one observes an enlargement of the exclusive electron distribution beyond the sharp kinematic boundaries, similar to the expansion previously seen in the inclusive positron distributions (cf. section 4.3).

In order to directly compare the values of the exclusive electron distribution of pulsed-perturbative trident integrated over ϕ_2 with the respective monochromatic case, we consider a slice through the distribution displayed in figure 4.12 for $p_{T2} = 0.6\,m$. The resulting

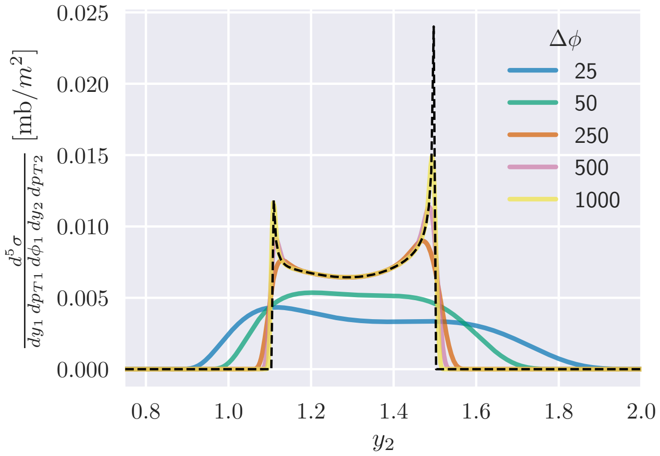

Figure 4.13: The exclusive ϕ_2-integrated electron distribution with the same setting as in figure 4.12 but as a function of y_2 for $p_{T2} = 0.6\,m$. Additionally, the case of an ultra-wide pulse with $\varDelta\varphi = 1000$ is exhibited as well as the respective monochromatic distribution obtained from equation (C.9) by transformation to transverse coordinates due to table A.2 and equation (A.35), repsectively.

curves are depicted in figure 4.13 for the already considered values of $\varDelta\varphi = 25, 50, 250, 500$ as well as an ultra-wide pulse with $\varDelta\varphi = 1000$. Additionally, we insert the respective slice through the monochromatic exclusive electron distribution (black dashed line), which is given by the transformation of equation (C.9) to transverse coordinates according to table A.2 and equation (A.35). For increasing values of $\varDelta\varphi$, one has again a near perfect match of the pulsed-perturbative QED calculation with the monochromatic distribution. We mention especially the formation of the steep edges of the distribution, which are kinematically indicated by the coordinate singularities outlined in appendix A.4 for the monochromatic case.

4.5 Experimental capability

Within this section, we illustrate briefly the (possible) experimental scenarios in order to measure in principle the features of the trident process w.r.t. the dependence to the finite spectrum of the impinging electromagnetic field, as illustrated in sections 4.2, 4.3 and 4.4, respectively. We point out that this can be done within this thesis only as a conceptional study excluding concerns directly related to the experimental setup, e.g. electron bunching, repetition rates, synchronization, laser focusing and detector specification, to name a few. The evaluation of these issues is beyond the present thesis and will be left for further investigations.

Considering the pulsed-perturbative trident investigated within this chapter, the following parameter constraints need to be met in an experiment.

high center-of-momentum energy: As we observed in several distributions of pulsed-perturbative trident, the strongest impact of the pulse width can be seen near to the monochromatic threshold of $\sqrt{s_{\text{th}}} = 3\,m$. Therefore, it seems convenient to choose an experimental setup, where the encountered center-of-momentum energy is in the region of this threshold. In the assumed case of a laser-electron collision with a fixed central frequency (energy) of the laser, this can, in principle, be achieved by a high-energetic electron beam. However, for optical laser frequencies, say $\omega = 1\,\text{eV}$, the needed electron energy would be $E \sim 10^6\,m \approx 0.5\,\text{TeV}$, which is not reachable by current electron accelerators (for comparison, the Large Electron–Positron Collider LEP [210] had a maximal electron energy of $\approx 104\,\text{GeV}$). We honorably mention the upcoming capabilities of laser wake-field acceleration (cf. [51]), which predict electron energies in the 100 GeV to TeV range. However, for this conceptional study, it is more convenient to go to higher central frequencies of the used photon source in order to decrease the needed electron energy up to a manageable level. For instance, in a heads-on collision of 10 keV photons (e.g. from an x-ray free-electron laser or a secondary x-ray source; see below) with an electron beam, the electron energy needs to be at least 50 MeV to operate slightly above the monochromatic trident threshold.

low-to-medium laser intensity parameter: Since the pulsed-perturbative QED introduced in chapter 3 is a low-a_0 approximation to the pulsed plane-wave approach of strong-field QED, we consider experimental setups with $a_0 < 1$. As we indicated in section 3.2, the first order approximation in a_0 is reasonably close to the full calculation of the vertex function for $a_0 \leq 0.1$ (as shown for the phase integral B_1 in figure 3.2), where we assume the pulsed-perturbative QED to be a valid approximation. Considering the above mentioned x-ray sources, this constraint is naturally fulfilled, because for a fixed laser peak intensity I, the respective laser intensity parameter a_0 scales inversely proportional with photon energy: $a_0 \sim \frac{1}{\omega}$. For instance, if one has a light source with an intensity of $I = 10^{18}\,\mathrm{W/cm^2}$ and central frequency of $\omega = 10\,\mathrm{keV}$ (both reachable with the modern XFEL experiments; see below) the resulting intensity parameter yields $a_0 \approx 10^{-4}$.

short pulses/wide spectra: As we observed in section 4.3 and 4.4, the strongest impact of the laser spectrum can be seen, of course, in the short-pulse regime. However, considering for instance the exclusive electron distributions near the monochromatic threshold (cf. section 4.4), we observe that even for relatively large pulse widths, e.g. in the order of $\Delta\varphi \sim 10^2$, the dimensional broadening of the distribution is not negligible: even for $\Delta\varphi = 250$, there is significant signal strength outside of the monochromatic phase space (see figure 4.7 middle row). Accordingly, we assume that an experimental setup needs to produce pulses shorter than $\Delta\varphi \sim 10^2$ in order to be capable to observe the spectral effects in the trident process near the monochromatic threshold. Admittedly, this is the most difficult task to be accomplished, because if one considers a temporal duration τ of a laser pulse with a reference energy of ω, the corresponding pulse width behaves like $\Delta\varphi \sim \omega\tau/2$, where we neglect spatial inhomogeneities. Therefore, if we assume a high-energy light source, according to the reasoning given above, the resulting pulse width $\Delta\varphi$ yields naturally larger values. Accordingly, one needs to be aware of a compromise between the reference energy (i.e. the central frequency) of a light source and its pulse width. As we will see below, especially the upcoming/planned attosecond (sub-femtosecond) sources in the soft x-ray regime might be such a compromise.

In order to evaluate the above mentioned parameter ranges w.r.t. present or planed experimental facilities, we consider the following light sources/collision experiments.

- The European X-Ray Free-Electron Laser Facility (European XFEL; [11, 211]) as used from the HiBEF collaboration [130] in order to detect i.a. vacuum birefringence [259], here representative of a primary x-ray source,
- LCLS-II XLEAP [171] (see also [1, 75, 115, 172, 260]) as an example for the upcoming sub-femtosecond x-ray sources,
- SYLOS-SHHG@ELI-ALPS [165] (see also [195, 201]) representative of an upcoming secondary source with planed applications in attosecond science (see for instance [111] and the references given there),
- LUXE@DESY [2] (see also [34, 46, 114]) as an example for an electron collision experiment with an optical high-power laser. Additionally, we consider the pioneering

E-144@SLAC [20, 40, 41, 47], where through the combined Compton- and Breit-Wheeler process, multi-photon interactions were experimentally verified for the first time. In a similar category of these experiments, we mention also the upcoming FACET-II experiment [310].

We note that the above list is not complete and only representative for certain experimental aspects w.r.t. the above mentioned parameter ranges for pulsed-perturbative trident.

In figure 4.14, the experimental parameters of the above considered light sources are depicted. On the l.h.s., the Mandelstam-s (i.e. the square of the center-of-momentum energy $\sqrt{s}$) is displayed as a function of the energy E of the initial electron for several reference energies of the incident photon (i.e. of the background field in the context of strong-field QED). Additionally to the above considered experiments (blue dots), we inserted several regimes of the photon energy: the optical regime ($\omega \sim 1\,\mathrm{eV}$; turquoise line), the typical XFEL regime ($\omega \sim 1 - 10\,\mathrm{keV}$; red area) and the typical synchrotron regime ($\omega \sim 1\,\mathrm{MeV}$; green line), respectively, as well as the monochromatic threshold $s_{\mathrm{th}} = 9\,m^2$

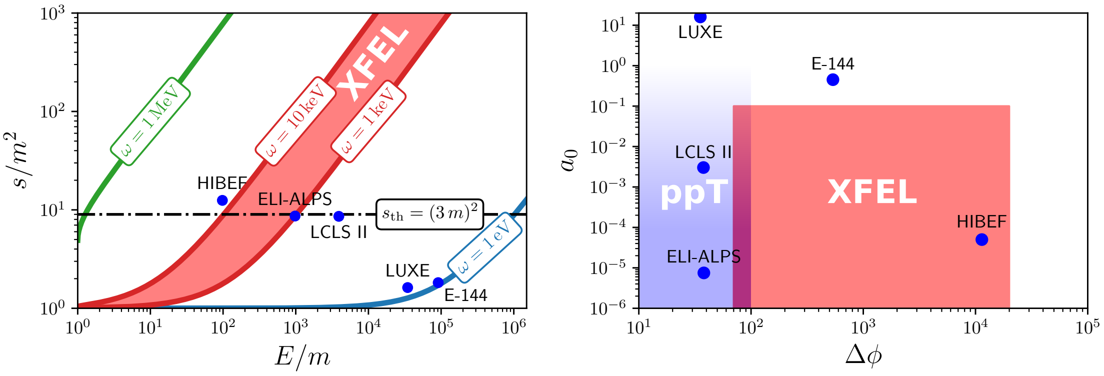

Figure 4.14: Characteristic quantities of several (partially) assumed experimental setups depicted in the (s, E)-plane (left panel), where s is the Mandelstam variable and E the electron energy, as well as in the $(a_0, \varDelta\varphi)$-plane (right panel), where a_0 denotes the laser intensity parameter and $\varDelta\varphi$ the pulse width in an pulsed plane-wave approach for the light-source. The experimental values are considered from: HiBEF [11] ($\omega = 15\,\mathrm{keV}, E = 50\,\mathrm{MeV}, a_0 = 5 \times 10^{-5}, \varDelta\varphi = 11.4 \times 10^3$), LUXE [2] ($\omega = 1.55\,\mathrm{eV}, E = 17.7\,\mathrm{GeV}, a_0 = 16, \varDelta\varphi = 35.3$), LCLS-II [1] ($\omega = 248\,\mathrm{eV}, E = 2\,\mathrm{GeV}, a_0 = 3 \times 10^{-3}, \varDelta\varphi = 37.7$), ALPS [165] ($\omega = 1\,\mathrm{keV}, E = 250\,\mathrm{MeV}, a_0 = 7.5 \times 10^{-6}, \varDelta\varphi = 38$) and E-144 [20] ($\omega = 1.18\,\mathrm{eV}, E = 46.6\,\mathrm{GeV}, a_0 = 0.45, \varDelta\varphi = 536.7$), respectively. If necessary, the electron energies are assumed according to the operation near the monochromatic trident threshold (black dot-dashed line) and the quantities are calculated from the referenced parameters. Additionally, several reference regimes are depicted. Left panel: optical laser regime ($\omega \sim 1\,\mathrm{eV}$; turquoise line), typical XFEL regime ($\omega \sim 1 - 10\,\mathrm{keV}$; red area) and synchrotron regime ($\omega \sim 1\,\mathrm{MeV}$; green line), as well as, right panel: the assumed parameter regime for pulsed-perturbative trident (blue shaded) and the typical XFEL regime (red area).

of the trident process (black dot-dashed line). In order to reach the monochromatic trident threshold, we consider possible electron energies of $E = 50\,\mathrm{MeV}$ (HiBEF), $250\,\mathrm{MeV}$ (ALPS) and $2\,\mathrm{GeV}$ (LCLS-II), respectively. For the considered collision experiments (LUXE, E-144) we depicted the actual electron energies used or planed in the respective experiment: $E = 17.7\,\mathrm{GeV}$ (LUXE) and $46.6\,\mathrm{GeV}$ (E-144). We mention that the considered examples of light-sources in the x-ray regime are capable to operate near the monochromatic trident threshold using manageable electron energies and therefore might be sensitive for the spectral broadening w.r.t. the pulsed-perturbative trident. The situation is different for the considered optical experiments, which operate far below the monochromatic trident threshold and therefore they are more sensitive for genuine multi-photon effects at higher $a_0 > 1$, where the pulsed-perturbative QED approach is not applicable; this is/was, of course, the intension of these experiments.

A further light source class not exhibited in the left panel of figure 4.14 is related to Compton-backscattered and coherent bremsstrahlung photons. These operate currently in the energy range of $1 - 10\,\mathrm{GeV}$ and above, however, as photon beams and not as coherent electromagnetic fields. Despite their high degree of (linear) polarisation – which is of paramount interest for hadron physics experiments [3, 12] – they are in our context valuable as probe photons, e.g. in non-linear Breit-Wheeler process. We emphasize that the azimuthal angle distribution of the "recoil electron" in the trident process is routinely used to control the polarisation of such photon beams [72, 95]. The "recoil electron" is here the slowest outgoing electron $e^{-\prime}$ in the process $\gamma + e^- \to e^{-\prime} + (e^+e^-)$ at atomic target-material electrons e^- (cf. appendix C.3).

In the right panel of figure 4.14, the parameters of the considered experiments are depicted in the $(a_0, \mathit{\Delta}\varphi)$-plane. Additionally we inserted the typical XFEL regime (red area) as well as the parameter regime, where we assume the pulsed-perturbative trident yields a measurable contribution (blue shaded area). Firstly, we mention that the considered optical collision experiments have parameters outside the sensitivity area of pulsed-perturbative trident due to high laser intensity parameters a_0 in the case of LUXE and wide pulses in the case of E-144, respectively. Secondly, the considered collision experiment at the european-XFEL (e.g. as conceivable for HiBEF) is also not sensitive to the spectral effects described by the pulsed-perturbative trident due to the narrow bandwidth of the XFEL. However, the considered secondary (soft) x-ray sources (here LCLS-II XLEAP and SYLOS-SHHG at ELI-ALPS) might be sensitive for the bandwidth effects of pulsed-perturbative trident. Combined with the energy properties of these (conceivable) experiments mentioned above, we assume that the phenomena due to broad bandwidth of the light source become important for a precise data analysis of the detected particles produced by the collision.

5 | Summary and Outlook

Within this thesis, we investigated the strong-field trident process at low to medium intensity parameters, but by considering the spectral information of the light source involved in the scattering due to its short temporal structure. Thereby we revealed in a transparent manner, that the correct regularisation of the dressed vertex in momentum space (see section 2.71) is key for the reconstruction of the perturbative monochromatic QED in the combined limiting cases of infinitely wide pulses and weak fields. Consequently, we introduced in chapter 3 an approximation to strong-field QED for low intensity parameters a_0 but arbitrary finite pulse widths. This fills a missing gap on the pathway from the general pulsed plane-wave approach to the common perturbative monochromatic QED, as we illustrated in section 3.1. Furthermore, we showed that this new approximation leads to a factorisation of the dressed vertex w.r.t. the dependence to the background field in terms of its Fourier transform (see equation (3.10)), which is directly connected to the spectrum of the used light source, as we discussed in section 3.3.

In chapter 4, we applied this new approximation to the trident process and numerically calculated a portfolio of different distributions, e.g. differential and total cross sections, respectively. In section 4.1 we derived the pulsed-perturbative trident matrix element for arbitrary pulse shapes and polarisations, where revealed that the mentioned factorisation is also present in the trident matrix element and to some extent on the probability level as well. This led to a general proof of the convergence of the pulsed-perturbative trident for infinitely wide pulses to the monochromatic case[2], where we considered both levels, the matrix element and the differential cross section, respectively.

In order to numerically evaluate the pulsed-perturbative trident process, we first considered in section 4.2 the dependence of the trident total cross section at low-to-medium intensities

---

[2] This proofs by implication also the convergence of the strong-field trident to the monochromatic case in the combined limit of infinitely wide pulses and weak fields.

to the finite width of a smooth pulse envelope function[3]. This reveals for the first time, that for short pulses the trident process produces a non-vanishing total cross section below its monochromatic threshold, even if the intensity parameter a_0 is below unity. A similar behavior was observed in the Breit-Wheeler process, for instance in [221, 290].

Following this, in section 4.3 we numerically calculated the inclusive positron distribution by integrating fully over the final electrons, which mimics the experimental case, where the positron is measured accumulatively for all possible final electron states. This is motivated by the consideration, that the positron can be used as a trigger particle in order to select the trident signals in a laser-electron collision. Considering these inclusive positron distributions, we observed and quantified an enhancement of the physical phase space of the positron w.r.t. the monochromatic case, which is originated in the finite bandwidth of the used light source. Furthermore, we revealed that there is a finite inclusive distribution of the positron with non-negligible height, even if there is no physical phase space according to the monochromatic case. This will be an important property if one assumes an experimental laser-collision setup, where the central frequency of the used light source is too low to succeed the monochromatic trident threshold but has such a short temporal structure, that the tails of the laser spectrum will provide enough energy to yet cause the trident process.

In order to continue the elaboration of the trigger particle approach w.r.t. the positron, we subsequently calculated in section 4.4 the exclusive electron distributions as well as its azimuthal distribution by considering a fixed phase space point for the positron momentum. This mimics the trigger in a conceivable experimental setup. According to these exclusive electron distributions, we clarified that the enhancement of the trident final phase space observed in the inclusive distributions is originated in a dimensional extension of the phase space due to the appearance of an additional degree of freedom for the final particles. This is a common property for processes in pulsed plane-wave background fields. However, we quantified this dimension-related behavior in the case of the trident process and showed transparently that it is originated in the finite pulse width of the used laser. Furthermore we derived an analytical formula for the assumed dimensional extent based on the width of the laser spectrum, which we were able to verify by comparison with the numerically calculated exclusive electron distributions. Finally, we demonstrated an application of this analytical formula by using it to adapt the domain of the azimuthal angle of the electron to regions with assumingly the most importance, which led to numerically very stable

---

[3] There are similar results given in [69, 133], but without the consideration of a smooth pulse envelope function.

integration schemes.
On every stage of calculation of the pulsed-perturbative trident distributions, i.e. the total cross section, the inclusive as well as the exclusive distributions, we compare the resulting curves (or several slices) with a direct calculation of the perturbative monochromatic trident (see appendix C). For large values of the pulse width, we found in every considered case a smooth approach of the pulsed-perturbative QED calculations with the monochromatic results, which finally led to near perfect agreements. Accordingly, we conclude that the pulsed-perturbative QED approach can be seen from two different points of view. First as a low-intensity approximation on the general strong-field QED in pulsed plane-wave background fields in order to provide a numerically staple framework for processes at the lower intensity parameter range. Second as a clean extension of the monochromatic QED calculations in order to involve the broad spectrum of modern short-pulsed light sources. Conclusively, we examined in section 4.5 several existing or planned experimental facilities due to their provided light sources w.r.t. the capability to measure the spectral effects according to pulsed-perturbative trident calculations. As it turns out, a combination of the sub-femtosecond soft x-ray sources with an electron beam of $\sim 10\,\mathrm{MeV}$ up to several GeV energy would be sensitive for the pulsed-perturbative trident effects elaborated within this thesis.

Outlook

From the conceptional point of view, an important problem to treat, would be the behavior of the trident process for intensity parameters a_0 approaching unity. In the context of our pulsed-perturbative approach, going to larger values of the laser intensity parameter means checking whether an analogue of the Fourier transform of the electromagnetic field can be isolated as a crucial element of the phase space distribution of produced particles. Accordingly, a direct comparison to the calculations coming from investigations for higher values of a_0, for instance from [69, 70], would provide very interesting insights into the analytical structure of the trident process.
Another conceivable direction for further investigations is the application of pulsed-perturbative trident to a broader range of properties given by recent or future experiments. For instance, the distribution of the final “recoil” electron is key for the polarisation control of high energy gamma-ray sources, which could benefit from the involvement of the spectral information via the pulsed-perturbative trident process. Therefore, the investigation of pulsed-perturbative trident for more general polarisations as well as a more explicit consideration of these experimental setups seems to be a promising starting point for such investigations.

Speaking of the experimental applications, another important extension of the investigations within this thesis is the consideration of more general laser field configurations. For instance, the factorisation of the amplitude w.r.t. the pulse shape dependence in pulsed-perturbative QED could be convenient for the development of a more data-driven approach for the considered scattering processes. Thereby, one could analyse the spectrum of the laser field instead of an a-priori field model (e.g. by using external data from experiments or simulations) and still would be able to predict the probability of the considered process[4]. Since the pulsed-perturbative QED processes can be implemented in a numerically stable fashion – among other things due to the above mentioned factorisation – there is another conceivable application closely related to the data-driven approach mentioned above: based on a Monte Carlo event generator, our pulsed-perturbative approach could be implemented in large-scale simulations like the prolific particle-in-cell codes. This would be a rather complementary approach to the locally constant field approximation w.r.t. the involvement of (non-linear) QED processes in such simulations for plasma-related investigations and the computation of QED cascades. Thus, our pulsed-perturbative approach can be seen as a modification of the monochromatic QED, which includes spectral effects from the lower end of the intensity scale, i.e. the description evolves in the same direction as further experimental developments.

Conclusively, we mentioned in appendix C.4, another different kind of application lies in the dark matter search, where the trident process might be capable to give access to dark photon resonances. Accordingly, an interesting direction for further investigations is the consideration of the phase space modifications according to our pulsed-perturbative approach in order to generalise the respective monochromatic treatments.

---

[4] This might be somewhat similar to the data-driven form factor approach applied in the parton model of hadrons (see for instance [311] and the references given there).

Appendix

A Relativistic Kinematics

In this section, the conventions and notations from relativistic particle kinematics used within this thesis are summarised. These explanations are rather incomplete, and we refer the reader to the extensive literature about this topic related to particle physics and classical electrodynamics: e.g. [48, 108, 179, 235], chapter 47 of [286].

A.1 Preliminary remarks

Generally, a particle is described in the theory of special relativity by its 4-momentum $p^\mu = \big(p^0, p^1, p^2, p^0\big) = \big(p^0, \underline{p}\big)$, where the components are given in Cartesian coordinates of the respective Minkowski space and the spatial components $\underline{p} = (p^1, p^2, p^3)$ denote the 3-momentum of the particle. We mention, to distinguish the spatial components of a 4-momentum from the position vector x^μ, we refer the 3-momentum axes as $(1, 2, 3)$ rather than (x, y, z).

The 4-momentum of a particle causes a splitting in two distinct classes: a particle is called on-shell, if its 4-momentum obeys

$$p^\mu p_\mu = g_{\mu\nu} p^\mu p^\nu = m^2, \tag{A.1}$$

where m is the particles rest mass and $g_{\mu\nu} = \mathrm{diag}(1, -1, -1, -1)$ the Minkowski metric. Otherwise, if $p^\mu p_\mu \neq m^2$, the particle is called off-shell (also loosely referred as a virtual particle). Most often, off-shell particles appear as intermediate particles in scattering and decay processes, such as the trident process investigated within this thesis. For an on-shell particle, the components of its 4-momentum are not independent, but connected due to the energy-momentum relation $E^2 := \big(p^0\big)^2 = \big(p^1\big)^2 + \big(p^2\big)^2 + \big(p^3\big)^2 + m^2 = \underline{p}^2 + m^2$, where in this case, the 0-th component of the 4-momentum is referred as the energy E of the particle, which obeys $E \geq m$. The set of all possible 4-momenta describing an on-shell particle is within this thesis referred to as the (one-particle) phase space of the particle.

The invariant integral measure on such a phase space reads

$$\mathrm{d}\Phi_1 = \left.\frac{\mathrm{d}^3\underline{p}}{(2\pi)^3 2p^0}\right|_{p^\mu p_\mu = m^2} = \frac{\mathrm{d}p^1\mathrm{d}p^2\mathrm{d}p^3}{(2\pi)^3 2E}, \tag{A.2}$$

where the energy $E = \sqrt{\underline{p}^2 + m^2}$ is understood as a dependent quantity and the factor $(2\pi)^{-3}$ is conventionally inserted concerning the normalisation of possible Fourier transforms between position and momentum space descriptions of the particle within a quantum field theory. However, in a physical process, the involved momenta need to obey kinematical conditions, e.g. global energy-momentum conservation, which causes constraints of the respective phase space. Consequently, the set of all momenta of all particles involved in a physical process, which fulfil the respective kinematical conditions is also referred to as the physical phase space to this process.

A.2 Coordinate systems: parametrisation of 4-momenta

The 4-momentum p^μ of a particle is generally regarded with its Cartesian components. However, in some cases, it is convenient to transform these components into a coordinate system, which is more suitable to the respective circumstances, e.g. the encountered mathematical expressions become more handy in special coordinate systems, or if in an experiment a specific kinematical quantity is measured.

Spherical coordinates

In a spherical coordinate system, the 4-momentum of a particle is given in terms of the energy E, the magnitude of the 3-momentum ϱ, the polar angle θ and the azimuth angle ϕ, which are defined by

$$E := p^0, \tag{A.3}$$

$$\varrho := \sqrt{(p^1)^2 + (p^2)^2 + (p^3)^2} \tag{A.4}$$

$$\theta := \arccos\left(\frac{p^3}{\rho}\right), \tag{A.5}$$

$$\phi := \operatorname{atan2}\left(p^2, p^1\right) \in [0, 2\pi), \tag{A.6}$$

where atan2 denotes the 2-argument arctangent [313], which defines the angle between the 1-axis and the vector (p^1, p^2) in the (1,2)-plane of the particle's phase space, i.e. it shifts the $\arctan(p^2/p^1)$ w.r.t. the correct quadrant to yield an azimuth angle in the interval

$[0,2\pi)$. The on-shell condition from equation (A.1) is then given as

$$\varrho = \sqrt{E^2 - m^2}, \tag{A.7}$$

where the remaining independent spherical coordinates are (E,θ,ϕ). The inverse transformation is given by

$$p^0 = E, \tag{A.8}$$
$$p^1 = \varrho \sin\theta \cos\phi, \tag{A.9}$$
$$p^2 = \varrho \sin\theta \sin\phi, \tag{A.10}$$
$$p^3 = \varrho \cos\theta. \tag{A.11}$$

For an on-shell particle the invariant phase space measure transformed to spherical coordinates reads

$$(2\pi)^3 \, \mathrm{d}\Phi_1 = \frac{\varrho^2}{2E} \mathrm{d}\varrho \, \mathrm{d}\cos\theta \, \mathrm{d}\phi = \frac{\varrho}{2} \mathrm{d}E \, \mathrm{d}\cos\theta \, \mathrm{d}\phi, \tag{A.12}$$

where in the last step we used the identity $\varrho \, \mathrm{d}\varrho = E \, \mathrm{d}E$. We mention, within this thesis we often use $\cos\theta \in [-1,1]$ as a coordinate instead of θ itself.

Light-cone coordinates

In the light-cone coordinate system w.r.t. the 3-axis of the Minkowski space (also referred as light-front coordinates), the 4-momentum of a particle is described in terms of

$$p^- := \frac{1}{2}\left(p^0 - p^3\right), \tag{A.13}$$
$$p^+ := \frac{1}{2}\left(p^0 + p^3\right), \tag{A.14}$$
$$p^x := p^1, \tag{A.15}$$
$$p^y := p^2, \tag{A.16}$$

where we often use the abbreviation $p^\perp := (p^x, p^y)$ for the projection of the respective 3-momentum $\underline{p}$ to the plane perpendicular to the 3-axis. These coordinates are proven to be practical to describe massless particles, whose kinematical behavior is strongly related to the light-cone (here w.r.t. the 3-axis), e.g. if one has a photon propagating along the 3-axis, only one of the light-cone coordinates does not vanish, i.e. only $p^+ \neq 0$ ($p^- \neq 0$) if the photon moves in the positive (negative) 3-direction. The on-shell condition (A.1) is in light-cone coordinates given as $4p^+p^- - \left(p^\perp\right)^2 = m^2$ or equivalently as the coordinate relation

$$p^{+} = \frac{\left(p^{\perp}\right)^{2} + m^{2}}{4p^{-}}. \tag{A.17}$$

The inverse transformation from light-cone coordinates to cartesian coordinates reads

$$p^{0} = p^{+} + p^{-}, \tag{A.18}$$
$$p^{1} = p^{x}, \tag{A.19}$$
$$p^{2} = p^{y}, \tag{A.20}$$
$$p^{3} = p^{+} - p^{-}, \tag{A.21}$$

which leads to the invariant phase space integral measure transformed to light-cone coordinates:

$$(2\pi)^{2}\, \mathrm{d}\Phi_{1} = \Theta(p^{-}) \frac{\mathrm{d}p^{-}\, \mathrm{d}^{2}p^{\perp}}{2p^{-}}, \tag{A.22}$$

where $\Theta(x)$ denotes the Heaviside step-function.

Transverse coordinates

In a transverse coordinate system w.r.t. the 3-axis, the 4-momentum of a particle is parameterised in terms of the rapidity y, the transverse energy m_T, the transverse momentum p_T and the azimuth angle ϕ, which are given by

$$y := \frac{1}{2} \ln \left(\frac{p^{0} + p^{3}}{p^{0} - p^{3}} \right) \tag{A.23}$$
$$m_T := \sqrt{(p^{0})^{2} - (p^{3})^{2}} \tag{A.24}$$
$$p_T := \sqrt{(p^{1})^{2} + (p^{2})^{2}} \tag{A.25}$$
$$\phi := \operatorname{atan2}\left(p^{2}, p^{1}\right) \in [0, 2\pi), \tag{A.26}$$

where atan2 is the 2-argument arctangent, firstly mentioned w.r.t. the spherical coordinates in definition (A.6). According to these coordinates, the on-shell condition (A.1) is equivalent to the coordinate relation

$$m_T = \sqrt{p_T^{2} + m^{2}}, \tag{A.27}$$

where m denotes the particle's mass. The relation (A.27) is the reason, why m_T is referred as transversal energy of the particle. The transverse coordinates are widely used in the

description of collision experiments in particle physics [286]. The advantage of these coordinates lies in their properties w.r.t. Lorentz boosts along its defining axis (here the 3-axis). As it turns out, all transverse coordinates except the rapidity are invariant under such boost transformations. The rapidity itself is additive w.r.t. the boost from one system to another, i.e. the rapidity in a new system is given by $y' = y + y_S$, where y ist the particle rapidity in the old system and y_S denotes the relative rapidity the systems move w.r.t. each other. This leads to an easy understanding of Lorentz invariant observables in different systems: to get a certain invariant quantity in another system, one only needs to shift (i.e. rescale) the respective distribution along its rapidity axis by the relative rapidity y_S between the systems, where the shape of the distribution itself, expressed in the other transverse coordinates, remains unchanged.
The inverse transformation from transverse to cartesian coordinates reads

$$p^0 = m_T \cosh y, \tag{A.28}$$

$$p^1 = p_T \cos\phi, \tag{A.29}$$

$$p^2 = p_T \sin\phi, \tag{A.30}$$

$$p^3 = m_T \sinh y, \tag{A.31}$$

where the invariant phase space integral measure transformed to transverse coordinates results in

$$(2\pi)^3 \,\mathrm{d}\Phi_1 = \frac{p_T}{2}\,\mathrm{d}y\,\mathrm{d}p_T\,\mathrm{d}\phi. \tag{A.32}$$

Transformation between the coordinate systems

Using the definitions of the coordinate systems in terms of the Cartesian coordinates as well as their respective inverse transform within the section above, one can easily derive the transform between each coordinate system via bypassing: old coordinates → Cartesian coordinates → new coordinates. In table A.1 we depicted the respective coordinate transforms, where the columns denote the original coordinates and the respective row the target coordinate system. The coordinate transforms are given in the general formulation suitable for either on- or off-shell particle, respectively. For the special case of an on-shell momentum, the respective coordinate transform eventually becomes simpler due to relations between the coordinates. The respective Jacobian determinants necessary

Table A.1: Coordinate transforms between spherical, light-cone and transverse coordinates, respectively. The top row denotes the source coordinates and the first column denotes the target coordinates. The coordinate systems are defined in section A.2.

	spherical	light-cone	transverse
spherical		$E = p^+ + p^-$ $\varrho = ((p^- - p^+)^2 + (p^\perp)^2)^{\frac{1}{2}}$ $\cos\theta = \dfrac{p^+ - p^-}{\varrho}$ $\phi = \operatorname{atan2}(p^y,p^x)$	$E = m_T \cosh y$ $\varrho = \sqrt{(p_T^2 + m_T^2 \sinh^2 y)}$ $\cos\theta = \dfrac{m_T}{\varrho} \sinh y$ $\phi_{\text{sph}} = \phi_{\text{trans}}$
light-cone	$p^- = \dfrac{1}{2}(E - \varrho\cos\theta)$ $p^x = \varrho \sin\theta \cos\phi$ $p^y = \varrho \sin\theta \sin\phi$ $p^+ = \dfrac{1}{2}(E + \varrho\cos\theta)$		$p^- = \dfrac{m_T}{2} e^{-y}$ $p^x = p_T \cos\phi$ $p^y = p_T \sin\phi$ $p^+ = \dfrac{m_T}{2} e^{y}$
transverse	$y = \tanh^{-1}\left(\dfrac{\varrho\cos\theta}{E}\right)$ $m_T = \sqrt{E^2 - \rho^2\cos^2\theta}$ $p_T = \varrho\sin\theta$ $\phi_{\text{trans}} = \phi_{\text{sph}}$	$y = \dfrac{1}{2}\ln\left(\dfrac{p^+}{p^-}\right)$ $m_T = \sqrt{4p^+p^-}$ $p_T = \sqrt{(p^x)^2 + (p^y)^2}$ $\phi = \operatorname{atan2}(p^y,p^x)$	

for the transformation of the invariant phase space integral measures are given as

$$\Theta(p^-)\,\mathrm{d}p^-\,\mathrm{d}^2p^\perp = \varrho p^-(E,\theta)\,\mathrm{d}E\,\mathrm{d}\cos\theta\,\mathrm{d}\phi \qquad \text{(light-cone} \to \text{spherical)}, \tag{A.33}$$

$$\Theta(p^-)\,\mathrm{d}p^-\,\mathrm{d}^2p^\perp = p^-(y,p_T)p_T\,\mathrm{d}y\,\mathrm{d}p_T\,\mathrm{d}\phi \qquad \text{(light-cone} \to \text{transverse)}, \tag{A.34}$$

$$\mathrm{d}E\,\mathrm{d}\cos\theta\,\mathrm{d}\phi = \frac{p_T}{\varrho(y,p_T)}\,\mathrm{d}y\,\mathrm{d}p_T\,\mathrm{d}\phi \qquad \text{(spherical} \to \text{transverse)}, \tag{A.35}$$

where the Jacobians of the inverse transformations simply result from the reciprocal expressions.

A.3 Frames of reference

Within this thesis, we mostly investigate processes of the form $2 \to N$ with two incoming and N outgoing particles. In this section we outline the frames of reference the incoming particles are described in. However, due to global energy-momentum conservation during an examined process, the phase space distribution of the outgoing particles depend on the choice of the frame of reference.

Let $p_A^\mu = (E_A, \underline{p}_A)$ and $p_B^\mu = (E_B, \underline{p}_B)$ be the 4-momenta of the two incoming particles A and B, respectively, where these particles are on-shell, i.e. $E_i = \sqrt{\underline{p}_i^2 + m_i}$ with $i = A,B$. In particle physics, an important parameter to describe two-particle scattering is the Mandelstam-s [108, 182, 235], which is defined by

$$s = (p_A + p_B)^2 = (E_A + E_B)^2 - (\underline{p}_A + \underline{p}_B)^2 = m_A^2 + m_B^2 + 2(E_A E_B - \underline{p}_A \underline{p}_B), \tag{A.36}$$

where the square in the first equation is performed w.r.t. the Minkowski metric, which makes the Mandelstam-s a Lorentz scalar. We mention, due to $E_i \geq m_i$ for $i = A, B$, the Mandelstam-s obeys $s \geq (m_A + m_B)^2$. Within this thesis, as well as commonly in particle physics, we often use $\sqrt{s}$ as the parameter instead the Mandelstam-s itself and refer $\sqrt{s}$ as the center-of-momentum energy of the incoming particles.

The relation between s, p_A and p_B becomes eventually simpler, if one chooses a special frame of reference for the 4-momenta p_A^μ, p_B^μ. However, an important feature is, the change of the frame may change the relation of the Mandelstam-s to the momentum coordinates, but not the value of s due to its Lorentz invariance.

One particle at rest: the laboratory system

Within this thesis, we refer to a frame of reference as laboratory frame (shortly: lab frame), where one of the scattering partners is at rest. Without loss of generality we choose the particle B to be at rest, i.e.

$$\underline{p}_B^{\text{lab}} = \underline{0}, \tag{A.37}$$

where this implies $E_B^{\text{lab}} = m_B$, due to the on-shell condition. The Mandelstam-s from equation (A.36) results in this frame as $s = m_A^2 + m_B^2 + 2m_B E_A^{\text{lab}}$. This implies the energy of particle A only depends on the particle masses and the Mandelstam-s:

$$E_A^{\text{lab}} = \frac{s - m_A^2 - m_B^2}{2m_B}. \tag{A.38}$$

We mention, equation (A.38) is in our case only reasonable, if $m_B \neq 0$, which means the lab frame is only well defined w.r.t. a massive particle. However, there are exceptions, e.g. the infinite momentum frame used in hadron physics, but this is beyond the ambition of this thesis.

Since there is kinematically no other spatial direction given in the lab frame except the direction of $\underline{p}_A$, we can without loss of generality choose the 3-vector $\underline{p}_A$ to lie along the 3-axis, which yields for the 4-momenta of the incoming particles as

$$p_A^\mu\Big|_{\text{lab}} = \Big(E_A^{\text{lab}}(s), 0, 0, \varrho_A^{\text{lab}}(s)\Big)\,, \tag{A.39}$$

$$p_B^\mu\Big|_{\text{lab}} = (m_B, 0, 0, 0)\,, \tag{A.40}$$

where $\varrho_A^{\text{lab}} = \sqrt{(E_A^{\text{lab}})^2 - m_A^2}$ and the energy is given by equation (A.38). This shows the importance of the Mandelstam-s: the incoming momenta in the lab frame only depend on the masses and the Mandelstam-s.

Vanishing total 3-momentum: the center-of-momentum frame

Another often used frame of reference is the center-of-momentum frame, where the total 3-momentum of the incoming particles vanish:

$$\underline{p}_A^{\text{cms}} + \underline{p}_B^{\text{cms}} = \underline{0}. \tag{A.41}$$

This leads to a relation between both energies of the incoming particles:

$$E_B^{\text{cms}} = \sqrt{(E_A^{\text{cms}})^2 - m_A^2 + m_B^2}. \tag{A.42}$$

In this case, the Mandelstam-s reads:

$$s = (E_A^{\text{cms}} + E_B^{\text{cms}})^2\,, \tag{A.43}$$

which is the reason, why the quantity $\sqrt{s}$ is referred as center-of-momentum energy, i.e. it is the total energy of the incoming particles w.r.t. the center-of-momentum frame. Using (A.43), the energies of particles A and B in the center-of-momentum frame only depend on the masses and the Mandelstam-s:

$$E_A^{\text{cms}} = \frac{s + m_A^2 - m_B^2}{2\sqrt{s}}, \tag{A.44}$$

$$E_B^{\text{cms}} = \frac{s + m_B^2 - m_A^2}{2\sqrt{s}}. \tag{A.45}$$

Since the defining equation (A.41) is only satisfiable if the 3-momenta $\underline{p}_A, \underline{p}_B$ lying along the same axis, i.e. the particles are either co- or counter propagating, we can choose without loss of generality the 3-direction as the propagation axis. Consequently, the 4-momenta of the two incoming particles result in the center-of-momentum frame as

$$p_A^\mu\Big|_{\text{cms}} = \left(E_A^{\text{cms}}(s), 0, 0, \varrho_A^{\text{cms}}(s)\right), \tag{A.46}$$

$$p_B^\mu\Big|_{\text{cms}} = \left(E_B^{\text{cms}}(s), 0, 0, \varrho_B^{\text{cms}}(s)\right), \tag{A.47}$$

where $\varrho_i^{\text{cms}}(s) = \sqrt{(E_i^{\text{cms}}(s))^2 - m_i^2}$ for $i = A, B$ and the energies expressed in terms of the Mandelstam-s are given in the equations (A.44) and (A.45).

Transition between lab and center-of-momentum frame

Since the Mandelstam-s (with that also the center-of-mass energy $\sqrt{s}$) is a Lorentz scalar, one may directly derive a relation of lab and center-of-momentum quantities. However, within this thesis, this is not necessary, because the investigated observable quantities, e.g. cross sections, are also Lorentz invariant, hence the relation between the energies of the incoming particles to $\sqrt{s}$ depends on the frame, albeit the relation of $\sqrt{s}$ to the respective quantity is independent to the choice of the frame of reference. Although we note, that the dependence of the investigated quantity to the phase space coordinates of the outgoing particles may depend on the frame of reference due to the global energy-momentum conservation.

A.4 Kinematics of $2 \to 3$ processes

Within this section, we outline some useful kinematical relations for the scattering of one photon with momentum k and one electron with momentum p producing three outgoing fermions, as encountered in the (perturbative) trident process (see appendix C and the references given there). Since the electrons and the positron in the final state are kinematically equivalent, we refer the outgoing particles as A (with four-momentum p_a), B (with four-momentum p_b), and C (with four-momentum p_c), respectively, without distinguishing the kind of fermion these momenta describe. Then the external momenta obey the global energy-momentum conservation

$$p + k = p_a + p_b + p_c, \tag{A.48}$$

where we refer to $p_t := p + k$ as the total momentum transferred through the process.

The invariant three-body phase space integral measure

We assume the external particles to obey the on-shell condition (A.1) as well as having the same masses, i.e. $m_a = m_b = m_c = m$, where m denotes the electron mass. Then the invariant physical 3-particle phase space integral measure reads

$$\begin{aligned} \mathrm{d}\Phi_3^{\text{phys}} &:= (2\pi)^4\, \delta^{(4)}(p + k - p_a - p_b - p_c)\ \mathrm{d}\Phi_3 && \text{(A.49)} \\ &= \delta^{(4)}(p + k - p_a - p_b - p_c)\, \frac{1}{(2\pi)^5} \frac{\mathrm{d}^3 p_a}{2E_a} \frac{\mathrm{d}^3 p_b}{2E_b} \frac{\mathrm{d}^3 p_c}{2E_c} && \text{(A.50)} \\ &= \frac{1}{4\,(2\pi)^5} \frac{\mathrm{d}^3 p_a\, \mathrm{d}^3 p_b}{E_a E_b} \delta(p_c^2 - m^2)\Theta(E_c)\Big|_{p_c = p_t - p_a - p_b}, && \text{(A.51)} \end{aligned}$$

where E_i with $i = a, b, c$ denotes the energy of the respective particle. In the last step we used $\frac{\mathrm{d}^3 p_c}{2E_c} = \mathrm{d}^4 p_c \delta(p_c^2 - m^2)\Theta(E_c)$ with the Heaviside step-function Θ and integrated over $\mathrm{d}^4 p_c$ applying the delta-distribution in equation (A.50). Using spherical coordinates (see section A.2), the physical phase space integral measure ensues from equation (A.51) as

$$\mathrm{d}\Phi_3^{\text{phys}} = \frac{\varrho_a \varrho_b}{4\,(2\pi)^5} \mathrm{d}E_a\, \mathrm{d}\cos\theta_a\, \mathrm{d}\phi_a\, \mathrm{d}E_b\, \mathrm{d}\cos\theta_b\, \mathrm{d}\phi_b\, \delta(p_c^2 - m^2)\Theta(E_c)\Big|_{p_c = p_t - p_a - p_b}. \tag{A.52}$$

Without loss of generality we assume the spatial components $\underline{p}_t$ of the total momentum $p + k = p_t =: (E_t, \underline{p}_t)$ is aligned along the 3-axis, which causes the polar angles θ_i and the azimuthal angles φ_i with $i = a, b, c$ to be defined w.r.t the axis defined along $\underline{p}_t$. As an example, the schematic figure A.1 displays the three-momenta involved in a 2 → 3 process in spherical coordinates in the special case of the laboratory system of the initial electron, which was defined in section A.3.

According to the delta-distribution in equation (A.52), there is an additional condition for the remaining coordinates, which leads to a relation of one coordinate, say ϕ_b, to the other coordinates $\xi := (E_a, \cos\theta_a, \phi_a, E_b, \cos\theta_b)$. Using the abbreviation $h(\phi_b|\xi) := p_c^2(\phi_b|\xi) - m^2$, where the coordinates ξ are assumed to be fixed and applying the energy-momentum conservation $p_c = p_t - p_a - p_b$, the condition due to the remaining delta-function in equation (A.52) is equivalent to

$$0 = h(\phi_b|\xi) = p_t^2 + m^2 + 2\,(p_a p_b - p_t p_a - p_t p_b)\,. \tag{A.53}$$

Since the terms $p_t p_a$ and $p_t p_a$ are not dependent on ϕ_b, we mention $p_a p_b = E_a E_b - \varrho_a \varrho_b \cos\theta_{ab}$, where θ_{ab} denotes the angle between $\underline{p}_a$ and $\underline{p}_b$. According to the assumption to define the angles of the particles w.r.t. the total three-momentum $\underline{p}_t$, one has $\cos\theta_{ab} =$

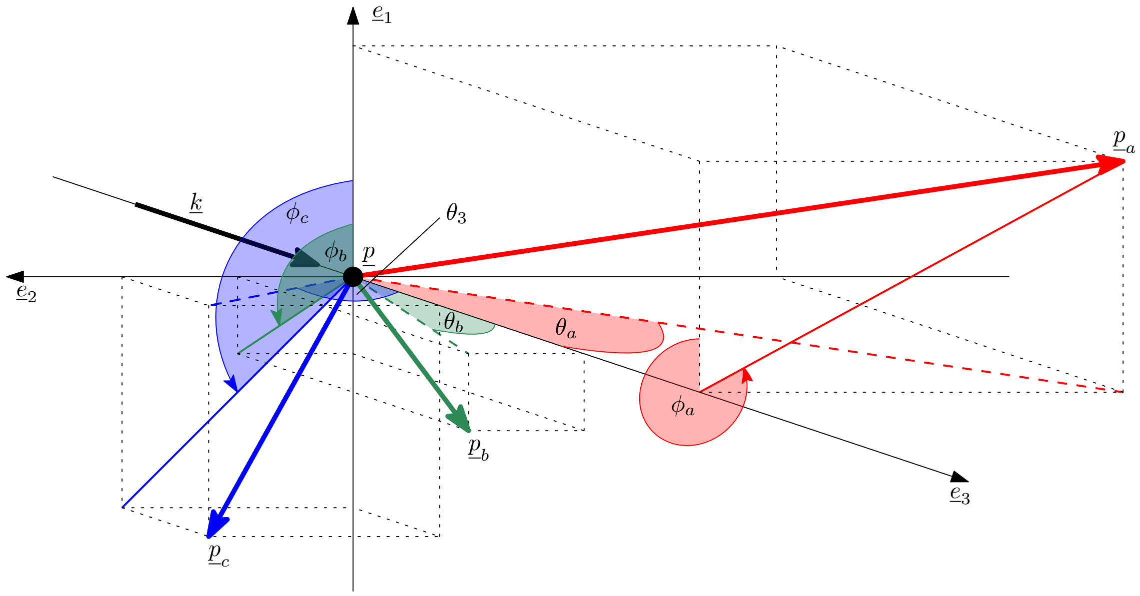

Figure A.1: Schematic illustration of the three-momenta during a 2 → 3 scattering of a photon and an electron in the rest frame of the latter in spherical coordinates. The momenta of the incoming photon is represented by the black arrow aligned along the 3-axis and the target electron is situated at the point of origin, represented by a black dot. The three-momenta of the outgoing particles are represented by coloured arrows (red: $\underline{p}_a$, green: $\underline{p}_b$, blue: $\underline{p}_c$), where the respective polar angle is assigned between the projection of the three-momentum on the $(2,3)$-plane (coloured dashed line) and the 3-axis. The respective azimuthal angle is assigned between the projection of the three-momentum on the $(1,2)$-plane (thin coloured solid line) and the 1-axis. The longitudes of the depicted arrows are not correctly scaled.

$\cos\theta_a\cos\theta_b + \sin\theta_a\sin\theta_b\cos(\phi_b - \phi_a)$. Therefore the condition (A.53) results in

$$0 = h(\phi_b|\xi) = a_1(\xi) - b_1(\xi)\cos(\phi_b - \phi_a), \tag{A.54}$$

where the coefficients are given as

$$a_1 = p_t^2 + m^2 - 2p_t(p_a + p_b) + 2(E_aE_b - \rho_a\rho_b\cos\theta_a\cos\theta_b), \tag{A.55}$$

$$b_1 = 2\rho_a\rho_b\sin\theta_a\sin\theta_b. \tag{A.56}$$

Consequently, the equation (A.54) has two solutions given as

$$\phi_b^{(1)} = \arccos\left(\frac{a_1}{b_1}\right) + \phi_a, \qquad \phi_b^{(2)} = 2\pi - \arccos\left(\frac{a_1}{b_1}\right) + \phi_a, \tag{A.57}$$

where $\phi_b^{(1)}, \phi_b^{(2)}$ denote the physical values of ϕ_b for a given set of coordinates $\xi = (E_a, \cos\theta_a, \phi_a, E_b, \cos\theta_b)$. Furthermore, one has $\frac{\partial h(\phi_b|\xi)}{\partial \phi_b} = -b_1 \sin(\phi_b - \phi_a)$, which leads to

$$\left|\frac{\partial h(\phi_b|\xi)}{\partial \phi_b}\right|_{\phi_b=\phi_b^{(1)}} = \left|\frac{\partial h(\phi_b|\xi)}{\partial \phi_b}\right|_{\phi_b=\phi_b^{(2)}} = \sqrt{b_1^2 - a_1^2}, \tag{A.58}$$

where we applied the identity $\sin(\arccos(x)) = \sqrt{1-x^2}$. Summarising, the physical three-body phase space integral measure (A.52) results in

$$\mathrm{d}\Phi_3^{\mathrm{phys}} = \frac{\varrho_a \varrho_b}{4\,(2\pi)^5} \frac{\mathrm{d}E_a \,\mathrm{d}\cos\theta_a \,\mathrm{d}\phi_a \,\mathrm{d}E_b \,\mathrm{d}\cos\theta_b \,\mathrm{d}\phi_b}{\sqrt{b_1^2 - a_1^2}} \left(\delta(\phi_b - \phi_b^{(1)}) + \delta(\phi_b - \phi_b^{(2)})\right), \tag{A.59}$$

where the physical values for ϕ_b are given in (A.57) and the coefficients a_1, b_1 are defined in (A.55) and (A.56), respectively. We mention the denominator in equation (A.59) possibly produces a coordinate singularity, which we need to be aware of below.

Boundaries of the physical phase space

We mention, that the physical values for ϕ_b given in equations (A.57) only exist, if the remaining coordinates $\xi = (E_a, \cos\theta_a, \varphi_a, E_b, \cos\theta_b)$ fulfil the condition

$$\left|\frac{a_1(\xi)}{b_1(\xi)}\right| \leq 1, \tag{A.60}$$

where a_1, b_1 are given in equations (A.55) and (A.56), respectively. This condition restricts the allowed values of all coordinates ξ and defines the physical phase space of the $2 \to 3$ process. The condition (A.60) leads to $a_1^2 - b_1^2 \leq 0$, which is for fixed E_a, E_b and $\cos\theta_b$ equivalent to a conditional equation for the coordinate $\cos\theta_a$:

$$0 \geq a_2 \cos^2\theta_a + b_2 \cos\theta_a + c_2, \tag{A.61}$$

where we define the coefficients as

$$a_2 = 4\varrho_a^2 \left(\varrho_t^2 + \varrho_b^2 - 2\varrho_t\varrho_b\cos\theta_b\right), \tag{A.62}$$

$$b_2 = 4\varrho_a \left(\varrho_t - \varrho_b\cos\theta_b\right)\left(p_t^2 + m^2 - 2(p_t p_b) + 2E_aE_b - 2E_aE_t\right), \tag{A.63}$$

$$c_2 = \left(p_t^2 + m^2 - 2(p_t p_b) + 2E_aE_b - 2E_aE_t\right)^2 - 4\varrho_a^2\varrho_b^2\sin^2\theta_b, \tag{A.64}$$

where $\varrho_t = |\underline{p}_t|$. Assuming $a_2 \neq 0$, the inequality (A.61) yields

$$\min(\cos\theta_a^-, -1) \leq \cos\theta_a \leq \max(\cos\theta_a^+, 1) \tag{A.65}$$

where $\cos\theta_a^-, \cos\theta_a^+$ denote the lower and upper boundary of the coordinate $\cos\theta_a$, respectively, which are given by

$$\cos\theta_a^\pm := \frac{1}{2a_2}\left(-b_2 \pm \sqrt{b_2^2 - 4a_2c_2}\right). \tag{A.66}$$

Since these boundaries are assumed to be real values, the radicand of the definition (A.66) must be positive, which leads to a restriction of the coordinate $\cos\theta_b$, if the energies E_a, E_b as well as the momenta of the incoming particles are fixed:

$$\min(\cos\theta_b^-, -1) \leq \cos\theta_b \leq \max(\cos\theta_b^+, 1), \tag{A.67}$$

where $\cos\theta_b^+, \cos\theta_b^-$ denote the upper and lower boundary of $\cos\theta_b$, respectively, which result in

$$\cos\theta_b^\pm := \frac{1}{2a_3}\left(-b_3 \pm \sqrt{b_3^2 - 4a_3c_3}\right). \tag{A.68}$$

$$\tag{A.69}$$

The occurring coefficients are given as

$$a_3 = \varrho_b\varrho_t^2, \tag{A.70}$$

$$b_3 = 2\varrho_t\varrho_b\left(\varrho_a^2 + d_3\right), \tag{A.71}$$

$$c_3 = -\varrho_a^2\varrho_t^2 + \varrho_a^2\varrho_b^2 + d_3^2, \tag{A.72}$$

$$d_3 = \frac{p_t^2 + m^2}{2} - E_t(E_a + E_b) + E_aE_b. \tag{A.73}$$

Again we assume the boundaries of $\cos\theta_b$ to be real values, i.e. the radicand of definition (A.68) must be positive, which results in a constraint for the energy E_a:

$$\min(E_a^-, m) \leq E_a \leq E_a^+, \tag{A.74}$$

where the boundaries of E_a result to

$$E_a^{\pm} := \frac{1}{2}\left(E_t - E_b \pm (\varrho_t - \varrho_b)\sqrt{1 - \frac{4m^2}{d_4}}\right), \tag{A.75}$$

with the abbreviation $d_4 = p_t^2 + m^2 - 2E_tE_b + 2\varrho_t\varrho_b$. The positivity of the radicand of definition (A.75) yields a constraint for E_b:

$$\min(E_b^-,m) \leq E_b \leq E_b^+, \tag{A.76}$$

where the boundaries only depend on the momenta of the incoming particles and are given as

$$E_b^{\pm} := \frac{1}{2p_t^2}\left(E_t(p_t^2 - 3m^2) \pm \varrho_t\sqrt{(p_t^2 - m^2)(p_t^2 - 9m^2)}\right). \tag{A.77}$$

Using the definition of the Mandelstam-s given in equation (A.36) as well as the interpretation as the center-of-momentum energy (see equation (A.43)), we mention, the positivity of the radicand in the definition (A.77) leads to the threshold condition:

$$\sqrt{s} = \sqrt{(k+p)^2} = \sqrt{p_t^2} \geq 3m =: \sqrt{s_{\text{th}}}, \tag{A.78}$$

where $\sqrt{s_{\text{th}}}$ is called the threshold of the 2 → 3 process. The existence of this threshold has another simple explanation (cf. [145]). Since the threshold of a 2 → 3 process is defined as the least total energy of the incoming particle (in their center-of-momentum frame; see section A.3) which is needed to produce the outgoing particle. This threshold energy is reached, if all outgoing particles are produced at rest, where all the remaining energy of the outgoing particles is condensed in their masses. According to the assumption from the beginning of this section, we have equal masses of the outgoing particles, the threshold results in $\sqrt{s_{\text{th}}} = 3m$.

Coordinate singularity

As we mentioned earlier, the physical three-body phase space integral measure given in equation (A.59) possibly forms a singularity due to the choice of the coordinate system. First, we want to understand the singularity to be formed in one coordinate, say $\cos\theta_a$, if the other coordinates are assumed to be fixed. Expressed w.r.t. $\cos\theta_a$, the singularity is formed if the radicand of the denominator in equation (A.59) vanished, which yields

$$0 = b_1^2 - a_1^2 = -a_2 \cos^2\theta_a - b_2 \cos\theta_a - c_2, \tag{A.79}$$

where the coefficients a_2, b_2, c_2 are given in the equations (A.62) to (A.64). Since the equation (A.79) happens to be the edge case of the conditional equation (A.61) of the coordinate $\cos\theta_a$, the solution of equation (A.79) are the boundaries $\cos\theta_a^\pm$ of $\cos\theta_a$, which are defined in equation (A.66). This leads to a factorisation of the radicand of the denominator in equation (A.59), where the physical three-body phase space integral measure results in

$$\begin{aligned} \mathrm{d}\Phi_3^{\mathrm{phys}} = {} & \frac{\varrho_a \varrho_b}{4\,(2\pi)^5} \frac{\mathrm{d}E_a \,\mathrm{d}\cos\theta_a \,\mathrm{d}\phi_a \,\mathrm{d}E_b \,\mathrm{d}\cos\theta_b \,\mathrm{d}\phi_b}{\sqrt{a_2 \left(\cos\theta_a^+ - \cos\theta_a\right) \left(\cos\theta_a - \cos\theta_a^-\right)}} \\ & \times \left[\delta\left(\phi_b - \phi_b^{(1)}\right) + \delta\left(\phi_b - \phi_b^{(2)}\right)\right]. \end{aligned} \tag{A.80}$$

Assuming $a_2 \neq 0$ and the other coordinates $E_a, \phi_a, E_b, \cos\theta_b$ to be fixed, i.e. the boundaries $\cos\theta_a^\pm$ are fixed, the singularity is caused by $\cos\theta_a$ reaching its boundaries: $\cos\theta_a \to \cos\theta_a^\pm$. However, since the function $x \mapsto \sqrt{x}$ is integrable on the whole positive real line, there is a transformation in the coordinate $\cos\theta_a$, which regularises the coordinate singularity. As shown in [13], a suitable transformation is given by the Euler substitution:

$$\tau := \frac{\cos\theta_a^+ - \cos\theta_a}{\cos\theta_a - \cos\theta_a^-}, \tag{A.81}$$

where the $\cos\theta_a$-dependent part of the physical three-body phase space integral measure results in

$$\frac{\mathrm{d}\cos\theta_a}{\sqrt{\left(\cos\theta_a^+ - \cos\theta_a\right)\left(\cos\theta_a - \cos\theta_a^-\right)}} = \frac{2\,\mathrm{d}\tau}{1+\tau^2}. \tag{A.82}$$

Here the boundaries of the Euler coordinate τ result to

$$\tau \to \infty \qquad \left(\Leftrightarrow \cos\theta_a \to \cos\theta_a^-\right), \tag{A.83}$$

$$\tau \to 0 \qquad \left(\Leftrightarrow \cos\theta_a \to \cos\theta_a^+\right). \tag{A.84}$$

Finally the physical three-body phase space integral measure of a 2 → 3 process results in

$$\mathrm{d}\varPhi_3^{\mathrm{phys}} = \frac{\varrho_a \varrho_b}{2\,(2\pi)^5} \frac{\mathrm{d}E_a\,\mathrm{d}\tau\,\mathrm{d}\phi_a\,dE_b\,\mathrm{d}\cos\theta_b\,\mathrm{d}\phi_b}{\sqrt{a_2}(1+\tau^2)} \left[\delta\left(\phi_b - \phi_b^{(1)}\right) + \delta\left(\phi_b - \phi_b^{(2)}\right)\right], \tag{A.85}$$

where the coefficient a_2 is defined in equation (A.62). This integral measure is essentially 5-dimensional due to the delta-distributions w.r.t. ϕ_b and finite due to the introduction of the Euler coordinate τ defined in equation (A.81).

Transformation to transverse coordinates

Since the transverse coordinates (see section A.2) are widely used within this thesis due to the simple behavior under Lorentz boosts w.r.t. the beam axis, here we summarise some relation similar to those derived above in spherical coordinates, but here for transverse coordinates. The latter are given by the rapidity y_i, the transverse momentum p_{Ti} and the azimuthal angle ϕ_i of the respective particle $i = a, b, c$. First we recapitulate that all constraints derived for spherical coordinates are based on a single delta-distribution in the three-body invariant phase space measure (A.51):

$$0 \overset{!}{=} p_c^2 - m^2, \tag{A.86}$$

combined with the relation $p_c = p_t - p_a - p_b$, where $p_t = p + k$ denotes the total four-momentum of the incoming particles. Since this is independent of the choice of the coordinate systems, one can evaluate the condition (A.86) obtained from the mentioned delta-distribution directly in transverse coordinates. Accordingly, for the fixed values of the azimuthal angle ϕ_b, the version of equation (A.57) in transverse coordinates reads

$$\phi_b^{(1)} = \arccos\left(\frac{\tilde{a}_1}{\tilde{b}_1}\right) + \phi_a, \qquad \phi_b^{(1)} = 2\pi - \arccos\left(\frac{\tilde{a}_1}{\tilde{b}_1}\right) + \phi_a, \tag{A.87}$$

where the coefficients are given by

$$\begin{aligned} \tilde{a}_1 &= p_t^2 + m^2 - 2m_{Ta}\left(E_t \cosh(y_a) - \varrho_t \sinh(y_a)\right) \\ &\quad - 2m_{Tb}\left(E_t \cosh(y_b) - \varrho_t \sinh(y_b)\right) \\ &\quad + 2m_{Ta}m_{Tb}\cosh(y_a - y_b), &\text{(A.88)} \\ \tilde{b}_1 &= 2p_{Ta}p_{Tb}. &\text{(A.89)} \end{aligned}$$

Here $m_T := \sqrt{p_T^2 + m^2}$ denotes the transverse energy and the quantities related to the incoming total momentum are given in the laboratory system by $p_t^2 = s$, $E_t = \frac{s+m^2}{2m}$ and $\varrho_t = \frac{s-m^2}{2m}$, where s is the already mentioned Mandelstam variable. Similarly, one can obtain all boundaries of the transverse coordinates as derived above in spherical coordinates. For instance, one has $p_{Tb}^- \leq p_{Tb} \leq p_{Tb}^+$, there the boundaries for the transverse momentum p_{Tb} yield

$$p_{Tb}^{\pm} = \frac{\tilde{a}_2\tilde{c}_2 \pm \sqrt{\tilde{a}_2^2\tilde{b}_2^2 - \tilde{b}_2^4 + \tilde{c}_2^2\tilde{b}_2^2}}{\tilde{b}_2^2 - \tilde{c}_2^2}. \tag{A.90}$$

Here the coefficients are given as

$$\tilde{a}_2 = p_t^2 + m^2 - 2m_{Ta}\left(E_t\cosh(y_a) - \varrho_t\sinh(y_a)\right), \tag{A.91}$$

$$\tilde{b}_2 = -2\left(E_t\cosh(y_b) - \varrho\sinh(y_2)\right) + 2m_{Ta}\cosh(y_a - y_b), \tag{A.92}$$

$$\tilde{c}_2 = -2p_{Ta}. \tag{A.93}$$

Furthermore, instead of the azimuthal angle ϕ_b it is sometimes convenient to fix another coordinate, say p_{Tb}, especially if one is interested in the azimuthal dependence w.r.t. the particle b. Therefore, assuming a fixed set of coordinates $(y_a, p_{Ta}, \phi_a, y_b, \phi_b)$, the values of p_{Tb} in order to fulfil the condition (A.86) are given as

$$p_{Tb}^{(1,2)} = \frac{\tilde{a}_3\tilde{c}_3 \pm \sqrt{\tilde{a}_3^2\tilde{b}_3^2 - \tilde{b}_3^4 + \tilde{c}_3^2\tilde{b}_3^2}}{\tilde{b}_3^2 - \tilde{c}_3^2}, \tag{A.94}$$

where the coefficients $\tilde{a}_3 = \tilde{a}_2, \tilde{b}_3 = \tilde{b}_2$, are the same as for the boundaries of p_{Tb} in the fixed-ϕ_b case and the coefficient $\tilde{c}_3$ is given as $\tilde{c}_3 = -2p_{Ta}\cos(\phi_b - \phi_a)$. Note that these are fixed values for p_{Tb} and not boundaries as derived above, i.e. in the three-body invariant integral measure, there are in this case delta-distributions $\delta\left(p_{Tb} - p_{Tb}^{(1)}\right) + \delta\left(p_{Tb} - p_{Tb}^{(2)}\right)$, similar to those in equation (A.59).

Finally, we mention that in practice, especially if one integrates over all momentum components of one particle, it is more convenient to perform the occurring integrals in spherical coordinates as well as using the mentioned Euler substitution (A.81) in order to improve numerical stability and transform the remaining coordinate dependence to transverse coordinates afterwards.

B | Feynman rules of QED

Within this section, we summarise the Feynman rules of the perturbative monochromatic QED. Therefore, in table B.1 we listed the respective Feynman rules in momentum space as used within this thesis, for instance to derive the matrix element of the perturbative monochromatic trident (see section C). Excluding the vertex, these rules are also appearing to some extent as the momentum space rules in strong-field and pulsed-perturbative QED (see section 2.3 and 3.2). In order to numerically compute probabilities using the rules listed in table B.1, we displayed the explicitly used formulas in the second column, where the respective spinor bases are given by

$$\eta_1 = (1,0,0,0)^T, \qquad \eta_2 = (0,1,0,0)^T, \tag{B.1}$$

$$\chi_1 = (0,0,1,0)^T, \qquad \chi_2 = (0,0,0,1)^T. \tag{B.2}$$

The respective fundamental bi-spinors obey the Dirac equation in momentum space:

$$0 = (\not{p} - m)u_{\sigma p}, \quad 0 = \overline{u}_{\sigma p}(\not{p} - m), \quad 0 = (\not{p} + m)v_{\sigma p}, \quad 0 = \overline{v}_{\sigma p}(\not{p} + m). \tag{B.3}$$

The used polarisation vectors are given by

$$\epsilon_1^\mu = (0,1,0,0), \qquad \epsilon_2^\mu = (0,0,1,0), \tag{B.4}$$

for the incoming photon, and

$$\epsilon_1'^\mu = (0, \cos\theta' \cos\phi', \cos\theta' \sin\phi', -\sin\theta'), \tag{B.5}$$

$$\epsilon_2'^\mu = (0, -\sin\phi', \cos\theta', 0), \tag{B.6}$$

for the outgoing photon, where θ', ϕ' denote the polar and azimuthal angle of the momentum $\underline{k}'$ of the outgoing photon in spherical coordinates. Additionally, we deployed the Feynman slash notation $\not{a} = \gamma^\mu a_\mu$, where γ^μ denote the Dirac gamma matrices, which obey the

Table B.1: Momentum space rules of perturbative monochromatic QED (e.g. from [236]). In the first column the diagrammatical representation of the respective rule is depicted, in the second column the mathematical expression used within this thesis is shown, the third column indicates the common name of the expression.

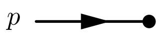	$u_{\sigma p} = \frac{\not p+m}{\sqrt{\lvert p_0\rvert+m}}\eta_\sigma$	incoming fermion
	$\overline{v}_{\sigma p} = v^\dagger_{\sigma p}\gamma^0$	incoming anti-fermion
	$\overline{u}_{\sigma p} = u^\dagger_{\sigma p}\gamma^0$	outgoing fermion
	$v_{\sigma p} = \frac{-\not p+m}{\sqrt{\lvert p_0\rvert+m}}\chi_\sigma$	outgoing anti-fermion
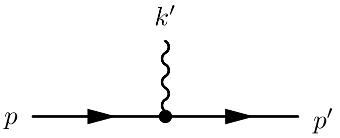	$-ie\gamma^\mu$	QED vertex
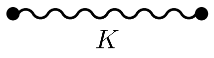	$D_{\mu\nu}(K) = \frac{ig_{\mu\nu}}{K^2+i\epsilon}$	photon propagator
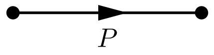	$S(P) = \frac{i(\not P+m)}{P^2-m^2+i\epsilon}$	fermion propagator
	$\varepsilon'^{\mu}_{\lambda}(k')$	incoming photon
	$\varepsilon'^{*\mu}_{\lambda}(k')$	outgoing photon

Clifford algebra $\{\gamma^\mu, \gamma^\nu\} = 2g^{\mu\nu}$ with the Minkowski metric $g_{\mu\nu} = \mathrm{diag}(1,-1,-1,-1)$. For numerical calculations, we used the gamma matrices in its Dirac representation

$$\gamma^0 = \begin{pmatrix} 1 & 0 & 0 & 0 \\ 0 & 1 & 0 & 0 \\ 0 & 0 & -1 & 0 \\ 0 & 0 & 0 & -1 \end{pmatrix}, \qquad \gamma^1 = \begin{pmatrix} 0 & 0 & 0 & -1 \\ 0 & 0 & -1 & 0 \\ 0 & 1 & 0 & 0 \\ 1 & 0 & 0 & 0 \end{pmatrix}, \tag{B.7}$$

$$\gamma^2 = \begin{pmatrix} 0 & 0 & 0 & i \\ 0 & 0 & -i & 0 \\ 0 & -i & 0 & 0 \\ i & 0 & 0 & 0 \end{pmatrix}, \qquad \gamma^3 = \begin{pmatrix} 0 & 0 & -1 & 0 \\ 0 & 0 & 0 & -1 \\ 1 & 0 & 0 & 0 \\ 0 & 1 & 0 & 0 \end{pmatrix}. \tag{B.8}$$

For further details on the usage of these Feynman rules and their properties the reader is referred to the common text books on quantum field theory, e.g. [25, 107, 139, 145, 179, 236, 253, 282, 308, 309].

C | Perturbative trident pair production

Within this thesis, we refer to as perturbative trident pair production the collision of a single photon with an electron causing the production of one positron as well as two electrons $\gamma + e^- \to e^+ + e^- + e^-$ in the framework of perturbative quantum electrodynamics. As the infinite plane-wave limit of pulsed-perturbative trident, therefore as the simultaneous infinite plane-wave and weak-field limit of strong-field trident, the perturbative trident pair production plays a crucial role for the understanding of the more general cases, both kinematically and on the level of (differential) cross sections.

The investigation of perturbative trident has a long history. Starting with the pioneering work of [32, 33, 96, 118–120, 144, 160, 197, 198, 284, 302, 303, 306] and others (see the reviews [200] and [147] as well as [145]) to comprehend the upcoming quantum electrodynamics by calculating higher-order tree-level processes and to develop a variety of approximations of the perturbative trident differential and total cross sections. Furthermore, there are also more recent investigations of perturbative trident in the context of astrophysical questions [13, 55, 56, 138, 184, 185, 239], related to polarisation effects [13, 31, 49, 93, 95], as well as possible dark-photon capabilities [94].

Since the perturbative trident is used within this thesis as a verification limit of more general treatments (pulsed-perturbative and strong-field trident), we outline the calculations of cross sections including all encountered contributions, i.e. without any approximations except the tree-level approach of perturbative QED.

C.1 Matrix element and cross section

The perturbative trident process is described on tree-level by the Feynman diagrams depicted in figure C.1, where p, k denote the momenta of the incoming electron and photon, respectively, p_1 is the momenta of the outgoing positron and p_2, p_3 are the momenta of the two outgoing electrons. The first pair of Feynman diagrams depicted in figure

C.1(a) are called virtual Compton diagrams, due to their similarity to the perturbative Compton process on tree-level, except the scattered photon stays virtual and produces an electron-positron pair. Analogously, the second pair of diagrams in figure C.1(b) are called virtual Breit-Wheeler diagrams, since these are similar to the perturbative Breit-Wheeler process on tree-level, but one of the initial photons is virtual due to the coupling to an additional fermion line. The momenta of the intermediate particles are given by the local energy momentum conservation at each vertex: $k'_{\mathrm{C}} = k''_{\mathrm{C}} = p_1 + p_2$, and $p'_{\mathrm{C}} = p + k, p''_{\mathrm{C}} = p_3 - k$ for the intermediate photons and electrons in the virtual Compton diagrams as well as $k'_{\mathrm{BW}} = k''_{\mathrm{BW}} = p - p_3$, and $p'_{\mathrm{BW}} = k - p_1, p''_{\mathrm{BW}} = p_2 - k$ for the intermediate photons and electrons in the virtual Breit-Wheeler diagrams, respectively. Considering the indistinguishability of the final electrons, there is an additional set of four Feynman diagrams emerging from the diagrams depicted in figure C.1 by the exchange $p_2 \leftrightarrow p_3$, which are also referred the exchange diagrams.

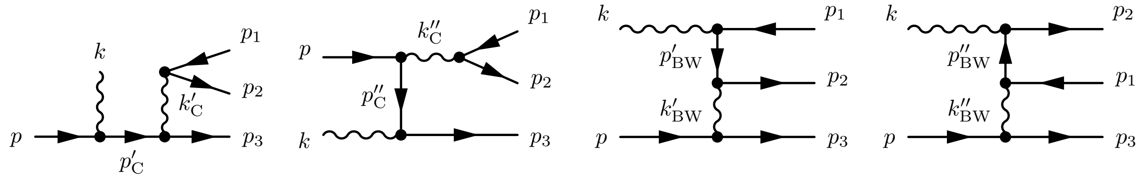

(a) Virtual Compton diagrams. **(b)** Virtual Breit-Wheeler diagrams.

Figure C.1: Feynman diagrams of perturbative trident on tree-level, where p, k, p_1, p_2, p_3 denote the momenta of the initial electron and photon as well as the final positron, and the two final electrons, respectively. The two diagrams C.1(a) on the l.h.s. are referred as the virtual Compton diagrams, where $k'_{\mathrm{C}} = p_1 + p_2, p'_{\mathrm{C}} = p + k$ and $k''_{\mathrm{C}} = p_1 + p_2, p''_{\mathrm{C}} = p_3 - k$ denote the momenta of the intermediate photon and electron, respectively. The two diagrams C.1(b) on the r.h.s. are referred as the virtual Breit-Wheeler diagrams, where $k'_{\mathrm{BW}} = p - p_3, p'_{\mathrm{BW}} = k - p_1$ and $k''_{\mathrm{BW}} = p - p_3, p''_{\mathrm{BW}} = p_2 - k$ denote the momenta of the intermediate photon and electron, respectively. Additionally, the exchange diagrams are given by the substitution $p_2 \leftrightarrow p_3$ w.r.t. the depicted diagrams.

Using the Feynman rules of perturbative QED given in table B.1, the part of matrix element related to the sum of the virtual Compton diagrams C.1(a) is given by

$$M_{\mathrm{C}} = -ie^3 \frac{g_{\mu\tau}}{(p_1 + p_2)^2 + i\epsilon} \left[\overline{u}(p_3)\mathcal{C}^{\mu\nu}(p, p_3|k)u(p)\right] \times \left[\overline{u}(p_2)\gamma^\tau v(p_1)\right] \varepsilon_\nu, \tag{C.1}$$

where we suppress the spins and photon polarisation for now. Here, e is the electric charge of the electron, $g_{\mu\nu}$ the Minkowski metric, ϵ is the regulator of the photon propagator and γ^μ denote the Dirac gamma matrices. The occurring function $\mathcal{C}^{\mu\nu}$ denotes the Compton tensor [145], which is given by

$$\mathcal{C}^{\mu\nu}(q_1,q_2|k) := \frac{\gamma^\mu(\not{q}_1+\not{k}+m)\gamma^\nu}{(q_1+k)^2-m^2+i\epsilon}+\frac{\gamma^\nu(\not{q}_2-\not{k}+m)\gamma^\mu}{(q_1-k)^2-m^2+i\epsilon}, \tag{C.2}$$

where q_1, q_2 are two arbitrary four-momenta, m denotes the electron mass and ϵ is the regulator of the appearing fermion propagators. We use the Feynman slash notation $\not{q} := \gamma^\mu q_\mu$ with an arbitrary four-momentum q^μ. Analogously, the part of the matrix element related to the sum of the virtual Breit-Wheeler diagrams C.1(b) results in

$$M_{\mathrm{BW}} = -ie^3\frac{g_{\mu\nu}}{(p-p_3)^2+i\epsilon}\left[\overline{u}(p_3)\gamma^\mu u(p)\right]\times\left[\overline{u}(p_2)\mathcal{C}^{\nu\tau}(-p_1,p_2|k)v(p_1)\right]\varepsilon_\tau, \tag{C.3}$$

where $\mathcal{C}^{\mu\nu}$ again denotes the Compton tensor given in equation (C.2). The parts of the matrix element related to the respective exchange diagrams ensue from the interchange of the final electron momenta:

$$M_{\mathrm{Cx}} = M_{\mathrm{C}}(p_2\leftrightarrow p_3), \qquad M_{\mathrm{BWx}} = M_{\mathrm{BW}}(p_2\leftrightarrow p_3). \tag{C.4}$$

The full matrix element of perturbative trident on tree-level is then given as

$$M_{\mathrm{pT}} = \frac{1}{2}\left(M_{\mathrm{C}}+M_{\mathrm{BW}}-M_{\mathrm{Cx}}-M_{\mathrm{BWx}}\right), \tag{C.5}$$

where the relative signs between the direct and the exchange parts are a consequence of the Pauli exclusion principle, caused by the exchange of two fermions and the prefactor results from the normalisation of this exchange. Additionally, we mention the crossing symmetry between the virtual Compton and virtual Breit-Wheeler part of the matrix element apparitional in the relations

$$M_{\mathrm{C}} = M_{\mathrm{BWx}}(p\leftrightarrow -p_1, u(p)\leftrightarrow v(p_1)), \qquad M_{\mathrm{Cx}} = M_{\mathrm{BW}}(p\leftrightarrow -p_1, u(p)\leftrightarrow v(p_1)), \tag{C.6}$$

where the mixing between direct and exchange parts is caused by the arbitrary naming convention of the two unchanged final electrons. Consequentially, there is only one independent part of the matrix element, e.g. M_{C}, and the other parts result from M_{C} due to exchange and crossing symmetry.

Using the matrix element given in equation (C.5) the polarisation and spin averaged (fivefold) differential cross section of perturbative trident on tree-level is given as

$$\mathrm{d}\sigma_{\mathrm{pT}} = \frac{1}{4I}\frac{1}{N}\sum_{\text{spins,pols}} |M_{\mathrm{pT}}|^2\,(2\pi)^4\,\delta^{(4)}(p+k-p_1-p_2-p_3)\,\mathrm{d}\varPhi_3, \tag{C.7}$$

where $I = (kp)$ denotes the incident energy flux and $N = \frac{1}{4}$ is the normalisation factor caused by averaging over the spin and polarisation from the incoming electron and photon, respectively. Additionally, we sum over the spins of the final particles, but considering the case of a polarised initial photon, we mention the usage of the normalisation factor $N = \frac{1}{2}$, due to the absence of the polarisation average. Here, $\mathrm{d}\varPhi_3$ denotes the three-particle invariant phase space integral measure given by

$$\mathrm{d}\varPhi_3 := \frac{\mathrm{d}^3p_1}{(2\pi)^3\,2p_1^0}\frac{\mathrm{d}^3p_2}{(2\pi)^3\,2p_2^0}\frac{\mathrm{d}^3p_3}{(2\pi)^3\,2p_3^0}, \tag{C.8}$$

which results from the product of three one-particle measures defined in equation (A.2), i.e. one for each outgoing particle. The treatment of the physical invariant three-body phase space integral measure, i.e. the invariant integral measure $\mathrm{d}\varPhi_3$ combined with the delta-distribution in equation (C.7), is treated in section A.4. Here, we leave the choice, which momentum of p_a, p_b, p_c in equation (A.49) represents which particle in the perturbative trident process, and we will specify the assignment in the respective example. Summarising, the (five-fold) differential cross section of perturbative trident pair production is given in spherical coordinates as

$$\begin{aligned}\mathrm{d}\sigma_{\mathrm{pT}} = \frac{1}{4I}\frac{1}{N}\frac{\varrho_a\varrho_b}{4\,(2\pi)^5}&\sum_{\text{spins,pols}} |M_{\mathrm{pT}}|^2 \\ &\times \left.\frac{\mathrm{d}E_a\,\mathrm{d}\cos\theta_a\,\mathrm{d}\phi_a\,\mathrm{d}E_b\,\mathrm{d}\cos\theta_b}{\sqrt{a_2\left(\cos\theta_a^+ - \cos\theta_a\right)\left(\cos\theta_a - \cos\theta_a^-\right)}}\right|_{\phi_b\in\{\phi_b^{(1)},\phi_b^{(2)}\}},\end{aligned} \tag{C.9}$$

where the boundaries $\cos\theta_a^\pm$ are defined in the equations (A.66) and the physical values $\phi_b^{(1,2)}$ are given in equations (A.57). The boundaries of the remaining coordinates are derived in section A.4.

C.2 Numerical implementation and comparison to literature

Since the analytical structure of the matrix element (C.5) in terms of scalar products of the occurring four-momenta (using the common technics of Casimir's trick and trace technology; cf. [236]) is very extensive (see e.g. [13, 93, 118, 197]), the numerical implementation of the differential cross section (C.9) is very cumbersome. Therefore, we choose a different path and start the implementation on the fundamental level of the occurring mathematical expressions: spinors, matrices and four-vectors. We understand these mathematical objects as abstract multidimensional arrays and use extensive numerical libraries (in our case the python libraries "numpy" and "scipy"; cf. [300, 304]) to manipulate them in a numerical linear algebraic way. This leads directly to numerical representations of the products of spinors, matrices and four-vectors occurring in the matrix element (C.5) and results in a numerical representation of the differential cross section (C.9) depending on the coordinate tuple $(\sqrt{s}, E_a \cos\theta_a, \phi_a, E_b, \cos\theta_b)$. Here, the assignment of those coordinates to the respective particles is optional and can be adjusted to specific cases of distributions. In order to verify this kind of implementation, we compare several distributions given in literature with a recalculation using our numerical code (the respective data we compare with is extracted using a plot digitizer).

As an example, we calculate the double-differential cross section w.r.t. the outgoing positron in spherical coordinates $E_1, \cos\theta_1$ in the rest frame of the initial electron, i.e. the laboratory system defined in section A.3. For this purpose, we assign the general coordinates used in equation (C.9) as $a = 2$ (first final electron), $b = 1$ (final positron) and $c = 3$ (second final electron). Then the double-differential cross section of the final positron is given by the integration of (C.9) over the coordinates of the remaining final electron:

$$\frac{\mathrm{d}\sigma_{\mathrm{pT}}}{\mathrm{d}E_1\,\mathrm{d}\cos\theta_1} = \frac{1}{4I}\frac{1}{N}\int \frac{\mathrm{d}E_2\,\mathrm{d}\cos\theta_2\,\mathrm{d}\phi_2}{4\,(2\pi)^5} \times \frac{\varrho_1\varrho_2\sum_{\mathrm{spins,pols}}|M_{\mathrm{pT}}|^2}{\sqrt{a_2\left(\cos\theta_2^+ - \cos\theta_2\right)\left(\cos\theta_2 - \cos\theta_2^-\right)}}\Bigg|_{\phi_1\in\{\phi_1^{(1)},\phi_1^{(2)}\}}, \quad \text{(C.10)}$$

where the boundaries $\cos\theta_2^\pm$ are defined in the equations (A.66) and the physical values $\phi_1^{(1,2)}$ are given in equations (A.57), with the assignment of the subscripts a, b, c to the final particles as given above.

In figure C.2 the double differential cross section defined in equation (C.10) is depicted as a function of the positron energy E_1 for several values of its polar angle $\cos\theta_1$. In order to perform the integral in equation (C.10), we used the VEGAS algorithm, which is a Monte

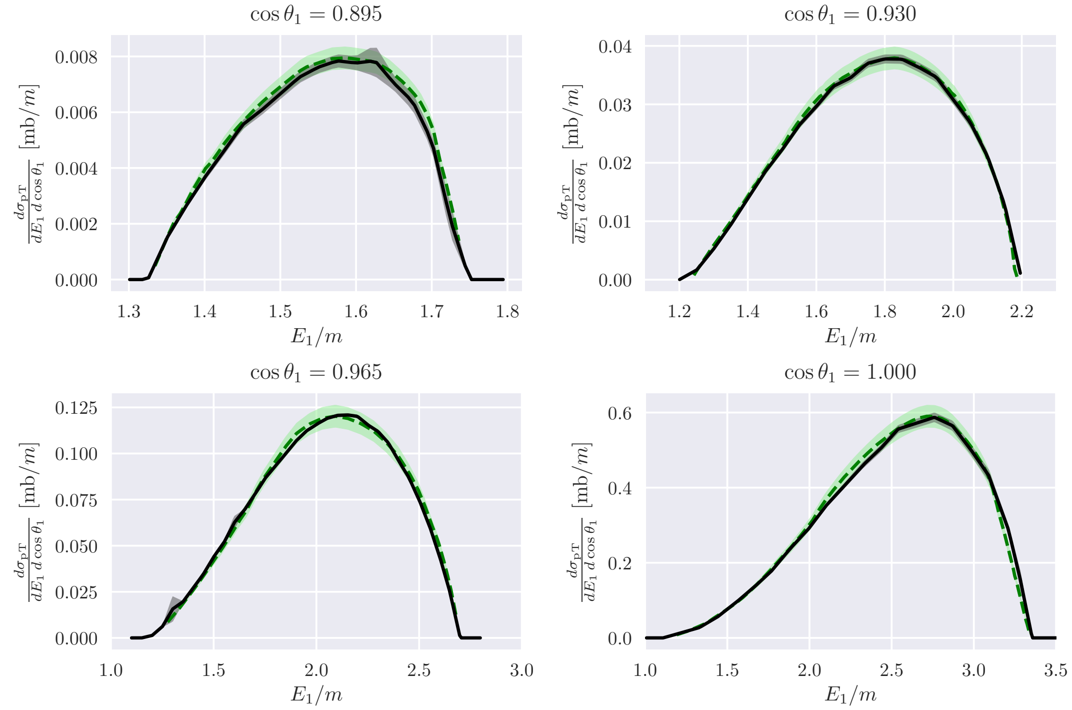

Figure C.2: The double differential cross section $\frac{\mathrm{d}\sigma_{\mathrm{pT}}}{\mathrm{d}E_1\,\mathrm{d}\cos\theta_1}$ of perturbative trident w.r.t. the outgoing positron in the laboratory system as a function of the positron energy E_1 (scaled with the electron mass m) for several values of the positron polar angle $\cos\theta_1$ (top row: $\cos\theta_1 = 0.895, 0.93$, bottom row: $\cos\theta_1 = 0.965, 1.0$), with the center-of-momentum energy $\sqrt{s} = 3.353\, m$, which corresponds to a photon energy of $\omega = k^0 = 5.12\, m$ and the initial electron at rest, i.e. $E = m$ (choice of the values is made to compare results to [144]). The results obtained from equation (C.10) are depicted as black solid curves, and the respective statistical error estimation is shown as grey shadowed area. The respective literature data was taken from [144] (figure 7) and are depicted as green dashed curves. The stated relative statistical accuracy of this data was indicated as $< 5\%$ and is depicted as green shadowed area.

Carlo method for numerical integration including importance sampling to iteratively adapt the evaluation points to regions with the highest contribution to the integral (cf. [167, 168, 222]). Additionally, we depicted the reference data extracted from [144] (figure 7) along with the stated numerical error of up to 5%. We mention the sufficiently good match of our calculation with the literature data in the stated error limits, where the numerical instabilities in our results are originated in the used Monte Carlo integration, which is depicted as statistical error in figure C.2 as well.

Another example, where we compare our implementation to literature data, is the total

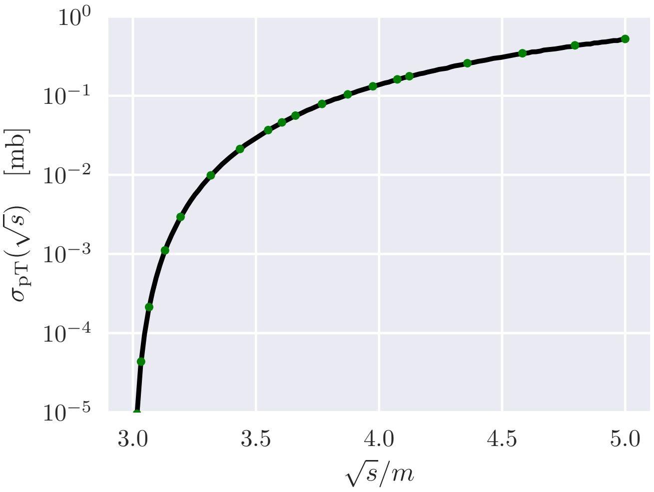

Figure C.3: Total cross section σ_{pT} of perturbative trident as a function of the center-of-momentum energy $\sqrt{s}$ (scaled with the electron mass m). The result of equation (C.11) is depiced as a solid black curve. The literature data points were taken from [118] (table 1) and is depicted as a green dots.

cross section of perturbative trident, which is defined as the five-fold integral

$$\sigma_{\mathrm{pT}} := \int \mathrm{d}\sigma_{\mathrm{pT}}, \tag{C.11}$$

where the differential cross section is given in equation (C.9). In figure C.3 the total cross section of perturbative trident is depicted as a function of the center-of-momentum energy $\sqrt{s}$ scaled by the electron mass m, where we used again the VEGAS algorithm for the five-fold integration. We mention the near perfect match of our calculation to the literature data, as well as the vanishing of the total cross section for values of $\sqrt{s}$ lower than the threshold-energy of $\sqrt{s_{\mathrm{th}}} = 3m$, as afore-stated in equation (A.78).

C.3 Differential cross sections in transverse coordinates

Within this section, we consider the exclusive electron distribution of the perturbative trident, i.e. the double-differential cross section similar to equation (C.10), but with the particle assignment: $a = 1$ (for the final positron), $b = 2$ (first final electron) and $c = 3$ (second final electron). Here we integrate over the momentum components of the final positron (cf. equation (C.9)), which leads to

$$\frac{\mathrm{d}\sigma_{\mathrm{pT}}}{\mathrm{d}E_2\,\mathrm{d}\cos\theta_2} = \frac{1}{4I}\frac{1}{N}\int\frac{\mathrm{d}E_1\,\mathrm{d}\cos\theta_1\,\mathrm{d}\phi_1}{4\left(2\pi\right)^5} \\ \times\frac{\varrho_1\varrho_2\sum_{\mathrm{spins,pols}}|M_{\mathrm{pT}}|^2}{\sqrt{a_2\left(\cos\theta_1^+-\cos\theta_1\right)\left(\cos\theta_1-\cos\theta_1^-\right)}}\Bigg|_{\varphi_2\in\{\phi_2^{(1)},\phi_2^{(2)}\}}, \quad \text{(C.12)}$$

where the coordinate boundaries $\cos\theta_1^\pm$ as well as the physical values of the electron azimuths $\phi_2^{(1,2)}$ are given in equation (A.66) and (A.57), respectively. In order to have a simple behavior of the inclusive electron distribution w.r.t. a Lorentz boost along the beam axis (i.e. along $\underline{k}$), we transform the double-differential cross section (C.12) to transverse coordinates (cf. section A.2). In figure C.4 the resulting $\frac{\mathrm{d}\sigma_{\mathrm{pT}}}{\mathrm{d}y_2\,\mathrm{d}p_{T2}}$ is depicted as a contour plot in the (y_2, p_{T2})-plane for the center-of-momentum energies of $\sqrt{s} = 3.353\,m$ (near to the threshold) and $\sqrt{s} = 10\,m$ (far above the threshold). We mention, that a priori the final electrons are not distinguishable due to the anti-symmetrisation of the matrix element following the Pauli principle. Thus, in the left panel of figure C.4 one observes a

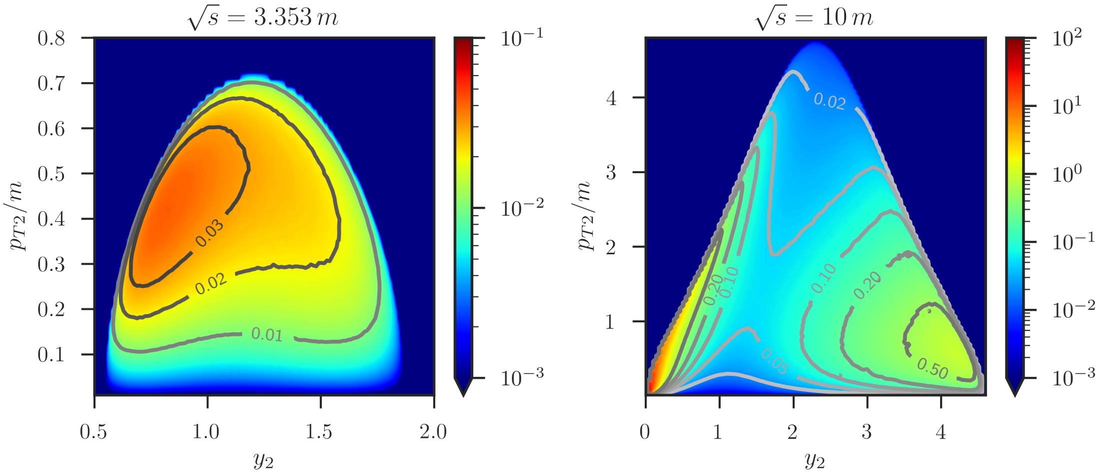

Figure C.4: The contour plot of the inclusive electron distribution of perturbative trident $\frac{\mathrm{d}\sigma_{\mathrm{pT}}}{\mathrm{d}y_2\,\mathrm{d}p_{T2}}$ in units of mb/m depicted in the (y_2, p_{T2})-plane for two values of the center-of-momentum energies: $\sqrt{s} = 3.353\,m$ (left panel) and $\sqrt{s} = 10\,m$ (right panel).

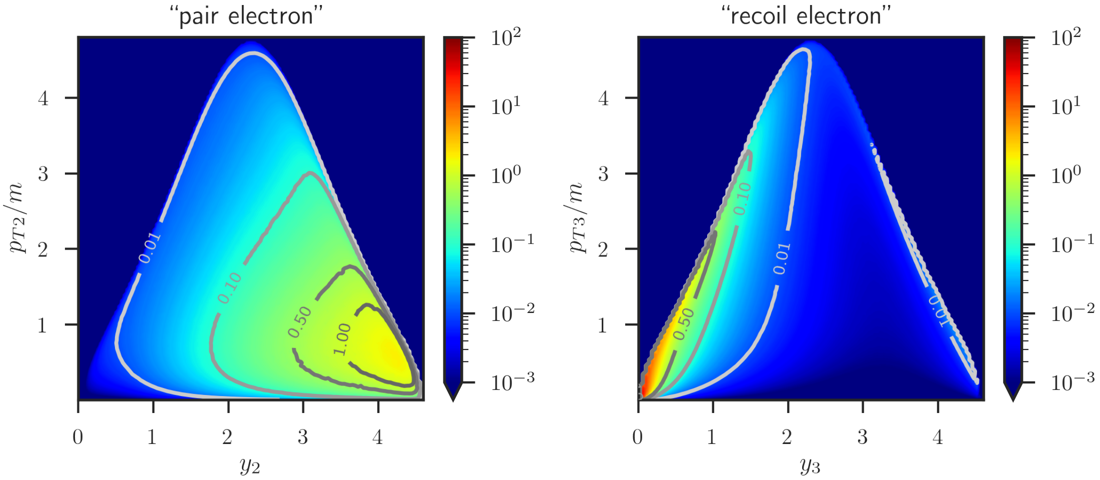

Figure C.5: Same as in the right panel of figure C.4, but without the exchange part of the matrix element (see text), depicted as a function of y_2, p_{T2} for the pair electron (left panel) and y_3, p_{T3} for the recoil electron (right panel). Over the respective remaining momentum components is integrated.

smooth single blob, where the interference of the direct and exchange parts of the matrix element (C.5) leads to the mentioned indistinguishability of the final electrons. However, in contrast to that, in the right panel of figure C.4, there is a separation of the final electron distribution for high center-of-momentum energies in two distinct sub-distributions: (i) near the origin and (ii) around the point $y_2 = 4, p_{T2} = 0.5\,m$.

In order to assign these two sub-distributions to the respective electron, we consider a similar exclusive electron distribution, except we omit the exchange terms: $M_{\mathrm{pT}} \to M_{\mathrm{pT}}^{\mathrm{noex}} := M_{\mathrm{C}} + M_{\mathrm{BW}}$, where the direct virtual Compton part M_{C} and the virtual Breit-Wheeler part M_{BW} are given in equation (C.1) and (C.3), respectively. Furthermore, we omit the normalisation factor $\frac{1}{2}$ from the anti-symmetrisation. Note that this leads to an unphysical distribution, but allows to directly distinguish the two electrons in the pair electron with momentum p_2 and the recoil electron with momentum p_3, according to the diagrams depicted in figure C.1.

In figure C.5 these the two distributions are depicted w.r.t. the recoil and the pair electron, respectively. There we observe that the recoil electron distribution is situated near the origin and the pair electron distribution turns out to be around the point $y_2 = 4, p_{T2} = 0.5\,m$. Therefore, by comparing these (unphysical) distributions with figure C.4, one can assume, that in the full distribution in the right panel of figure C.4 the two distinct sub-distributions can be assigned to the recoil electron (near the origin) and the pair electron (around the point $y_2 = 4, p_{T2} = 0.5\,m$). This kinematic distinction of the two kinds of electrons in perturbative trident was also discussed in [55, 56, 138] and it leads to the estimation of the polarisation of the incoming photon according to the measurement of recoil electron (cf. [72]). A similar distinction can also be observed in the strong field case (e.g. in [158] for constant crossed background fields), which leads to an interesting conceivable transfer of experience w.r.t. the polarisation measurements in strong laser fields using the trident process.

C.4 Dark photons

A currently discussed extension of the standard model of particle physics assumes the (hypothetical) existence of a massive photon-like particle as a quantum of an additional $U(1)$ symmetry [21, 94, 250], which is termed as dark photon or U-boson. Via kinetic mixing, the standard model photon can convert itself into such dark photon, which appears in the Feynman diagrams by using diagram elements of the type , where the double wiggly line stands for the dark photon. This scenario implies that the diagram in figure C.1 must be supplemented by the ones in figure C.6.

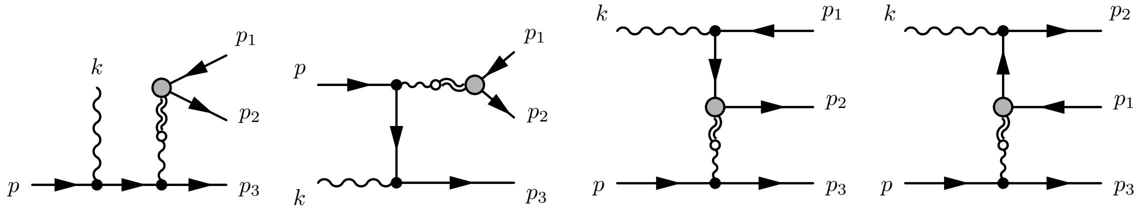

(a) Virtual Compton diagrams. **(b)** Virtual Breit-Wheeler diagrams.

Figure C.6: Feynman diagrams for the (hypothetical) contribution of a dark photon to the perturbative (monochromatic) trident process. Same as in figure C.1 but with kinetic mixing propagator  instead of the photon propagator and the dark photon vertex  coupled to the electron-positron pair.

The vertex  stands for the decay of the dark photon into an electron-positron pair. The dark photon propagator generates a resonance type contribution (cf. [24] for instance), which – when strong enough – leads to a peak structure at $(p(e^+) + p(e^-))^2 = m^2_{\text{darkphoton}}$. In such a way, the (hypothetical) kinematic mixing strength is accessible in experiments. Given the urgent interest in standard model extensions w.r.t. the dark matter/energy problem in cosmology, a plenty of experimental searches as been performed or are under construction (cf. [52] for a review). Up to now, only upper limits on the kinetic mixing have been reported.

Some authors (e.g. [94]) analysed the perturbative (monochromatic) trident w.r.t. the discovery potential of dark photons. In particular, one has to find a kinematical situation, where the virtual Compton diagrams C.1(a) and C.6(a) deliver a significant contribution to the (differential) cross section, since only these cause a resonant contribution. For a first inspection, it is sufficient to consider the diagrams in figure C.1. In order to evaluate the relevant parts of the differential cross section of the perturbative trident, we consider the invariant mass distribution of the produced pair w.r.t. either of the final electrons:

$$\frac{\mathrm{d}^2\sigma_{\mathrm{pT}}}{\mathrm{d}s_{12}\,\mathrm{d}s_{13}} = \int \delta(s_{12} - (p_1+p_2)^2)\delta(s_{13} - (p_1+p_3)^2)\, d\sigma_{\mathrm{pT}}, \tag{C.13}$$

where $s_{1i} = (p_1 + p_i)^2$ with $i = 2, 3$ denotes the invariant mass of the trident pair w.r.t. the outgoing electron with the four-momentum p_i and $d\sigma_{\mathrm{pT}}$ is the differential trident cross section given in equation (C.9). For the virtual Compton and the virtual Breit-Wheeler parts of the differential cross section, we replace the full perturbative trident matrix element by the respective matrix element of the subprocess and neglect the interference terms:

$$\frac{\mathrm{d}^2\sigma_{\mathrm{vBW}}}{\mathrm{d}s_{12}\,\mathrm{d}s_{13}} := \left.\frac{\mathrm{d}^2\sigma_{\mathrm{pT}}}{\mathrm{d}s_{12}\,\mathrm{d}s_{13}}\right|_{M_{\mathrm{pT}}\to M_{\mathrm{BW}}}, \tag{C.14}$$

$$\frac{\mathrm{d}^2\sigma_{\mathrm{vC}}}{\mathrm{d}s_{12}\,\mathrm{d}s_{13}} := \left.\frac{\mathrm{d}^2\sigma_{\mathrm{pT}}}{\mathrm{d}s_{12}\,\mathrm{d}s_{13}}\right|_{M_{\mathrm{pT}}\to M_{\mathrm{C}}}, \tag{C.15}$$

where M_{BW} (M_{C}) denotes the matrix element of the virtual Breit-Wheeler (Compton) subprocess given in equation (C.3) and (C.1), respectively. In figure C.7 the resulting double-differential cross sections are exhibited as contour plots in the (s_{12}, s_{13})-plane for a center-of-momentum energy of $\sqrt{s} = 3.353\,m$, which is somewhat above the threshold $\sqrt{s_{\mathrm{th}}}$.

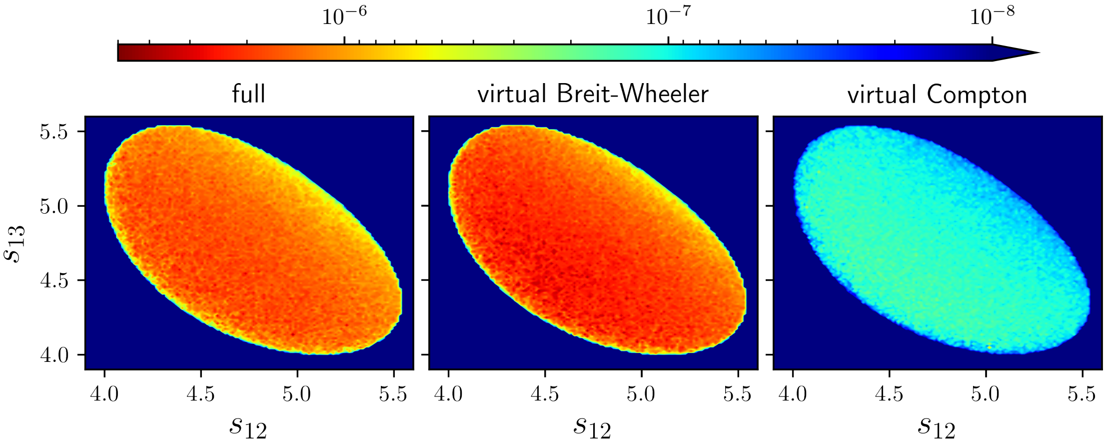

Figure C.7: Contour plots of the invariant mass distributions $\frac{\mathrm{d}^2\sigma_{\mathrm{pT}}}{\mathrm{d}s_{12}\,\mathrm{d}s_{13}}$ (left panel), $\frac{\mathrm{d}^2\sigma_{\mathrm{vBW}}}{\mathrm{d}s_{12}\,\mathrm{d}s_{13}}$ (middle panel) and $\frac{\mathrm{d}^2\sigma_{\mathrm{vC}}}{\mathrm{d}s_{12}\,\mathrm{d}s_{13}}$ (right panel) in units of mb$/m^4$, depicted in the (s_{12}, s_{13})-plane for $\sqrt{s} = 3.353\,m$.

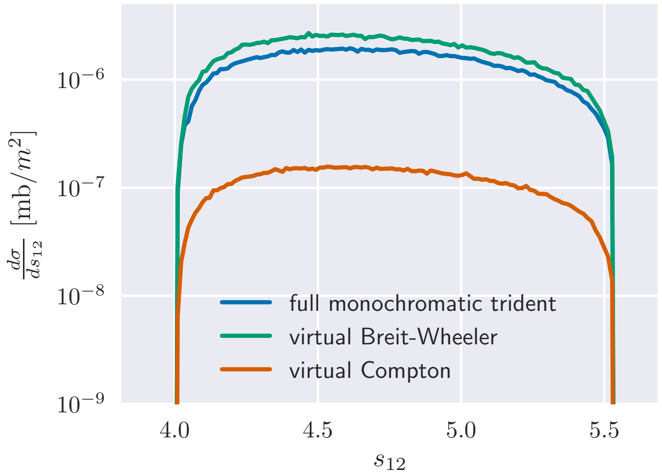

Figure C.8: Contour plot of the single differential invariant mass distribution $\frac{\mathrm{d}\sigma}{\mathrm{d}s_{12}}$ for the cases of the full monochromatic trident, the virtual Breit-Wheeler- and the virtual Compton subprocesses.

First we mention for all considered cases the same elliptically shaped phase space regime with sharp boundaries, where inside the invariant mass distributions are smooth and only slow varying. We mention also the symmetry of the distributions w.r.t. the interchange $s_{12} \leftrightarrow s_{13}$. Furthermore, one observes that the case of the full perturbative trident (C.13) and the virtual Breit-Wheeler part (C.14) have comparable signal strength, where the virtual Compton part (C.15) is suppressed by almost an order of magnitude. This kind of behavior of the monochromatic trident cross section is well known (see for instance [56]) and was even one of the first approximations considered for the monochromatic trident [32, 33]. Nevertheless, this suppression of the virtual Compton contribution does not exclude the dark photon capabilities, but makes the observation of a dark photon resonance in the invariant mass spectrum of the trident pair fairly challenging. However, the inclusion of spectral effects via the pulsed-perturbative trident, especially the modifications of the respective phase space might provide a kinematical regime with more promising capabilities. A similar behavior can be seen in the single-differential invariant mass distribution w.r.t. for instance s_{12}, i.e. the cross sections (C.13), (C.14) and (C.15) integrated over s_{13}. In figure C.8, the resulting single-differential invariant mass distribution $\frac{\mathrm{d}\sigma}{\mathrm{d}s_{12}}$ is depicted for the considered cases. Again, we observe a similar signal strength of the full perturbative trident calculation and the virtual Breit-Wheeler subprocess. We mention that the larger height of the virtual Breit-Wheeler distribution w.r.t. the full calculation indicates, that the interference terms have a decreasing contribution to the full perturbative trident distribution. Similar to the double-differential invariant mass distribution, the virtual

Compton contribution exhibited in figure C.8 is again suppressed by almost an order of magnitude. Nevertheless, especially at the boundaries of the single-differential invariant mass distribution, the respective contributions become to some extent comparable. This is important, since one can assume that the involvement of the spectrum of the used light-source causes a modification of these boundaries in the same manner as shown in section 4.3 in the case of the inclusive positron distribution. Consequently, it remains an open question, whether strong-field (multi-photon) effects could lift dedicated trident investigations on a competitive level.

D | Useful mathematical statements

Within this section, we summarise mathematical statements related to the pulse envelope function. Firstly, we recapitulate the definition: let $\varDelta\varphi \in \mathbb{R}$ with $\varDelta\varphi \neq 0$ be a pulse width, then a smooth function $g_{\varDelta\varphi} : \mathbb{R} \to \mathbb{R}^+$ is referred as a pulse envelope function, if for an arbitrary but fixed $\varDelta\varphi$ the function $g(\varphi, \varDelta\varphi)$ has a local maximum at $\varphi = 0$ and is monotonically increasing (decreasing) for all $\varphi < 0$ ($\varphi > 0$) as well as the assumptions

$$g(0, \varDelta\varphi) = 1 \text{ for all } \varDelta\varphi, \tag{D.1}$$

$$\lim_{\varphi\to\infty} g(\varphi, \varDelta\varphi) = 0 \text{ for all } \varDelta\varphi, \tag{D.2}$$

$$\lim_{\varDelta\varphi\to\infty} g(\varphi, \varDelta\varphi) = 1 \text{ for all } \varphi, \tag{D.3}$$

are fulfilled. Additionally, one assumes the characteristic moments

$$\nu_n[g] := \frac{1}{\varDelta\varphi} \int_{-\infty}^{\infty} g^n(\varphi, \varDelta\varphi) \, \mathrm{d}\varphi \tag{D.4}$$

does not depend on $\varDelta\varphi$ for all $n > 0$.

Lemma D.1

Let $g_{\varDelta\varphi} : \mathbb{R} \to \mathbb{R}^+$ be a pulse envelope function with width $\varDelta\varphi$ and

$$F_g(l, \varDelta\varphi) := \int_{-\infty}^{\infty} g(\varphi, \varDelta\varphi) e^{il\varphi} \, \mathrm{d}\varphi, \tag{D.5}$$

its (inverse) Fourier transform. Then for all $l \in \mathbb{R}$ one has

$$\lim_{\varDelta\varphi\to\infty} F_g(l, \varDelta\varphi) = 2\pi\delta(l) \tag{D.6}$$

Proof: Since the function g is smooth and bounded above, one can exchange the limit and the integral, which leads to the limit of the Fourier transform defined in equation (D.5)

$$\begin{aligned}\lim_{\Delta\varphi\to\infty} F_g(l,\Delta\varphi) &= \lim_{\Delta\varphi\to\infty}\int_{-\infty}^{\infty} g(\varphi,\Delta\varphi)e^{il\varphi}\,\mathrm{d}\varphi &\text{(D.7)}\\ &= \int_{-\infty}^{\infty}\lim_{\Delta\varphi\to\infty} g(\varphi,\Delta\varphi)e^{il\varphi}\,\mathrm{d}\varphi &\text{(D.8)}\\ &= \int_{-\infty}^{\infty} e^{il\varphi}\,d\varphi &\text{(D.9)}\\ &= 2\pi\delta(l). &\text{(D.10)}\end{aligned}$$

□

Similarly, the limit of the complex-conjugate results in

$$\lim_{\Delta\varphi\to\infty} F_g^*(l,\Delta\varphi) = 2\pi\delta(l). \tag{D.11}$$

In contrast to the limit shown in lemma D.1, the limit of the function $F_g^2(l,\Delta\varphi)$ for $\Delta\varphi\to\infty$ diverges for all $l\in\mathbb{R}$. However, including an additional suppressing factor results in a finite limit in the distributional sense.

Lemma D.2

Let $g_{\Delta\varphi}:\mathbb{R}\to\mathbb{R}^+$ be a pulse envelope function with width $\Delta\varphi$,

$$F_g(l,\Delta\varphi) := \int_{-\infty}^{\infty} g(\varphi,\Delta\varphi)e^{il\varphi}\,\mathrm{d}\varphi, \tag{D.12}$$

its (inverse) Fourier transform. Then, assuming g is an even function, one has for all $l\in\mathbb{R}$ and all l_1,$l_2\in\mathbb{R}$ with $l_1\neq l_2$

(i) $\lim_{\Delta\varphi\to\infty}\frac{F_g^2(l,\Delta\varphi)}{\Delta\varphi} = 2\pi\nu_2[g]\delta(l)$,

(ii) $\lim_{\Delta\varphi\to\infty}\frac{F_g(l_1,\Delta\varphi)F_g(l_2,\Delta\varphi)}{\Delta\varphi} = 0$,

where $\nu_2[g]$ denotes the second characteristic moment of g defined in (D.4).

Proof: Considering the case (i) and using the convolution theorem (see e.g. [16, 35]) for the product of Fourier transforms, one has

$$\lim_{\Delta\varphi\to\infty}\frac{F_g^2(l,\Delta\varphi)}{\Delta\varphi} = \lim_{\Delta\varphi\to\infty}\frac{1}{\Delta\varphi}\int_{-\infty}^{\infty}\left(g*g\right)(\varphi)e^{il\varphi}\,\mathrm{d}\varphi, \tag{D.13}$$

where $(g * g)(\varphi)$ denotes the convolution of g w.r.t. itself, which is defined by

$$(g * g)(\varphi) := \int_{-\infty}^{\infty} g(\varphi')g(\varphi - \varphi') \, \mathrm{d}\varphi'. \tag{D.14}$$

Expanding this convolution in φ leads to

$$(g * g)(\varphi) = \mathit{\Delta}\varphi \nu_2[g] + \int_{-\infty}^{\infty} g(\varphi') \sum_{n=1}^{\infty} \frac{\partial^n}{\partial \varphi^n} g(\varphi - \varphi') \, \mathrm{d}\varphi', \tag{D.15}$$

where the second term is suppressed by a factor of $\frac{1}{\mathit{\Delta}\varphi}$ compared to the first summand and therefore negligible for $\mathit{\Delta}\varphi \gg 1$. This approximation is also referred to as the slowly varying envelope approximation and was illustrated in [212, 269, 271, 290]. Inserting this expansion into (D.13) results in

$$\lim_{\mathit{\Delta}\varphi \to \infty} \frac{F_g^2(l, \mathit{\Delta}\varphi)}{\mathit{\Delta}\varphi} = \lim_{\mathit{\Delta}\varphi \to \infty} \left[\nu_2[g] \int_{-\infty}^{\infty} e^{il\varphi} \, \mathrm{d}\varphi + \mathcal{O}\left(\frac{1}{\mathit{\Delta}\varphi} \right) \right] \tag{D.16}$$

$$= 2\pi \nu_2[g] \delta(l), \tag{D.17}$$

where we used the integral representation of the delta-distribution $2\pi\delta(l) = \int_{-\infty}^{\infty} e^{il\varphi} \, \mathrm{d}\varphi$. For the case (ii), we apply equation (D.6) to both factors yielding

$$\lim_{\mathit{\Delta}\varphi \to \infty} \frac{F_g(l_1, \mathit{\Delta}\varphi) F_g(l_2, \mathit{\Delta}\varphi)}{\mathit{\Delta}\varphi} = \lim_{\mathit{\Delta}\varphi \to \infty} (2\pi)^2 \frac{\delta(l_1)\delta(l_2)}{\mathit{\Delta}\varphi} = 0, \tag{D.18}$$

considering the assumption $l_1 \neq l_2$. □

List of Figures

List of Tables

Bibliography

[1] P. Abbamonte, F. Abild-Pedersen, P. Adams, M. Ahmed, F. Albert, R. A. Mori, et al., *New science opportunities enabled by LCLS-II x-ray lasers*, tech. rep. (SLAC National Accelerator Laboratory, 2015).

[2] H. Abramowicz, M. Altarelli, R. Assmann, T. Behnke, Y. Benhammou, O. Borysov, M. Borysova, R. Brinkmann, F. Burkart, et al., 'Letter of Intent for the LUXE Experiment', arXiv:1909.00860 [physics.ins-det] (2019).

[3] S. Adhikari, A. Ali, M. Amaryan, E. Anassontzis, A. Austregesilo, F. Barbosa, J. Barlow, et al., 'The GlueX Beamline and Detector', arXiv: 2005.14272 [physics.ins-det] (2020).

[4] S. L. Adler, 'Photon splitting and photon dispersion in a strong magnetic field', Annals Phys. **67**, 599–647 (1971).

[5] P. H. Adrian, N. Baltzell, M. Battaglieri, M. Bondi, S. Boyarinov, S. Bueltmann, et al. (HPS), 'Search for a dark photon in electroproduced e^+e^- pairs with the Heavy Photon Search experiment at JLab', Phys. Rev. D **98**, 091101 (2018).

[6] M. Ahlers, H. Gies, J. Jaeckel, J. Redondo, and A. Ringwald, 'Laser experiments explore the hidden sector', Phys. Rev. D **77**, 095001 (2008).

[7] I. Akal, S. Villalba-Chávez, and C. Müller, 'Electron-positron pair production in a bifrequent oscillating electric field', Phys. Rev. D **90**, 113004 (2014).

[8] S. Z. Akhmadaliev, G. Y. Kezerashvili, S. Klimenko, R. Lee, V. Malyshev, et al., 'Experimental investigation of high-energy photon splitting in atomic fields', Phys. Rev. Lett. **89**, 061802 (2002).

[9] I. Aleksandrov, G. Plunien, and V. Shabaev, 'Dynamically assisted Schwinger effect beyond the spatially-uniform-field approximation', Phys. Rev. D **97**, 116001 (2018).

[10] I. Aleksandrov, G. Plunien, and V. Shabaev, ‘Electron-positron pair production in external electric fields varying both in space and time’, Phys. Rev. D **94**, 065024 (2016).

[11] M. Altarelli, R. Brinkmann, and M. Chergui, *The European X-ray free-electron laser. Technical design report*, tech. rep. (DESY XFEL Project Group, 2007).

[12] P. Ambrozewicz, L. Ye, Y. Prok, I. Larin, A. Ahmidouch, K. Baker, V. Baturin, L. Benton, A. Bernstein, V. Burkert, et al. (PrimEx), ‘High Precision Measurement of Compton Scattering in the 5 GeV region’, Phys. Lett. B **797**, 134884 (2019).

[13] V. Anguelov, S. Petrov, L. Gurdev, and J. Kourtev, ‘On the numerical analysis of triplet pair production cross-sections and the mean energy of produced particles for modeling electron photon cascade in a soft photon field’, J. Phys. G **25**, 1733 (1999).

[14] T. Aoyama, M. Hayakawa, T. Kinoshita, and M. Nio, ‘Tenth-order electron anomalous magnetic moment: contribution of diagrams without closed lepton loops’, Phys. Rev. D **91**, 033006 (2015).

[15] T. Aoyama, M. Hayakawa, T. Kinoshita, and M. Nio, ‘Tenth-order qed contribution to the electron g- 2 and an improved value of the fine structure constant’, Phys. Rev. Lett. **109**, 111807 (2012).

[16] G. B. Arfken, H. J. Weber, and F. E. Harris, ‘Chapter 20 - Integral Transforms’, in *Mathematical methods for physicists*, Seventh Edition (Academic Press, Boston, 2013), pp. 963–1046.

[17] V. G. Bagrov and D. Gitman, *Exact solutions of relativistic wave equations* (Springer Science & Business Media, 1990).

[18] V. Baier and V. Katkov, ‘Pair creation by a photon in an electric field’, Phys. Lett. A **374**, 2201–2206 (2010).

[19] V. Baier, V. Katkov, and V. Strakhovenko, ‘Higher-order effects in external field: pair production by a particle’, Sov. J. Nucl. Phys. **14** (1972), [Yadern. Fiz. 14.5:1020 (1971)].

[20] C. Bamber, S. Boege, T. Koffas, T. Kotseroglou, A. Melissinos, D. Meyerhofer, D. Reis, W. Ragg, C. Bula, K. McDonald, et al., ‘Studies of nonlinear qed in collisions of 46.6 gev electrons with intense laser pulses’, Phys. Rev. D **60**, 092004 (1999).

[21] M. Bauer, P. Foldenauer, and J. Jaeckel, ‘Hunting All the Hidden Photons’, JHEP **18**, 094 (2020).

[22] A. Bell and J. G. Kirk, ‘Possibility of Prolific Pair Production with High-Power Lasers’, Phys. Rev. Lett. **101**, 200403 (2008).

[23] I. Belousov, ‘On resonance compton scattering in the field of an intense electromagnetic wave’, Opt. Commun. **20**, 205–208 (1977).

[24] T. Beranek, H. Merkel, and M. Vanderhaeghen, ‘Theoretical framework to analyze searches for hidden light gauge bosons in electron scattering fixed target experiments’, Phys. Rev. D **88**, 015032 (2013).

[25] V. Berestetskii, L. Pitaevskii, and E. Lifshitz, *Quantum electrodynamics: volume 4* (Elsevier Science, 2012).

[26] D. Bernard, ‘Polarimetry of cosmic gamma-ray sources above e^+e^- pair creation threshold’, Nucl. Instrum. Meth. A **729**, 765–780 (2013).

[27] T. Blackburn, C. Ridgers, J. Kirk, and A. Bell, ‘Quantum radiation reaction in laser-electron beam collisions’, Phys. Rev. Lett. **112**, 015001 (2014).

[28] T. Blackburn, D. Seipt, S. Bulanov, and M. Marklund, ‘Benchmarking semiclassical approaches to strong-field QED: nonlinear Compton scattering in intense laser pulses’, Phys. Plasmas **25**, 083108 (2018).

[29] M. Boca and V. Florescu, ‘Nonlinear Compton scattering with a laser pulse’, Phys. Rev. A **80**, 053403 (2009).

[30] M. Boca and V. Florescu, ‘Thomson and compton scattering with an intense laser pulse’, Eur. Phys. J. D **61**, 449–462 (2011).

[31] V. Boldyshev, E. Vinokurov, N. Merenkov, and Y. Peresunko, ‘Measurement of photon beam linear polarization using asymmetry of the recoil electrons from the photoproduction of e^+e^- pairs on electrons’, Phys. Part. Nucl. **25**, 292–331 (1994).

[32] A. Borsellino, ‘Über die Materialisierung der gamma-Strahlen im Felde eines Elektrons’, Helv. phys. acta **20**, 136–138 (1947).

[33] A. Borsellino, ‘Momentum Transfer and Angle of Divergence of Pairs Produced by Photons’, Phys. Rev. **89**, 1023–1025 (1953).

[34] O. Boryso (LUXE), ‘Study of QED in strong field regime at LUXE experiment’, Frascati Phys. Ser. **69**, edited by G. Corcella, E. De Lucia, P. Di Nezza, P. Gianotti, and G. Pancheri, 74–80 (2019).

[35] R. N. Bracewell and R. N. Bracewell, *The fourier transform and its applications*, Vol. 31999 (McGraw-Hill New York, 1986).

[36] S. Bragin, S. Meuren, C. H. Keitel, and A. Di Piazza, ‘High-Energy Vacuum Birefringence and Dichroism in an Ultrastrong Laser Field’, Phys. Rev. Lett. **119**, 250403 (2017).

[37] E. Brezin and C. Itzykson, ‘Pair production in vacuum by an alternating field’, Phys. Rev. D **2**, 1191–1199 (1970).

[38] L. S. Brown and T. Kibble, ‘Interaction of intense laser beams with electrons’, Phys. Rev. **133**, A705 (1964).

[39] L. S. Brown and T. Kibble, ‘Interaction of Intense Laser Beams with Electrons’, Phys. Rev. **133**, A705–A719 (1964).

[40] C. Bula, K. T. McDonald, E. Prebys, C. Bamber, S. Boege, T. Kotseroglou, A. Melissinos, D. Meyerhofer, W. Ragg, D. Burke, et al., ‘Observation of nonlinear effects in compton scattering’, Phys. Rev. Lett. **76**, 3116 (1996).

[41] C. Bula and K. McDonald, ‘The Weizsacker-Williams approximation to trident production in electron photon collisions’, arXiv:0004117 [hep-ph] (1997).

[42] S. Bulanov, V. Mur, N. Narozhny, J. Nees, and V. Popov, ‘Multiple colliding electromagnetic pulses: a way to lower the threshold of e^+e^- pair production from vacuum’, Phys. Rev. Lett. **104**, 220404 (2010).

[43] S. Bulanov, N. Narozhny, V. Mur, and V. Popov, ‘On e^+e^- pair production by a focused laser pulse in vacuum’, Phys. Lett. A **330**, 1–6 (2004).

[44] S. Bulanov, C. Schroeder, E. Esarey, and W. Leemans, ‘Electromagnetic cascade in high energy electron, positron, and photon interactions with intense laser pulses’, Phys. Rev. A **87**, 062110 (2013).

[45] F. Bunkin and M. Fedorov, ‘Bremsstrahlung in a strong radiation field’, Sov. Phys. JETP **22**, 844–847 (1966).

[46] F. Burkart, R. Aßmann, R. Brinkmann, W. Decking, N. Golubeva, B. Heinemann, M. Hüning, J. List, and M. Wing, ‘LUXE - a QED Experiment at the European XFEL’, in 10th International Particle Accelerator Conference (2019), TUPRB008.

[47] D. Burke, R. Field, G. Horton-Smith, J. Spencer, D. Walz, S. Berridge, W. Bugg, K. Shmakov, A. Weidemann, C. Bula, et al., ‘Positron production in multiphoton light-by-light scattering’, Phys. Rev. Lett. **79**, 1626 (1997).

[48] E. Byckling and K. Kajantie, *Particle kinematics* (Wiley-Interscience, London and New York, 1973).

[49] V. Bytev, E. Kuraev, M. Galynskii, and A. Potylitsyn, ‘Polarized triplet production by circularly polarized photons’, JETP Lett. **75**, 452–456 (2002).

[50] F. Curciarello, ‘Review on Dark Photon’, EPJ Web Conf. **118**, edited by G. D’Ambrosio, M. Iacovacci, M. Passera, G. Venanzoni, P. Massarotti, and S. Mastroianni, 01008 (2016).

[51] A. Debus, R. Pausch, A. Hübl, K. Steiniger, R. Widera, T. E. Cowan, U. Schramm, and M. Bussmann, ‘Circumventing the Dephasing and Depletion Limits of Laser-Wakefield Acceleration’, Phys. Rev. X **9**, 031044 (2019).

[52] A. Denig, ‘Review of dark photon searches’, EPJ Web Conf. **130**, edited by A. Wrońska, A. Magiera, C. Guaraldo, and H. Ströher, 01005 (2016).

[53] O. Denisenko and S. Roshchupkin, ‘Nonresonant Scattering of an Electron by a Positron in the Field of a Plane Electromagnetic Wave of an Arbitrary Intensity’, Laser Phys. **3** (1993).

[54] O. Denisenko and S. Roshchupkin, ‘Resonant scattering of an electron by a positron in the field of a light wave’, Laser Phys. **9**, 1108–1112 (1999).

[55] G. Depaola and M. Iparraguirre, ‘Angular distribution for the electron recoil in pair production by linearly polarized gamma-rays on electrons’, Nucl. Instrum. Meth. A **611**, 84–92 (2009).

[56] G. Depaola and M. I. D. Palacios, ‘About electrons and position in Triplet Production: some remarks’, arXiv:1406.3001 [hep-ph] (2014).

[57] A. Di Piazza, E. Lotstedt, A. Milstein, and C. Keitel, ‘Barrier control in tunneling e^+ - e^- photoproduction’, Phys. Rev. Lett. **103**, 170403 (2009).

[58] A. Di Piazza, E. Lotstedt, A. Milstein, and C. Keitel, ‘Effect of a strong laser field on e^+ - e^- photoproduction by relativistic nuclei’, Phys. Rev. A **81**, 062122 (2010).

[59] A. Di Piazza, A. Milstein, and C. Keitel, ‘Photon splitting in a laser field’, Phys. Rev. A **76**, 032103 (2007).

[60] A. Di Piazza, A. Milstein, and C. Müller, ‘Polarization of the electron and positron produced in combined Coulomb and strong laser fields’, Phys. Rev. A **82**, 062110 (2010).

[61] A. Di Piazza, C. Müller, K. Hatsagortsyan, and C. Keitel, ‘Extremely high-intensity laser interactions with fundamental quantum systems’, Rev. Mod. Phys. **84**, 1177 (2012).

[62] A. Di Piazza, M. Tamburini, S. Meuren, and C. Keitel, ‘Implementing nonlinear Compton scattering beyond the local constant field approximation’, Phys. Rev. A **98**, 012134 (2018).

[63] A. Di Piazza, M. Tamburini, S. Meuren, and C. Keitel, ‘Improved local-constant-field approximation for strong-field QED codes’, Phys. Rev. A **99**, 022125 (2019).

[64] D. A. Dicus, A. Farzinnia, W. W. Repko, and T. M. Tinsley, ‘Muon decay in a laser field’, Phys. Rev. D **79**, 013004 (2009).

[65] B. M. Dillon and B. King, ‘ALP production through non-linear Compton scattering in intense fields’, Eur. Phys. J. C **78**, 775 (2018).

[66] V. Dinu, T. Heinzl, A. Ilderton, M. Marklund, and G. Torgrimsson, ‘Vacuum refractive indices and helicity flip in strong-field QED’, Phys. Rev. D **89**, 125003 (2014).

[67] V. Dinu and G. Torgrimsson, ‘Approximating higher-order nonlinear QED processes with first-order building blocks’, arXiv:1912.11015 [hep-ph] (2019).

[68] V. Dinu and G. Torgrimsson, ‘Single and double nonlinear Compton scattering’, Phys. Rev. D **99**, 096018 (2019).

[69] V. Dinu and G. Torgrimsson, ‘Trident pair production in plane waves: Coherence, exchange, and spacetime inhomogeneity’, Phys. Rev. D **97**, 036021 (2018).

[70] V. Dinu and G. Torgrimsson, ‘Trident process in laser pulses’, Phys. Rev. D **101**, 056017 (2020).

[71] W. Dittrich and H. Gies, *Probing the quantum vacuum. Perturbative effective action approach in quantum electrodynamics and its application*, Vol. 166 (2000).

[72] M. Dugger, B. Ritchie, N. Sparks, K. Moriya, R. Tucker, R. Lee, B. Thorpe, T. Hodges, F. Barbosa, N. Sandoval, et al., ‘Design and construction of a high-energy photon polarimeter’, Nucl. Instrum. Meth. A **867**, 115–127 (2017).

[73] G. V. Dunne, H. Gies, and R. Schützhold, ‘Catalysis of Schwinger Vacuum Pair Production’, Phys. Rev. D **80**, 111301 (2009).

[74] G. V. Dunne and C. Schubert, ‘Worldline instantons and pair production in inhomogeneous fields’, Phys. Rev. D **72**, 105004 (2005).

[75] M. Dunne, *LCLS Strategic Facility Development Plan*, tech. rep. (SLAC National Accelerator Laboratory, 2017), p. 55.

[76] F. J. Dyson, ‘The radiation theories of Tomonaga, Schwinger, and Feynman’, Phys. Rev. **75**, 486 (1949).

[77] J. H. Eberly, ‘VII interaction of very intense light with free electrons’, in *Progress in optics*, Vol. 7 (Elsevier, 1969), pp. 359–415.

[78] J. H. Eberly and H. R. Reiss, ‘Electron self-energy in intense plane-wave field’, Phys. Rev. **145**, 1035 (1966).

[79] F. Ehlotzky, K. Krajewska, and J. Kamiński, ‘Fundamental processes of quantum electrodynamics in laser fields of relativistic power’, Rep. Prog. Phys. **72**, 046401 (2009).

[80] A. Einstein, ‘Zur Quantentheorie der Strahlung’, Phys. Z. **18**, 121–128 (1917).

[81] N. Elkina, A. Fedotov, I. Kostyukov, M. Legkov, N. Narozhny, E. Nerush, and H. Ruhl, ‘QED cascades induced by circularly polarized laser fields’, Phys. Rev. ST Accel. Beams **14**, 054401 (2011).

[82] C. Escobar and L. Urrutia, ‘Invariants of the electromagnetic field’, J. Math. Phys. **55**, 032902 (2014).

[83] R. Escribano and E. Masso, ‘High precision tests of QED and physics beyond the standard model’, Eur. Phys. J. C **4**, 139–143 (1998).

[84] A. Farzinnia, D. A. Dicus, W. W. Repko, and T. M. Tinsley, ‘Muon decay in a linearly polarized laser field’, Phys. Rev. D **80**, 073004 (2009).

[85] A. Fedotov, N. Narozhny, G. Mourou, and G. Korn, ‘Limitations on the attainable intensity of high power lasers’, Phys. Rev. Lett. **105**, 080402 (2010).

[86] C. Fey and R. Schützhold, ‘Momentum dependence in the dynamically assisted Sauter-Schwinger effect’, Phys. Rev. D **85**, 025004 (2012).

[87] R. P. Feynman, ‘Mathematical formulation of the quantum theory of electromagnetic interaction’, Phys. Rev. **80**, 440 (1950).

[88] R. P. Feynman, ‘Space-time approach to quantum electrodynamics’, Phys. Rev. **76**, 769 (1949).

[89] F. Fillion-Gourdeau, E. Lorin, and A. D. Bandrauk, ‘Enhanced Schwinger’s pair production in many-center systems’, J. Phys. B **46**, 175002 (2013).

[90] E. S. Fradkin, D. M. Gitman, S. M. Shvartsman, and D. M. Gitman, *Quantum electrodynamics: with unstable vacuum* (Springer Berlin, 1991).

[91] Z. Fried and J. H. Eberly, ‘Scattering of a high-intensity, low-frequency electromagnetic wave by an unbound electron’, Phys. Rev. **136**, B871 (1964).

[92] W. Furry, ‘On Bound States and Scattering in Positron Theory’, Phys. Rev. **81**, 115–124 (1951).

[93] G. Gakh, M. Konchatnij, I. Levandovsky, and N. Merenkov, ‘Analysis of triplet production by a circularly polarized photon at high energies’, J. Exp. Theor. Phys. **117**, 48–61 (2013).

[94] G. Gakh, M. Konchatnij, and N. Merenkov, ‘The triplet photoproduction on a free electron as a possible way to search for a dark photon’, arXiv:1711.01770 [hep-ph] (2017).

[95] G. Gakh, M. Konchatnij, and N. Merenkov, ‘Triplet production by a polarized photon beam on a polarized electron target’, arXiv:1511.05722 [hep-ph] (2015).

[96] D. C. Gates, R. W. Kenney, and W. P. Swanson, ‘Electron triplet production by high-energy photons in hydrogen’, Phys. Rev. **125**, 1310 (1962).

[97] E. Gelfer, A. Mironov, A. Fedotov, V. Bashmakov, E. Nerush, I. Y. Kostyukov, and N. Narozhny, ‘Optimized multibeam configuration for observation of QED cascades’, Phys. Rev. A **92**, 022113 (2015).

[98] F. Gelis and N. Tanji, ‘Schwinger mechanism revisited’, Prog. Part. Nucl. Phys. **87**, 1–49 (2016).

[99] H. Gies, ‘Strong laser fields as a probe for fundamental physics’, Eur. Phys. J. D **55**, 311–317 (2009).

[100] S. L. Glashow, ‘The renormalizability of vector meson interactions’, Nucl. Phys. **10**, 107–117 (1959).

[101] R. J. Glauber, ‘Coherent and incoherent states of the radiation field’, Phys. Rev. **131**, 2766 (1963).

[102] R. J. Glauber, ‘The quantum theory of optical coherence’, Phys. Rev. **130**, 2529 (1963).

[103] I. Goldman, ‘Intensity effects in Compton scattering’, Sov. Phys. JETP **19**, 954 (1964), [Phys. Lett. 8:103–106 (1964)].

[104] A. Gonoskov, A. Bashinov, S. Bastrakov, E. Efimenko, A. Ilderton, A. Kim, M. Marklund, I. Meyerov, A. Muraviev, and A. Sergeev, ‘Ultrabright GeV Photon Source via Controlled Electromagnetic Cascades in Laser-Dipole Waves’, Phys. Rev. X **7**, 041003 (2017).

[105] A. Gonoskov, S. Bastrakov, E. Efimenko, A. Ilderton, M. Marklund, I. Meyerov, A. Muraviev, A. Sergeev, I. Surmin, and E. Wallin, ‘Extended particle-in-cell schemes for physics in ultrastrong laser fields: Review and developments’, Phys. Rev. E **92**, 023305 (2015).

[106] A. Gonoskov, I. Gonoskov, C. Harvey, A. Ilderton, A. Kim, M. Marklund, G. Mourou, and A. Sergeev, ‘Probing nonperturbative QED with optimally focused laser pulses’, Phys. Rev. Lett. **111**, 060404 (2013).

[107] W. Greiner and J. Reinhardt, *Quantum electrodynamics* (Springer Science & Business Media, 2008).

[108] D. Griffiths, *Introduction to elementary particles* (John Wiley & Sons, 2008).

[109] P. Gros, S. Amano, D. Attié, P. Baron, D. Baudin, D. Bernard, P. Bruel, D. Calvet, P. Colas, S. Daté, et al., ‘Performance measurement of HARPO: a Time Projection Chamber as a gamma-ray telescope and polarimeter’, Astropart. Phys. **97**, 10–18 (2018).

[110] P. Gros and D. Bernard, ‘γ-ray polarimetry with conversions to e^+e^- pairs: polarization asymmetry and the way to measure it’, Astropart. Phys. **88**, 30–37 (2017).

[111] D. Hammerland, P. Zhang, S. Kühn, P. Jojart, I. Seres, V. Zuba, Z. Varallyay, D. Charalambidis, K. Osvay, T. T. Luu, et al., ‘Reconstruction of attosecond pulses in the presence of interfering dressing fields using a 100 khz laser system at eli-alps’, J. Phys. B **52**, 23LT01 (2019).

[112] D. Hanneke, S. F. Hoogerheide, and G. Gabrielse, ‘Cavity control of a single-electron quantum cyclotron: Measuring the electron magnetic moment’, Phys. Rev. A **83**, 052122 (2011).

[113] A. Hartin, ‘Strong field QED in lepton colliders and electron/laser interactions’, Int. J. Mod. Phys. A **33**, 1830011 (2018).

[114] A. Hartin, A. Ringwald, and N. Tapia, ‘Measuring the Boiling Point of the Vacuum of Quantum Electrodynamics’, Phys. Rev. D **99**, 036008 (2019).

[115] N. Hartmann et al., ‘Attosecond time–energy structure of x-ray free-electron laser pulses’, Nature Photon. **12**, 215–220 (2018).

[116] C. Harvey, A. Ilderton, and B. King, ‘Testing numerical implementations of strong field electrodynamics’, Phys. Rev. A **91**, 013822 (2015).

[117] C. Harvey, T. Heinzl, and A. Ilderton, ‘Signatures of High-Intensity Compton Scattering’, Phys. Rev. A **79**, 063407 (2009).

[118] E. Haug, ‘Bremsstrahlung and Pair Production in the Field of Free Electrons’, Z. Naturforsch. A **30**, 1099–1113 (1975).

[119] E. Haug, ‘Differential cross-section of electron-positron bremsstrahlung’, Phys. Rev. D **31**, 2120–2128 (1985).

[120] E. Haug, 'Simple Analytic Expressions for the Total Cross Section for $\gamma - e$ Pair Production', Z. Naturforsch. A **36**, 413–414 (1981).

[121] F. Hebenstreit and F. Fillion-Gourdeau, 'Optimization of Schwinger pair production in colliding laser pulses', Phys. Lett. B **739**, 189–195 (2014).

[122] F. Hebenstreit, A. Ilderton, and M. Marklund, 'Pair production: the view from the lightfront', Phys. Rev. D **84**, 125022 (2011).

[123] T. Heinzl, B. King, and A. Macleod, 'The locally monochromatic approximation to QED in intense laser fields', arXiv:2004.13035 [hep-ph] (2020).

[124] T. Heinzl, D. Seipt, and B. Kämpfer, 'Beam-Shape Effects in Nonlinear Compton and Thomson Scattering', Phys. Rev. A **81**, 022125 (2010).

[125] T. Heinzl and A. Ilderton, 'A Lorentz and gauge invariant measure of laser intensity', Opt. Commun. **282**, 1879–1883 (2009).

[126] T. Heinzl, A. Ilderton, and M. Marklund, 'Finite size effects in stimulated laser pair production', Phys. Lett. B **692**, 250–256 (2010).

[127] T. Heinzl, A. Ilderton, and M. Marklund, 'Pair production in laser fields: finite size effects', PoS **LC2010**, edited by J. Papavassiliou, V. Vento, A. Aguilar, A. Courtoy, and J. Portoles, 007 (2010).

[128] T. Heinzl, B. Liesfeld, K.-U. Amthor, H. Schwoerer, R. Sauerbrey, and A. Wipf, 'On the observation of vacuum birefringence', Opt. Commun. **267**, 318–321 (2006).

[129] W. Heisenberg and H. Euler, 'Folgerungen aus der diracschen theorie des positrons', Z. Phys. **98**, 714–732 (1936).

[130] *Helmholtz International Beamline for Extreme Fields at the European XFEL*, (2020) `https://www.hzdr.de/db/Cms?pNid=694` (Last accessed June 21, 2020).

[131] U. Hernandez Acosta and B. Kämpfer, 'Laser pulse-length effects in trident pair production', Plasma Phys. Control. Fusion **61**, 084011 (2019).

[132] H. Hu and J. Huang, 'Trident pair production in colliding bright x-ray laser beams', Phys. Rev. A **89**, 033411 (2014).

[133] H. Hu, C. Müller, and C. H. Keitel, 'Complete QED theory of multiphoton trident pair production in strong laser fields', Phys. Rev. Lett. **105**, 080401 (2010).

[134] A. Ilderton, B. King, and D. Seipt, 'Extended locally constant field approximation for nonlinear Compton scattering', Phys. Rev. A **99**, 042121 (2019).

[135] A. Ilderton, 'Trident pair production in strong laser pulses', Phys. Rev. Lett. **106**, 020404 (2011).

[136] A. Ilderton, J. Lundin, M. Marklund, et al., ‘Strong field, noncommutative QED’, Symmetry Integr. Geom. **6**, 041 (2010).

[137] A. Ilderton and A. J. MacLeod, ‘The analytic structure of amplitudes on backgrounds from gauge invariance and the infra-red’, JHEP **04**, 078 (2020).

[138] M. Iparraguirre and G. Depaola, ‘Pair production by gamma-rays on electrons. Threshold for the momentum recoil detection’, Eur. Phys. J. C **71**, 1778 (2011).

[139] C. Itzykson and J.-B. Zuber, *Quantum field theory* (Courier Corporation, 2012).

[140] D. Ivanov, G. Kotkin, and V. Serbo, ‘Complete description of polarization effects in e^+e^- pair production by a photon in the field of a strong laser wave’, Eur. Phys. J. C **40**, 27–40 (2005).

[141] J. D. Jackson, *Classical electrodynamics* (American Association of Physics Teachers, 1999).

[142] M. J. A. Jansen and C. Müller, ‘Strongly enhanced pair production in combined high- and low-frequency laser fields’, Phys. Rev. A **88**, 052125 (2013).

[143] M. J. Jansen and C. Müller, ‘Pair Creation of Scalar Particles in Intense Bichromatic Laser Fields’, J. Phys. Conf. Ser. **594**, 012051 (2015).

[144] S. Jarp and K. J. Mork, ‘Differential cross sections for pair production by photons on electrons’, Phys. Rev. D **8**, 159 (1973).

[145] J. Jauch and F. Rohrlich, *The theory of photons and electrons. The relativistic quantum field theory of charged particles with spin one-half*, 2nd ed., Texts and Monographs in Physics (Springer, Berlin, 1976).

[146] M. Jirka, O. Klimo, S. Bulanov, T. Esirkepov, E. Gelfer, S. Bulanov, S. Weber, and G. Korn, ‘Electron dynamics, gamma and electron-positron production by colliding laser pulses’, Phys. Rev. E **93**, 023207 (2016).

[147] J. Joseph and F. Rohrlich, ‘Pair production and bremsstrahlung in the field of free and bound electrons’, Rev. Mod. Phys **30**, 354 (1958).

[148] F. Karbstein, H. Gies, M. Reuter, and M. Zepf, ‘Vacuum birefringence in strong inhomogeneous electromagnetic fields’, Phys. Rev. D **92**, 071301 (2015).

[149] F. Karbstein and C. Sundqvist, ‘Probing vacuum birefringence using x-ray free electron and optical high-intensity lasers’, Phys. Rev. D **94**, 013004 (2016).

[150] T. Kibble, ‘Frequency Shift in High-Intensity Compton Scattering’, Phys. Rev. **138**, B740–B753 (1965).

[151] B. King, ‘Double Compton scattering in a constant crossed field’, Phys. Rev. A **91**, 033415 (2015).

[152] B. King, ‘Double Compton scattering in a constant crossed field and approximations used in simulation’, J. Phys. Conf. Ser. **594**, 012053 (2015).

[153] B. King, A. Di Piazza, and C. Keitel, ‘A matterless double slit’, Nature Photon. **4**, 92–94 (2010).

[154] B. King, A. Di Piazza, and C. Keitel, ‘Double-slit vacuum polarisation effects in ultra-intense laser fields’, Phys. Rev. A **82**, 032114 (2010).

[155] B. King, B. Dillon, K. Beyer, and G. Gregori, ‘Axion-like-particle decay in strong electromagnetic backgrounds’, JHEP **19**, 162 (2020).

[156] B. King, N. Elkina, and H. Ruhl, ‘Photon polarisation in electron-seeded pair-creation cascades’, Phys. Rev. A **87**, 042117 (2013).

[157] B. King and A. Fedotov, ‘Effect of interference on the trident process in a constant crossed field’, Phys. Rev. D **98**, 016005 (2018).

[158] B. King and H. Ruhl, ‘Trident pair production in a constant crossed field’, Phys. Rev. D **88**, 013005 (2013).

[159] C. Kohlfurst, M. Mitter, G. von Winckel, F. Hebenstreit, and R. Alkofer, ‘Optimizing the pulse shape for Schwinger pair production’, Phys. Rev. D **88**, 045028 (2013).

[160] G. Kopylov, L. Kulyukina, and I. Polubarinov, ‘Photoproduction of electron and muon pairs on electrons’, Sov. Phys. JETP **19**, 1158–1162 (1964).

[161] K. Krajewska and J. Kaminski, ‘Breit-Wheeler pair creation by finite laser pulses’, J. Phys. Conf. Ser. **497**, 012016 (2014).

[162] K. Krajewska and J. Kaminski, ‘Breit-Wheeler Process in Intense Short Laser Pulses’, Phys. Rev. A **86**, 052104 (2012).

[163] K. Krajewska and J. Kaminski, ‘Compton Process in Intense Short Laser Pulses’, Phys. Rev. A **85**, 062102 (2012).

[164] P. Kryukov, A. Nikishov, V. Ritus, and V. Sergienko, ‘Feasibility of experimental investigation of nonlinear qed processes—photon emission by electrons and pair creation by photons in strong laser field’, J. Russ. Laser Res. **15**, 351–376 (1994).

[165] S. Kühn, M. Dumergue, S. Kahaly, S. Mondal, M. Füle, T. Csizmadia, B. Farkas, B. Major, Z. Várallyay, E. Cormier, et al., ‘The eli-alps facility: the next generation of attosecond sources’, J. Phys. B **50**, 132002 (2017).

[166] G. Landi, *An introduction to noncommutative spaces and their geometries*, Vol. 51 (Springer Science & Business Media, 2003).

[167] G. P. Lepage, ‘A new algorithm for adaptive multidimensional integration’, J. Comput. Phys **27**, 192–203 (1978).

[168] G. P. Lepage, *Vegas-an adaptive multi-dimensional integration program*, tech. rep. (Cornell University, 1980).

[169] E. Lötstedt, U. D. Jentschura, and C. H. Keitel, ‘Evaluation of laser-assisted bremsstrahlung with Dirac-Volkov propagators’, Phys. Rev. Lett. **98**, 043002 (2007).

[170] E. Lötstedt and U. D. Jentschura, ‘Nonperturbative Treatment of Double Compton Backscattering in Intense Laser Fields’, Phys. Rev. Lett. **103**, 110404 (2009).

[171] J. MacArthur, J. Duris, Z. Huang, and A. Marinelli, ‘High Power Sub-Femtosecond X-Ray Pulse Study for the LCLS’, in 8th International Particle Accelerator Conference (2017), WEPAB118.

[172] J. P. MacArthur, ‘Electron beam manipulations at the angstrom level and attosecond timescale for X-ray FELs’, PhD thesis (Stanford U., 2020).

[173] F. Mackenroth and A. Di Piazza, ‘Nonlinear Compton scattering in ultra-short laser pulses’, Phys. Rev. A **83**, 032106 (2011).

[174] F. Mackenroth and A. Di Piazza, ‘Nonlinear Double Compton Scattering in the Ultrarelativistic Quantum Regime’, Phys. Rev. Lett. **110**, 070402 (2013).

[175] F. Mackenroth and A. Di Piazza, ‘Nonlinear trident pair production in an arbitrary plane wave: a focus on the properties of the transition amplitude’, Phys. Rev. D **98**, 116002 (2018).

[176] F. Mackenroth, A. Di Piazza, and C. Keitel, ‘Determining the carrier-envelope phase of intense few-cycle laser pulses’, Phys. Rev. Lett. **105**, 063903 (2010).

[177] F. K. Mackenroth, ‘Quantum radiation in ultra-intense laser pulses’, PhD thesis (Ruprecht-Karls Universität, Heidelberg, 2012).

[178] F. K. Mackenroth and A. R. Holkundkar, ‘Determining the duration of an ultra-intense laser pulse directly in its focus’, Sci. Rep. **9**, 19607 (2019).

[179] M. Maggiore, *A modern introduction to quantum field theory* (Oxford University Press, 2005).

[180] L. Maiani, R. Petronzio, and E. Zavattini, ‘Effects of Nearly Massless, Spin Zero Particles on Light Propagation in a Magnetic Field’, Phys. Lett. B **175**, 359–363 (1986).

[181] T. H. Maiman, ‘Stimulated optical radiation in ruby’, Nature **187**, 493–494 (1960).

[182] S. Mandelstam, ‘Determination of the pion - nucleon scattering amplitude from dispersion relations and unitarity. General theory’, Phys. Rev. **112**, 1344–1360 (1958).

[183] M. Marklund and P. K. Shukla, ‘Nonlinear collective effects in photon-photon and photon-plasma interactions’, Rev. Mod. Phys. **78**, 591–640 (2006).

[184] A. Mastichiadis, ‘Relativistic electrons in photon fields-Effects of triplet pair production on inverse Compton gamma-ray spectra’, Mon. Not. R. Astron. Soc. **253**, 235–244 (1991).

[185] A. Mastichiadis, A. Marscher, and K. Brecher, ‘Electron-positron pair production by ultrarelativistic electrons in a soft photon field’, Astrophys. J **300**, 178–189 (1986).

[186] S. Meuren, ‘Probing strong-field QED at FACET-II (SLAC E-320)’, in Third conference on extremely high intensity laser physics (exhilp) (2019).

[187] S. Meuren, C. Keitel, and A. Di Piazza, ‘Polarization operator for plane-wave background fields’, Phys. Rev. D **88**, 013007 (2013).

[188] S. Meuren, ‘Nonlinear quantum electrodynamic and electroweak processes in strong laser fields’, PhD thesis (Ruprecht-Karls Universität, Heidelberg, 2015).

[189] S. Meuren, K. Z. Hatsagortsyan, C. H. Keitel, and A. Di Piazza, ‘Polarization operator approach to pair creation in short laser pulses’, Phys. Rev. D **91**, 013009 (2015).

[190] S. Meuren, C. H. Keitel, and A. Di Piazza, ‘Nonlinear neutrino-photon interactions inside strong laser pulses’, JHEP **06**, 127 (2015).

[191] S. Meuren, C. H. Keitel, and A. Di Piazza, ‘Semiclassical picture for electron-positron photoproduction in strong laser fields’, Phys. Rev. D **93**, 085028 (2016).

[192] H. Mitter, ‘Quantum Electrodynamics in Laser Fields’, Acta Phys. Austriaca Suppl. **14**, 397–498 (1975).

[193] R. Mohammadi and S.-S. Xue, ‘Laser photons acquire circular polarization by interacting with a Dirac or Majorana neutrino beam’, Phys. Lett. B **731**, 272–278 (2014).

[194] P. J. Mohr, D. B. Newell, and B. N. Taylor, ‘CODATA recommended values of the fundamental physical constants: 2014’, Rev. Mod. Phys. **88**, 035009 (2016), `https://link.aps.org/doi/10.1103/RevModPhys.88.035009`.

[195] S. Mondal, M. Shirozhan, N. Ahmed, M. Bocoum, F. Boehle, A. Vernier, S. Haessler, R. Lopez-Martens, F. Sylla, C. Sire, et al., ‘Surface plasma attosource beamlines at ELI-ALPS’, JOSA B **35**, A93–A102 (2018).

[196] A. Monin and M. Voloshin, ‘Photon-stimulated production of electron-positron pairs in electric field’, Phys. Rev. D **81**, 025001 (2010).

[197] K. Mork, *Differential cross sections for pair production by photons on electrons*, tech. rep. (Univ. of Trondheim, Norway, 1971).

[198] K. J. Mork, ‘Pair production by photons on electrons’, Phys. Rev. **160**, 1065 (1967).

[199] D. Morozov and V. Ritus, ‘Elastic electron scattering in an intense field and two-photon emission’, Nucl. Phys. B **86**, 309–332 (1975).

[200] J. Motz, H. A. Olsen, and H. Koch, ‘Pair production by photons’, Rev. Mod. Phys **41**, 581 (1969).

[201] G. A. Mourou, G. Korn, W. Sandner, and J. L. Collier, ‘ELI-Extreme Light Infrastructure: Science and Technology with Ultra-Intense Lasers, Whitebook’, THOSS Media GmbH (2011).

[202] G. A. Mourou, T. Tajima, and S. V. Bulanov, ‘Optics in the relativistic regime’, Rev. Mod. Phys. **78**, 309–371 (2006).

[203] B. Müller, H. Peitz, J. Rafelski, and W. Greiner, ‘Solution of the Dirac equation for strong external fields’, Phys. Rev. Lett. **28**, 1235 (1972).

[204] B. Müller, J. Rafelski, and W. Greiner, ‘Solution of the Dirac equation with two Coulomb centers’, Phys. Lett. B **47**, 5–7 (1973).

[205] C. Müller, A. Di Piazza, A. Shahbaz, T. Burvenich, J. Evers, K. Hatsagortsyan, and C. Keitel, ‘High-energy, nuclear, and QED processes in strong laser fields’, Laser Phys. **18**, 175–184 (2008).

[206] C. Müller, K. Z. Hatsagortsyan, and C. H. Keitel, ‘Muon pair creation from positronium in a linearly polarized laser field’, Phys. Rev. A **78**, 033408 (2008).

[207] C. Müller, K. Z. Hatsagortsyan, and C. H. Keitel, ‘Muon pair creation from positronium in a circularly polarized laser field’, Phys. Rev. D **74**, 074017 (2006).

[208] N. Muramatsu, Y. Kon, S. Daté, Y. Ohashi, H. Akimune, J. Chen, M. Fujiwara, S. Hasegawa, T. Hotta, T. Ishikawa, et al. (LEPS), ‘Development of high intensity laser-electron photon beams up to 2.9 GeV at the SPring-8 LEPS beamline’, Nucl. Instrum. Meth. A **737**, 184–194 (2014).

[209] N. Muramatsu (LEPS2/BGOegg), 'Recent Progress and Prospects of the LEPS2/BGOegg Experiment at SPring-8', Acta Phys. Polon. B **51**, 231–238 (2020).

[210] S. Myers, *The LEP collider, from design to approval and commissioning*, tech. rep. (European Organization for Nuclear Research, 1991).

[211] M. Nakatsutsumi, K. Appel, G. Priebe, I. Thorpe, A. Pelka, B. Muller, and T. Tschentscher, *Technical design report: Scientific instrument high energy density physics (HED)*, tech. rep. (European X-Ray Free-Electron Laser Facility, 2014).

[212] N. Narozhnyi and M. Fofanov, 'Photon emission by an electron in a collision with a short focused laser pulse', J. Exp. Theor. Phys. **83**, 14–23 (1996), [Zh. Eksp. Teor. Fiz. 110:26-46 (1996)].

[213] N. Narozhnyi, A. I. Nikishov, and V. Ritus, 'Quantum processes in the field of a circularly polarized electromagnetic wave', Sov. Phys. JETP **20**, 622 (1965), [Zh. Eksp. Teor. Fiz. 47:930 (1964)].

[214] E. Nerush, I. Kostyukov, A. Fedotov, N. Narozhny, N. Elkina, and H. Ruhl, 'Laser field absorption in self-generated electron-positron pair plasma', Phys. Rev. Lett. **106**, 035001 (2011), [Erratum: Phys.Rev.Lett. 106, 109902 (2011)].

[215] R. Neville, 'Null-plane quantum electrodynamics in an external radiation field', Can. J. Phys **54**, 2246–2271 (1976).

[216] A. Nikishov and V. Ritus, 'Pair production by a photon and photon emission by an electron in the field of an intense electromagnetic wave and in a constant field', Sov. Phys. JETP **25**, 1135–1142 (1967).

[217] A. Nikishov and V. Ritus, 'Quantum Processes in the Field of a Plane Electromagnetic Wave and in a Constant Field', Sov. Phys. JETP **19**, 1191 (1964), [Zh. Eksp. Teor. Fiz. 46:1768-1781 (1964)].

[218] A. Nikishov and V. Ritus, 'Quantum Processes in the Field of a Plane Electromagnetic Wave and in a Constant Field 1', Sov. Phys. JETP **19**, 529–541 (1964), [Zh.Eksp.Teor.Fiz.46:776-796 (1964)].

[219] A. Nikishov and V. Ritus, 'Nonlinear effects in Compton scattering and pair production owing to absorption of several photons', Sov. Phys. JETP **20**, 757 (1965), [Zh. Eksp. Teor. Fiz. 47:1130 (1964)].

[220] T. Nousch, A. Otto, D. Seipt, B. Kämpfer, A. Titov, D. Blaschke, A. Panferov, and S. Smolyansky, 'Laser assisted Breit-Wheeler and Schwinger processes', FIAS Interdisc. Sci. Ser., edited by S. Schramm and M. Schäfer, 253–262 (2017).

[221] T. Nousch, D. Seipt, B. Kämpfer, and A. Titov, ‘Pair production in short laser pulses near threshold’, Phys. Lett. B **715**, 246–250 (2012).

[222] T. Ohl, ‘Vegas revisited: adaptive monte carlo integration beyond factorization’, Comput. Phys. Commun. **120**, 13–19 (1999).

[223] V. Oleinik, ‘Resonance effects in field of an intense laser beam’, Sov. Phys. JETP **25**, 697–708 (1967).

[224] V. Oleinik, ‘Resonance effects in the field of an intense laser ray. II’, Sov. Phys. JETP **26**, 1132–1138 (1968).

[225] F. W. Olver, D. W. Lozier, R. F. Boisvert, and C. W. Clark, *NIST handbook of mathematical functions hardback and CD-ROM* (Cambridge University Press, 2010).

[226] M. Orthaber, F. Hebenstreit, and R. Alkofer, ‘Momentum Spectra for Dynamically Assisted Schwinger Pair Production’, Phys. Lett. B **698**, 80–85 (2011).

[227] A. Otto, T. Nousch, D. Seipt, B. Kämpfer, D. Blaschke, A. Panferov, S. Smolyansky, and A. Titov, ‘Pair production by Schwinger and Breit–Wheeler processes in bi-frequent fields’, J. Plasma Phys. **82**, 655820301 (2016).

[228] A. Otto, D. Seipt, D. Blaschke, B. Kämpfer, and S. Smolyansky, ‘Lifting shell structures in the dynamically assisted Schwinger effect in periodic fields’, Phys. Lett. B **740**, 335–340 (2015).

[229] A. Otto and B. Kämpfer, ‘Afterglow of the dynamical Schwinger process: soft photons amass’, Phys. Rev. D **95**, 125007 (2017).

[230] A. Otto, D. Seipt, D. Blaschke, S. A. Smolyansky, and B. Kämpfer, ‘Dynamical Schwinger process in a bifrequent electric field of finite duration: survey on amplification’, Phys. Rev. D **91**, 105018 (2015).

[231] P. Panek, J. Kamiński, and F. Ehlotzky, ‘Analysis of resonances in Møller scattering in a laser field of relativistic radiation power’, Phys. Rev. A **69**, 013404 (2004).

[232] P. Panek, J. Kamiński, and F. Ehlotzky, ‘Relativistic electron-atom scattering in an extremely powerful laser field: relevance of spin effects’, Phys. Rev. A **65**, 033408 (2002).

[233] A. D. Panferov, S. A. Smolyansky, A. Otto, B. Kämpfer, D. B. Blaschke, and Ł. Juchnowski, ‘Assisted dynamical Schwinger effect: pair production in a pulsed bifrequent field’, Eur. Phys. J. D **70**, 56 (2016).

[234] V. O. Papanyan and V. I. Ritus, ‘Vacuum polarization and photon splitting in an intense field’, Sov. Phys. JETP **34** (1972).

[235] D. H. Perkins, *Introduction to high energy physics* (Cambridge University Press, 2000).

[236] M. E. Peskin and D. V. Schroeder, *An Introduction to quantum field theory* (Addison-Wesley, Reading, USA, 1995).

[237] J. Plemelj, ‘Problems in the sense of Riemann and Klein’, in *Interscience tracts in pure and applied mathematics* (Interscience Publishers, New York, 1964).

[238] S. Porto, A. Hartin, and G. Moortgat-Pick, ‘Methods for evaluating physical processes in strong external fields at e+e− colliders: Furry picture and quasi-classical approach’, PoS **Corfu2012**, edited by K. Anagnostopoulos, I. Bakas, N. Irges, J. Kalinowski, A. Kehagias, R. Pittau, M. N. Rebelo, G. Wolschin, and G. Zoupanos, 039 (2013).

[239] R. Protheroe, A. Mastichiadis, and C. Dermer, ‘Pair-Compton cascading in a spatially varying anisotropic radiation field’, Astropart. Phys. **1**, 113–127 (1992).

[240] J. Rafelski, L. P. Fulcher, and W. Greiner, ‘Superheavy elements and an upper limit to the electric field strength’, Phys. Rev. Lett. **27**, 958–961 (1971).

[241] J. Rafelski, B. Müller, and W. Greiner, ‘Spontaneous vacuum decay of supercritical nuclear composites’, Z. Phys. A **285**, 49 (1978).

[242] M. Raggi, ‘Status of the PADME experiment and review of dark photon searches’, EPJ Web Conf. **179**, edited by G. D’Ambrosio, M. Iacovacci, M. Passera, G. Venanzoni, and S. Mastroianni, 01020 (2018).

[243] H. R. Reiss, ‘Absorption of light by light’, J. Math. Phys **3**, 59–67 (1962).

[244] C. P. Ridgers, J. G. Kirk, R. Duclous, T. Blackburn, C. Brady, K. Bennett, T. Arber, and A. Bell, ‘Modelling gamma-ray photon emission and pair production in high-intensity laser-matter interactions’, J. Comput. Phys **260**, 273–285 (2014).

[245] C. Ridgers, C. S. Brady, R. Duclous, J. Kirk, K. Bennett, T. Arber, A. Robinson, and A. Bell, ‘Dense electron-positron plasmas and ultraintense γ rays from laser-irradiated solids’, Phys. Rev. Lett. **108**, 165006 (2012).

[246] A. Ringwald, ‘Pair production from vacuum at the focus of an X-ray free electron laser’, Phys. Lett. B **510**, 107–116 (2001).

[247] V. I. Ritus, ‘Quantum effects of the interaction of elementary particles with an intense electromagnetic field’, J. Sov. Laser Res. **6**, 497–617 (1985), `https://doi.org/10.1007/BF01120220`.

[248] V. Ritus, ‘Radiative corrections in quantum electrodynamics with intense field and their analytical properties’, Annals Phys. **69**, 555–582 (1972).

[249] V. Ritus, ‘Vacuum polarization correction to elastic electron and muon scattering in an intense field and pair electro-and muoproduction’, Nucl. Phys. B **44**, 236–252 (1972).

[250] T. G. Rizzo, ‘Kinetic Mixing and Portal Matter Phenomenology’, Phys. Rev. D **99**, 115024 (2019).

[251] S. Roshchupkin, ‘Resonant effects in collisions of relativistic electrons in the field of a light wave’, Laser Phys. **6**, 837–858 (1996).

[252] M. Ruf, G. R. Mocken, C. Müller, K. Z. Hatsagortsyan, and C. H. Keitel, ‘Pair production in laser fields oscillating in space and time’, Phys. Rev. Lett. **102**, 080402 (2009).

[253] L. H. Ryder, *Quantum field theory* (Cambridge university press, 1996).

[254] A. Salam and J. C. Ward, ‘Weak and electromagnetic interactions’, Il Nuovo Cimento **11**, 568–577 (1959).

[255] Y. Salamin and C. Keitel, ‘Electron acceleration by a tightly focused laser beam’, Phys. Rev. Lett. **88**, 095005 (2002).

[256] Y. I. Salamin, S. Hu, K. Z. Hatsagortsyan, and C. H. Keitel, ‘Relativistic high-power laser-matter interactions’, Phys. Rept. **427**, 41–155 (2006).

[257] F. Sauter, ‘Über das Verhalten eines Elektrons im homogenen elektrischen Feld nach der relativistischen Theorie Diracs’, Z. Phys. **69**, 742–764 (1931).

[258] A. L. Schawlow and C. H. Townes, ‘Infrared and optical masers’, Phys. Rev. **112**, 1940 (1958).

[259] H.-P. Schlenvoigt, T. Heinzl, U. Schramm, T. E. Cowan, and R. Sauerbrey, ‘Detecting vacuum birefringence with x-ray free electron lasers and high-power optical lasers: a feasibility study’, Phys. Scr. **91**, 023010 (2016).

[260] W. F. Schlotter, ‘Soft X-ray Free Electron Laser Science at LCLS and Opportunities at LCLS II’, in Laser science (Optical Society of America, 2016), LF3I–3.

[261] S. Schnez, E. Lötstedt, U. D. Jentschura, and C. H. Keitel, ‘Laser-assisted bremsstrahlung for circular and linear polarization’, Phys. Rev. A **75**, 053412 (2007).

[262] R. Schützhold, H. Gies, and G. Dunne, ‘Dynamically assisted Schwinger mechanism’, Phys. Rev. Lett. **101**, 130404 (2008).

[263] J. Schwinger, ‘On gauge invariance and vacuum polarization’, Phys. Rev. **82**, 664 (1951).

[264] J. Schwinger, ‘On quantum-electrodynamics and the magnetic moment of the electron’, Phys. Rev. **73**, 416 (1948).

[265] J. Schwinger, ‘Quantum electrodynamics. I. A covariant formulation’, Phys. Rev. **74**, 1439 (1948).

[266] J. Schwinger, ‘The Theory of Quantized Fields. III’, Phys. Rev. **91**, 728–740 (1953).

[267] D. Seipt and B. Kämpfer, ‘Asymmetries of azimuthal photon distributions in non-linear Compton scattering in ultra-short intense laser pulses’, Phys. Rev. A **88**, 012127 (2013).

[268] D. Seipt and B. Kämpfer, ‘Laser assisted Compton scattering of X-ray photons’, Phys. Rev. A **89**, 023433 (2014).

[269] D. Seipt and B. Kämpfer, ‘Non-Linear Compton Scattering of Ultrashort and Ultraintense Laser Pulses’, Phys. Rev. A **83**, 022101 (2011).

[270] D. Seipt and B. Kämpfer, ‘Two-photon Compton process in pulsed intense laser fields’, Phys. Rev. D **85**, 101701 (2012).

[271] D. Seipt, S. Rykovanov, A. Surzhykov, and S. Fritzsche, ‘Narrowband inverse Compton scattering x-ray sources at high laser intensities’, Phys. Rev. A **91**, 033402 (2015).

[272] D. Seipt, A. Surzhykov, S. Fritzsche, and B. Kämpfer, ‘Caustic structures in x-ray Compton scattering off electrons driven by a short intense laser pulse’, New J. Phys. **18**, 023044 (2016).

[273] D. Seipt, ‘Strong-Field QED Processes in Short Laser Pulses’, PhD thesis (Technische Universität Dresden, 2012).

[274] D. Seipt, ‘Volkov States and Non-linear Compton Scattering in Short and Intense Laser Pulses’, in Quantum Field Theory at the Limits: from Strong Fields to Heavy Quarks (2017), pp. 24–43.

[275] D. Seipt and B. Kämpfer, ‘Non-linear Compton scattering of ultrahigh-intensity laser pulses’, arXiv:1111.0188 [hep-ph] (2011).

[276] D. Seipt, V. Kharin, S. Rykovanov, A. Surzhykov, and S. Fritzsche, ‘Analytical results for nonlinear Compton scattering in short intense laser pulses’, J. Plasma Phys. **82**, 655820203 (2016).

[277] A. Shahbaz, T. J. Buervenich, and C. Müller, ‘Isotope effects in the harmonic response from hydrogenlike muonic atoms in strong laser fields’, Phys. Rev. A **82**, 013418 (2010).

[278] M. Sheik-Bahae, ‘Nonlinear optics basics. kramers-kronig relations in nonlinear optics’, Encyclopedia of modern optics, 234–239 (2005).

[279] B. Shen, Z. Bu, J. Xu, T. Xu, L. Ji, R. Li, and Z. Xu, ‘Exploring vacuum birefringence based on a 100 PW laser and an x-ray free electron laser beam’, Plasma Phys. Control. Fusion **60**, 044002 (2018).

[280] I. V. Sokolov, N. M. Naumova, J. A. Nees, and G. A. Mourou, ‘Pair Creation in QED-Strong Pulsed Laser Fields Interacting with Electron Beams’, Phys. Rev. Lett. **105**, 195005 (2010).

[281] A. Sommerfeld, *Atombau und Spektrallinien. II. Band* (Verlag Harry Deutsch, Thun, Frankkurt am Main, 1978).

[282] M. Srednicki, *Quantum field theory* (Cambridge University Press, 2007).

[283] D. Strickland and G. Mourou, ‘Compression of amplified chirped optical pulses’, Opt. Commun. **55**, [Erratum: Opt.Commun. 56, 219–221 (1985)], 447–449 (1985).

[284] K. S. Suh and H. Bethe, ‘Recoil momentum distribution in electron pair production’, Phys. Rev. **115**, 672 (1959).

[285] C. Szymanowski, V. Veniard, R. Taieb, A. Maquet, and C. Keitel, ‘Mott scattering in strong laser fields’, Phys. Rev. A **56**, 3846–3859 (1997).

[286] M. Tanabashi, K. Hagiwara, K. Hikasa, K. Nakamura, Y. Sumino, F. Takahashi, et al. (Particle Data Group), ‘Review of Particle Physics’, Phys. Rev. D **98**, 030001 (2018).

[287] A. Titov, B. Kämpfer, and H. Takabe, ‘Nonlinear Breit-Wheeler process in short laser double pulses’, Phys. Rev. D **98**, 036022 (2018).

[288] A. Titov, B. Kämpfer, H. Takabe, and A. Hosaka, ‘Neutrino pair emission off electrons in a strong electromagnetic wave field’, Phys. Rev. D **83**, 053008 (2011).

[289] A. Titov, A. Otto, and B. Kämpfer, ‘Multi-photon regime of non-linear Breit-Wheeler and Compton processes in short linearly and circularly polarized laser pulses’, Eur. Phys. J. D **74**, 39 (2020).

[290] A. Titov, H. Takabe, B. Kämpfer, and A. Hosaka, ‘Enhanced subthreshold electron-positron production in short laser pulses’, Phys. Rev. Lett. **108**, 240406 (2012).

[291] A. I. Titov and B. Kämpfer, ‘Non-linear Breit-Wheeler process with linearly polarized beams’, arXiv:2006.04496 [hep-ph] (2020).

[292] A. I. Titov, B. Kämpfer, A. Hosaka, T. Nousch, and D. Seipt, 'Determination of the carrier envelope phase for short, circularly polarized laser pulses', Phys. Rev. D **93**, 045010 (2016).

[293] A. I. Titov, B. Kämpfer, A. Hosaka, and H. Takabe, 'Non-linear quantum dynamics in strong and short electromagnetic fields', in Quantum Field Theory at the Limits: from Strong Fields to Heavy Quarks (2017), pp. 58–67.

[294] A. I. Titov, B. Kämpfer, T. Shibata, A. Hosaka, and H. Takabe, 'Laser pulse-shape dependence of Compton scattering', Eur. Phys. J. D **68**, 299 (2014).

[295] S. Tomonaga, 'On a relativistically invariant formulation of the quantum theory of wave fields.', Prog. Theor. Exp. Phys. **1**, 27–42 (1946).

[296] G. Torgrimsson, J. Oertel, and R. Schützhold, 'Doubly assisted Sauter-Schwinger effect', Phys. Rev. D **94**, 065035 (2016).

[297] G. Torgrimsson, C. Schneider, J. Oertel, and R. Schützhold, 'Dynamically assisted Sauter-Schwinger effect — non-perturbative versus perturbative aspects', JHEP **06**, 043 (2017).

[298] G. Torgrimsson, C. Schneider, and R. Schützhold, 'Sauter-Schwinger pair creation dynamically assisted by a plane wave', Phys. Rev. D **97**, 096004 (2018).

[299] A. Vaidya, C. Farina, and M. Hott, 'Furry's picture in the path integral framework', Il Nuovo Cimento A **105**, 925–934 (1992).

[300] S. van der Walt, S. C. Colbert, and G. Varoquaux, 'The numpy array: a structure for efficient numerical computation', Comput. Sci. Eng. **13**, 22–30 (2011).

[301] F. C. Vélez, J. Z. Kamiński, and K. Krajewska, 'Electron Scattering Processes in Non-Monochromatic and Relativistically Intense Laser Fields', Atoms **7**, 34 (2019).

[302] E. Vinokurov and E. Kuraev, 'Production of triplets by polarized photons', Sov. Phys. JETP **36**, 602 (1973).

[303] E. Vinokurov and N. Merenkov, 'On the production of triplets by high energy polarized photons', Yadernaya Fizika **21**, 781–784 (1975).

[304] P. Virtanen et al., 'SciPy 1.0: Fundamental Algorithms for Scientific Computing in Python', Nat. Methods **17**, 261–272 (2020).

[305] D. Volkov, 'Über eine Klasse von Lösungen der Diracschen Gleichung', Z. Phys. **94**, 250–260 (1935).

[306] V. Votruba, 'Pair Production by γ-Rays in the Field of an Electron', Phys. Rev. **73**, 1468 (1948).

[307] S. Weinberg, ‘A model of leptons’, Phys. Rev. Lett. **19**, 1264 (1967).

[308] S. Weinberg, *The quantum theory of fields. Vol. 1: Foundations* (Cambridge University Press, 1995).

[309] S. Weinberg, *The quantum theory of fields. Vol. 2: Modern Applications* (Cambridge University Press, 1995).

[310] V. Yakimenko, L. Alsberg, E. Bong, G. Bouchard, C. Clarke, C. Emma, S. Green, C. Hast, M. Hogan, J. Seabury, et al., ‘FACET-II facility for advanced accelerator experimental tests’, Phys. Rev. Accel. Beams **22**, 101301 (2019).

[311] T.-M. Yan and S. D. Drell, ‘The Parton Model and its Applications’, Int. J. Mod. Phys. A **29**, 0071 (2014).

[312] P. Zhang, S. Bulanov, D. Seipt, A. Arefiev, and A. Thomas, ‘Relativistic Plasma Physics in Supercritical Fields’, Phys. Plasmas **27**, 050601 (2020).

[313] D. Zwillinger, *CRC standard mathematical tables and formulae* (CRC press, 2002).

Danksagung

Allen voran möchte ich Professor Dr. Burkhard Kämpfer danken, dass er mir dieses sehr interessante Thema eröffnet hat und mich im Zuge der Bearbeitungen immer wieder dazu brachte meinen wissenschaftlichen Horizont zu erweitern. Im gleichen Atemzug danke ich auch Prof. Dr. Thomas E. Cowan, welcher mich als Doktorand aufnahm und mir in seiner Position als Institutsdirektor und als Leiter des HIBEF Konsortiums eine exzellente Arbeitsumgebung geschaffen hat.
Des Weiteren danke ich Prof. Dr. Roland Sauerbrey und Dr. Ulrich Breuer, da ohne ihre Arbeit als Direktoren des HZDR die vorliegende Arbeit nicht möglich gewesen wäre.
Ebenfalls gilt mein Dank meinen Kollegen am Institut für Strahlenphysik, wobei ich vor allem Robert Greifenhagen, Dr. Andreas Otto, Dr. Roland Kotte, Dr. Lothar Naumann und Dr. Xingming Fan hervorheben möchte. Danken möchte ich auch Dr. Michael Bussmann und den Mitarbeitern der Arbeitsgruppe Computergestützte Strahlenphysik, dass sie mir stets einen Blick über meinen Tellerrand ermöglichten.
Außerdem danke ich Prof. Dr. Ralf Schützhold und seiner Arbeitsgruppe für ihre Gastfreundschaft in den letzten Phasen meiner Promotion. Die Kaffeerunden waren eine echte Bereicherung.

Besonders danken möchte ich meinen Freunden, welche mich in schwierigen Zeiten aufgebaut und in guten Zeiten ertragen haben.
Den herzlichsten Dank möchte ich meiner Familie zukommen lassen, allen voran meinen Eltern und meinen Geschwistern, welche mir über all die Jahre immer eine Stütze gewesen sind.

Meine tiefste Dankbarkeit gebührt meiner wundervollen Frau Susann, für ihr unbändiges Verständnis und ihre aufopferungsvolle Unterstützung. Te quiero mi corazón.

Erklärung

Hiermit versichere ich, dass ich die vorliegende Arbeit ohne unzulässige Hilfe Dritter und ohne Benutzung anderer als der angegebenen Hilfsmittel angefertigt habe; die aus fremden Quellen direkt oder indirekt übernommenen Gedanken sind als solche kenntlich gemacht. Die Arbeit wurde bisher weder im Inland noch im Ausland in gleicher oder ähnlicher Form einer anderen Prüfungsbehörde vorgelegt.

Diese Dissertation wurde am Helmholtz-Zentrum Dresden-Rossendorf unter der wissenschaftlichen Betreuung von Herrn Prof. Dr. Burkhard Kämpfer angefertigt. Ich habe bisher an keiner Institution, weder im Inland noch im Ausland, einen Antrag auf Eröffnung eines Promotionsverfahrens gestellt. Ferner erkläre ich, dass ich die Promotionsordnung der Fakultät Mathematik und Naturwissenschaften der Technischen Universität Dresden vom 23.02.2011 anerkenne.

Datum Unterschrift